Common-Aperture Dual-Polarized Transceiver Antenna Systems for Millimeter-Wave Polarimetric Radar

by

Tanner J. Douglas

A dissertation submitted in partial fulfillment
of the requirements for the degree of
Doctor of Philosophy
(Electrical and Computer Engineering)
in the University of Michigan
2022

Doctoral Committee:

Professor Kamal Sarabandi, Chair
Professor Anthony Grbic
Professor Xianglei Huang
Associate Research Scientist Adib Y. Nashashibi

Tanner J. Douglas

tjdoug@umich.edu

ORCID iD: 0000-0002-5553-9121

© Tanner J. Douglas 2022

To my late grandmother, Berenice Douglas

ACKNOWLEDGMENTS

The completion of this doctoral dissertation would not have been possible without the support of a great many individuals at the University of Michigan and elsewhere. I wish to acknowledge the contributions of these people, and to offer them my sincere gratitude.

First and foremost, I would like to thank my research advisor, Professor Kamal Sarabandi, for his guidance and support throughout my time as his Ph.D. student. With his wisdom, patience, and unparalleled electromagnetic intuition, he was always able to point me in the right direction any time I was stuck, and was always willing to stand up for me without hesitation. I have learned a tremendous amount from his knowledge, and been inspired by his philosophy. Next, I would like to thank Dr. Adib Nashashibi for all his assistance with laboratory equipment, measurement setups, and machining, as well as for his mentorship and collaboration on many of my projects. I would also like to thank Professors Anthony Grbic and Xianglei Huang for the valuable advice they provided while serving as members of my dissertation committee.

I wish to extend my gratitude to all of the former and current Radiation Laboratory students with whom I have shared experiences with during my graduate education. In particular, I would like to thank Dr. Mani Kashanianfard, Dr. Amr Ibrahim, Dr. Mohammad Amjadi, Dr. Behzad Yektakhah, Dr. Armin Jam, and Michael Benson for their mentorship as senior students, and for their patience and kindness when offering their assistance. Additionally, I am grateful to Dr. Menglou Rao, Abdelhamid Nasr, Aditya Muppala, Dr. David Geroski, Dr. Navid Barani, Dr. Fatemeh Akbar, Francis Salas, Dr. Brian Raeker, Dr. Luke Szymanski, Michael Giallorenzo, Lisa

Smith, Weihui Gu, Dr. Cody Scarborough, Dr. Abdulrahman Alaqeel, Jinkai Wu, Kaleo Roberts, Duncan Madden, Abdullah Alburadi, and Ehsan Hafezi for their friendship, academic discussions, collaboration, and other contributions to my experience.

I greatly appreciate the administrative support provided by current and former staff in the Electrical Engineering and Computer Science Department, including Leland Pierce, Michelle Chapman, Jennifer Feneley, Alesha Montgomery, Kate Godwin, Kim Novak, Anne Rhoades, Steven Pejuan, José-Antonio Rubio, and Kristen Thornton.

I would like to acknowledge the General Motors Company and the King Abdulaziz City for Science and Technology for their financial support of the projects I have worked on, and to thank the respective collaborators from these agencies, Stephen Decker and Dr. Hussein Shaman.

I would also like to acknowledge the Lurie Nanofabrication Facility at the University of Michigan for making available the tools and resources required for much of the fabrication done as part of this dissertation. I offer my thanks to the many staff members who operate the facility and who trained me to properly and efficiently utilize their resources. I am especially grateful to Katharine Beach for serving as my staff mentor, assisting with the development of my fabrication processes, and teaching me the majority of my micro- and nanofabrication knowledge.

I would like to thank my high school physics teacher, Alfred Fordiani, for challenging my mind, instilling in me a scientific mentality, and inspiring my pursuit of an engineering education. I also thank Professor James Bain at Carnegie Mellon University for fostering my aptitude for electromagnetics and encouraging me to pursue a doctoral degree.

Finally, I would like to thank my parents, Mark and Tracy Douglas, and my sister, Dr. Delaney Douglas, as well as my vast extended family, for their love and support throughout my life and during my graduate studies.

TABLE OF CONTENTS

LIST OF TABLES

LIST OF FIGURES

LIST OF ABBREVIATIONS

RADAR	Radio Detection and Ranging
RF	Radio Frequency
CW	Continuous Wave
FM	Frequency Modulation / Frequency-Modulated
PRISM	Polarimetric Radar Inversion for Soil Moisture
TEM	Transverse-Electric-and-Magnetic
V/H	Vertical/Horizontal (Polarization)
RHCP/LHCP	Right-/Left-Hand Circular Polarization
DAS/ADAS	Driver Assistance Systems / Advanced Driver Assistance Systems
LIDAR	Light Detection and Ranging
LASER	Light Amplification by Stimulated Emission of Radiation
MMIC	Monolithic Microwave Integrated Circuit
VCO	Voltage-Controlled Oscillator
CMOS	Complementary Metal-Oxide-Semiconductor
FCC	United States Federal Communications Commission
MIMO	Multiple-Input Multiple-Output
NASA	United States National Aeronautics and Space Administration

E-Band, J-Band	Waveguide Frequency Bands: 60 – 90 GHz, 220 – 325 GHz
GM	General Motors Company
KACST	King Abdulaziz City for Science and Technology
DRIE	Deep Reactive Ion Etching
OMT	Orthomode Transducer
PEC	Perfect Electric Conductor
CNC	Computer Numerical Control
RCS	Radar Cross-Section
MEFSS	Miniaturized Element Frequency Selective Surfaces
TE/TM	Transverse Electric / Transverse Magnetic
LNF	University of Michigan's Lurie Nanofabrication Facility
FEM	Finite Element Method
IACT	Isolated Antenna Calibration Technique
IE	Integral Equations
DC	Direct Current
PCB	Printed Circuit Board
IF	Intermediate Frequency
ISM	Industrial, Scientific, and Medical (Frequency Bands)
C-Band	Frequency Band: 4 – 8 GHz

ABSTRACT

The millimeter-wave radar is one of the key sensor technologies utilized in the automotive industry for advanced driver assistance systems and autonomous vehicles. Its ability to leverage phenomena such as the Doppler effect and the polarization of electromagnetic waves make it an extremely versatile sensor, capable of detecting position and velocity of potential roadway obstacles, as well as distinguishing between obstacles of different types (pedestrians, other vehicles, etc.) based on their polarization responses. Additionally, its relative insensitivity to precipitation and fog allows for all-weather operation, even in conditions that severely inhibit visibility. However, radar is not a perfect all-encompassing sensing solution; in particular, its most significant drawback is imaging resolution inferior to that of optical sensors like cameras and lidar.

A radar's resolution is closely linked to its antenna system. Angular resolution is improved with a narrow antenna beam, which translates to a large effective aperture. Similarly, fine range resolution is achieved using the frequency-modulated continuous-wave technique, which requires high transmit-to-receive antenna isolation. Typically, this isolation is accomplished with spatial separation between elements. Limited available mounting space on most vehicles prohibits the large antenna system size mandated by these requirements.

The focus of this dissertation is the development of an antenna system architecture which provides a very narrow beam and high isolation, while supporting dual-polarized transmit and receive capability for polarimetry applications. The use of a common transmit/receive aperture makes the antenna system relatively compact while eliminating parallax. The shared aperture is a

single dielectric lens, which focuses at both the transmit and receive feeds by means of a novel polarization-independent spatial power divider. This device was designed using concepts from the flourishing field of electromagnetic metamaterials and metasurfaces, and can be constructed using standard semiconductor fabrication techniques.

While modern automotive radars operate at the 79 GHz band, there is a strong interest in exploring higher millimeter-wave frequencies (particularly the 230 GHz band) for future systems. The shift to a shorter wavelength will result in improved angular and range resolution while reducing antenna size. Therefore, separate versions of the common-aperture dual-polarized transceiver antenna system have been designed for operation at the two bands. One of the challenges of moving to higher frequency is the availability and performance of millimeter-wave electronics and waveguide components. In support of high frequency dual-polarized radar antennas, an orthomode transducer with a simple structure has been designed for reduced fabrication complexity at the 230 GHz band.

Additionally, there is currently a lack of data on the backscattering properties of many target classes at 230 GHz. The antenna and orthomode transducer designs of this work have been incorporated as part of the front ends of radar systems operating at this band. As a demonstration of the utility of 230 GHz radar, as well as the antenna system itself, a set of polarimetric backscattering measurements of several road surfaces is presented. Such data can be used to inform algorithms for discrimination between different surfaces, and assessment of road conditions.

Another topic in this dissertation is the design of a low-profile passive reflector, which can enable radar sensors to detect and identify road markings, a task currently handled only by cameras. As an appendix, a planar antenna system with high isolation for wireless communication and radar applications at 6 GHz is presented.

CHAPTER 1
Introduction

1.1 Background and Motivation

The primary topic of this dissertation is the design of common-aperture dual-polarized transceiver antenna systems, the main application of which is in high-resolution polarimetric radar at millimeter-wave frequencies. In particular, this work has contributed to the construction of several radar systems for use in phenomenological studies of automotive environments. To develop an appreciation for the contributions presented herein, a brief history of the field of radar is provided, followed by a discussion of the role radar has played in the automotive industry. Finally, some of the state-of-the art technologies in this field are described, as well as current research trends. The unique antenna system designs contributed by this research are motivated and inspired by these concepts, with a specific goal to make use of the Doppler and polarimetry capabilities of radar while improving imaging resolution by taking advantage of new frontiers at high millimeter-wave frequencies.

1.1.1 History of Radar

The word “radar”, originally an acronym for Radio Detection and Ranging (RADAR), describes an active sensor system consisting of both a receiver and a transmitter of radio-frequency (RF) electromagnetic waves used to detect external objects [1]. A radar system typically functions by emitting an electromagnetic wave from the transmitter antenna, and recording a portion of that

wave that scatters from the environment to the receiver antenna. If the transmitter and receiver are collocated, the radar system is said to be monostatic; if the antennas are located at separate positions, the system is said to be bistatic. The first radar, then called a telemobiloskop by its inventor, Christian Hülsmeyer, was demonstrated to detect a ship more than a century ago in 1904 [2]. As the technology developed, it soon attracted great interest for military applications, and starting in 1922, scientists at the United States Naval Research Laboratory under Albert H. Taylor began experimenting with continuous-wave (CW) radar systems to detect ships and aircraft [3]. The first pulsed radar system was devised in 1925 by Gregory Breit and Merle A. Tuve to record echoes from the ionosphere, and thus measure its height [4]. Prior to World War II, frequency modulation (FM) techniques had been employed in early airborne radars serving as altimeters with accuracy superior to that of the traditional barometric variety [5]. Over the course of the next few decades, radar technology matured significantly, giving rise to a number of breakthroughs including imaging via mechanical antenna scanning, side-looking airborne radar, and synthetic aperture radar [6].

While many of these early radar systems were designed to detect and measure the distance to a target object such as a vehicle, the ground, or the ionosphere, it was soon realized that additional information about a target's velocity could be extracted by making use of the Doppler Effect. This phenomenon, first stated by Christian Doppler in 1842, refers to the dependence of the observed frequency of a wave on the relative velocity between its source and the sensor [7]. Just as one may notice that the pitch of the noise produced by the engine of a car seems to drop as the vehicle passes by, Doppler noticed a relative "redshift" and "blueshift" of the visible light emitted from stars in binary pairs as they orbit each other. The pioneers of both pulsed and CW radar noticed this same effect in RF electromagnetic waves, and by the late 1940s, Doppler radar

was being researched by the American and British militaries for the purpose of aircraft navigation [8]. It was later found to be useful in civilian applications, especially for allowing weather radar to measure the motion of storms, which lead to the eventual creation in 1988 of the Weather Surveillance (Doppler) Radar network, or WSR-88D, which now operates at over 160 locations providing coverage of the United States [6], [9]. In target detection applications, Doppler processing can be used to distinguish scattering signatures from multiple objects with different velocities, or to isolate the return of moving objects in the presence of strong clutter from a stationary background.

In addition to measuring position and velocity of discrete targets, radar can also be used in the classification of distributed targets, such as in the application of remote sensing of the earth from spaceborne platforms. Many types of earth terrain can be characterized as random rough surfaces, such as soils or water surfaces with waves; others, such as forest vegetation or snow, may be treated as random media [10]. Being random by nature, the electromagnetic scattering from such distributed targets are not exact, but follow some probabilistic distribution. Using a combination of computational modeling and databases of previously made in-situ and remote measurements, the scattering statistics recorded by imaging scatterometer radars can be used to identify terrain pixels, or even retrieve physical parameters through inverse scattering models. One of the first large-scale efforts making use of these ideas was an airborne radar mapping project that took place in Panama in 1967. The study provided detailed maps of terrain features such as water drainage, vegetation, and geological formations, in an area where frequent cloud cover prevented the generation of such data using optical photography [11].

Often such scattering measurements benefit from the polarization of electromagnetic waves, which refers to the orientation of the oscillating electric and magnetic fields that comprise

the wave. An example is the Polarimetric Radar Inversion for Soil Moisture (PRISM), which is a set of inversion algorithms for estimating soil surface roughness and moisture content from radar backscattering measured in several polarizations [12], [13]. In a transverse-electric-and-magnetic (TEM) wave, such as the spherical waves produced in the far field of transmitter antennas or scattering objects, the electric field, magnetic field, and wave vector form a right-handed orthogonal set. Thus the electric and magnetic fields lie in a plane perpendicular to the direction of propagation of the wave. Using the propagation direction along with some reference plane (typically chosen to be the plane containing the horizon and perpendicular to the zenith), the polarization of a wave may be described by decomposing the electric field into components along the vertical (V) and horizontal (H) directions. The polarization may be linear, circular, or elliptical, depending on the relative amplitude and phase of the V and H components. Discrete and distributed targets may exhibit preferential scattering of waves with a particular polarization. The scattering profile as a function of incident and scattered polarization is known as the polarization response of the target. The measurement and analysis of polarization response is referred to as polarimetry, and radars that exploit multiple polarizations are said to be polarimetric. For monostatic radar, the complete polarization response of the backscattering from any target can be described if the magnitude and phase of the V and H co-polarized and cross-polarized scattering coefficients are known. This concept is known as polarization synthesis, and it allows for the calculation of the backscattering that would result from any combination of incident and scattered polarizations without needing to design a radar with that specific antenna polarization configuration [14]. The same is true for other orthogonal polarization bases, such as two orthogonal linear polarizations with an angular rotation with respect to the V and H directions, or right-hand circular polarization (RHCP) and left-hand circular polarization (LHCP). The development of polarimetric radar saw

little progress until the 1970s and 1980s, after the work of J. R. Huynen [15] and Wolfgang-Martin Boerner [16], but has since become an important tool for remote sensing [17].

1.1.2 Radar in Automotive Applications

With the background information presented above, it is no surprise that radar has recently found applications in the automotive industry for both driver assistance systems and autonomous vehicle operation. The roadway environment contains a large number of very different objects which must be observed, interpreted, and often avoided. Traditionally this tremendous task is handled by the immense cognitive power of the human brains of vehicle operators. However, sensor systems for driver assistance seek to reduce some of that burden or provide redundancy in case of operation error, and sensors for autonomous vehicle applications hope to eliminate the need for a human driver altogether. Radar is an excellent sensor choice for these applications. In the most basic sense, radar can detect objects on the road that vehicles must navigate around, including pedestrians, animals, debris, and other vehicles. By exploiting the Doppler capabilities of radar, information about relative velocity can be acquired to determine the most immediate hazards. The asphalt of the road itself, as well as substances that may cover it such as water, ice, snow, or oil, can be regarded as combinations of random rough surfaces and random media, and thus the scattering from the road surface can provide information about driving conditions. Polarimetry can be leveraged in these surface measurements, as well as to discriminate between different types of obstacles which may exhibit different polarization responses.

In the automotive industry, features designed to ensure the safety of drivers, passengers, and pedestrians may be classified as either passive or active. Passive safety systems serve to mitigate the consequences of an accident, and examples include bumpers, seatbelts, and airbags. Active safety systems take a direct role in the prevention of such accidents, and may also be

referred to as Driver Assistance Systems (DAS) [18]. They do so using sensor information about the state of the vehicle, such as cruise control and antilock brakes [19]. An Advanced Driver Assistance System (ADAS) additionally makes use of information about the external environment around the vehicle [18]. DAS and ADAS can be categorized into one of several levels of automation defined by the Society of Automotive Engineers, ranging from no automation to full vehicle autonomy [20]. Descriptions of these automation levels are provided in Figure 1.1. The ADAS in the lower levels may simply provide additional information to the driver (Level 0), or intervene in control of the vehicle (Levels 1-2), and typically make use of perceptive instruments such as cameras, radar, and ultrasonic sensors. A list of some common ADAS technologies organized by automation level, and indicating the sensors they typically rely on, is provided in Table 1.1. Technologies that are categorized as Level 3 usually support the same sort of functionality as those in the lower levels, but with increased situational applicability and robustness. In particular, a requirement for this level is sensor redundancy. This is often achieved by the inclusion of "lidar", which is a word that originates in a manner similar to "radar" as an acronym of Light Detection and Ranging (LIDAR) and refers to a system that detects the backscattering of a pulsed "laser" (Light Amplification by Stimulated Emission of Radiation, LASER [21]) light source [22], to supplement other sensor instruments. Levels 4 – 5 are distinguished from 0 – 3 primarily by advanced computational algorithms for interpreting sensor input and making control decisions, rather than by the sensor technologies employed [18]. The progression of ADAS toward full vehicle autonomy requires advancement in both the algorithmic aspects and the sensor technologies, including the improvement of automotive radar system capabilities.

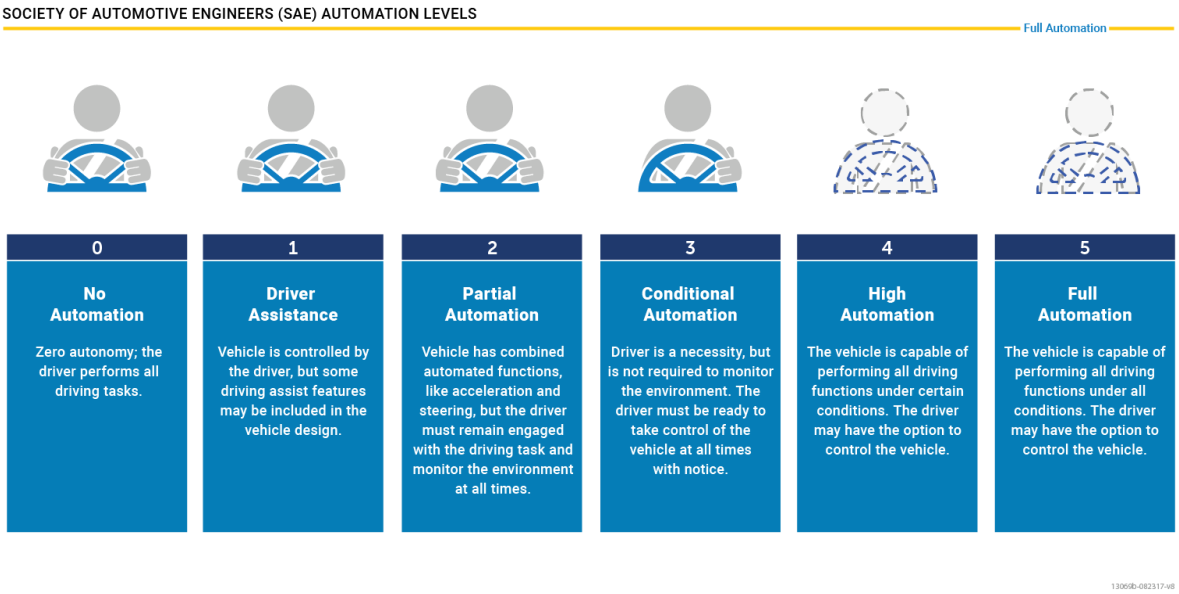

Figure 1.1. Description of automation levels defined by the Society of Automotive Engineers for classification of DAS technologies (reprinted from [20]).

Table 1.1
List of some common ADAS technologies, their automation levels, and the types of sensors they typically employ.

		Sensors Typically Employed		
Automation Level	**ADAS Technology**	**Camera**	**Radar**	**Ultrasonic**
Level 0	Parking Sensors			×
	Surround View	×		
	Traffic Sign Recognition	×		
	Lane Departure Warning	×		
	Night Vision	×		
	Blind Spot Detection		×	
	Rear Cross-Traffic Alert		×	
	Forward Collision Warning	×	×	
Level 1	Adaptive Cruise Control	×	×	
	Emergency Brake Assist	×	×	
	Lane Keeping/Centering	×		
Level 2	Highway Assist *	×	×	
	Autonomous Obstacle Avoidance	×	×	
	Autonomous Parking	×		×

* Combines functionality of Adaptive Cruise Control, Lane Centering, and Blind Spot Detection

Table 1.2
List of capabilities of current ADAS sensor technologies (adapted from [23]).

	Camera	Radar	Ultrasonic	Lidar	Fusion
Vehicle Detection	×	×	×	×	×
Texture Interpretation	×				×
Independent of Ambient Light		×	×	×	×
All-Weather Operation		×	×		×
Low Cost	×	×	×		×
Operation Range	mid-far	near-far	near	mid-far	near-far
Angular Resolution	high	medium	low	high	high
Specialty	classification, texture	motion	low cost	3D mapping	

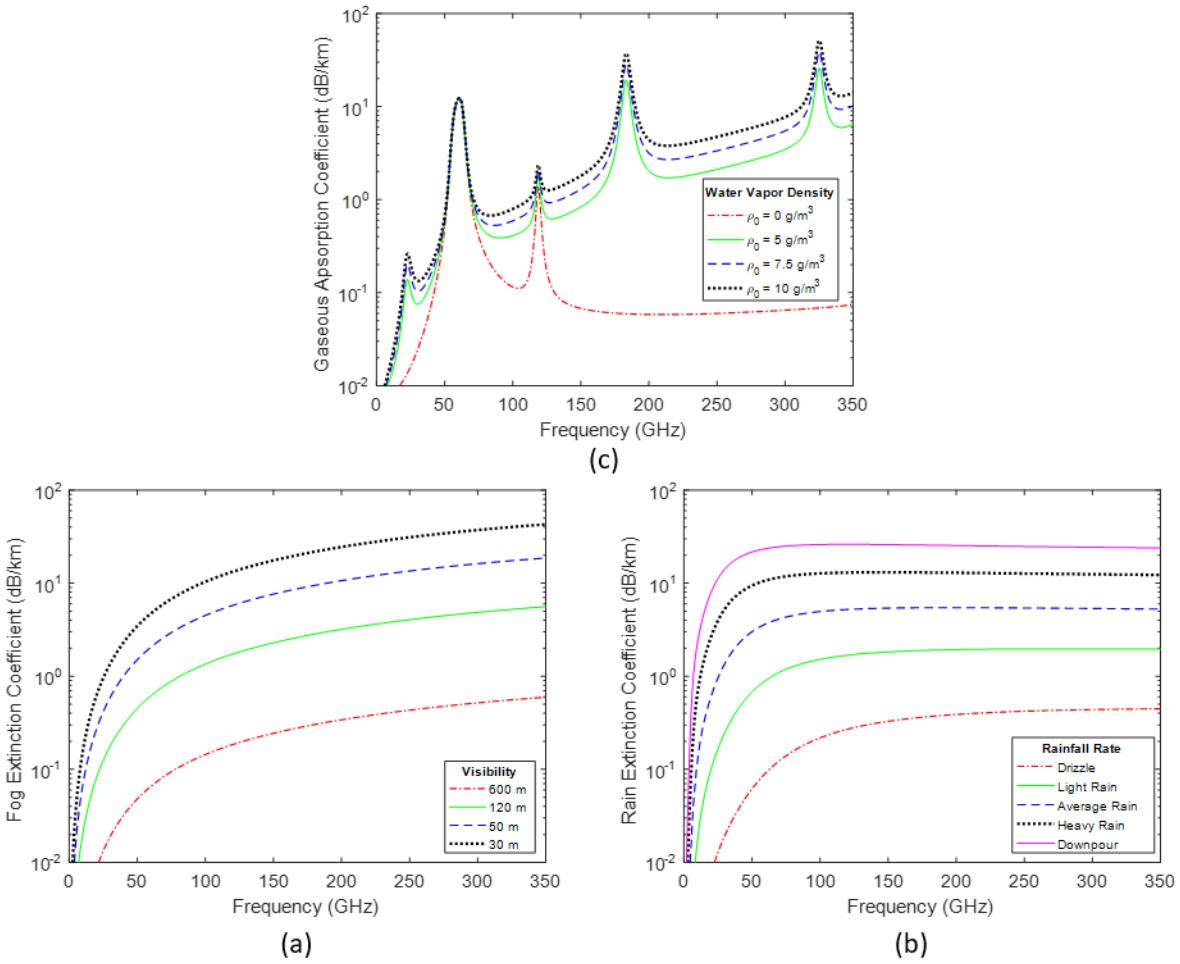

Figure 1.2. Plots showing attenuation of electromagnetic waves at microwave frequencies due to (a) oxygen and water vapor gasses, (b) fog, and (c) rain. Standard sea-level pressure and a temperature of 10°C are used (made with code from [24]).

Currently a combination of ultrasonic, camera, radar, and lidar sensors are employed to form a data fusion for ADAS technologies. Each of these sensor types has its own benefits and disadvantages, some of which are listed in Table 1.2 [23]. It can be seen that using them together helps produce a more complete picture of the environment. It is worth noting that radar and ultrasonic sensors are in many ways redundant with each other, with radar providing greater range and better resolution, but ultrasonic being less expensive. It is conceivable that radar could ultimately take over the duties currently handled by ultrasonic [23]. Compared with cameras and lidar, which struggle with weather conditions such as fog and precipitation, radar is able to perform quite well in these circumstances. This is because at microwave frequencies, attenuation due to atmospheric gas constituents and liquid water particles is relatively small. Figure 1.2 indicates that under reasonable levels of humidity, fog, and rain, attenuation across the entire microwave band (excepting close to a few oxygen and water vapor absorption lines) can be limited to the order of tens of dB/km, which corresponds to only several dB at the typical range for automotive radar applications [24]. Radar mainly falls short of cameras and lidar in terms of the angular resolution that is possible, and the ability of cameras to distinguish textures, such as road markings. While it will likely remain prudent to continue to utilize a fusion of different sensor types for redundancy in the future, discussions of how radar may overcome these limitations are among the topics addressed in this dissertation.

The earliest experiments in radar for automotive applications began in the 1960s in the United States, and involved placing active reflectors on the backs of cars, so that they may be detected by the radars mounted on other cars. This approach was quickly found to be unviable because the reflectors could easily end up in improper positions, and focus was shifted to detection of all passive targets [25]. In the 1970s, early radars were designed to operate at 10 GHz, and the

large systems were mounted on top of the vehicles. Increase of the frequency to 16 and later 35 GHz allowed the smaller radars to be mounted in front of the bumper and then integrated into the front of the car [26]. Blind spot detection was first implemented using a 16 GHz system by Dunlop and Bendix [27]. From the 1970s to 1990s, other frequency bands were explored as well: 94 GHz was accessible due to availability of components from previous military applications at this frequency, and Japanese companies lead by Toyota, Nissan, and Honda utilized the 60 GHz band for compatibility with existing components for communications applications [26], [28].

In the 1990s, focus began to shift to the 24 – 26 GHz band and the 77 GHz band. The 1995 side detection sensor from Hughes Electronics operated at 24 GHz, and this has since become the standard for side-looking automotive radar applications such as blind spot detection and rear cross-traffic alert [29]. German automotive engineers led the push for 77 GHz systems, which have become standard for long-range forward-looking radar used in applications such as forward collision warning, adaptive cruise control, and emergency brake assist. In general, the trend toward higher frequency operation was motivated by the increased availability of absolute bandwidth, which is important because of the improved resolution capability of FMCW radar, as well as the possibility of using frequency hopping schemes to reduce interference from the radars of nearby vehicles. Higher frequency also offers more compact radars due to the smaller wavelength. The 77 GHz band in particular was targeted due to the minimum in atmospheric attenuation at this frequency, as well as the emerging GaAs monolithic microwave integrated circuit (MMIC) technology at this time. MMICs enabled small integrated voltage-controlled oscillator (VCO), mixer, and amplifier components that could be made compatible with microstrip transmission lines and patch array antennas. Cost scaling was also possible, as the more sensor technologies moved to this band, the higher the demand for MMICs and the lower their per-unit production cost [28].

Only in the last decade has it been possible to replace the GaAs chips with complementary metal-oxide-semiconductor (CMOS) technologies operating at this high frequency [30].

While automotive radar development has progressed along with the technologies available, it has also seen considerable dependence on the opinions of the public. As an example, Eaton Corporation's 1992 forward collision warning system [31] was one of the first large-scale radar deployments, being installed on 1500 Greyhound busses and thousands of other trucks. The campaign demonstrated over the course of the year of 1993 that collision frequency and severity could be significantly reduced using radar sensor technology. However, the radars were eventually removed due to opposition from the unionized drivers, who felt that the data undermined their privacy [25], [26], [28]. Another example is Mercedes' 77 GHz Distronic line for adaptive cruise control, which was first produced in 1998, and later upgraded in 2006 for inclusion in some premium car models. It was initially not received well by customers, and only in 2011 after a re-branding as an emergency brake assistance system was it offered as a special feature in more standard models [32]. In 2014 it was made a standard feature for the Mercedes C-Class sedan [26]. These examples highlight the hesitancy of the public to adopt widespread use of ADAS, and this is still an important consideration today. Sensor technologies will need to be extremely reliable to convince the public to trust fully autonomous vehicles, for instance.

1.1.3 Current State of the Art

Current automotive radar systems usually utilize a silicon-based RF-CMOS transistor technology for the high frequency components, and employ the FMCW modulation scheme. They operate in one of several bands allocated for their use. The traditional 24 GHz band spans from 24.05 GHz to 24.25 GHz. The more modern 77 and 79 GHz bands, respectively range from 76 GHz to 77 GHz and from 77 GHz to 81 GHz [23]. There have also historically been ultra wideband

systems operating from 21.65 GHz 26.65 GHz. However, in 2017 the United States Federal Communications Commission (FCC) decided to phase out operation of automotive radar in this band in order to reallocate it for other purposes, and to encourage consolidation of future automotive radar to 76 – 81 GHz [33]. Thus going forward, focus will be on the 77 and 79 GHz bands. Additionally, the FCC lists allocations for radiolocation applications in higher frequency bands at 92 – 100 GHz, 136 – 148.5 GHz, 151.5 – 155.5 GHz, and 231.5 – 248 GHz [34].

One major trend in radar development is to improve the resolution so that imaging can be achieved. Imaging is much more easily performed with a camera or lidar than with a radar due to the wavelength of the respective light waves. At optical frequencies, a lens that is many times larger than the wavelength may be used, which results in very fine resolution. The angular resolution for an advanced camera system may be as fine as 0.027° [23]. For compact radar operating in the 77 and 79 GHz bands, the effective aperture formed by the radar's antenna, often implemented as a microstrip patch array, may only be a few wavelengths in size. The wide beam that results limits the resolution.

A cost-efficient technique to produce a larger effective aperture is to use a multiple-input multiple-output (MIMO) radar system [35], [36]. In this approach, multiple independent signals are transmitted from several transmit elements, and then detected by several receive elements. Signals propagating from each pair of transmitter and receiver element can be thought of as an independent virtual receive channel. The resolution of the system is determined by the number of virtual channels, which is the product of the number of transmit and receive elements, and thus a given effective aperture can be realized with fewer total antenna elements than with a single transmit element and physical array of receivers only, for example. Digital processing is used to estimate angle of arrival of backscattered signals from the targets [37]. In 2018, Magna revealed

the Icon radar, which is advertised as the automotive industry's first commercially available software-defined digital radar. The system uses 192 virtual elements and is capable of the detection of targets at ranges greater than 300 m with 1.5° angular resolution and 30 cm range resolution. It will be available in cars in 2022 [38]. Arbe's Phoenix radar uses 48 transmit and 48 receive channels, and quotes performance specifications very similar to the Icon [39]. Oculii's Eagle radar claims to achieve a 0.5°/1.0° azimuth/elevation resolution and a range of over 350 m with over 2000 virtual channels, enabled by their Virtual Aperture Imaging software [40].

Another perhaps more obvious approach is to utilize an antenna with a physically large aperture. This can be difficult to achieve with microstrip patch arrays due to increasing loss as the array size grows [41]. Other options include reflector [42] and lens [43] antennas, which collimate the wide beam of a small low-loss feed antenna into a highly directive one. This can be done relatively independently of frequency, which invites the consideration of using higher microwave frequencies. In terms of angular resolution, which is determined by antenna beamwidth, a shift to higher frequency is equivalent to increasing the aperture size since it is the electrical size (the size relative to a wavelength) of the aperture that is truly important. Additionally, at higher frequencies the absolute signal bandwidth afforded by a given fractional bandwidth is larger, which translates to finer range resolution in FMCW radar systems. Of particular interest is the band from about 220 GHz to 250 GHz. Recall that there is allocation for radiolocation at these frequencies [34], and that atmospheric absorption lines are conveniently avoided (see Figure 1.2). There has been increasing interest in radar operating at this submillimeter-wave band over the last decade in order to exploit these advantages. Of course, there are a number of challenges associated with such a shift, most notably the cost and limited availability of the required high frequency components [44]. However, recent developments in transistor and integrated circuit technologies have made

the idea possible [45]. There have since been advances in FMCW radar systems utilizing lens antennas at these frequencies [46], [47]. Additionally, lens antennas can feature dual-polarized feeds, which enables polarimetric radar measurements [48], [49], [50]. As noted previously, this may be useful in future automotive radar for classification of different objects and surfaces in road environments. Another antenna architecture worth mentioning is a travelling-wave antenna featuring a patch array excited by a micromachined meandered waveguide, capable of beam scanning via a frequency sweep. This antenna operates at 230 – 245 GHz and achieves a beamwidth of 2° in the azimuth plane [51].

While the primary application area for polarimetric radar discussed in this dissertation is in the automotive industry, it is important to note some of the other potential applications of this research. Radar is extremely useful in military, defense, and security applications for detection of distant objects or ones that may be otherwise concealed. Applications in remote sensing of the earth have been briefly discussed already, and radar can be used in atmospheric remote sensing applications as well. As a particular example, The United States National Aeronautics and Space Administration (NASA) is working on a new spaceborne instrument featuring a 239 GHz radar for studying cirrus clouds [52].

1.2 Dissertation Overview

The background information provided in the previous section includes a history of radar technology and some of the phenomena that make radar a unique category of sensor, such as Doppler processing, polarimetry, and weather penetration. It also highlights the importance of radar in the automotive industry through a discussion of past, present, and future trends in this field. Motivated by these ideas, the work of this dissertation relates to advancing automotive radar

technology by studying antenna designs that improve resolution while enabling polarimetric capability.

The focus of this dissertation is the realization of a dual-polarized two-port antenna system with a common aperture shared between the ports. This antenna has applications in fully polarimetric radar with very fine angular resolution, especially for use in future ADAS technologies and autonomous vehicles. Variations of this antenna design are completed at E-Band (60 – 90 GHz) and J-Band (220 – 325 GHz), the former being consistent with modern automotive radar standards and the latter following trends in pushing the operation frequency upward to enhance performance capability. The critical component of this antenna system is a novel polarization-independent spatial power divider, which serves to split an incident wave into two orthogonally directed components with equal amplitudes, regardless of its polarization. To utilize this antenna for J-band polarimetric radar, an orthomode transducer is developed to selectively excite a particular transmit polarization, as well as to simultaneously receive both vertically and horizontally polarized return signals. The antenna system was incorporated into E- and J-band radars for phenomenological studies of roadway environments. These radar projects were sponsored by the General Motors Company (GM) and the King Abdulaziz City for Science and Technology (KACST). For convenience, three radars will be referred to as “the GM E-band radar”, “the GM J-band radar”, and “the KACST J-band radar” or simply “the KACST radar” throughout this dissertation. As a demonstration of the benefits of radar with such an antenna, some measurements of the backscattering from various road surfaces at near-grazing incidence made with the GM J-band radar are presented.

Chapter 2 provides an overview of the common-aperture dual-polarized transceiver antenna design. The antenna uses a dielectric lens as the common aperture, which is illuminated

by two orthogonally oriented dual-polarized feeds. The feeds have their beams directed toward the lens by the polarization-independent spatial power divider. These components are held together in the proper locations by a 3D-printed housing. The measured performance of the implementations at E- and J-band are reported. The E-band antenna has a gain of about 36 dB and a beamwidth of about 1.5° for each port and polarization. Its isolation between ports is greater than 45 dB. The J-band antenna has a gain of about 39 dB and a beamwidth of about 1.0° for each port and polarization. Its isolation between ports is greater than 40 dB.

Chapter 3 describes in detail the design of the polarization-independent spatial power divider, which is key component of the antenna system. The operation theory of the power divider involves a structure of layered corrugated dielectric slabs, which act as artificial anisotropic dielectric materials. A combination of an analytical model and full-wave electromagnetic computations is used to optimize the slab parameters for the desired reflection and transmission coefficients from the entire structure. It is the reflection and transmission of a wave incident at 45° that splits it into two components in perpendicular directions. Fabrication of the power divider is completed using deep reactive ion etching (DRIE) of a silicon wafer. Two different power divider designs are completed for slightly different operation bands at J-band, and another is designed to operate at E-band. The measured reflection and transmission coefficients are presented for each. All instances exhibit a low difference between reflection and transmission for both polarizations, and around 1.1 dB of loss due to the conductivity of the silicon.

Chapter 4 covers the design of a simple-structure J-band orthomode transducer (OMT). An OMT is a three-port waveguide device which consists of one “common port” supporting two orthogonally polarized modes, and two single-mode ports with orthogonal polarization. When operating in transmission, either of the modes of the common port can be excited by the

corresponding single-mode port. During reception, the two modes of the common port become separated into the corresponding single-mode ports. Two OMTs are required for the front end circuitry supporting the two-port dual-polarized antenna. At J-band, the small features of the waveguides make the manufacture of such devices challenging. Many of the state-of-the-art OMT designs have geometry that is far too complex to machine with standard tools. The OMT presented here is simple enough to make fabrication easily amenable, while still providing satisfactory performance over the desired band. Simulation and measurement results are presented for two realizations at slightly different operation bands.

The antenna system and supporting components discussed in Chapters 2 – 4 were integrated into fully polarimetric radar systems operating at E-band and J-band. The GM J-band radar was used to make a series of measurements of various road surfaces at near-grazing incidence, which is the subject of Chapter 5. These measurements provide data on the typical polarization response of backscattering from surfaces likely to be encountered from the perspective of a radar mounted on a vehicle. Surfaces measured include smooth and rough asphalt, asphalt covered in a thin layer of water, snow, and ice, gravel, and concrete. The measurements are calibrated by comparison to a known conducting sphere to extract the backscattering coefficients of the surfaces. The radar system specifications are briefly discussed before presenting the measurement results.

Chapter 6 presents the design of a small passive reflector device which could be arranged on roadways to be observed by automotive radars. The reflectors are small enough to be embedded in the painted markings used to assist traffic flow. This would provide a mechanism by which an autonomous vehicle could detect such markings by means of radar, rather than relying on optical image processing from cameras. The reflectors can be arranged to produce specific sequences of

sharp radar returns, which may encode the type of marking they represent. The first prototypes of these reflectors are fabricated using standard microfabrication processes, and it is supposed that extension to mass production is feasible. The design process, along with fabrication details and simulation and measurement results are presented in this chapter.

The dissertation concludes in Chapter 7 with a brief summary of the contributions presented and a discussion of some of the future work being pursued in this area. A list of publications covering the content of this dissertation is also provided.

As an appendix, a discussion of a high-isolation two-port planar antenna system for full-duplex wireless communication applications is presented. While this work is not directly related to the content of the main body of the dissertation, it constitutes itself an important innovation with potential significance, and therefore warrants inclusion. This antenna system consists of a planar arrangement of four patch elements, forming two two-element arrays which can be used simultaneously for transmit and receive. The patch elements are arranged to exploit a ninety-degree rotational symmetry which, when combined with polarization orthogonality, enables a measured transmit-to-receive isolation of greater than 60 dB at the operation frequency of 6 GHz. The operation theory, design process, and measurement results for this antenna are presented, along with a discussion of a modification to this design to enhance the bandwidth.

CHAPTER 2

Common-Aperture Dual-Polarized Transceiver Antenna System

The automotive industry continues to progress toward vehicle autonomy, necessitating implementation of high-reliability sensor systems for obstacle detection and collision avoidance. An essential component of this evolving technology is the millimeter-wave radar for middle- to long-range sensing. Currently, automotive radars operating at the 77 GHz band are used in several driver-assistive applications, some of which are listed in Table 1.1. For more demanding applications, such as the forthcoming autonomous vehicle application, radars with much higher resolution (both in range and cross-range) than existing systems are needed. Enhancing cross-range resolution involves achieving a narrower antenna beamwidth, which can be attained by enlarging the electrical dimensions of the antenna aperture. While this can be accomplished using physically larger antennas, the allotted physical space for automotive radars on vehicles prohibits doubling or tripling the size of the antenna for the traditional 24 GHz and 77 GHz automotive radars. One alternative is to operate the radar at higher millimeter-wave frequencies. Recently, there has been an increased interest in automotive radar systems operating specifically at around 230 GHz [49], [50]. More bandwidth is readily available at this band, resulting in improved range resolution. In addition, for the same antenna size, a radar operating at 230 GHz will possess a beamwidth that is approximately 3 times narrower than that at 77 GHz, resulting in much improved angular resolution [51]. Phenomenological studies of the radar backscatter response of vehicles at J-band were performed recently to identify the scattering phase-centers on vehicles, the significance of

cross-polarized return, and the statistics governing the radar response of vehicles [49], [53]. Additional studies are being pursued at J-band to characterize the polarimetric radar response of road surfaces at near grazing incidence in support of road surface assessment and road hazards mitigation applications [54].

Many millimeter-wave radar systems utilize two separate antennas for transmit and receive, with some separation distance between them [55]. Such designs allow the antennas to be quite compact, for example, by constructing the transmitter and receiver using planar arrays of patch antennas [56]. However, radars utilizing dual-polarized lens antennas must dedicate a significant amount of space to accommodate the two apertures [46], [49], [50].

Additionally, this approach suffers from a phenomenon known as radar parallax [57]. Figure 2.1 shows an illustration of this concept. Spatially separated transmit and receive antennas may have beams that only align well with each other over a certain range of target distances. This is especially the case for very narrow-beam antennas which are desirable for high-resolution radars. Typically, this manifests in the form of a blind spot at close range. Mitigation techniques include the use of a wider-beam antenna for transmit, receive, or both (at the cost of resolution and gain), and angling the two antennas on intersecting lines of sight (at the risk of introducing additional blindness at long range). Parallax can be a useful phenomenon, for example in the field of astronomy, where it is used to determine the distance to cosmic entities [58]. However, in radar applications where ranging is achieved through FMCW modulation or other techniques, it functions only as a limitation on the field of view.

Another option is to use the standard dual-polarized lens antenna configuration [59], [60], which features two single-polarized feed elements that both illuminate a common lens via a wire-grid polarizer. This allows for good beam alignment, but makes it much more difficult to

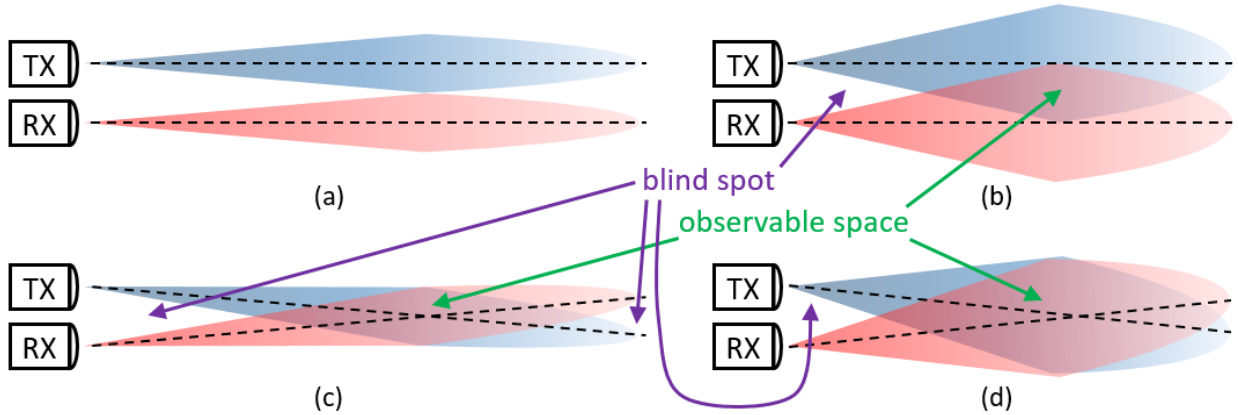

Figure 2.1. A conceptual illustration of radar parallax. For spatially separated transmit and receive antennas, especially ones with narrow beams, care must be taken to ensure the beams are aligned at the desired target area. (a) Parallel line of sight and narrow beam, (b) parallel line of sight and wider beam, (c) angled line of sight and narrow beam, (d) angled line of sight and wider beam.

implement a fully polarimetric radar system, which is important for distinguishing between obstacles and surfaces of different varieties [49], [61]. In this case, circulators would need to be used to isolate transmit and receive circuitry sharing the same single-polarized feed.

In either case, leakage from the transmitter to the receiver can be an issue, either through near-field coupling of the antenna elements, or through poor isolation of the circulators. This leakage signal from the transmitter can severely interfere with detection of backscatter from the target, even with the best analog and digital signal processing available [62], [63]. Given that both transmit-to-receive leakage and parallax are related to antenna separation, there exists a design trade-off between isolation and resolution for radars employing these aforementioned antenna systems.

2.1 Antenna System Overview

This dissertation describes an antenna system featuring a single lens with two dual-polarized feeds. Its geometry is similar to that of the standard dual-polarized lens antenna, except that the wire-grid polarizer has been replaced by a polarization-independent spatial power divider.

This is a device that, instead of completely reflecting one incident linear polarization and completely transmitting the other, transmits and reflects a certain fraction of the incident energy for both polarizations. Specifically, it has been designed with a goal of -3 dB reflection and transmission coefficients in mind. At 45-degree incidence, this will serve to split the incident wave into two equal-power portions directed along rays perpendicular to each other. More detail about the design of this spatial power divider will be presented in Chapter 3. The result of this substitution is an antenna system with perfect alignment between the beams of two dual-polarized ports, and high isolation due to the spatial separation of the feeds. One drawback is that half of the power will be lost every time a transmitted or received wave passes through the power divider. This is an acceptable concession, however, since the alignment between transmit and receive beams affords the use very high gain, which can more than compensate for these losses. With this type of antenna system, a radar can support parallax-free fully polarimetric operation with high isolation, fine resolution, and long range, and is more compact than a comparable two-aperture system.

A schematic of the antenna system is provided in Figure 2.2. Port 1, which in this depiction is acting as the transmit port, launches a wave into free space, which may be either vertically or horizontally polarized (elliptical polarization is also possible if desired, by simultaneously exciting the linear modes with a phase offset). The wave is then incident upon the spatial power divider, which is oriented at a 45-degree angle from the direction of propagation. The power divider is designed so that equal amounts of power are transmitted through and reflected from the surface, regardless of polarization. An absorber is placed to absorb the reflected wave, as otherwise the antenna would have a strong secondary beam, resulting in unwanted radar backscattering from an undesired direction. The transmitted wave continues until it reaches a lens, which serves to collimate the beam, providing a much larger effective aperture and greatly increasing the antenna's

gain. The backscattered signal passes back through the lens, which focuses the wave at the location of the feed horns. Again, half of the power is transmitted through the power divider, where it is disregarded by port 1. The remainder of the power is reflected from the power divider and collected by port 2, the receiver port. The transmit and receive ports may be interchanged, and the antenna system would function similarly.

The choice of a 45-degree incidence angle for the power divider surface has been made for convenience, as it allows the two horns to be oriented at a 90-degree angle from each other. A lower incidence angle would require feed 2 to be positioned closer to the lens, which may disrupt the radiation patterns and reduce transmit-to-receive isolation. A higher incidence angle may improve isolation, but would make placement of front-end circuitry more difficult, and require placing the absorber closer to the lens.

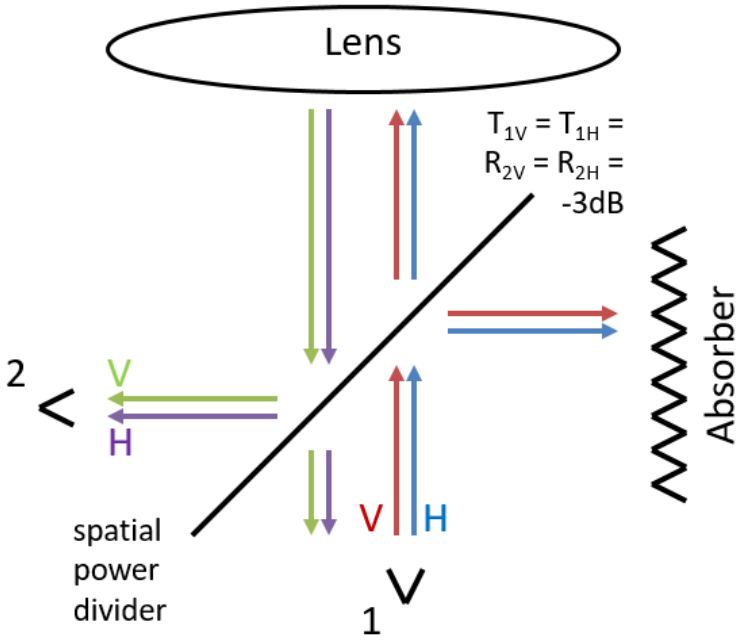

Figure 2.2. A schematic of the proposed antenna system. Two dual-polarized feed horns are oriented at a 90-degree angle from each other. Their beams are incident at 45 degrees on a 3 dB spatial power divider. Half of the transmitted power is lost to an absorber, while the other half propagates through a collimating lens, providing equal gain for both polarizations from both ports.

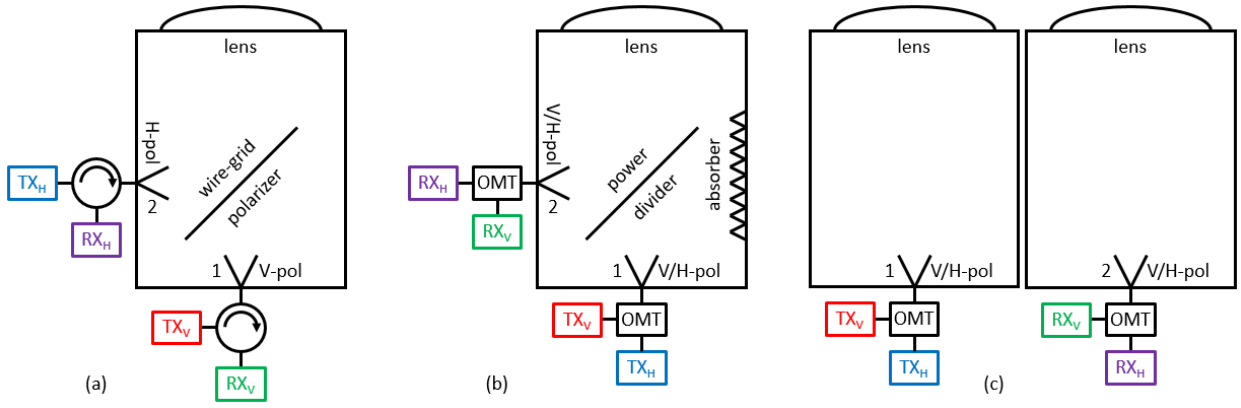

Figure 2.3. A comparison of the proposed antenna system architecture with common polarimetric radar lens antenna configurations. (a) Standard dual-polarized lens antenna and circulators for transmit and receive, (b) the common-aperture dual-polarized two-port antenna system of this work, and (c) separate dual-polarized antennas for transmit and receive.

Figure 2.3 shows the geometry of this antenna system in comparison to that of the standard dual-polarized lens antenna, and to separate lens antennas for transmit and receive. This antenna system combines the compactness and beam alignment of the former with the high isolation and support for polarimetric radar applications of the latter.

Three versions of this antenna have been designed and constructed for installation in three polarimetric radar systems. The E-band antenna was designed for use at the modern automotive radar band at 76 – 81 GHz. Two similar J-band antennas were designed for slightly different bands close to 230 GHz.

Each antenna was built by assembling several components: a dielectric lens, two feed horns, a polarization-independent spatial power divider, an absorber, and a 3D-printed housing. Chapter 3 will provide a detailed discussion on the polarization-independent spatial power divider. In the next section, a brief discussion of the design of the dielectric lenses used in these antennas is provided. The remainder of this chapter serves to provide additional information on the lenses,

feed horns, absorbers, and housings specific to each of the three antenna implementations, as well as to present the measurements used to characterize antenna performance.

2.2 Dielectric Lens Design

The purpose of the lens in a lens antenna is to transform a plane wave to a spherical wave, and vice versa. This behavior is depicted in Figure 2.4. When a plane wave illuminates the lens, its energy is concentrated at a single point, called a focal point or focus. Similarly, when energy is radiated from the focal point, the lens converts it into a local approximation of a plane wave. A feed antenna can be placed directly at the focal point of the lens to take advantage of this behavior. While the size of the feed element is typically on the order of the wavelength, the lens may be many times the wavelength across, providing a very large aperture.

In general, a dielectric lens is a single piece of a homogeneous isotropic dielectric material with two opposing surfaces that cause diffraction of an electromagnetic wave. The shapes of the surfaces are engineered to produce a desired behavior. For lens antenna applications, a plano-convex lens is typically used because it provides the required focusing behavior (for natural materials with a refractive index larger than 1) [43]. Additionally, the choice of one planar surface reduces the design complexity, requiring the calculation of only the convex surface profile.

There remains a choice of which side of the lens to place the focal point. Figure 2.5 shows illustrations of the two options. If the focal point is adjacent to the convex surface, then the planar surface does not cause refraction. On the other hand, if it is adjacent to the planar surface, then both lens surfaces cause refraction. For this antenna, the latter has been chosen due to consideration of reflections from the lens surfaces. As will be seen later in this chapter, the transmit-to-receive leakage within the antenna system is dominated by reflection from the lens. In the single refraction lens, the reflection from the planar surface is directed exactly back to the focal point, as shown in

Figure 2.6, which was expected to result in poor isolation. By contrast, the double refraction lens has reflections that propagate in other directions, away from the focal point.

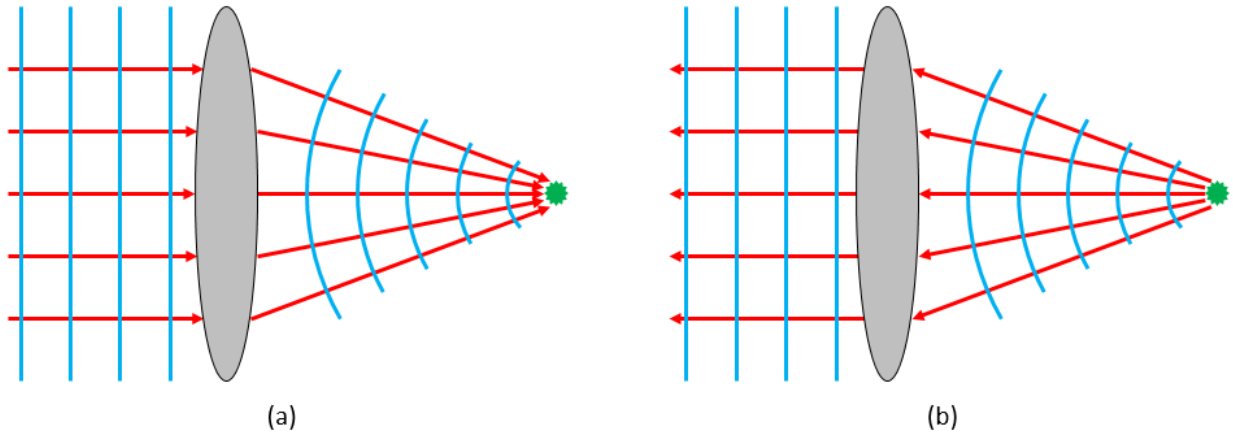

Figure 2.4. Desired behavior of a lens for use in a lens antenna. (a) The energy of an incident plane wave is concentrated at a single focal point. (b) Waves radiating from the focal point are collimated to a plane wave. Propagation direction is shown in red, and the corresponding phase fronts are shown in blue.

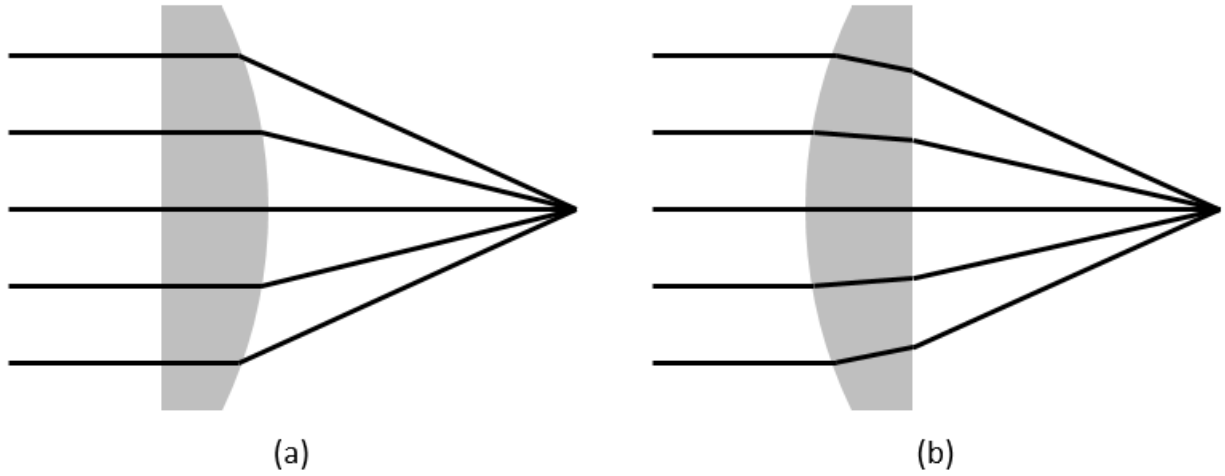

Figure 2.5. Two types of plano-convex lens: (a) single refraction lens with focal point adjacent to the convex surface, and (b) double refraction lens with focal point adjacent to the planar surface.

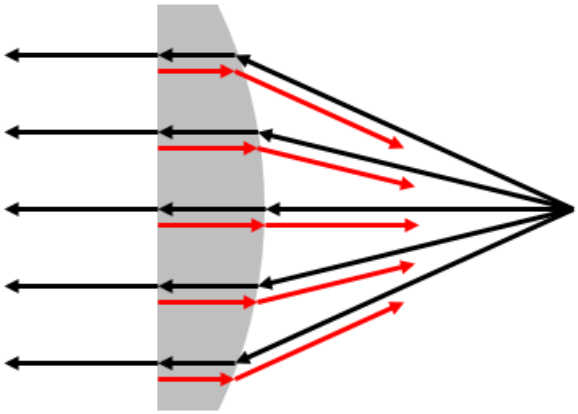

Figure 2.6. In the single refraction lens, the normal-incident reflection (shown in red) from the planar surface refracts directly back toward the focal point.

Finally, the profile of the convex surface of the double refraction plano-convex lens needs to be determined. A radial slice of the geometry of the lens is depicted in Figure 2.7. The focal point lies along the axis of revolution of the lens at a distance f from the planar surface. The lens has a center thickness d and an index of refraction n. A set of parametric equations describing a cross-section of the convex surface are derived by ensuring that the optical path length from the focal point to a plane in front of the lens' curved surface is equal for any ray originating at the focal point (i.e. for any y_1, the optical path length of the red path is equal to $f + nd$). In other words, the phase of the wave radiated from the focal point will become uniform on this planar surface. The equations are derived and presented in [43]:

$$x_2 = \left(\frac{(n-1)d + f - \sqrt{f^2 + {y_1}^2}}{n - \sqrt{1 - \frac{{y_1}^2}{n^2(f^2 + {y_1}^2)}}} \right) \sqrt{1 - \frac{{y_1}^2}{n^2(f^2 + {y_1}^2)}} \tag{2.1}$$

$$y_2 = y_1 \left(1 + \frac{x_2}{\sqrt{n^2(f^2 + {y_1}^2) - {y_1}^2}} \right). \tag{2.2}$$

For a given f, n, and d, these parametric equations describe the cross-section of the curved surface of the lens with a set of points given by (x_2, y_2) as a function of y_1, which is the height of an incident ray from the focus on the planar face of the lens. The lenses were made with Rexolite 1422, which is a low-loss microwave plastic with an index of refraction $n = 1.59$. The focal length f is related to the lens diameter $D = 2r$ through the focal ratio f/D. Several values of f and D have been chosen for different lenses. The remaining parameter d needs to be chosen for the desired flange thickness t. To do so, (2.1) and (2.2) need to be solved for y_1 and d when $x_2 = t$ and $y_2 = r$. This calculation has been done numerically.

The focal ratio has several implications for the antenna system. A small focal ratio will result in a lens with a convex surface that bulges outward significantly and is therefore very heavy. It also requires a feed with a wide beamwidth to illuminate efficiently, which may not be attainable. On the other hand, a large focal ratio will result in a thin lens, but requires the feed to be placed at a large distance from the lens, which drastically increases the amount of space needed for the antenna. For the E-band antenna, $f = 8\,in.$ and $D = 6\,in.$ were selected to balance these mechanical considerations and to provide a narrow beam of around 1.5°. The focal ratio is therefore $f/D = 4/3$. For the GM J-band radar, $f = 5.6\,in.$ and $D = 4\,in.$ were chosen ($f/D = 1.4$) to make the antenna both more compact and more directive than the E-band antenna, leveraging two of the benefits of moving to the higher frequency band. The second J-band antenna for the KACST radar was designed to have the ability to switch out lenses of different sizes for a variable beamwidth. 3 in. and 2 in. lenses with the same f/D were chosen so that the illumination profile would be approximately the same for all three. A convenient flange thickness of $t = 0.125\,in.$ was used for all of the lenses. With the values of n, f, D, and t fixed, r and d were found

and (2.1) and (2.2) were used to generate the lens models. The design parameters of the four lenses are summarized in Table 2.1.

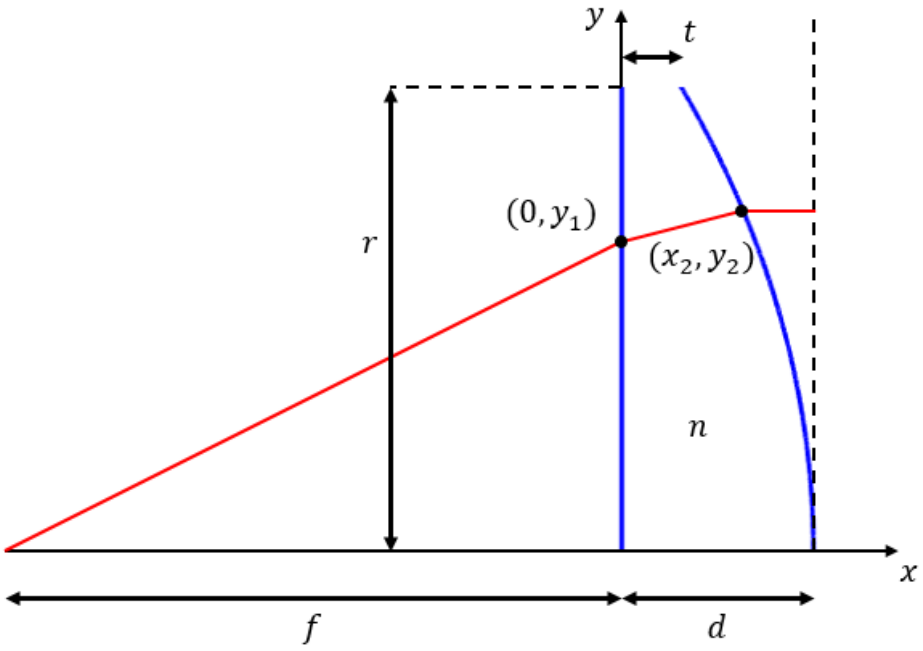

Figure 2.7. Geometry of the double refractive plano-convex lens, showing dimensions and coordinate system utilized in the derivation of equations (2.1) and (2.2) describing the convex surface. The lens surfaces are shown in blue. For any point $(0, y_1)$ and the corresponding (x_2, y_2), the optical path length of the red path must be equal to $f + nd$.

Figure 2.8. Photographs of the four double refraction plano-convex lenses. (a) Top view. (b) Angled view showing the curved surfaces.

Table 2.1
A list of the design parameters of the four double refraction plano-convex lenses used in the E-band and J-band antennas.

Lens	**Band**	n	f **(in.)**	D **(in.)**	t **(in.)**	r **(in.)**	d **(in.)**	f/D
6-inch	E-band	1.59	8	6	0.125	3	1.0388	4/3
4-inch	J-band	1.59	5.6	4	0.125	2	0.7046	1.4
3-inch	J-band	1.59	4.2	3	0.125	1.5	0.5579	1.4
2-inch	J-band	1.59	2.8	2	0.125	1	0.4111	1.4

A code was written in MATLAB based on ray-tracing optics and Snell's Law to verify that the lenses were designed properly. The code checks that parallel rays outside the convex surface converge to the intended focal point, and inversely that rays emanating from the focal point end up parallel. It should be noted that these design equations consider only the direct transmission path through the lens, and multiple reflections are not considered. For a low refractive index, the reflections are expected to have a small impact, but could be considered with more complex ray-tracing techniques if the application requires.

The 6-inch and 4-inch lenses were fabricated by the Scientific Instrument Shop of the University of Michigan College of Literature, Science, and the Arts. The 3-inch and 2-inch lenses were fabricated by Industrial Service & Design LLC. Figure 2.8 shows photos of the four lenses.

2.3 E-Band Antenna System Implementation

One of the remaining antenna components is a microwave absorber. Since the power divider always reflects and transmits half of the incident power, there is a strong secondary beam pointed in the direction opposite from feed 2 across the power divider. The purpose of the absorber is to remove that beam, and ensure that the radar does not receive a backscattered signal from objects at ninety degrees from the main beam of the antenna. A section of foam pyramidal

microwave absorber has been used in the E-band antenna for this purpose. This absorber has an attenuation of at least 20 dB across the microwave band, for both waves transmitted through it, and those reflected from a perfect electric conductor (PEC) positioned behind it. It therefore provides at least 40 dB reduction of any backscattered power from the area behind it.

2.3.1 Feed Horns

The final remaining components in the antenna system depicted in Figure 2.2 are two feed horns. A common type of feed used for lens and reflector antennas with good aperture and beam efficiency is the corrugated conical horn antenna. This antenna has a number of favorable characteristics for use as feeds, including low sidelobe and cross-polarization levels, a symmetric radiation pattern, and wideband operation [64].

The feed beamwidth should be chosen based on the focal ratio of the lens in such a manner as to balance illumination loss and spillover loss [65], [66]. A feed with a very narrow beamwidth will concentrate most of the radiated energy at a small area near the center of the lens, and will therefore result in poor aperture efficiency. This is known as illumination loss, and it will lead to a wider beam than desired. On the other hand, a feed with a very wide beam may illuminate the lens with nearly uniform amplitude to produce a sharp beam, but much of the energy radiated by the feed will miss the lens entirely and be wasted. This is known as spillover loss, and it will reduce the gain of the lens antenna. A common rule of thumb used in parabolic reflector feed design is to use a 10 dB edge taper, which means that the radiation pattern of the feed should drop by 10 dB relative to its maximum at the position of the edge of the reflector [65]. It is suggested in [66] that this guideline can be applied to lens antennas as well, although an edge taper of 7 or 8 dB may be more optimal for maximizing directivity. It is also supposed that the lens size and material, the

feed radiation pattern and polarization, and excitation of any resonances can all affect the optimal taper value, so an uncertainty of a few dB should be assumed.

The feeds used for the E-band antenna are corrugated horns, specifically the model 268W scalar feed horn supplied by MiWave Millimeter Products. Unfortunately, the 3-dB beamwidth of the horns received from the supplier was measured to be about 16°, which was in poor agreement with the advertised specification of 24° (actually 22° in E-plane and 26° in H-plane). The edge of the 6-inch lens is at about 20.5° from the feed boresight. It was hoped that an edge taper in accordance with the recommendations above would be realized, but a taper of more than 20 dB was found from the measured pattern at this angle. This resulted in significant illumination loss. To remedy this condition, the horns were shortened by removing material along their axes with a computer numerical control (CNC) mill. This reduced the aperture diameter of the horns from 0.72 in. to 0.48 in. to increase the beamwidth by a factor of 1.5.

The H-plane normalized radiation patterns of the 6-inch lens, illuminated by both the original corrugated horn and the shortened corrugated horn are displayed in Figure 2.9. It can be seen that the beamwidth has been improved from 1.9° to 1.6° by shortening the feed. A significant drawback is that the sidelobe level has been increased from -30 dB to -20 dB. This is another factor to take into consideration when choosing a feed pattern. Intuitively, a strongly tapered illumination field looks somewhat like a Gaussian curve, while a uniform illumination field looks like a rectangular function. The Fourier transform of the former is another Gaussian, while that of the latter is a sinc function. Therefore, it is not surprising that a broader feed pattern may result in larger sidelobes. For the radar application of interest, the antenna beamwidth is directly related to cross-range resolution, while a sidelobe level on the order of -20 dB to -30 dB is not expected to significantly interfere with backscatter from the main beam.

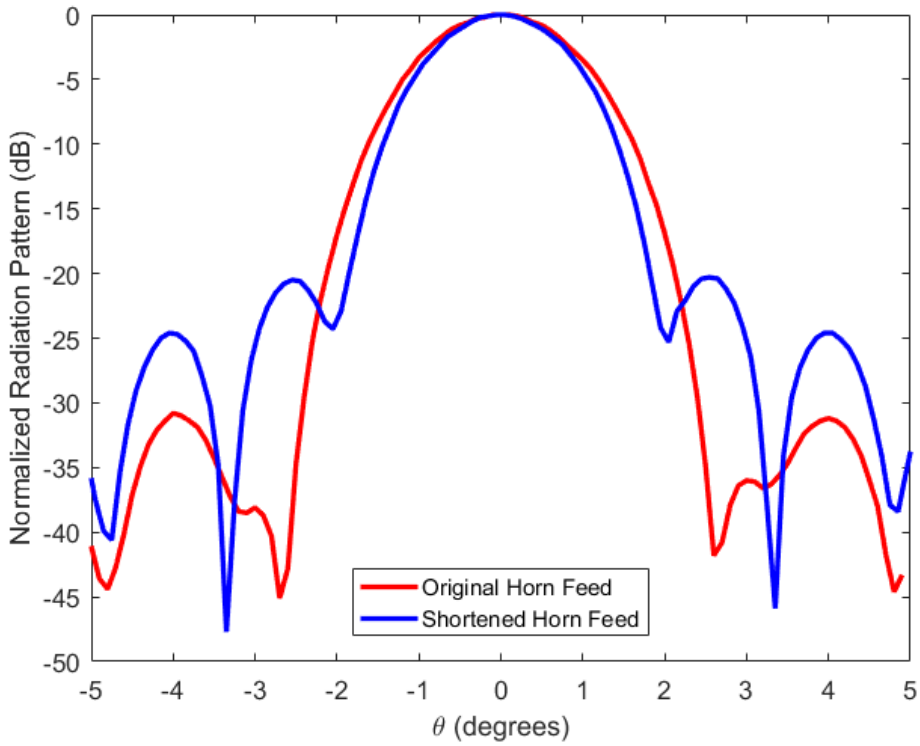

Figure 2.9. H-plane radiation pattern of 6-inch lens illuminated by the original MiWave corrugated conical horn, and the shortened version with a smaller aperture.

2.3.2 Determination of Phase Center

The dielectric lens was designed to focus to a single point. In reality, however, the feed antenna has a distributed aperture. It was therefore desired to identify a phase center of the feed horn. This is a position at which it appears that the far-field radiating spherical wave is emanating from [67]. To achieve a uniform phase front outside the lens, the phase center of the feed should be placed at the focal point of the lens.

Since the horn is rotationally symmetric, the phase center is assumed to lie along its central axis, but the position along this axis was not initially known. To find it, the gain of the horn-lens system was measured as a function of the distance from the horn aperture to the planar lens surface.

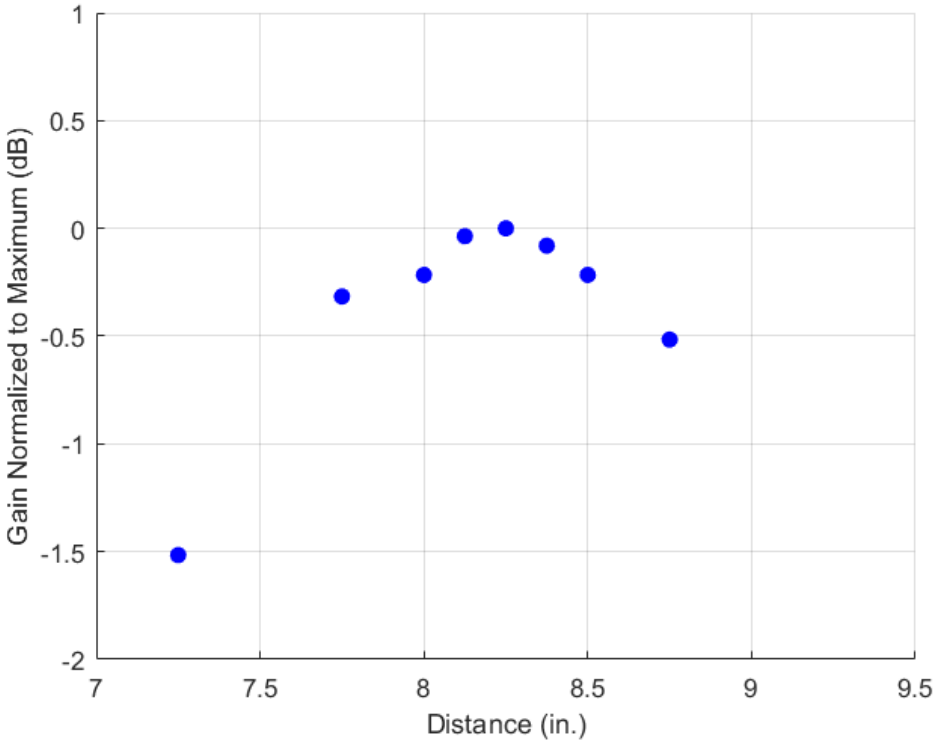

Figure 2.10. Measured gain (normalized to the maximum value) of the horn-lens system as a function of separation distance between the horn aperture and planar lens surface.

A plot of this measurement is shown in Figure 2.10. The gain was found to be maximized at a distance of 8.25 in. Since the designed focal length of the lens was 8 in., this indicates that the phase center of the horn is located slightly outside the aperture. This was thought to be surprising, as the phase center of horn antennas is typically inside the aperture [67]. A simulation of the horn's specific geometry was later performed which attested to this result.

2.3.3 Antenna Assembly

The components of the antenna system, namely the two feed horns, the power divider, the lens, and the absorber, need to be positioned in precise locations in three-dimensional space with separation distances of up to several inches. A housing unit was therefore designed to hold all of

the components in their proper positions and orientations relative to one another. The housing takes the form of a closed box, which has the added benefit of protecting the internal parts from the elements when the radar is used in outdoor measurements.

The most critical dimension is the distance between the lens and the feed horn aperture. Based on the measurement made in the previous section, a distance of 8.25 in. was used. The next dimension of interest is the distance from the feed aperture to the power divider. The power divider was designed assuming plane-wave incidence. The far-field distance of the horn is about 3 in., but it was determined that this was unfeasibly far due to practical spatial considerations. Instead, the horn aperture was positioned at a convenient distance of 2 cm away from the surface of the power divider. The power divider is therefore in the near field of the horn, but the wave radiated from the horn is still well collimated when it reaches the power divider, so the incident wave can be considered to be approximately a plane wave [68]. It should be noted that feed 1 is positioned directly at the focal point of the lens, while feed 2 is positioned at the image of the focal point across the power divider. The two feeds are therefore equidistant from the power divider surface. In terms of orientation, the central axes of the lens and feed 1 need to be exactly aligned with each other, while the axis of feed 2 needs to intersect the axis of feed 1 at a right angle at the position of the power divider. Finally, the power divider surface must be perpendicular to the plane defined by the axes of feeds 1 and 2, and oriented at a 45-degree angle from the planar lens surface. All of these requirements were carefully considered during the modeling of the housing.

The housing was also designed with the ability to adjust the position of the lens by up to 0.5 in. in either direction to account for possible error in the phase center measurement. After additional adjustments when the assembly was completed, the distance between the horn aperture and lens eventually settled at 8.125 in.

The housing was modeled in SolidWorks and fabricated by the University of Michigan's Duderstadt Center Fabrication Studio using 3D printing technology. Figure 2.11 shows images of the software model, and Figure 2.12 shows photos of the completed antenna assembly.

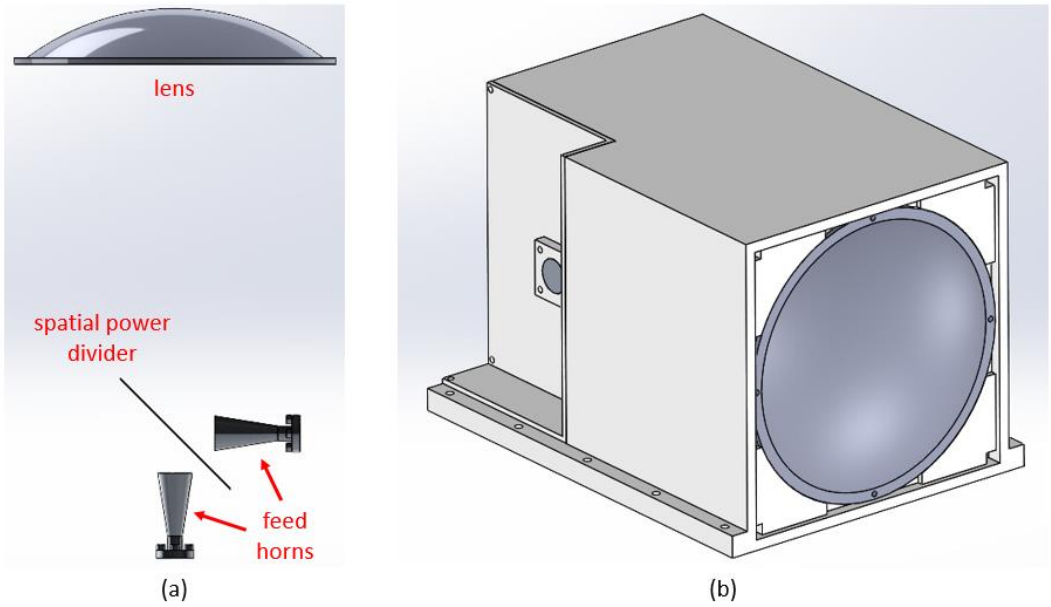

Figure 2.11. Images of the 3D software model of the E-band antenna components. (a) Relative positions of the feed horns, spatial power divider, and lens. (b) The components after being assembled inside the housing.

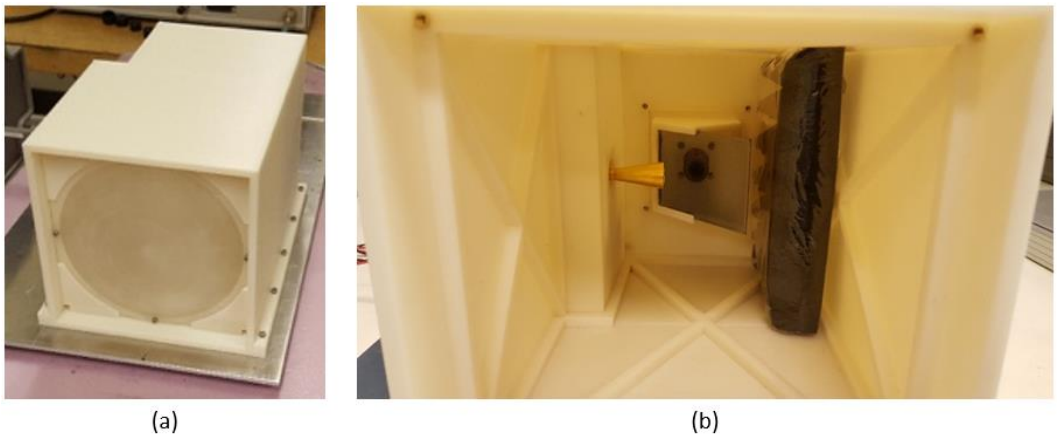

Figure 2.12. (a) Photo of the completed E-band antenna assembly. (b) Photo of the inside of the antenna assembly, showing position of feed horn, power divider, and foam absorber.

2.3.4 Measurement Results

The radiation pattern of the antenna system was measured at 77 GHz and 79 GHz using the standard far field pattern measurement technique [69]. An existing network-analyzer-based radar system at the 77 GHz band was utilized as a transmitter source, and the antenna under test was used in receive mode with the GM E-band radar receiver circuitry serving to mix the signal down for collection by a Keysight N9020A MXA Signal Analyzer. The far-field distance of the antenna is 12.2 m at 79 GHz, and the measurements were made in an anechoic chamber with an effective length of about 14 m. A photo showing a similar setup used for the J-band version of this antenna will be shown later in the chapter. The pattern was measured in the E- and H- planes for both polarizations, and both co- and cross- polarizations were measured.

Determining the gain of the antenna system was challenging because the feed horns have a circular waveguide input, and are transitioned to the receiver circuitry via OMTs. No standard horn with a circular waveguide input and known gain was available to be inserted into the measurement setup for a direct comparison [69]. Instead, the lens was removed from the housing and the received power was compared with and without the lens. Then the gains of the feed horns were measured using the three-antenna absolute gain method [69]. For that measurement, the three antennas were the two feed horns and an additional rectangular pyramidal horn, and the measurement was made with an HP 8510C network analyzer with two waveguide-based W85104A mm-wave Test Set frequency extenders, which enable measurements between 75 GHz and 100 GHz. However, while the pyramidal horn is matched to the rectangular waveguides of the frequency extenders, the feed horns, which have circular waveguide inputs, are not. Knowledge of the measured return loss was used to correct for the effect of impedance mismatch, but there may be some error in these gain measurements. The gain of the Port 1 horn at 77 GHz and 79 GHz is

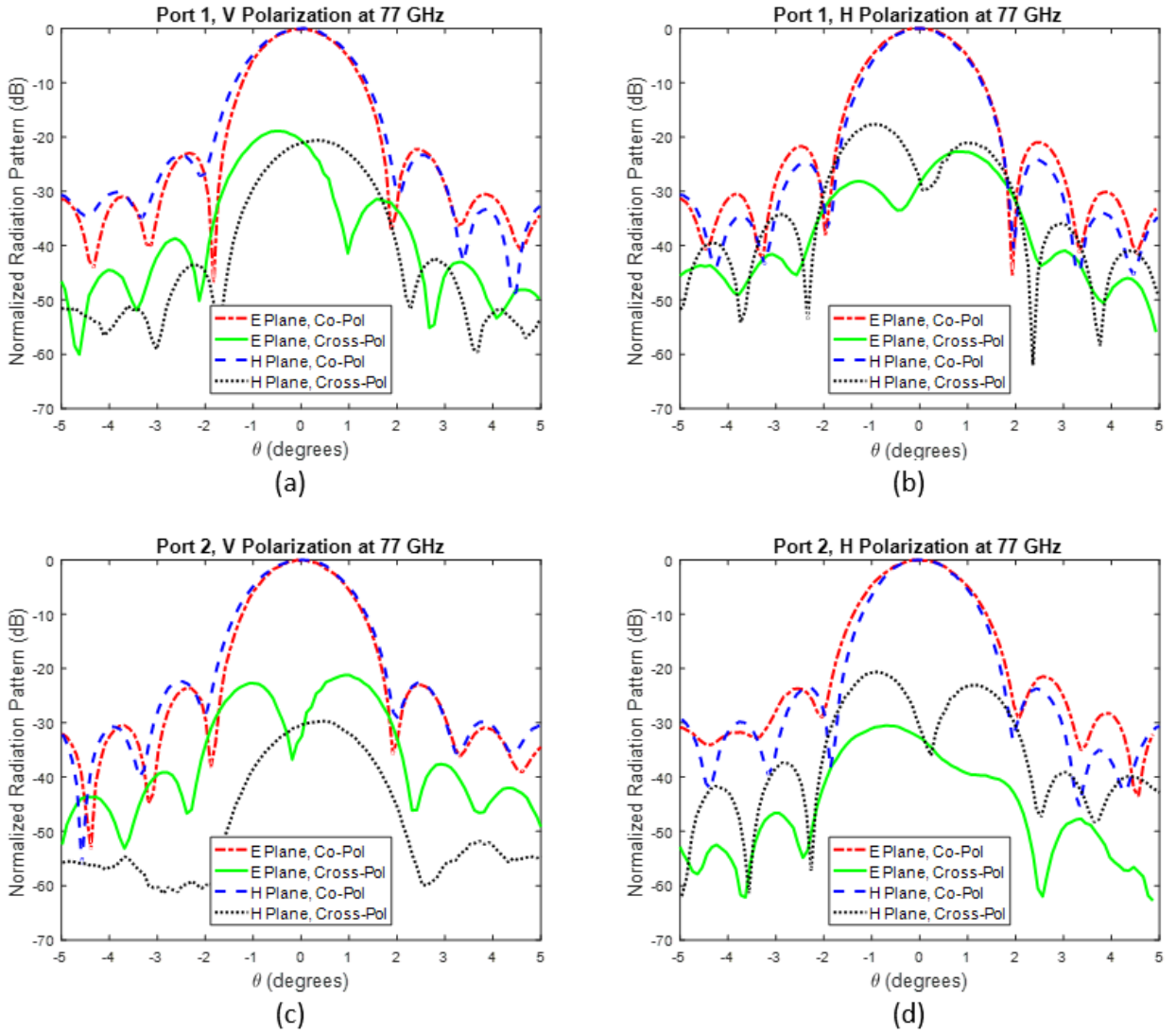

Figure 2.13. Measured radiation pattern of E-band antenna system at 77 GHz for: (a) port 1, V polarization, (b) port 1, H polarization, (c) port 2, V polarization, (d) port 2, H polarization.

Table 2.2
Measured radiation pattern characteristics of E-band antenna system at 77 GHz.

	Port 1, V Polarization	**Port 1, H Polarization**	**Port 2, V Polarization**	**Port 2, H Polarization**
Gain (dB)	35.5	35.7	37.1	36.4
E-Plane 3-dB Beamwidth (°)	1.5	1.6	1.5	1.6
H-Plane 3-dB Beamwidth (°)	1.6	1.5	1.6	1.5
Maximum Sidelobe Level (dB)	-22.2	-21.0	-22.4	-21.5
Maximum Cross-pol Level (dB)	-18.9	-17.6	-21.2	-20.6

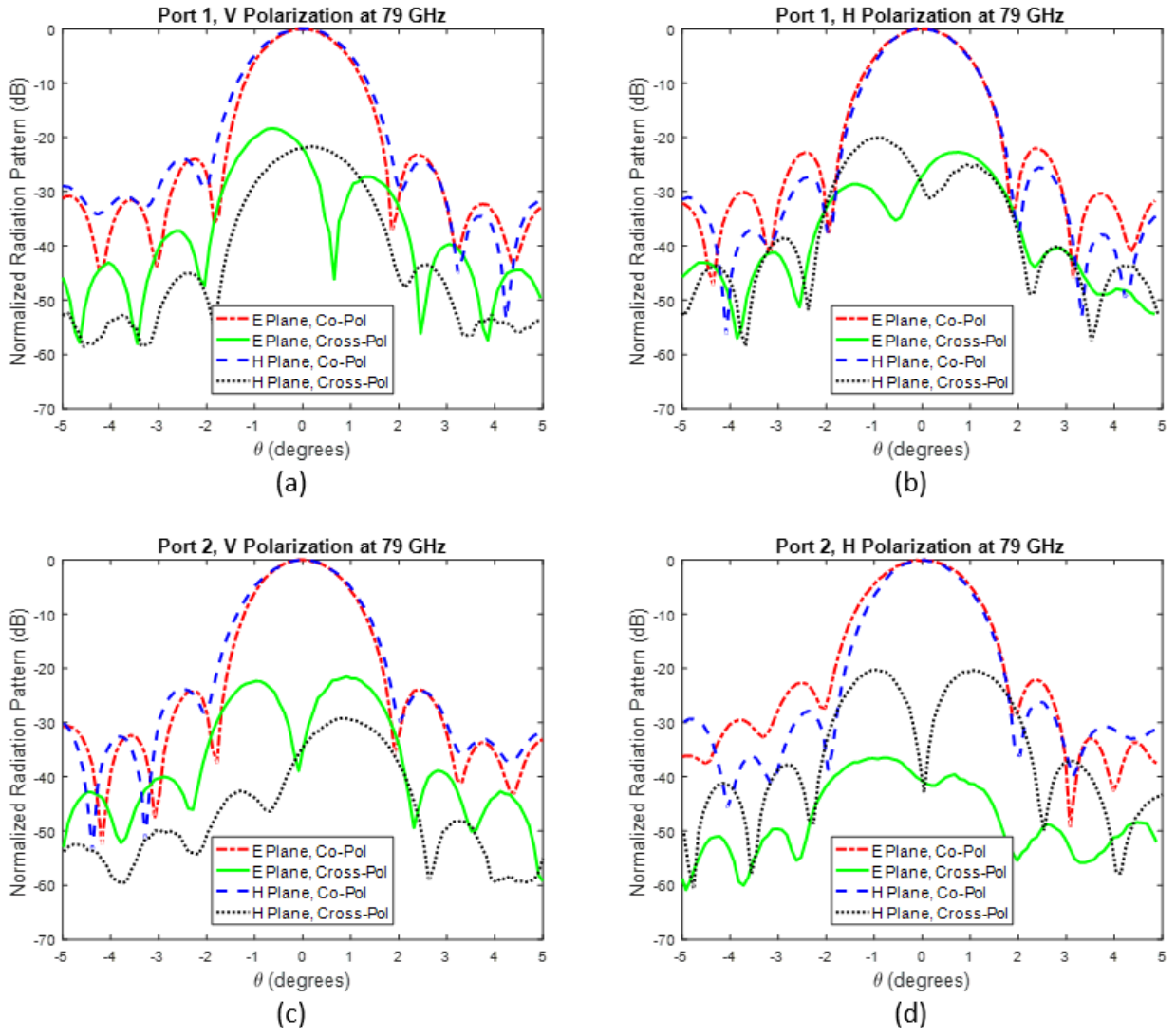

Figure 2.14. Measured radiation pattern of E-band antenna system at 79 GHz for: (a) port 1, V polarization, (b) port 1, H polarization, (c) port 2, V polarization, (d) port 2, H polarization.

Table 2.3
Measured radiation pattern characteristics of E-band antenna system at 79 GHz.

	Port 1, V Polarization	**Port 1, H Polarization**	**Port 2, V Polarization**	**Port 2, H Polarization**
Gain (dB)	36.5	36.3	37.4	35.9
E-Plane 3-dB Beamwidth (°)	1.5	1.5	1.5	1.6
H-Plane 3-dB Beamwidth (°)	1.6	1.5	1.6	1.5
Maximum Sidelobe Level (dB)	-23.2	-22.0	-23.8	-22.1
Maximum Cross-pol Level (dB)	-18.3	-20.0	-21.5	-20.3

17.0 dB and 17.5 dB, respectively. The gain of the Port 2 horn at 77 GHz and 79 GHz is 17.8 dB and 18.1 dB, respectively. The gain of the complete antenna system is estimated from these values, the comparison of received power with and without the lens, and the measured power divider properties (which will be discussed in Chapter 3).

The radiation patterns of the antenna system are shown in Figure 2.13 and Figure 2.14, and the characteristics of the pattern are summarized in Table 2.2 and Table 2.3.

The isolation between the two ports of the antenna system was measured with the HP 8510C network analyzer setup. A photo of the measurement setup is shown in Figure 2.15. The measurement was calibrated by connecting the output of the network analyzer's frequency extenders directly to each other as a reference of comparison. By examining the time domain response, it was determined that the dominate leakage path is via reflection from the surface of the lens. The next most significant paths are reflection from the absorber area, and direct leakage from one horn to the other. Time gating has been applied to the measurements around these most

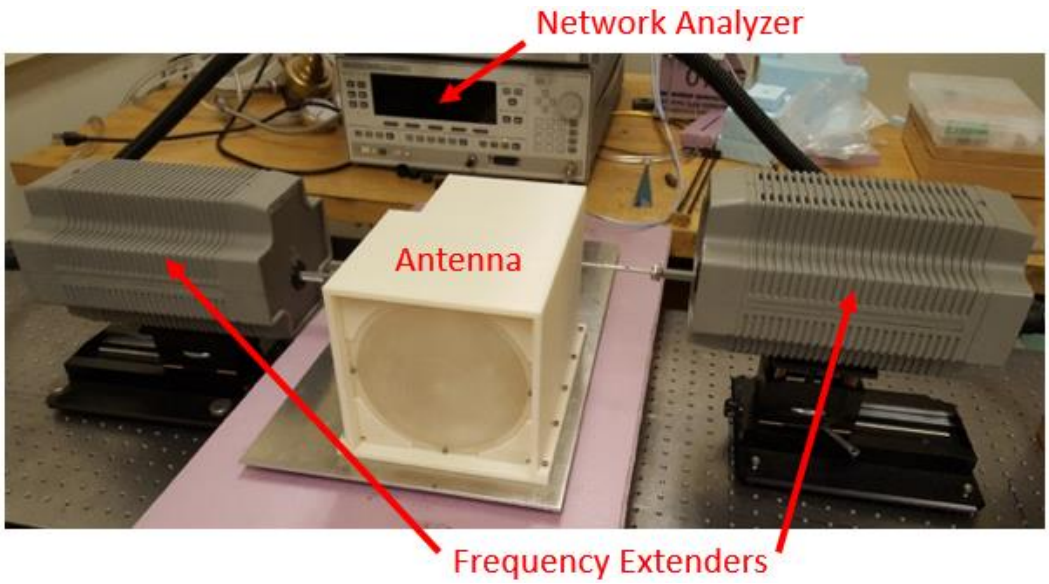

Figure 2.15. The setup for measurement of the E-band antenna isolation.

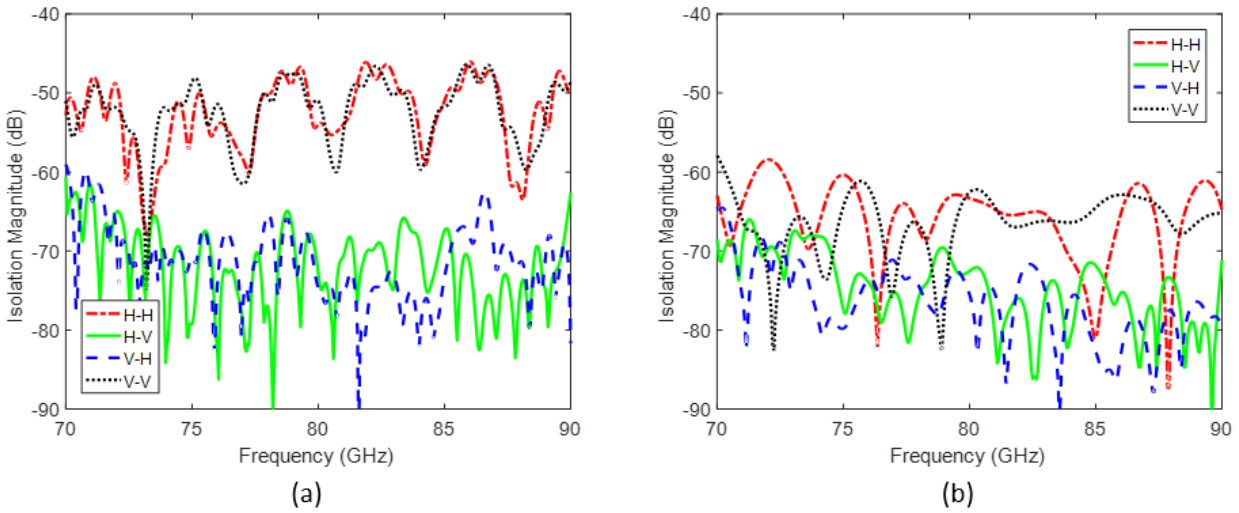

Figure 2.16. (a) Measured isolation of the E-band antenna system for all combinations of polarizations at the two ports (V-H represents V polarization at port 1 and H polarization at port 2). (b) Measured isolation when the lens is removed from the antenna system.

dominant peaks. The isolation is plotted in Figure 2.16. Over the band from 70 GHz to 90 GHz, the isolation is better than 45 dB. When the lens is removed from the antenna, the isolation improves to more than 60 dB. The sensitivity of the radar system is limited by the antenna isolation, so dealing with this large reflection caused by the lens has been a subject of ongoing investigation.

2.4 J-Band Antenna System Implementation

Another version of this antenna system was constructed for operation at J-band. It is similar to the E-band antenna in most aspects, but the differences will be discussed in this section. Instead of the 6-inch lens and pyramidal foam absorber, the J-band antenna uses the 4-inch lens and Laird Eccosorb HR-10 (a porous high-frequency microwave absorber). Over the band from 220 GHz to 250 GHz, this absorber exhibited an attenuation of at least 19 dB for both waves transmitted through it, and those reflected from a PEC positioned behind it, which is comparable to the E-band absorber. Another similar but smaller housing was designed and 3D-printed.

2.4.1 Feed Horns

It was initially planned to purchase a set of feed horns from an external vendor, as was done for the E-band antenna feeds. However, due to the major suppliers of millimeter-wave components being unable to meet the required beamwidth and frequency specifications, it was necessary to design and fabricate the horns in-house.

A set of conical horns was made from blocks of aluminum using CNC milling. The design and machining was done by Dr. Adib Nashashibi. The input is a circular waveguide with a diameter of 1.245 mm, consistent with the WR-04 standard circular waveguide. The diameter of the aperture is 3.875 mm. This aperture size was chosen to provide an appropriate beamwidth to efficiently illuminate the lens. The geometry of the conical horn is depicted in more detail in Figure 2.17. The shape of the horn profile was dictated by the set of drill bits available for the mill, and the different segments are intended to provide as smooth a transition as possible from the input waveguide.

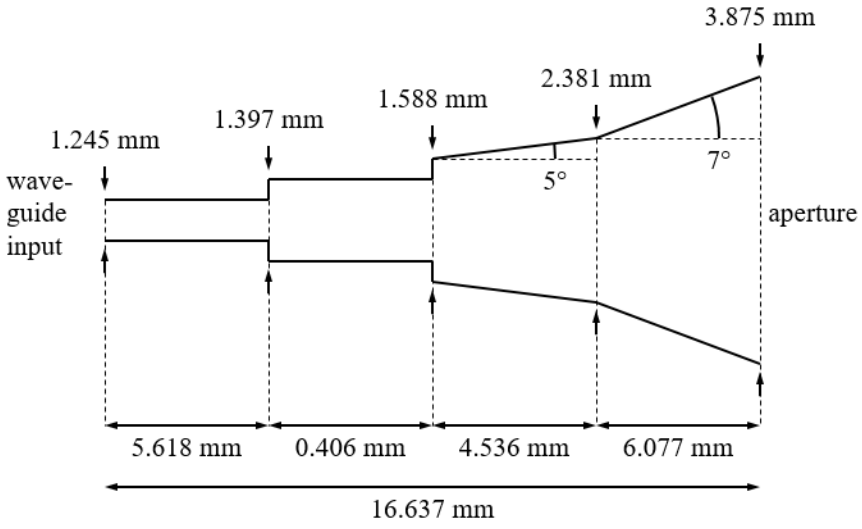

Figure 2.17. Geometry of the J-band conical horn (drawing not to scale). The horn has cylindrical symmetry, and the cross-section through the center is shown.

The radiation patterns of the two conical horn antennas are shown in Figure 2.18. The simulated cross-polarized pattern is below -50 dB at all angles relative to the co-polarized gain at boresight, thus it is not shown. The horn pattern characteristics are summarized in Table 2.4. It can be seen that the edge taper, defined at an angle of 19.7° corresponding to the outside of the lens with $f/D = 1.4$, is in fairly close agreement with the recommendations discussed previously. The measured pattern is a bit narrower than the simulation, which has edge tapers of 10.3 dB and 7.8 dB in the E- and H-planes, respectively.

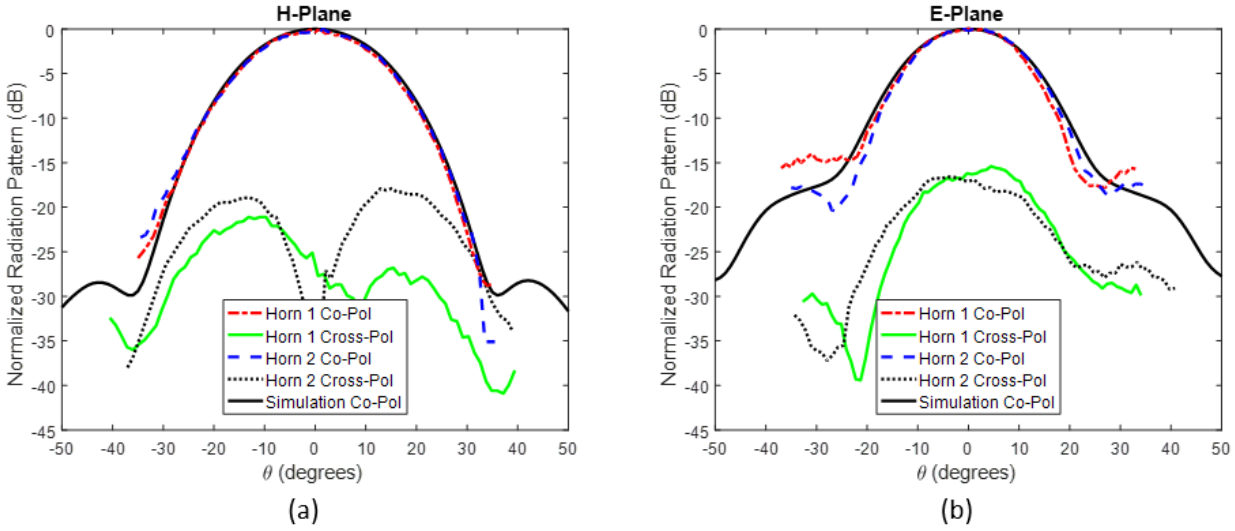

Figure 2.18. Measured (a) E-Plane and (b) H-Plane radiation pattern of conical horn antennas used as feeds for the J-band antenna system. Simulated cross-pol is omitted since it is nearly zero.

Table 2.4
Measured radiation pattern characteristics of J-band conical horn feed antennas.

		E-Plane		H-Plane		
Horn	**Gain (dB)**	**3-dB Beamwidth**	**Edge Taper**	**3-dB Beamwidth**	**Edge Taper**	**Maximum Cross-Pol Level (dB)**
1	17.9	21°	12.1 dB	24°	8.3 dB	-15.4
2	17.6	22°	11.9 dB	25°	8.0 dB	-16.6

During the construction of the E-band antenna system, it was found that when the feed horn had too narrow a beamwidth, the beam produced by the lens was wider than expected and desired due to illumination loss. The horns were therefore shortened to broaden their beams. Since the E-band corrugated horn feeds were very expensive, additional experimentation could not be done to try to optimize the illumination. However, some more flexibility existed at J-band due to the in-house horn fabrication. Another version of the J-band conical horn that was slightly shorter in length, and therefore had a smaller aperture, was fabricated. This horn had measured E- and H-plane beamwidths of 28° and 31°, and edge tapers of 6.3 dB and 4.7 dB, respectively. The gain and H-plane pattern of the 4-inch lens illuminated by both versions of the feed horn were measured and compared. While the smaller horn resulted in a beamwidth of 0.8° compared to 0.9° for the larger horn, it also produced 0.7 dB less gain. This indicates that spillover loss is beginning to become significant as the feed aperture is reduced beyond this point. These measurements help to verify the recommended edge taper values provides by sources such as [65] and [66]. Unfortunately, the dielectric lens is too electrically large to optimize the feed pattern through simulation.

2.4.2 Antenna Assembly

Since the J-band feed horns are much smaller and have a much shorter far-field distance (just over 2 cm) than the E-band horns, it was possible to position the power divider in their far field without difficulty. Therefore, the horns were positioned 3 cm away from the surface of the power divider. The housing was again designed with the ability to adjust the position of the lens. The nominal focal length of the 4-inch lens is 5.6 in., but the gain was found to be maximized when the lens was positioned at 5.475 in. from the aperture of the horn. In this case, the horn phase center is slightly inside the aperture. An early iteration of the housing was printed to measure the

antenna performance. Eventually, another was made with additional features like mounting holes and increased space for radar components, similar to the E-band antenna housing. Figure 2.19 shows images of the software model of the J-band antenna, and Figure 2.20 shows photos of the completed assembly.

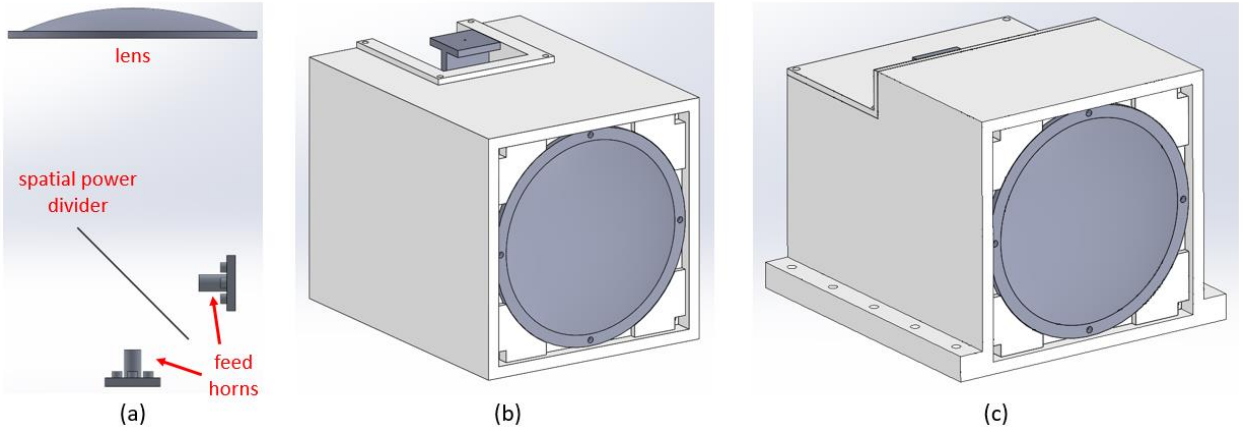

Figure 2.19. Images of the 3D software model of the J-band antenna components. (a) Relative positions of the feed horns, spatial power divider, and lens. (b) Components assembled inside the early housing. (c) Components assembled inside final housing.

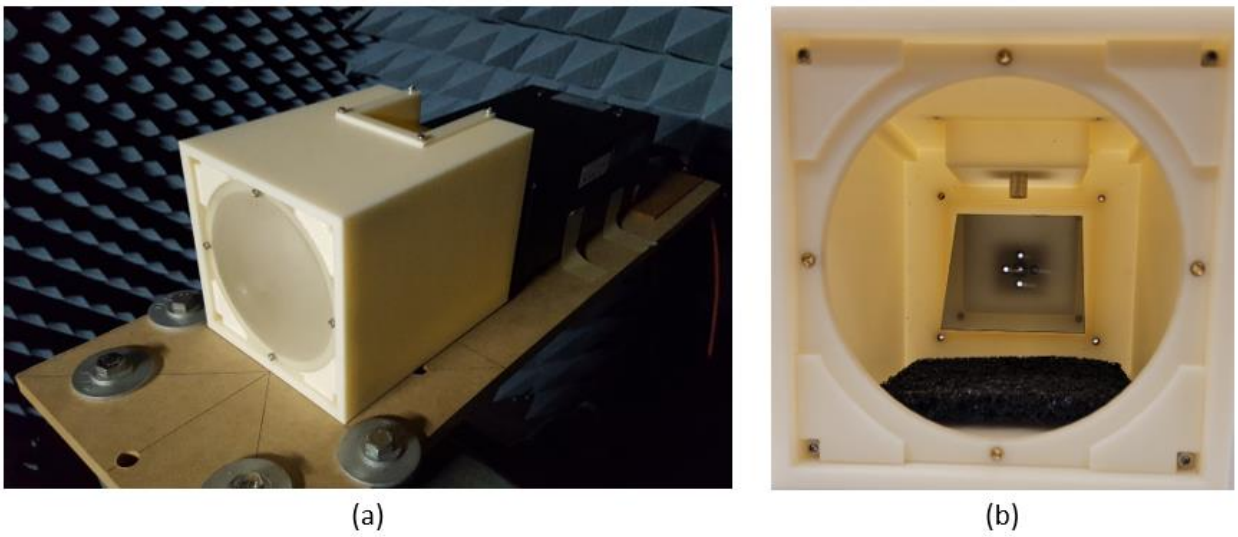

Figure 2.20. (a) Photo of the completed J-band antenna assembly. (b) Photo of the inside of the antenna assembly, showing position of feed horn, power divider, and absorber.

2.4.3 Measurement Results

The radiation pattern of both the conical horns and the complete antenna system was measured at 230 GHz, again using the standard far field pattern measurement technique. Similar to the E-band measurement setup, the J-band setup includes a different network-analyzer-based radar system, this one operating at the 230 GHz band, acting as a transmitter source. The antenna under test was used in receive mode, and the Keysight N9020A MXA Signal Analyzer was used to measure the received power, this time with a Virginia Diodes frequency extension module for down-conversion. The far-field distance of the J-band antenna is 15.8 m, so the transmit source is not quite in the far field in the 14 m anechoic chamber. A photo showing the J-band pattern measurement setup is shown in Figure 2.21. The pattern was again measured in the E- and H-planes for both polarizations, and both co- and cross- polarizations were measured.

The gain of the conical horns and complete antenna system were measured using the substitution method [69], comparing to the gain of a standard pyramidal horn. In this case, the Virginia Diodes module and the pyramidal horn are both matched to a WR-03 rectangular waveguide output/input, so the horn could be inserted into the measurement setup directly. This horn was studied in [70], and the gain at 230 GHz is 22.6 dB.

The radiation patterns of the full antenna system are shown in Figure 2.22, and the characteristics of the pattern are summarized in Table 2.5. Only the boresight of the beam of the horns is incident at exactly 45 degrees on the polarization-independent spatial power divider, while there is a small angular variation for areas of the power divider away from boresight. Measurement of the antenna assembly's radiation pattern from both ports in both polarizations therefore serves as verification that the power divider is functioning properly in the context of the antenna system as a whole.

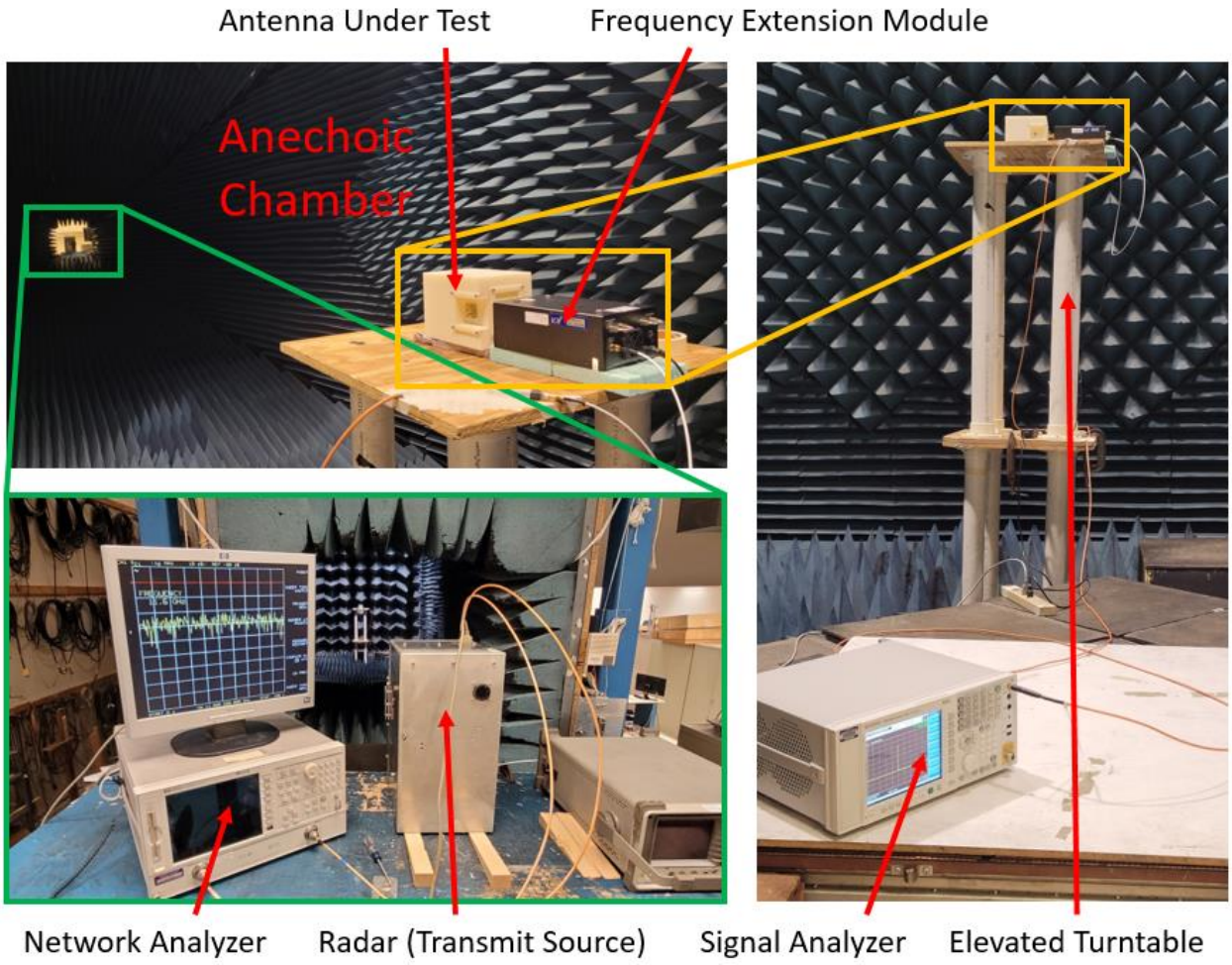

Figure 2.21. The setup for measurement of the J-band antenna gain and radiation pattern. A network-analyzer-based radar is placed at the narrow end of a 14 m anechoic chamber and used as a transmit source. The network analyzer is operated in continuous wave mode to provide a signal at a constant frequency. The antenna under test and frequency extension module are placed atop an elevated turntable at the other end of the chamber, providing elevation and azimuthal angle control. A signal analyzer measures the received power spectrum.

The isolation between the two ports of the antenna system was measured with an Agilent N5245 4-port PNA-X performance network analyzer with two waveguide-based OML frequency extenders, which enable measurements up to 325 GHz. A photo of the measurement setup is shown in Figure 2.23. The measurement was calibrated by connecting the output of the network analyzer's frequency extenders directly to each other as a reference of comparison. The isolation

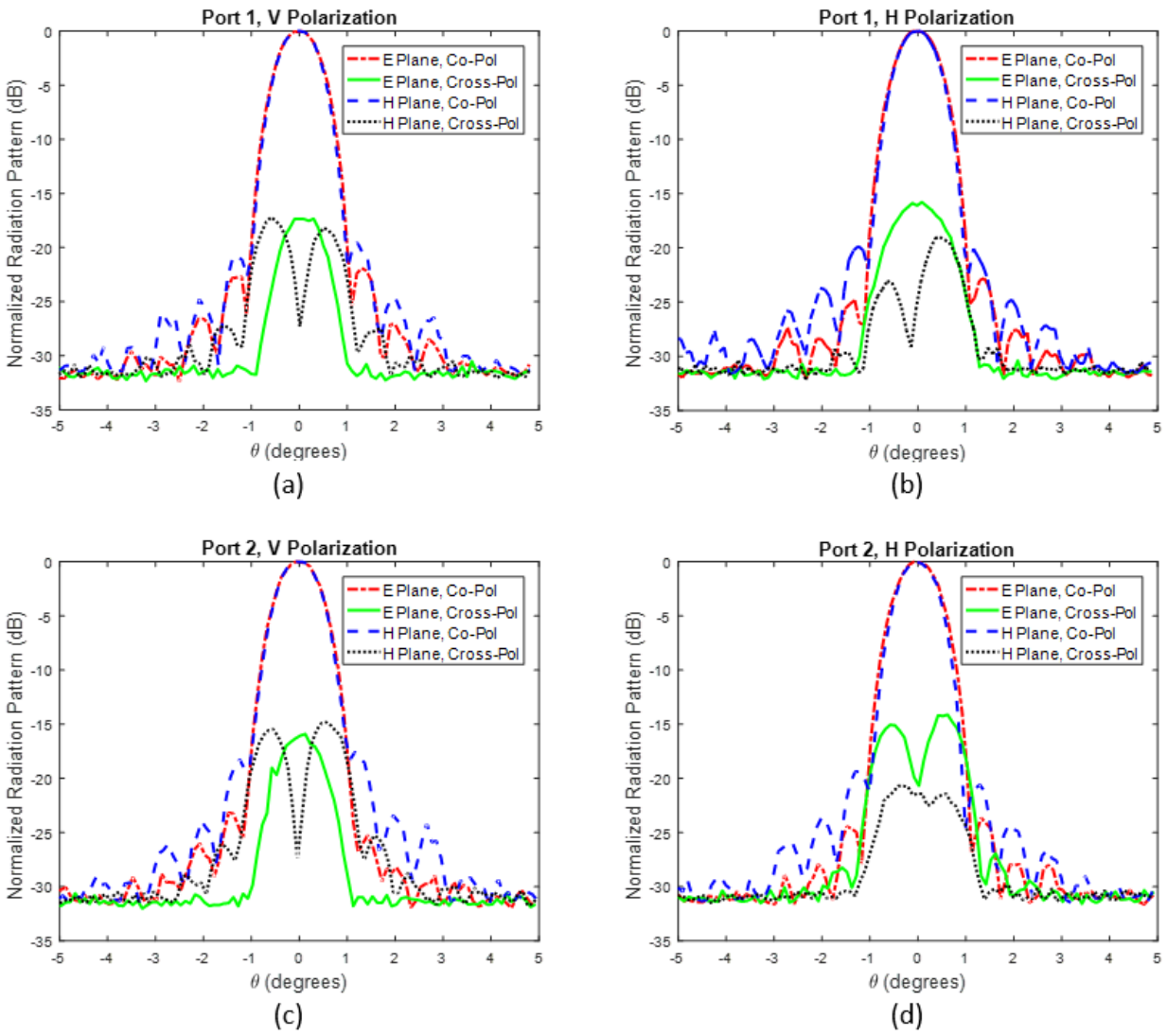

Figure 2.22. Measured radiation pattern of J-band antenna system at 230 GHz for: (a) port 1, V polarization, (b) port 1, H polarization, (c) port 2, V polarization, (d) port 2, H polarization.

Table 2.5
Measured radiation pattern characteristics of J-band antenna system at 230 GHz.

	Port 1, V Polarization	**Port 1, H Polarization**	**Port 2, V Polarization**	**Port 2, H Polarization**
Gain (dB)	39.2	39.1	39.1	38.6
E-Plane 3-dB Beamwidth (°)	1.0	1.0	1.0	1.0
H-Plane 3-dB Beamwidth (°)	0.9	0.9	0.9	0.9
Maximum Sidelobe Level (dB)	-19.6	-19.9	-17.6	-19.4
Maximum Cross-pol Level (dB)	-17.2	-15.8	-14.8	-14.2

is plotted in Figure 2.24. Over the band from 200 GHz to 250 GHz, the isolation is better than 40 dB. As with the E-band antenna, when the lens is removed, the isolation improves to more than 60 dB over most of the band.

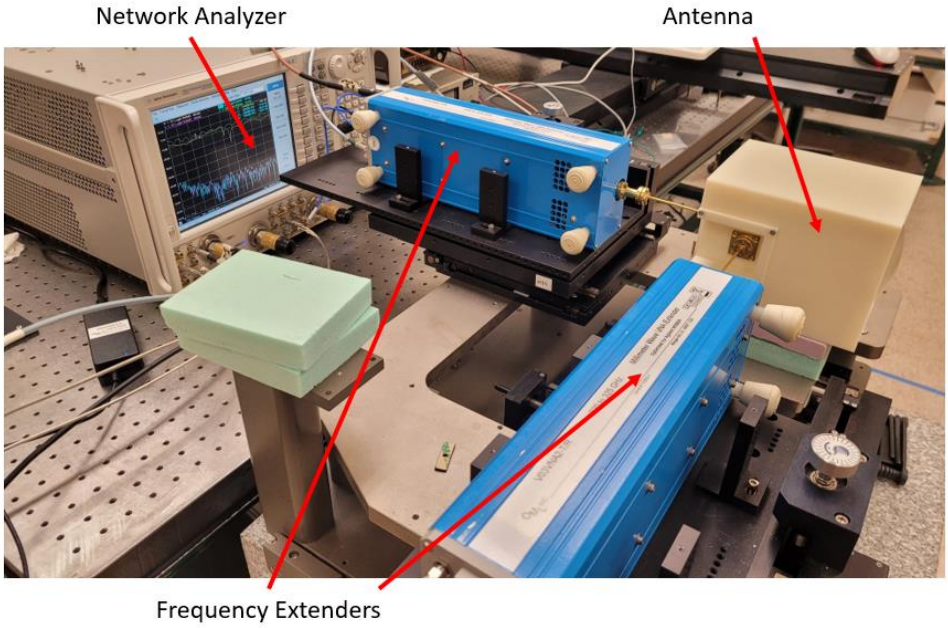

Figure 2.23. The setup for measurement of the J-band antenna isolation.

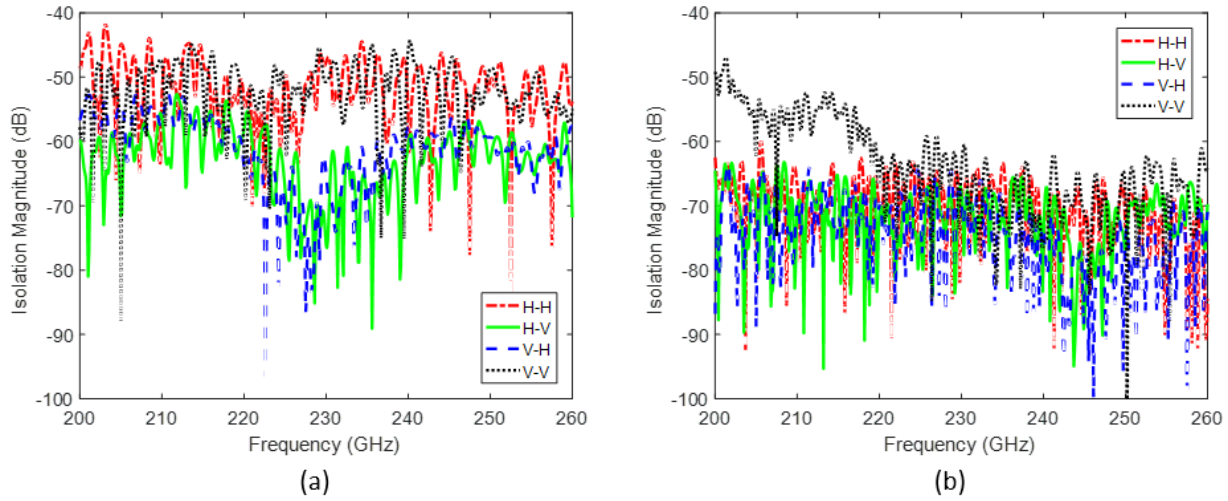

Figure 2.24. (a) Measured isolation of the J-band antenna system for all combinations of polarizations at the two ports (V-H represents V polarization at port 1 and H polarization at port 2). (b) Measured isolation when the lens is removed from the antenna system.

2.5 Second J-Band Antenna System

The first J-band antenna system discussed in the previous section was used in the GM radar which operates at 230 – 248 GHz. It was later desired to use a similar antenna in the KACST radar, operating at a slightly lower band of 220 – 230 GHz. The design remains mostly the same, but there are some minor differences. Most importantly, the polarization-independent spatial power divider was redesigned for better performance at the lower band. The same design was used for the feed horns, but this time they were milled out of brass instead of aluminum. Finally, it was found that the narrow beam provided by the 4-inch lens in the previous radar's antenna in some cases made it difficult to track certain types of targets with small areas. It was therefore desired to have the ability to change the lens size to choose an appropriate beam for the measurement of interest. For this purpose, the 2-inch and 3-inch lenses were designed, and the 3D-printed housing was modified to enable this flexibility. As shown in Table 2.1, the three lenses have the same focal ratio so that they would all be illuminated by approximately the same field profile. However, that means that they all have different focal lengths. Therefore, the housing was split into two parts, with three separate versions of the front portion to hold the respective lenses at the right positions. The housing parts were 3D-printed in-house using a Snapmaker A350 printer, with the assistance of resident printing expert Aditya Muppala. Photos of the different lens configurations are provided in Figure 2.25.

The position of each of the three lenses was once again optimized to maximize the antenna gain. The optimized distances from the horn aperture were 2.800 in., 4.200 in., and 5.725 in., for the 2-inch, 3-inch, and 4-inch lenses, respectively.

Gain and radiation patterns were measured at 225 GHz using the same setup previously described and shown in Figure 2.21. The only notable difference is that a wire-grid polarizer was

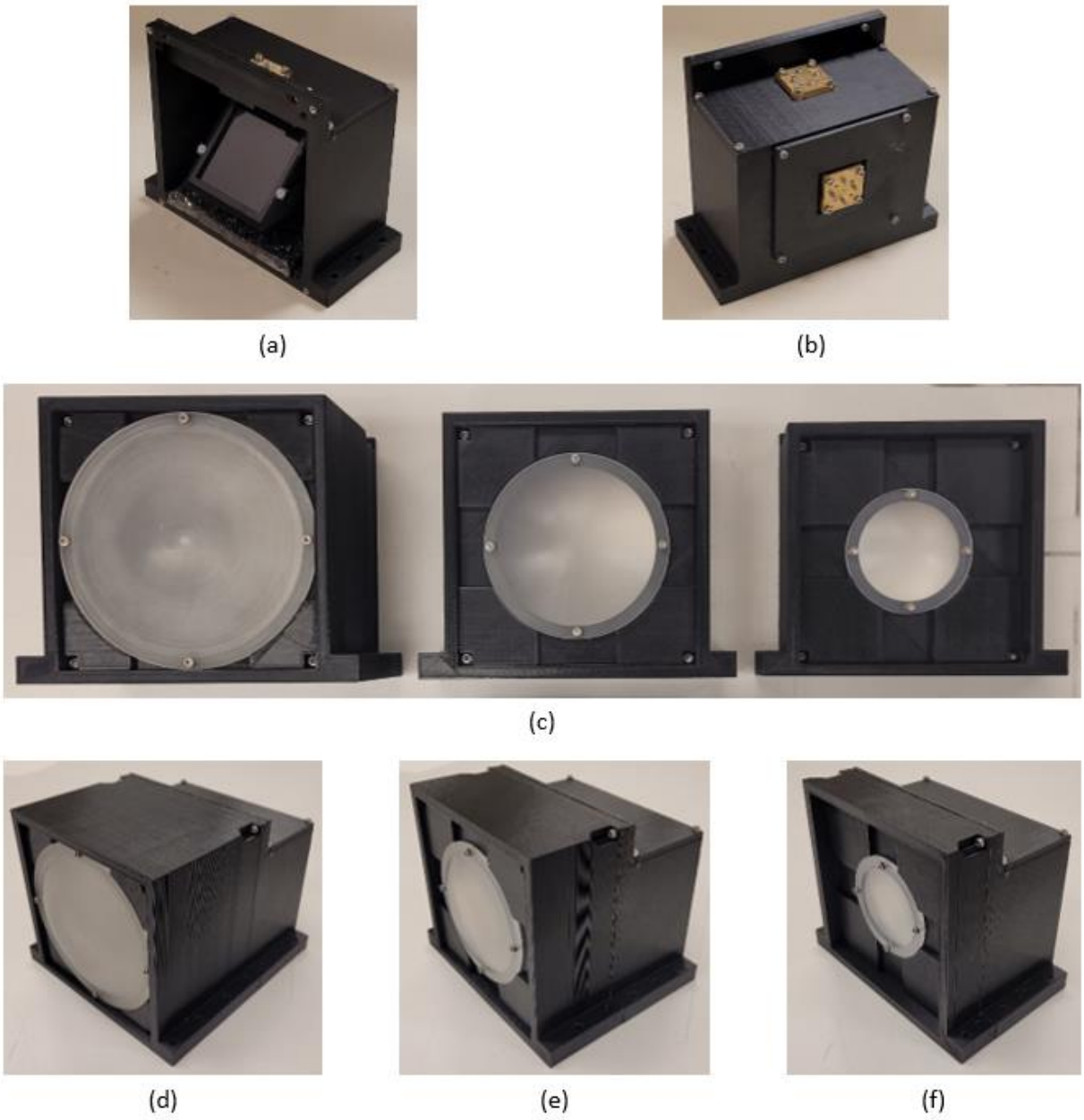

Figure 2.25. Photos of the second J-band antenna components and lens configurations: (a) back portion of the housing viewed from the front, showing positions of spatial power divider and absorber, (b) back portion of the housing viewed from the back, showing positions of feed horns, (c) separate front portions of the housing for 4-inch, 3-inch, and 2-inch lenses, (d) 4-inch lens configuration, (e) 3-inch lens configuration, (f) 2-inch lens configuration.

positioned in front of the antenna of the transmit source radar during the cross-polarization pattern measurements, in an effort to improve the polarization purity of the transmitted wave. This helped

in obtaining cross-pol patterns with nulls close to boresight as expected, rather than sometimes having a maximum. The maximum is believed to have been a result of a transmitted field with a significant component oriented along the co-pol direction of the antenna under test, and therefore not accurate. The gain of the standard horn reference at 225 GHz according to [70] is 22.7 dB.

The feed horns have patterns very similar to those used in the previous version, and agree well with the simulation. The pattern characteristics are summarized in Table 2.6. Cross-polarization could not be detected under the noise floor using the wire-grid polarizer.

The radiation patterns of the antenna system with the 2-inch, 3-inch, and 4-inch lens configurations are shown in Figures 2.26, 2.27, and 2.28, and the characteristics of the patterns are summarized in Tables 2.7, 2.8, and 2.9, respectively. The sidelobes reported for the 4-inch lens in Table 2.9 are those which are nearly merged with the main beam, as can be seen in Figure 2.28. While looking into possible polarization impurity of the transmit source, it was found to be useful to perform a small two-dimensional scan in both elevation and azimuth around boresight to get a sense of the shape of the cross-pol pattern. The values of maximum cross-polarization cited in the three tables take into consideration these 2D scans, as well as the standard E- and H- plane measurements, since the linear scans are not guaranteed to pass through a cross-pol maximum. Two examples of measured 2D cross-pol patterns are illustrated in Figure 2.29. In both shown cases, two peaks can be seen, with a valley between them. The valley seems to run parallel to the

Table 2.6
Measured radiation pattern characteristics of second set of J-band conical horn feed antennas.

		E-Plane		**H-Plane**	
Horn	**Gain (dB)**	**3-dB Beamwidth**	**Edge Taper**	**3-dB Beamwidth**	**Edge Taper**
1	17.3	20°	11.1 dB	23°	7.7 dB
2	17.7	21°	12.9 dB	24°	7.8 dB

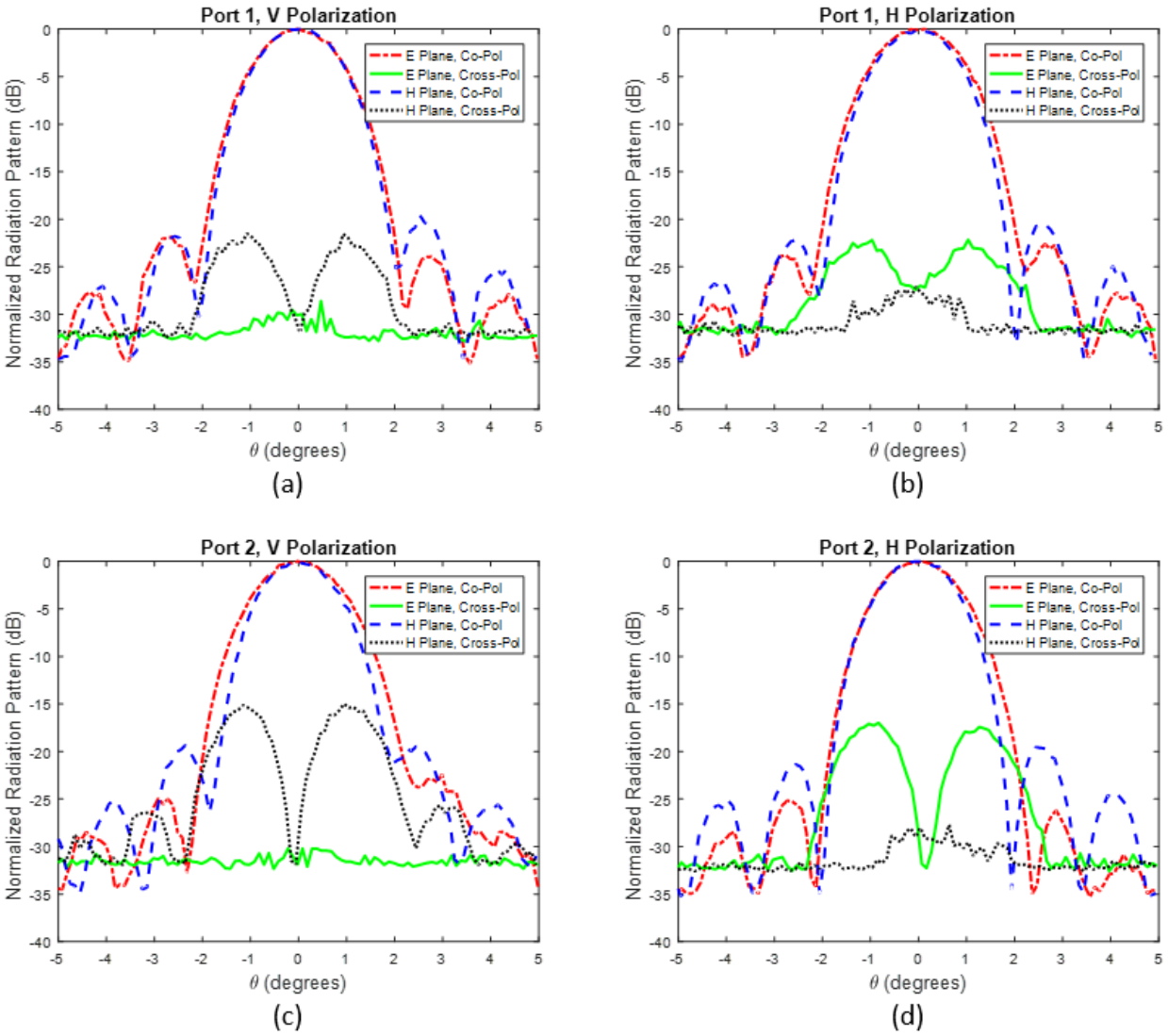

Figure 2.26. Measured radiation pattern of second J-band antenna system with 2-inch lens at 225 GHz for: (a) port 1, V polarization, (b) port 1, H polarization, (c) port 2, V polarization, (d) port 2, H polarization.

Table 2.7
Measured radiation pattern characteristics of second J-band antenna system with 2-inch lens at 225 GHz.

	Port 1, V Polarization	**Port 1, H Polarization**	**Port 2, V Polarization**	**Port 2, H Polarization**
Gain (dB)	33.6	33.6	33.4	34.0
E-Plane 3-dB Beamwidth (°)	1.7	1.8	1.8	1.7
H-Plane 3-dB Beamwidth (°)	1.7	1.6	1.5	1.6
Maximum Sidelobe Level (dB)	-19.6	-20.5	-19.3	-19.6
Maximum Cross-pol Level (dB)	-18.6	-20.4	-14.8	-15.8

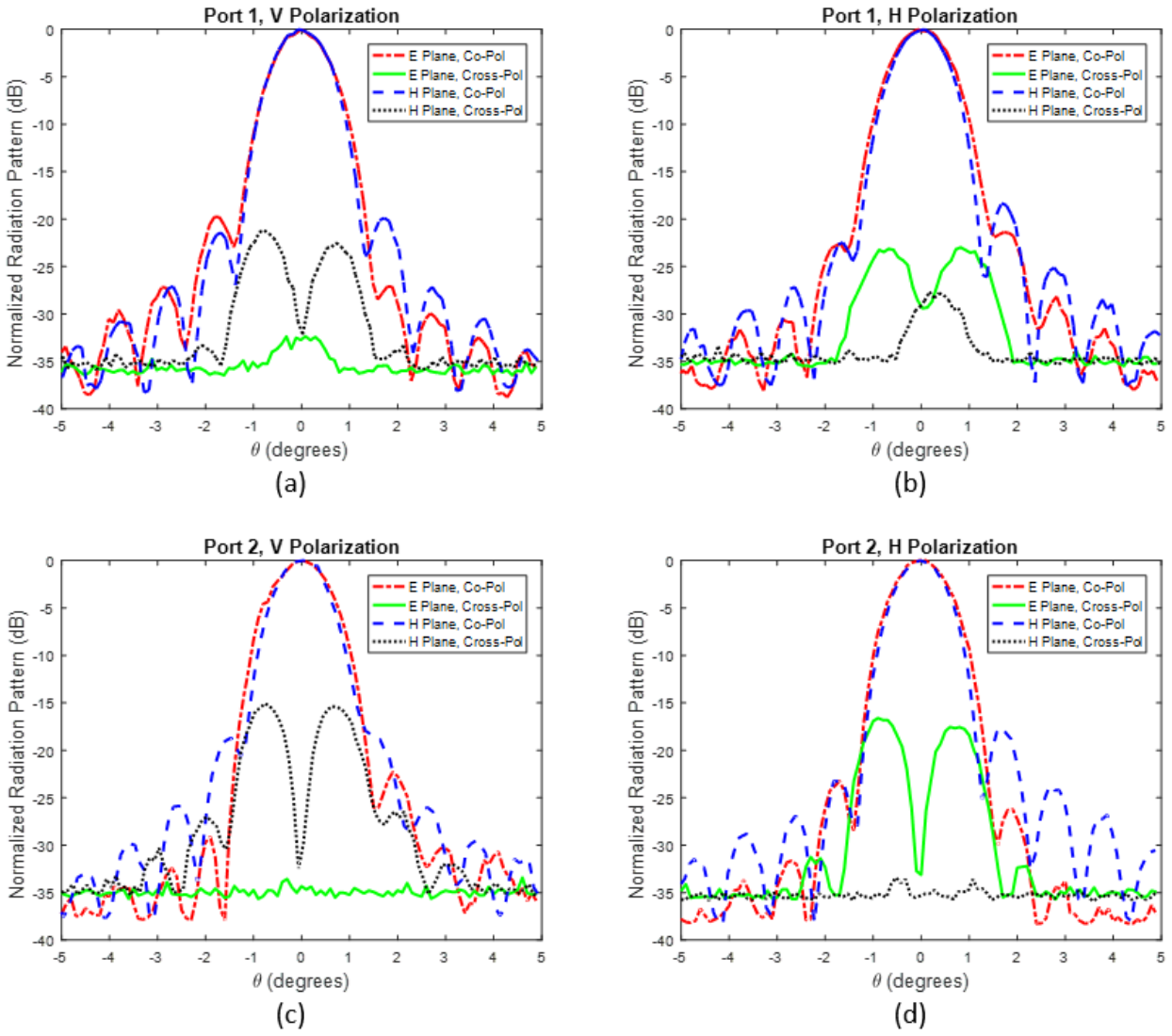

Figure 2.27. Measured radiation pattern of second J-band antenna system with 3-inch lens at 225 GHz for: (a) port 1, V polarization, (b) port 1, H polarization, (c) port 2, V polarization, (d) port 2, H polarization.

Table 2.8
Measured radiation pattern characteristics of second J-band antenna system with 3-inch lens at 225 GHz.

	Port 1, V Polarization	**Port 1, H Polarization**	**Port 2, V Polarization**	**Port 2, H Polarization**
Gain (dB)	37.1	36.9	36.2	37.5
E-Plane 3-dB Beamwidth (°)	1.1	1.2	1.2	1.2
H-Plane 3-dB Beamwidth (°)	1.1	1.1	1.0	1.1
Maximum Sidelobe Level (dB)	-19.8	-18.3	-18.3	-17.6
Maximum Cross-pol Level (dB)	-18.4	-20.0	-14.8	-15.7

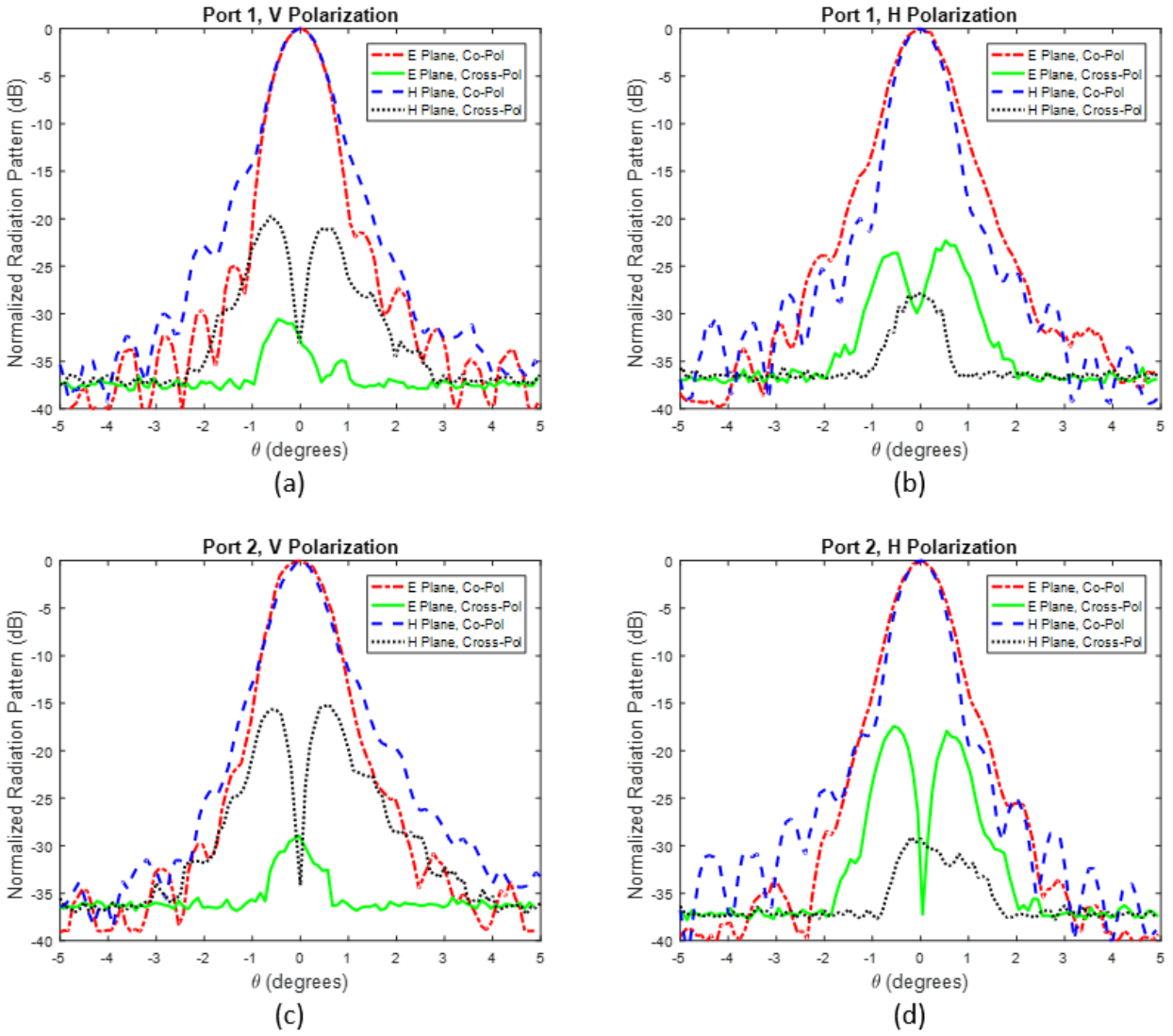

Figure 2.28. Measured radiation pattern of second J-band antenna system with 4-inch lens at 225 GHz for: (a) port 1, V polarization, (b) port 1, H polarization, (c) port 2, V polarization, (d) port 2, H polarization.

Table 2.9
Measured radiation pattern characteristics of second J-band antenna system with 4-inch lens at 225 GHz.

	Port 1, V Polarization	**Port 1, H Polarization**	**Port 2, V Polarization**	**Port 2, H Polarization**
Gain (dB)	38.7	38.7	37.7	39.1
E-Plane 3-dB Beamwidth (°)	0.8	0.9	1.0	0.9
H-Plane 3-dB Beamwidth (°)	0.9	0.8	0.8	0.8
Maximum Sidelobe Level (dB)	-15.2	-15.0	-12.0	-15.7
Maximum Cross-pol Level (dB)	-18.8	-19.8	-15.0	-16.7

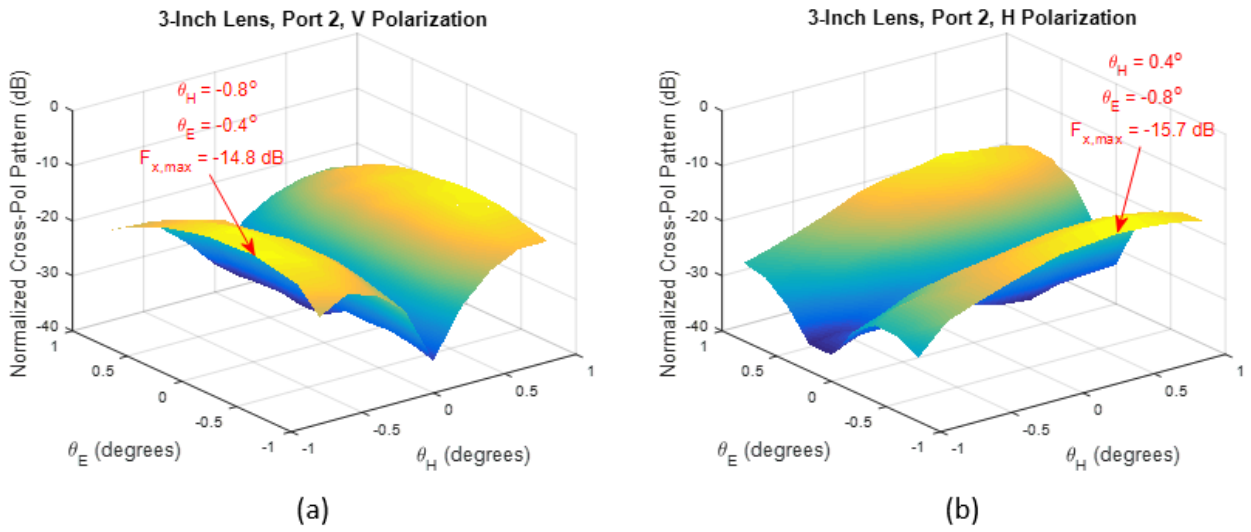

Figure 2.29. Examples of measured 2D cross-polarization patterns of the second J-band antenna system with 3-inch lens are illustrated: (a) port 2, V polarization, and (b) port 2, H polarization. The orientation of the valley is parallel to the plane of incidence of the spatial power divider. The maximum does not fall on an E-plane or H-plane cut.

plane of incidence of the spatial power divider in all cases. It can also be seen that the cross-pol maximum does not fall directly on either an E-plane or H-plane pattern cut. The insertion loss of the wire-grid polarizer has also been measured to be 2.7 dB, and this has been included in the calculation of the cross-pol, which is why the noise floor is elevated compared to that of co-pol.

The antenna's isolation was measured using the setup described previously and shown in Figure 2.23. The isolation is plotted in Figure 2.30. Over the band from 200 GHz to 260 GHz, the isolation is better than 40 dB for any lens configuration. When the lens is removed, the isolation once again improves, but is as low as 47 dB at particular frequencies, which doesn't quite compare to the 60 dB seen in the E-band or previous J-band antennas. However, over the 220 – 230 GHz band of interest, it is mostly greater than 55 dB, and drops to around 50 dB at 220 GHz. A summary of isolation by lens configuration and polarization in the 220 – 230 GHz range is provided in Table 2.10.

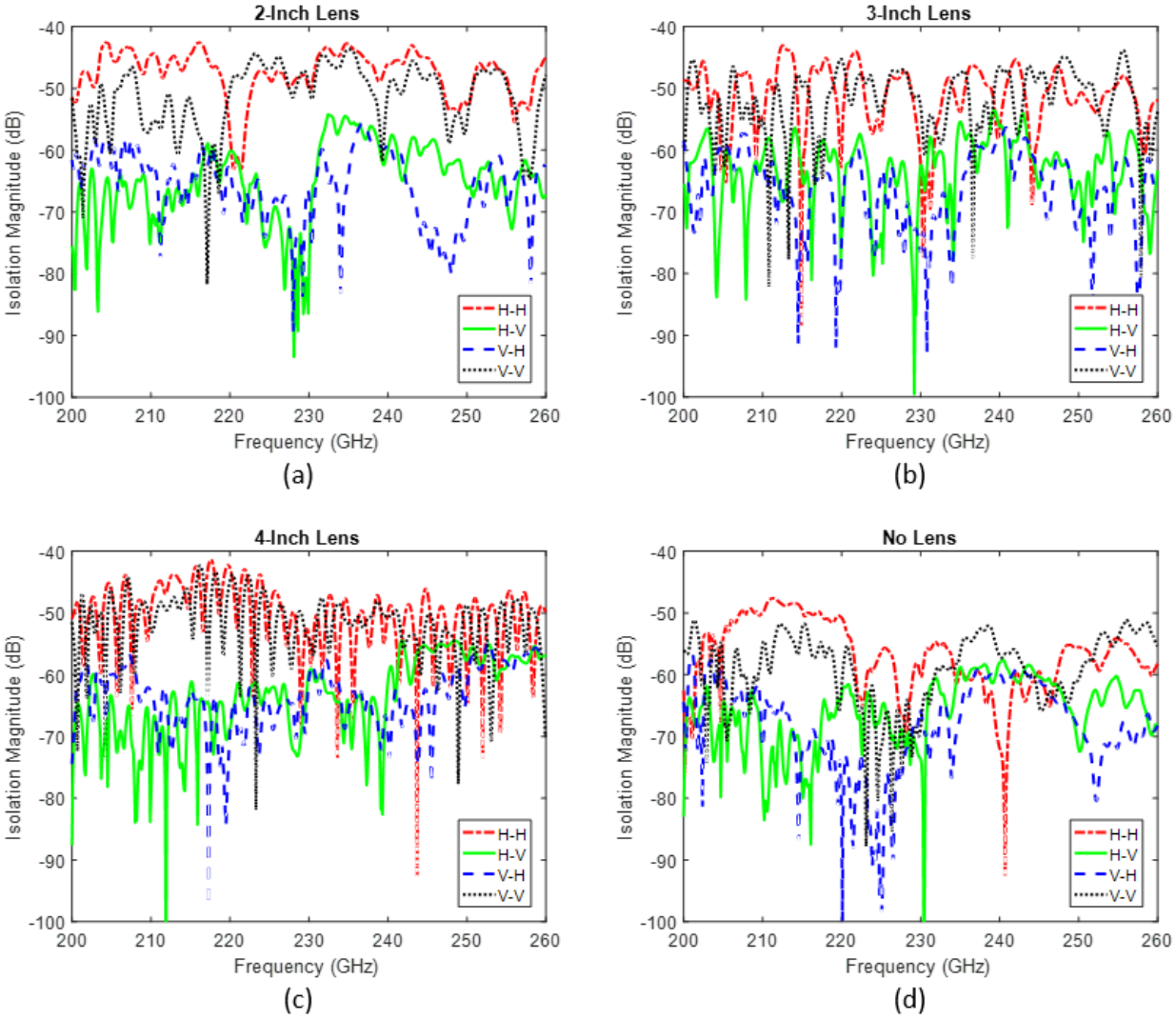

Figure 2.30. Measured isolation of the second J-band antenna system for all combinations of polarizations at the two ports (V-H represents V polarization at port 1 and H polarization at port 2). (a) 2-inch lens configuration, (b) 3-inch lens configuration, (c) 4-inch lens configuration, and (d) lens removed.

Table 2.10
Summary of minimum isolation over the 220 – 230 GHz band for each lens configuration and each combination of polarizations.

	Minimum Isolation Over 220 – 230 GHz (dB)			
	H-H Polarization	**H-V Polarization**	**V-H Polarization**	**V-V Polarization**
2-inch Lens	47.2	60.1	63.3	44.4
3-inch Lens	44.0	57.4	59.9	45.3
4-inch Lens	42.7	59.6	60.8	43.8
No Lens	50.8	61.5	65.5	55.3

2.6 Discussion

It is useful to compare the measured antenna gain and pattern characteristics to the theoretical expectations to get a sense of how well the antenna is functioning. An antenna's effective aperture A_e is defined in relation to its directivity D [71]:

$$D = \frac{4\pi}{\lambda^2} A_e \,. \tag{2.3}$$

For antennas with electrically large apertures, the physical aperture size is the upper limit in the case of perfect illumination with uniform amplitude and phase. The effective aperture can therefore be related to the physical aperture A_p through an aperture efficiency η_a [71]:

$$A_e = \eta_a A_p \,. \tag{2.4}$$

The directivity and half-power beamwidth β of a uniformly illuminated circular aperture are related approximately by [71]:

$$D \approx 0.78 \frac{4\pi}{\beta^2} \,. \tag{2.5}$$

Using (2.3), (2.4), and (2.5), and assuming perfect aperture efficiency ($\eta_a = 1$), theoretical ideal values of directivity and beamwidth can be calculated for a circular lens antenna with a given physical aperture and wavelength λ:

$$D_t = \frac{4\pi}{\lambda^2} A_p \tag{2.6}$$

$$\beta_t \approx 0.88 \frac{\lambda}{\sqrt{A_p}} \,. \tag{2.7}$$

The measured 3-dB beamwidths β_m of the E-band and J-band antennas can be used to estimate their aperture efficiency:

$$\beta_m \approx 0.88 \frac{\lambda}{\sqrt{A_e}} \tag{2.8}$$

$$\eta_a = \frac{A_e}{A_p} = \frac{{\beta_t}^2}{{\beta_m}^2}. \tag{2.9}$$

Table 2.11 shows a summary of the measured gains and beamwidths of the E-band and J-band antennas, as well as calculations of their estimated aperture efficiencies and losses. The first row in the table lists the characterization frequency of each of the antennas. The corresponding free-space wavelength and lens size are used in (2.7) to obtain the minimum theoretical beamwidth. The following row displays the average measured beamwidth, which is obtained from the mean of the eight beamwidth entries (across E-/H-plane, port 1/2, V/H polarization) in each of Tables 2.2, 2.3, 2.5, 2.7, 2.8, and 2.9. The aperture efficiency is calculated from the measured and theoretical beamwidths using (2.9). Next the maximum theoretical directivity calculated with (2.6) and the average (across port 1/2, V/H polarization) measured gain are shown. The average power divider loss values are taken from measured reflection and transmission coefficients of the polarization-independent spatial power dividers, as will be discussed in Chapter 3. It is also interesting to note that the gain of the second J-band antenna was measured in all three lens configurations with the power divider removed to provide another estimate of the average power divider loss, and the two measurements agree within 0.1 dB. The final row of the table shows the remaining loss in the antenna system after removing the contributions of aperture efficiency and power divider loss.

Table 2.11
Summary of measured gain and beamwidth of E-band and J-band antenna systems, and estimation of aperture efficiency and system loss.

Antenna	**E-Band**		**J-Band 1**	**J-Band 2**		
Lens	**6-inch**	**6-inch**	**4-inch**	**2-inch**	**3-inch**	**4-inch**
Frequency (GHz)	77	79	230	225	225	225
Minimum Theoretical Beamwidth (°)	1.46	1.42	0.73	1.50	1.00	0.75
Average Measured Beamwidth (°)	1.55	1.55	0.95	1.70	1.10	0.85
Aperture Efficiency (dB)	-0.5	-0.7	-2.3	-1.1	-0.8	-1.1
Maximum Theoretical Directivity (dB)	41.8	42.0	47.8	41.6	45.1	47.6
Average Measured Gain (dB)	36.2	36.5	39.0	33.7	36.9	38.6
Average Power Divider Loss (dB)	4.1	4.1	4.2	4.1	4.1	4.1
Remaining System Loss (dB)	1.0	0.7	2.3	2.7	3.3	3.8

There are several possible factors that can account for the remaining system loss, including mismatch loss, conductive loss, dielectric loss, and spillover loss.

Mismatch loss is related the impedance match between the horns and their feed waveguides. Conductive loss refers to power dissipation within the feed horns. The feed horns used in the J-band antennas have circular waveguide inputs and were attached directly to WR-03 rectangular waveguides, so significant mismatch is expected. Additionally, they were fabricated from either aluminum or brass, so some conductive loss is anticipated as well. The combination of mismatch and conductive loss of the aluminum feeds of the first J-band antenna was estimated to be approximately 1.8 dB through a series of time-gated reflection coefficient measurements. By comparison, more effort was put into correcting for mismatch in the E-band antenna gain

measurements, as described in Section 2.3.4. Additionally, the corrugated feed horns were gold plated by the manufacturer, so conductive loss is expected to be lower, especially at the lower frequency band. These factors could help explain the considerable difference in loss between the E-band and J-band antennas.

True dielectric loss in the lens is expected to be quite small, as the Rexolite material has a loss tangent on the order of $10^{-4} – 10^{-3}$ up to 500 GHz. Other sources of loss related to the dielectric lens include roughness of the lens surfaces and reflections at each boundary. The surfaces were machined and polished to a roughness much smaller than the wavelength, so that is not expected to have much impact either. However, the reflectivity at normal incidence for an interface between air and Rexolite is around 0.05. To a first-order approximation, this may result in an insertion loss through the lens of around 0.5 dB for the two interfaces.

As discussed previously, spillover loss is a result of a fraction of the energy radiated from the feed horns missing the lens, and therefore not contributing to the total gain. Since the taper of the horn's pattern at the edge of the lens is approximately 10 dB, it is expected that the lens intercepts most of the energy radiated from the feed. Based on the simulated J-band horn pattern, an estimated spillover loss of 0.5 dB has been calculated.

The measured beamwidths are somewhat surprising, since they are fairly close to the ideal values for a uniform amplitude illumination, when in fact the illumination is known to be strongly tapered. The pattern measurements were made with a resolution of 0.1°, so there is uncertainty of that order in the measured beamwidths. The high sidelobes in Figure 2.28 indicate possible diffraction from the edges of the lens, which may also contribute to the narrow beam. Additionally, there is some error associated with the gain measurements due to the relative gain technique employed and fluctuations in recorded power. With these uncertainties in mind, the losses from

mismatch, conduction, lens reflection, and spillover can very reasonably account for the observed differences between the measured gain and theoretical directivity of these antenna systems. Overall, they seem to be functioning very well, providing high gain and a narrow beam to help the sensitivity and angular resolution of the associated radar systems.

2.7 Summary

A unique antenna system with two dual-polarized ports sharing a common aperture has been conceived by combining the best aspects of more traditional radar lens antenna systems. It is geometrically similar to a standard dual-polarized lens antenna, except that the wire-grid polarizer has been replaced with a polarization-independent spatial power divider. With this architecture, the antenna system has perfect alignment between its beams, and takes up only half as much space in the radar as would two separate lens antennas for transmit and receive. The inclusion of the power divider enables the transmit and receive functions to be separated to different ports, which eliminates the need for lossy and leaky circulators. As a result, this antenna system has high-isolation and low-loss performance more similar to the two-antenna scheme. The cost of all these benefits is 6 dB: the two-way insertion loss of the power divider. Operating at high millimeter-wave frequencies offers directivity, size reduction, and absolute bandwidth. A radar using this antenna system is compact, has high isolation and fine resolution, and supports fully polarimetric operation free of parallax.

Three versions of this antenna system were designed and constructed at 76 – 81 GHz, 230 – 248 GHz, and 220 – 230 GHz. Each has been installed in a different polarimetric radar system. Depending on the band and lens size, a narrow beam of 0.8° to 1.7° and a high gain of 33 to 39 dB have been achieved. The transmit-to-receive isolation is 40 dB at a minimum, and in many cases better.

CHAPTER 3
Polarization-Independent Spatial Power Divider

The antenna system discussed in Chapter 2 features two dual-polarized feeds which both illuminate a single aperture lens. This property relies on a polarization-independent spatial power divider to direct V- and H-polarized modes from each of the feeds toward the lens.

The standard dual-polarized lens antenna depicted in Figure 2.3.a uses a wire-grid polarizer to accomplish this task for two single-polarized feeds. This works because the wire-grid polarizer completely reflects H polarization and completely transmits V polarization. In order to avoid the use of lossy and poorly-isolated circulators, it is desired to transmit from only one dual-polarized feed, and receive at another dual-polarized feed, as in Figure 2.3.b. Unfortunately, the wire-grid polarizer will not work in this case, because the H-polarized transmit wave will be reflected from the polarizer and will not illuminate the lens. Similarly, a V-polarized backscattered wave will pass through the polarizer and will not be directed to the receive port. Instead, a device is required to allow a fraction of the power of both V- and H- polarized waves to be transmitted through it, and the remainder to be reflected. That way at least some of the transmitted power makes it to the lens, and some of the backscattered energy makes it to the receiver. Such a device is referred to in general as a power divider, and in this case, since the incident beam is split into two different directions in space, it is a spatial power divider.

To determine what fraction of power division for V and H polarization would provide optimal performance, consider the radar equation for a point target [72]:

$$\frac{P_r^p}{P_t^q} = \frac{G_r^p G_t^q \lambda^2}{(4\pi)^3 {R_r}^2 {R_t}^2} \sigma_{pq} \,. \tag{3.1}$$

Here P_r^p and P_t^q are the received p-polarized and transmitted q-polarized powers, G_r^p and G_t^q are the p-polarized receiver and q-polarized transmitter antenna gains, R_r is the distance between target and receiver, R_t is the distance between target and transmitter, σ_{pq} is the pq-polarized radar cross-section (RCS) of the target, and λ is the wavelength. The indices p and q may represent either V or H polarization. For the application of interest, the transmitter and receiver are collocated, so let $R_r = R_t = R$. Additionally, assume the gain of the horn-lens system is G_0 for both the transmitter and receiver in both polarizations. Next, suppose the spatial power divider is a passive, lossless, and reciprocal device. Then its power transmission coefficient (the fraction of power transmitted through the power divider) for a given polarization is independent of transmission direction. Furthermore, its power reflection coefficient (the fraction of power reflected from the power divider) and transmission coefficient must sum to unity. Thus p-polarized reflection and transmission coefficients Γ_p and T_p may be defined, where $\Gamma_p + \mathrm{T}_p = 1$. With port 1 designated as the transmitter and port 2 designated as the receiver, it can be seen that $G_r^p = G_0 \Gamma_p$ and $G_t^q = G_0 \mathrm{T}_q$. Substituting these relations into (3.1) results in:

$$\frac{P_r^p}{P_t^q} = \frac{G_0^2 \Gamma_p \left(1 - \Gamma_q\right) \lambda^2}{(4\pi)^3 R^4} \sigma_{pq} \,. \tag{3.2}$$

Let $\Xi_{pq} = \Gamma_p \left(1 - \Gamma_q\right)$ be the round-trip channel transmission coefficient of the spatial power divider associated with the pq polarization configuration of the radar. It can be seen that the quantity Ξ_{pq} can be optimized to maximize the p-polarized power received due to q-polarized

transmission. A wire-grid polarizer with $\Gamma_V = 0$ and $\Gamma_H = 1$ has $\Xi_{HV} = 1$, and will maximize received power in the HV polarization configuration. However, in this case no power will be received for any other configuration. Received power for VV and HH polarization are maximized when $\Gamma_V = \Gamma_H = 0.5$. In that case, $\Xi_{VV} = \Xi_{VH} = \Xi_{HV} = \Xi_{HH} = 0.25$, which seems like a reasonable intuitive guess at the optimal set of reflection coefficients for a radar with balanced sensitivity across all polarization configurations.

To confirm this mathematically, a fitness function can be defined as the geometric mean of the channel transmission coefficients:

$$F = \left(\prod_{p,q \in \{V,H\}} \Xi_{pq} \right)^{1/4} . \tag{3.3}$$

This fitness function has the largest values when no Ξ_{pq} is much smaller than the others, and will therefore serve to find a set of reflection coefficients providing balanced received power across polarization configurations. Figure 3.1 plots F as a function of Γ_V, and Γ_H, and F is indeed maximized when $\Gamma_V = \Gamma_H = 0.5$, as expected.

For this reason, it is desirable to have a polarization-independent spatial power divider with equal transmission and reflection coefficients. The design of a device with these properties is described in this chapter.

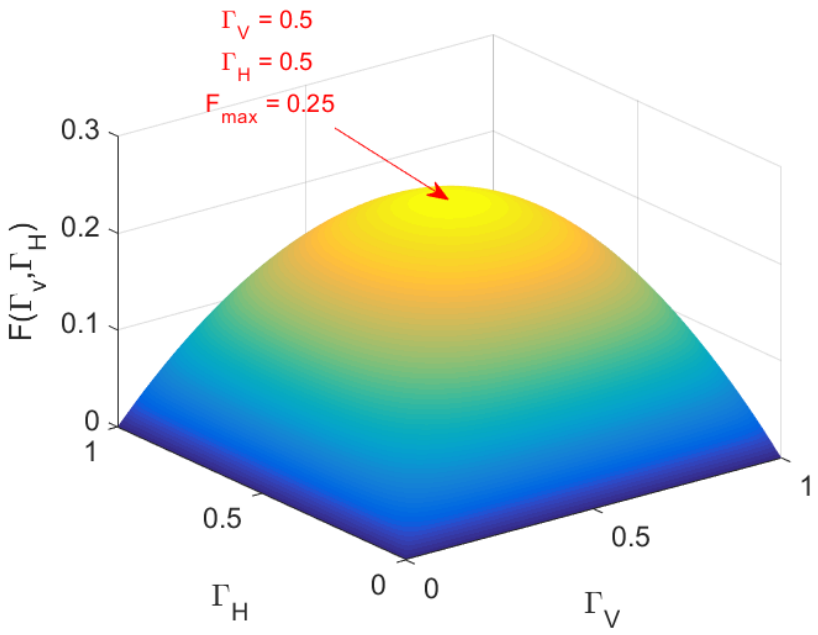

Figure 3.1. A plot of the fitness function defined in (3.3) as a function of a spatial power divider's reflection coefficients for V and H polarization.

3.1 Spatial Power Divider Overview

The emerging area of electromagnetic metamaterials is introducing new ways in which propagation can be controlled in a wide variety of application areas [73], [74], [75]. All-dielectric metasurface approaches have been used to demonstrate control over phase and polarization over a range of incidence angles [76], [77]. Similar behaviors can be achieved using sub-wavelength periodic metallic structures called miniaturized element frequency selective surfaces (MEFSS) [78], [79], [80].

The polarization-independent spatial power dividers used in the J-band radar antenna systems were designed using a type of dielectric metamaterial called a corrugated dielectric slab. The E-band power divider also utilizes a corrugated slab, but also includes MEFSS elements.

The first approach considered was actually one based entirely on MEFSS. It was found that some of these structures could produce nearly equal reflection and transmission coefficients over a wide bandwidth. However, basic MEFSS elements are two-dimensional and lie in a plane, and several stacked layers of these elements were required to achieve the desired behavior. For fabrication of such structures, a dielectric substrate would be needed to connect and support the metallic layers. With that restriction, it becomes difficult to design for 45-degree incidence. Since the reflection and transmission coefficients of a dielectric slab are polarization-dependent at oblique incidence, any design based purely on a metallic MEFSS structure will no longer work after the introduction of the dielectric substrate. Therefore, the dielectric component must be considered from the beginning of the design process. For this reason, attention was turned to look into dielectric designs without metal, eventually leading to the final J-band power divider implementations. Later, during the design of the E-band power divider, some simple metallic elements were added to adjust the response of the base dielectric design. A similar power divider concept using a MEFSS approach was presented in [81], but the imbalance between reflection and transmission is considerably higher than what is possible with the approach presented here.

To explain how the power divider was designed, a detailed discussion of the principle of operation is provided. Ultimately, the power divider is fabricated using standard micromachining techniques, which result in non-ideal geometries that are not directly captured in the theory of operation. As a result, computational tools are used as an intermediate design step to transition from the basic geometry associated with this theory, to a realistic design that can be fabricated. Following this design flow, both an analytical model for identifying initial ballpark designs, and full-wave electromagnetic simulations for increased accuracy and optimization are presented. The fabrication process can be fine-tuned experimentally to produce the desired outcome.

3.2 Principle of Operation

3.2.1 Intuition: The Dielectric Slab

To develop intuition for understanding the dielectric metamaterial approach used in these power divider designs, it is useful to first consider a simple dielectric slab (i.e. a sheet of ideally lossless dielectric material, infinite in extent along two coordinate axes, and with a constant finite thickness along the third axis). The reflection and transmission coefficients for a plane wave incident on this structure can be calculated fairly easily using Snell's Law of refraction and the Fresnel equations [82]. Figure 3.2 shows plots of reflection and transmission coefficients for several cases of particular interest described below. At normal incidence, a quarter-wave slab with a dielectric constant of approximately 5.83 provides equal reflection and transmission. At an oblique incidence angle, transmission is reduced for transverse electric (TE) polarization, but increased for transverse magnetic (TM) polarization. On the other hand, if the dielectric constant of the slab is allowed to vary at normal incidence, it can be seen that reducing the dielectric constant increases transmission, while increasing the dielectric constant reduces transmission. From these observations, it seems that to compensate for the effect of oblique incidence and maintain equal reflection and transmission, a smaller dielectric constant is needed for TE polarization and a larger dielectric constant is needed for TM polarization. This is in fact the case, and using quarter-wave slabs with dielectric constants of 3.41 and 11.1, equal reflection and transmission can be achieved at 45-degree incidence for TE and TM polarization, respectively. Notice that in each case the equality is maintained over a substantial bandwidth. However, neither case provides equal reflection and transmission for both polarizations simultaneously. The latter solution is the better of the two, having closer TE reflection and transmission coefficients than the TM coefficients of the former solution. However, this slab only achieves $\Xi_{VV} = 0.1425$, which represents a loss of

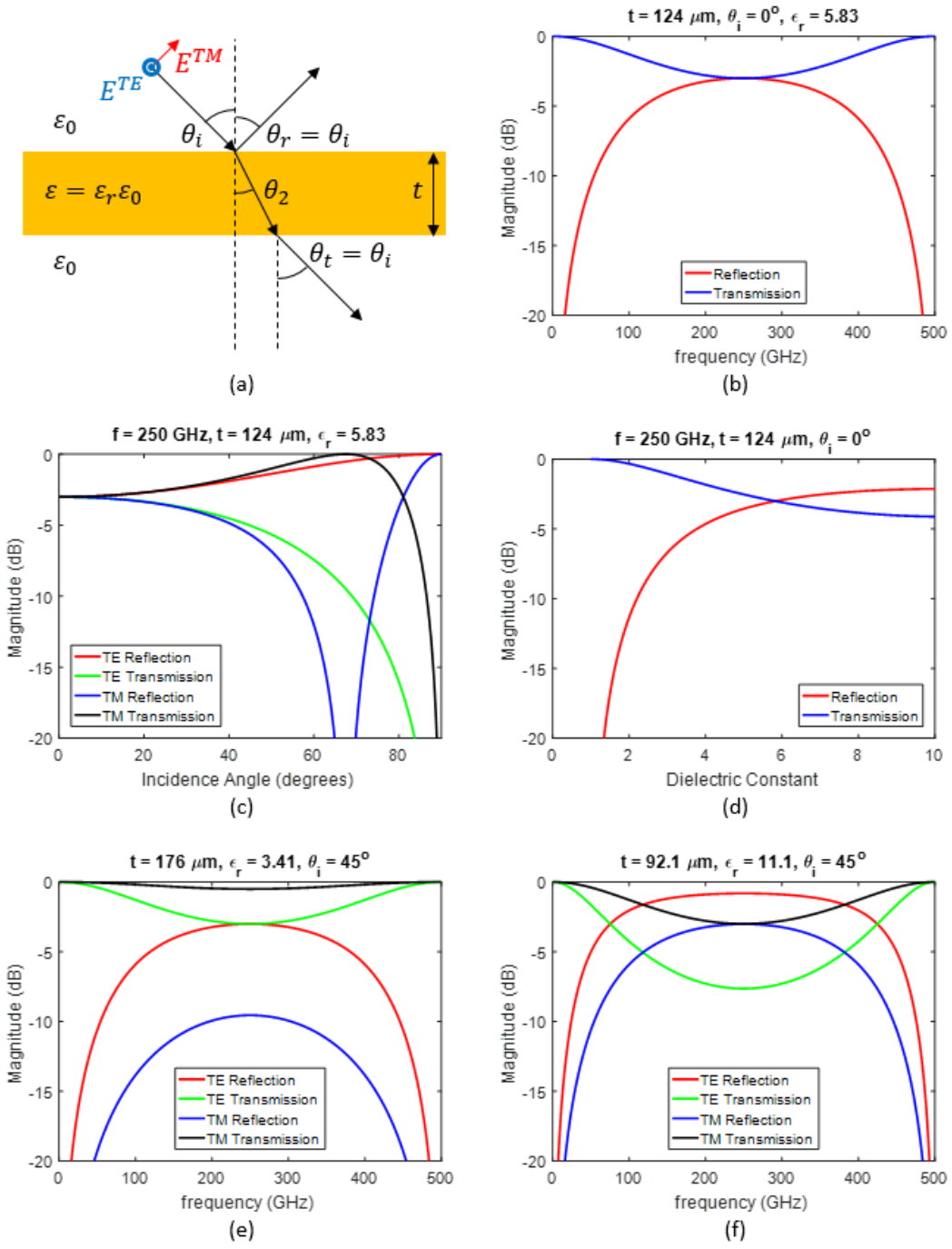

Figure 3.2. Reflection and transmission coefficients of dielectric slabs for several cases of interest, with a center frequency of 250 GHz. (a) Geometry of the slab showing incidence, reflection, and transmission angles, and directions of TE and TM electric fields. (b) Dielectric constant and thickness chosen for equal reflection and transmission at normal incidence. (c) Change in coefficients as a function of incidence angle. (d) Change in coefficients as a function of dielectric constant. (e) Dielectric constant and thickness chosen for equal TE reflection and transmission at 45-degree incidence. (f) Dielectric constant and thickness chosen for equal TM reflection and transmission at 45-degree incidence.

2.44 dB compared to the ideal $\Xi_{VV} = 0.25$. A better solution is desired for the polarization-independent spatial power divider.

3.2.2 The Corrugated Dielectric Slab

The observations in the previous section suggest that an anisotropic material with a lower dielectric constant for TE polarization than for TM polarization might be able to achieve the desired power divider characteristics. One way to implement a material with such an anisotropic dielectric behavior is by using a dielectric with periodic corrugations, as shown in Figure 3.3. This structure can be analyzed first by considering the electromagnetic behavior of a periodic array of slabs infinite in the y and z directions. Once the behavior of this medium is known, the corrugations can be treated as a layer of this material with a finite thickness in the y direction, as done in [83]. If the dimension L is small compared to the wavelength, the relative permittivity tensor of the corrugated medium is given by fairly simple approximate expressions:

$$\bar{\bar{\boldsymbol{\varepsilon}}}_{\boldsymbol{r}} = \begin{bmatrix} \varepsilon_r^x & 0 & 0 \\ 0 & \varepsilon_r^y & 0 \\ 0 & 0 & \varepsilon_r^z \end{bmatrix} \tag{3.4}$$

$$\varepsilon_r^x = \frac{\varepsilon_r^s}{\varepsilon_r^s(1 - d/L) + d/L} \tag{3.5}$$

$$\varepsilon_r^y = \varepsilon_r^z = 1 + (\varepsilon_r^s - 1)\, d/L \tag{3.6}$$

where ε_r^s is the relative permittivity of the substrate dielectric material.

Thus the corrugated slab behaves as a uniaxial medium with its optical axis along the x direction.

Figure 3.4 shows a plot of (3.5) and (3.6) as a function of the corrugation ratio d/L, revealing that $\varepsilon_r^x < \varepsilon_r^y$. This suggests that ε_r^x should be used for TE polarization and ε_r^y for TM polarization. Thus the plane of incidence will be the yz-plane so that the TE electric and displacement fields are parallel to the x-axis (parallel to the optical axis of the uniaxial medium), and the TM electric and displacement fields are parallel to the yz-plane (perpendicular to the optical axis). If the material is non-magnetic ($\mu = \mu_0$), then the extraordinary modes of the uniaxial medium are not excited, and the TE and TM cases can simply be treated independently, with $\varepsilon^{TE} = \varepsilon_r^x$ and $\varepsilon^{TM} = \varepsilon_r^y$ as the respective effective relative permittivities in the layer corresponding to the corrugated slab.

It should be noted that for other applications it may be desirable to use the xy-plane as the plane of incidence, in which case the propagation of ordinary and extraordinary waves in a uniaxial medium must be considered to describe the behavior of TE and TM incident waves. This is described in [83].

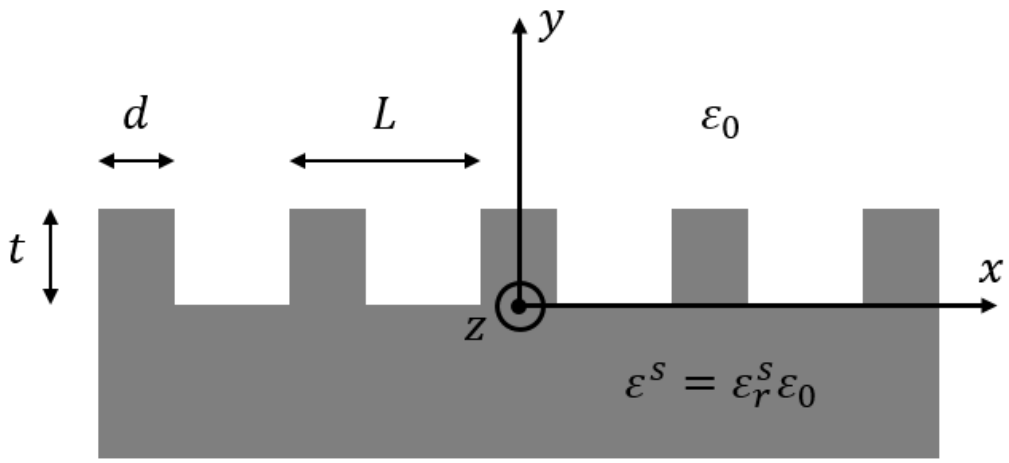

Figure 3.3. The geometry of a corrugated dielectric slab is depicted. The coordinate system used in this discussion is also defined.

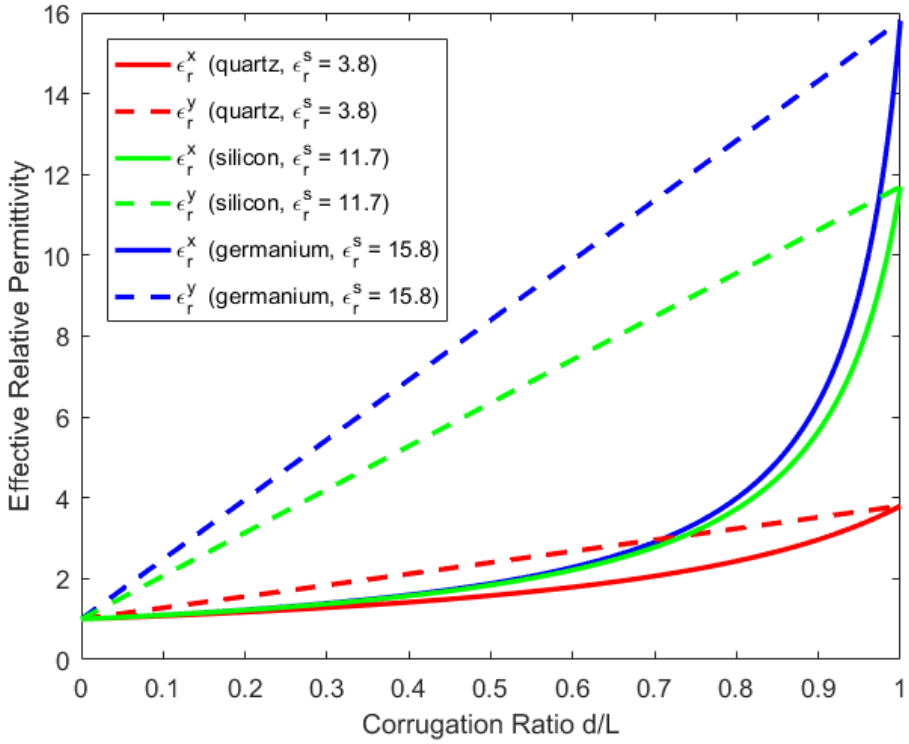

Figure 3.4. Plot of the effective relative permittivity of a corrugated dielectric slab along x and y directions as a function of corrugation ratio. Several common microelectronics substrates with different dielectric constants are shown.

3.2.3 Cascades of Multiple Layers

To calculate the total transmission through and reflection from a single corrugated slab layer, the transfer matrix method is used [84]. This technique is readily extended to a cascade of multiple dielectric layers. For each interface between layers, a transfer matrix is defined relating the incident and reflected fields on one side of the interface to those on the other side. Similarly, a transfer matrix is defined for propagation through each layer. Multiplying the matrices together yields the total transfer matrix for the entire cascade.

The transfer matrices for TE and TM incidence are given as follows for the corrugated dielectric medium:

$$k_{y,n}^{TE} = 2\pi f\sqrt{\mu_0\varepsilon_0\varepsilon_n^{TE}}\,cos\,\theta_n^{TE} \tag{3.7}$$

$$k_{y,n}^{TM} = 2\pi f\sqrt{\mu_0\varepsilon_0\varepsilon_n^{TM}}\,cos\,\theta_n^{TM} \tag{3.8}$$

$$\boldsymbol{M_{I,n}^{TE}} = \frac{1}{2}\begin{bmatrix} 1+\dfrac{k_{y,n}^{TE}/\mu_0}{k_{y,n+1}^{TE}/\mu_0} & 1-\dfrac{k_{y,n}^{TE}/\mu_0}{k_{y,n+1}^{TE}/\mu_0} \\ 1-\dfrac{k_{y,n}^{TE}/\mu_0}{k_{y,n+1}^{TE}/\mu_0} & 1+\dfrac{k_{y,n}^{TE}/\mu_0}{k_{y,n+1}^{TE}/\mu_0} \end{bmatrix} \tag{3.9}$$

$$\boldsymbol{M_{I,n}^{TM}} = \frac{1}{2}\begin{bmatrix} 1+\dfrac{k_{y,n}^{TM}/\varepsilon_n^{TM}}{k_{y,n+1}^{TM}/\varepsilon_{n+1}^{TM}} & 1-\dfrac{k_{y,n}^{TM}/\varepsilon_n^{TM}}{k_{y,n+1}^{TM}/\varepsilon_n^{TM}} \\ 1-\dfrac{k_{y,n}^{TM}/\varepsilon_n^{TM}}{k_{y,n+1}^{TM}/\varepsilon_{n+1}^{TM}} & 1+\dfrac{k_{y,n}^{TM}/\varepsilon_{n+1}^{TM}}{k_{y,n+1}^{TM}/\varepsilon_{n+1}^{TM}} \end{bmatrix} \tag{3.10}$$

$$\boldsymbol{M_{P,n}^{TE}} = \frac{1}{2}\begin{bmatrix} exp(i\cdot k_{y,n}^{TE}\cdot t_n) & 0 \\ 0 & exp(-i\cdot k_{y,n}^{TE}\cdot t_n) \end{bmatrix} \tag{3.11}$$

$$\boldsymbol{M_{P,n}^{TM}} = \tfrac{1}{2}\begin{bmatrix} exp(i\cdot k_{y,n}^{TM}\cdot t_n) & 0 \\ 0 & exp(-i\cdot k_{y,n}^{TM}\cdot t_n) \end{bmatrix}. \tag{3.12}$$

Here $k_{y,n}$ is the propagation constant in the y direction in the n^{th} layer, and t_n is the physical thickness of the n^{th} layer. $\boldsymbol{M_{P,n}}$ is the transfer matrix for propagation through the n^{th} layer, and $\boldsymbol{M_{I,n}}$ is the transfer matrix for the interface between the n^{th} and $(n+1)^{th}$ layers. The index n ranges from 0 to $N+1$ for a cascade of N dielectric layers (indices 0 and $N+1$ represent the air on either side). θ_n is the angle between the propagation vector and the y-axis in the n^{th} layer, and the angles are related by Snell's Law:

$$\sqrt{\varepsilon_n^{TE}}\,sin\,\theta_n^{TE} = \sqrt{\varepsilon_{n+1}^{TE}}\,sin\,\theta_{n+1}^{TE} \tag{3.13}$$

$$\sqrt{\varepsilon_n^{TM}}\, sin\, \theta_n^{TM} = \sqrt{\varepsilon_{n+1}^{TM}}\, sin\, \theta_{n+1}^{TM}\,. \tag{3.14}$$

The total transfer matrices for the entire cascade are calculated by multiplying the interface and propagation transfer matrices in sequential order, as follows:

$$\boldsymbol{M_{total}^{TE}} = \boldsymbol{M_{I,N}^{TE} M_{P,N}^{TE} M_{I,N-1}^{TE} M_{P,N-1}^{TE} \cdots M_{I,1}^{TE} M_{P,1}^{TE} M_{I,0}^{TE}} \tag{3.15}$$

$$\boldsymbol{M_{total}^{TM}} = \boldsymbol{M_{I,N}^{TM} M_{P,N}^{TM} M_{I,N-1}^{TM} M_{P,N-1}^{TM} \cdots M_{I,1}^{TM} M_{P,1}^{TM} M_{I,0}^{TM}}\,. \tag{3.16}$$

Then the scattering matrices are calculated with the transformation [85]:

$$\boldsymbol{M} = \begin{bmatrix} M_{11} & M_{12} \\ M_{21} & M_{22} \end{bmatrix} \tag{3.17}$$

$$\boldsymbol{S} = \begin{bmatrix} S_{11} & S_{12} \\ S_{21} & S_{22} \end{bmatrix} = \begin{bmatrix} -M_{21}/M_{22} & 1/M_{22} \\ M_{11} - M_{12}M_{21}/M_{22} & M_{12}/M_{22} \end{bmatrix}. \tag{3.18}$$

Here, the matrix $\boldsymbol{M}$ represents either $\boldsymbol{M_{total}^{TE}}$ or $\boldsymbol{M_{total}^{TM}}$, the equivalent transfer matrices of the entire cascade. Equation (3.18) is used to calculate the reflection and transmission coefficients.

3.3 First J-Band Power Divider Implementation

An all-dielectric structure consisting of a cascade of corrugated dielectric slabs serves as the basis of the first J-band power divider operating at 230 – 248 GHz. This power divider was designed by first using an analytical model to calculate reflection and transmission coefficients from (3.5) – (3.18). Full-wave simulations in Ansys HFSS were then used to refine the results. Finally, prototypes were fabricated using deep reactive ion etching (DRIE) in the University of Michigan's Lurie Nanofabrication Facility (LNF).

3.3.1 Analytical Modeling

A simple code was written in MATLAB to calculate the reflection and transmission coefficients for a cascade of N corrugated dielectric slab layers using (3.5) – (3.18). An incidence angle of 45 degrees was used.

For each layer, there are up to three parameters that can be used to design for a desired response: the layer thickness t, the corrugation ratio d/L, and the permittivity ε. In practice, not all three parameters can be chosen arbitrarily for each layer. For example, to make fabrication feasible, at least one of the layers should have $d/L = 1$, i.e. the layer is not corrugated, but is instead uniformly composed of a solid isotropic dielectric material.

A more significant restriction applies to the permittivity of the material in each layer, since only values corresponding to a real material may be selected. Silicon ($\varepsilon_r = 11.7$) has been chosen as the sole material for this design because at near 230 GHz the wavelength necessitates fabrication of periodic structures on the micron scale. DRIE is a standard process used to cut trenches into silicon wafers with nearly vertical side walls [86]. Additionally, silicon's relatively high permittivity is beneficial, since quite large differences in the effective permittivity for TE and TM polarizations can be produced by choosing the corrugation ratios in the corrugated layers appropriately (refer to (3.5) and (3.6), as well as Figure 3.4).

Therefore, using $\varepsilon_r^s = 11.7$ and treating the layer thickness and corrugation ratio as free parameters, the MATLAB code was run for cascades of 1 to 5 layers and a built-in genetic algorithm was used to find optimal solutions. It was found that neither a single corrugated slab layer, nor a cascade of two layers were sufficient to produce approximately equal reflection and transmission for both polarizations over any substantial bandwidth at the desired frequency. A three-layer cascade consisting of two anisotropic layers and one isotropic layer was found to

provide satisfactory behavior, while having four or more layers was not found to significantly improve performance.

To include the impact of the dielectric loss of the silicon, an imaginary part of the dielectric constant was introduced. As will be discussed in the upcoming sections on fabrication and measurement, it was found that an imaginary part of the relative dielectric constant of $\varepsilon'' = 0.455$ is an appropriate estimate for the silicon wafers used. Additionally, for feasibility of fabrication, $d/L = 1$ has been required for one of the layers, and the total thickness of the cascade has been constrained to 525 μm, the thickness of a standard wafer. The inclusion of loss and the removal of two free parameters results in a minor degradation of the performance that is possible to achieve.

The solution to the optimization is not unique, as different combinations of the parameters can lead to similar performance. Row 1 of Table 3.1 shows a chosen set of parameters which give optimal performance over a 20 GHz bandwidth centered at 235 GHz, and which define a structure that can be fabricated using DRIE. The difference between reflection and transmission is less than 0.25 dB for both polarizations from 225 GHz to 246 GHz.

3.3.2 Simulation Results

The analytical modelling process described above is necessary in order to quickly identify potential geometries that will yield viable solutions, but additional computations are needed to obtain a final design. The combination of parameters found with the MATLAB model were used as a starting point for full-wave electromagnetic simulation using Floquet analysis in Ansys HFSS. Figure 3.5 shows several views of the simulated geometry. This simulation allowed for verification of the analytical model, including the validity of the approximations (3.5) and (3.6). Figure 3.6 displays the reflection and transmission coefficients calculated by both MATLAB and HFSS for the solution given in Row 1 of Table 3.1. The plane of incidence is the yz-plane, and the incidence

angle is 45 degrees. The two calculations agree very well. It can be seen that at higher frequencies, there seems to be a slight frequency shift between the analytical solution and simulation, particularly for TE polarization. This is due to reduced accuracy of the approximations in the analytical model as the wavelength becomes smaller compared to the size of the unit cell.

Simulation also helps to capture non-ideal features in the etch profile of DRIE, including non-vertical side walls and curvature of the trench bottom. The structure depicted in Figure 3.5 has an exaggerated side wall angle of 2 degrees so that this feature can be seen clearly. The curvature of the bottom of the trench is modeled as an ellipse with a major-to-minor axis ratio of 4. The analytical model is not able to take the non-ideal geometry into consideration. After including these factors, additional optimization was performed. The cost function is defined as an L2 norm of two quantities, the difference between the magnitudes of the reflection and transmission coefficients for TE polarization, and the corresponding difference for TM polarization, evaluated over the frequency range of interest. This serves to search for solutions where reflection and transmission are equal for both polarizations. After optimization, a second order design was reached. The parameters are listed in Row 2 of Table 3.1, and the reflection and transmission coefficients simulated in HFSS are plotted in Figure 3.7.

The difference between reflection and transmission is at most 0.5 dB for both polarizations over the band from 220 GHz to 250 GHz. Here the total thickness of the structure has been constrained to 525 μm, as this is the standard silicon wafer thickness available in the LNF. As a result, frequency scaling is somewhat limited. However, with non-standard wafer thicknesses or precise wafer thinning, this restriction can be bypassed.

Table 3.1
The layer thickness and corrugation ratios of the first three-layer J-band spatial power divider are provided for several different design stages: Row 1: initial starting point found using the MATLAB analytical model, Row 2: optimized HFSS simulation, Row 3: measured dimensions of fabricated prototype, and Row 4: ideal simulation assuming lossless substrate and full control over all available design parameters.

		Layer Thickness (μm)			**Layer Corrugation Ratio**			
Row	**Description**	t_1	t_2	t_3	d_1/L	d_2/L	d_3/L	L **(μm)**
1	Analytical Model	289.8	10.0	225.2	1	0.8223	0.6150	-
2	Simulation	297.3	2.5	225.2	1	0.8223	0.5916	200
3	Fabrication	278.5	3.6	241.9	1	0.8580	0.5738	200
4	Ideal Simulation	278.4	52.2	194.4	1	0.8252	0.5875	200

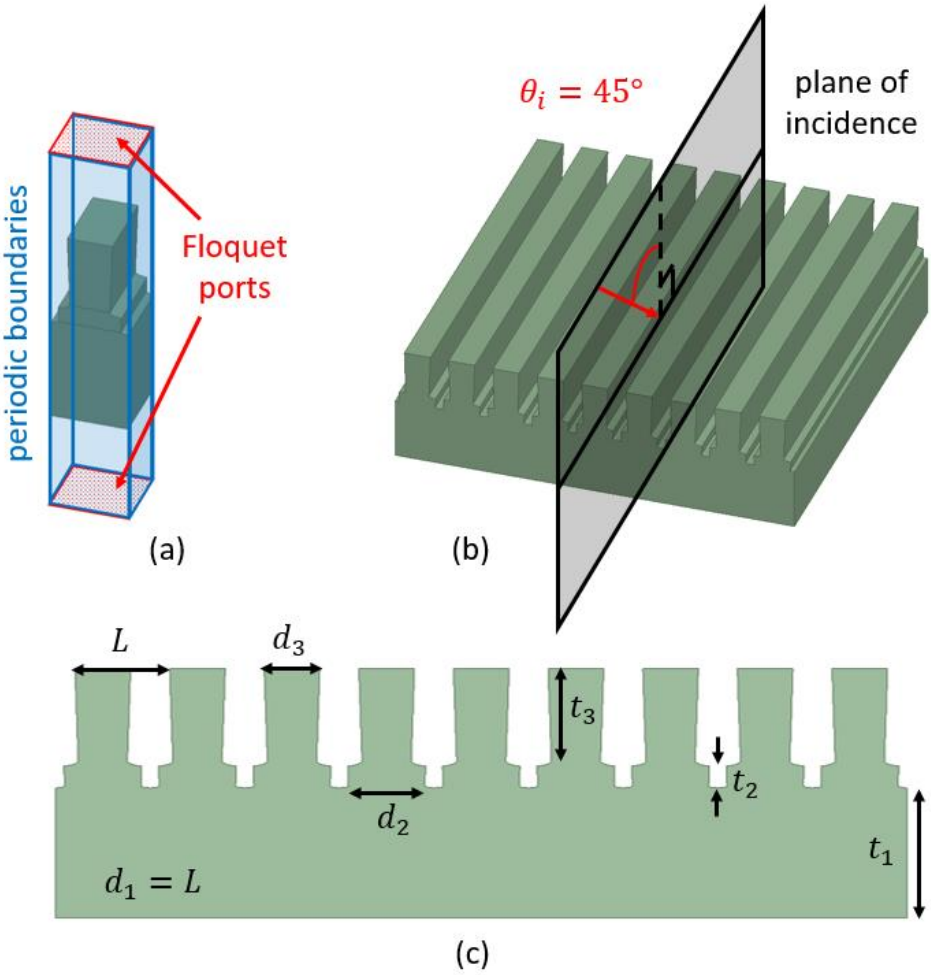

Figure 3.5. Geometry of the simulated three-layer J-band spatial power divider structure. (a) A single unit cell, and positions of the Floquet ports and periodic boundaries in the simulation setup. (b) A perspective view of several unit cells, and the plane of incidence and incidence angle of the excitation mode. (c) A cross-sectional view of the structure showing the model parameters.

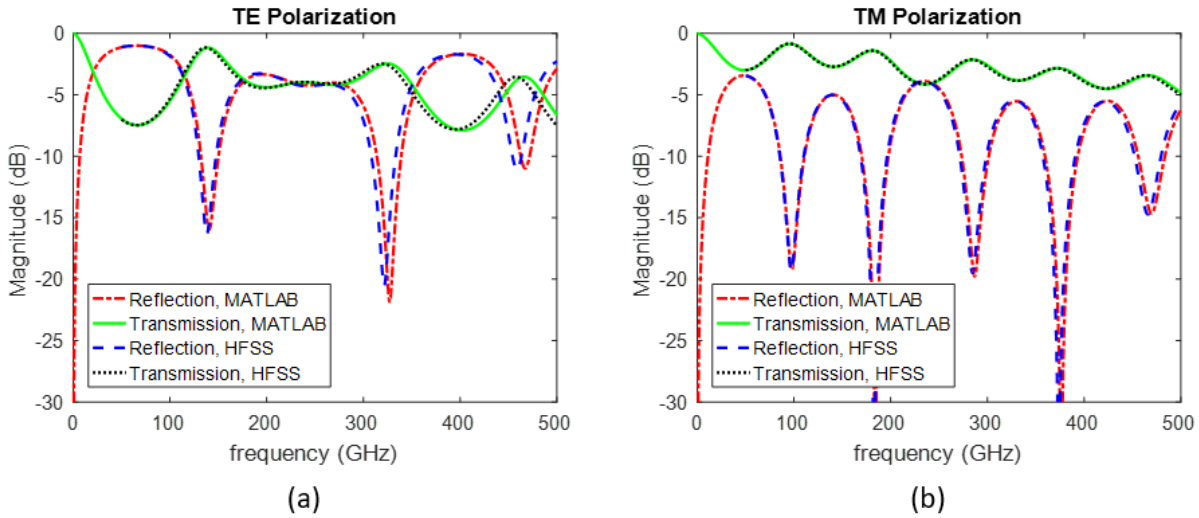

Figure 3.6. The reflection and transmission coefficients for the spatial power divider with the parameters in Row 1 of Table 3.1 are shown for (a) TE polarization and (b) TM polarization. Good agreement is observed between the analytical solution implemented in MATLAB and the simulation in HFSS over a wide frequency range.

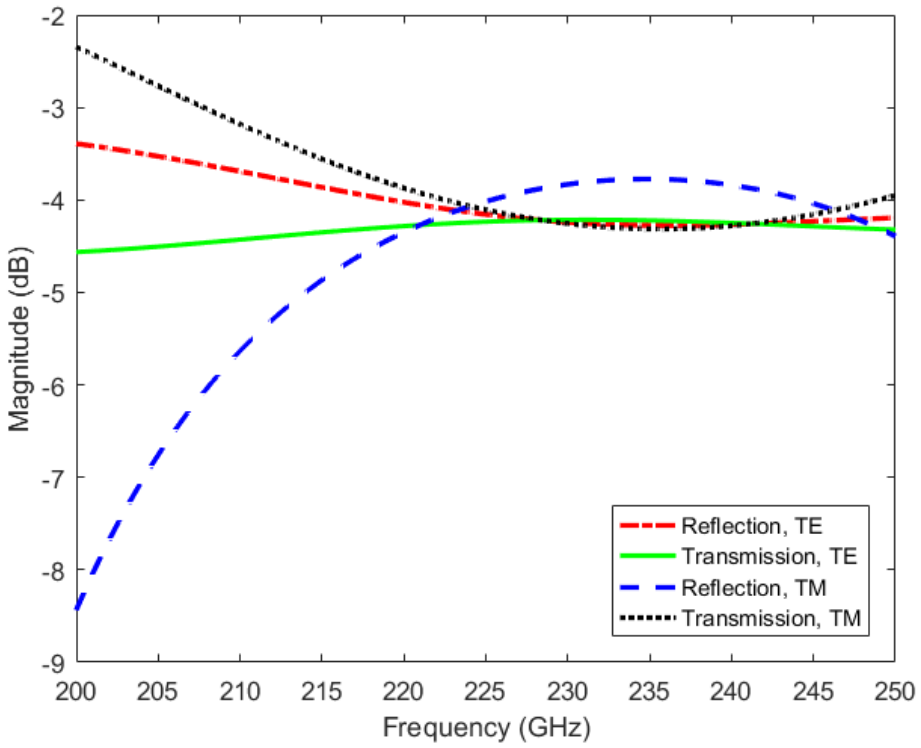

Figure 3.7. The reflection and transmission coefficients, simulated in HFSS, for the spatial power divider with the parameters in Row 2 of Table 3.1 are shown for both polarizations.

3.3.3 Fabrication Process

The spatial power divider is fabricated on a 100 mm silicon wafer with a thickness of 525 μm. The two layers of corrugations are created by performing a two-step etch with DRIE.

First, a 500 nm layer of silicon dioxide is grown on the wafer through thermal oxidation. Then photolithography and RIE are used to etch a series of stripes into the oxide layer. This pattern will act as a mask for the second DRIE etch step. Then a second mask of SPR 220 photoresist is patterned over top of the oxide layer with a set of thinner stripes. The first DRIE step is then performed, etching a trench into the silicon which will eventually become the middle layer of the three-layer corrugated slab. The photoresist mask is removed, and the oxide mask is used for the second DRIE step, which forms the top layer of the corrugated slab, as well as completing the middle. This process is depicted in Figure 3.8. The features are etched over the majority of the surface of the wafer, which is then diced into a rectangle with dimensions 60 mm and 72 mm in the x- and z-directions, respectively.

The fabrication process is fairly straightforward, but there are some factors that make it difficult to do successfully. The first is that the silicon is not a perfect insulator, but rather has a finite resistivity that was not known precisely before beginning fabrication. After fabrication of the first set of prototypes, it was determined through comparison of measurements to simulations that loss in the silicon is best modeled by introducing a conductivity of 5.82 S/m, corresponding to a resistivity of 17.2 Ωcm and an imaginary part of the relative dielectric constant of $\varepsilon'' = 0.455$ at 230 GHz (measurement results will be discussed more thoroughly in the next section of this chapter). The manufacturer specification for these wafers is given as a resistivity ranging from 10 to 20 Ωcm, which is in agreement with the measured value. The result of this oversight was that

the first fabrication cycle yielded poor results, and the power divider had to be redesigned with the new knowledge of the dielectric loss.

The most significant fabrication concern is the phenomenon of etch lag in the second etch step, which is depicted in Figure 3.9. Because the plasma cannot access the narrower area at the bottom of the trench as easily as it can the wider area at the top, the bottom etches more slowly than the top during the second etch step. This means that the first etch step needs to be significantly deeper than the intended depth of the middle layer, as it will shrink during the second etch. Unfortunately, the etch rate in the bottom of the trench is neither easily predictable nor perfectly consistent. As a result, it is difficult to predict the thickness of the middle layer of the corrugated slab before attempting the process, and even after characterizing the etch rates they have not been perfectly repeatable.

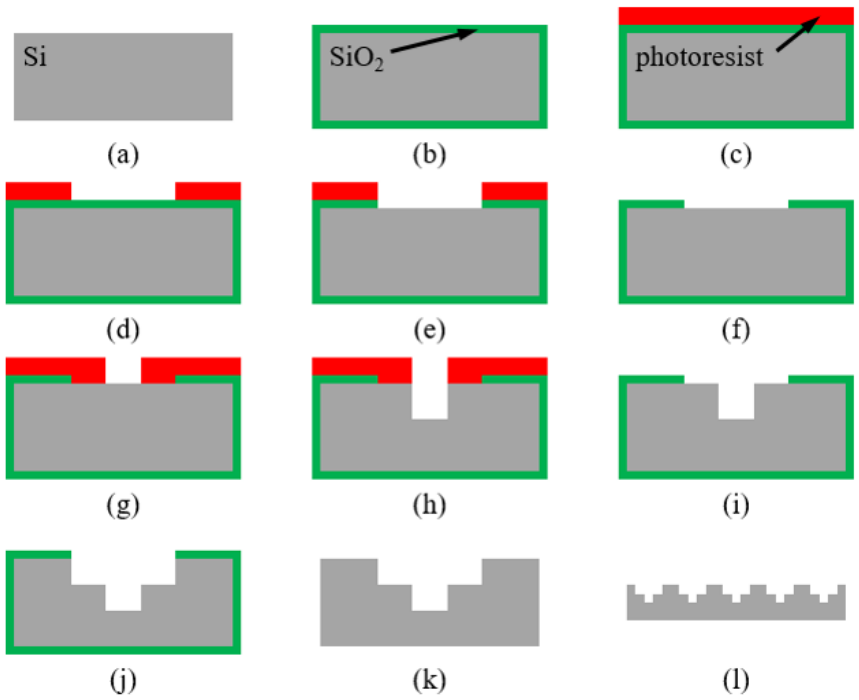

Figure 3.8. Illustration of J-band power divider fabrication process: (a) start with silicon wafer, (b) thermal oxidation, (c) spin photoresist, (d) expose and develop first mask, (e) RIE of oxide layer, (f) remove photoresist, (g) spin, expose, and develop second mask, (h) first DRIE step, (i) remove photoresist, (j) second DRIE step, (k) remove oxide with HF. (l) Zoomed-out view showing several unit cells.

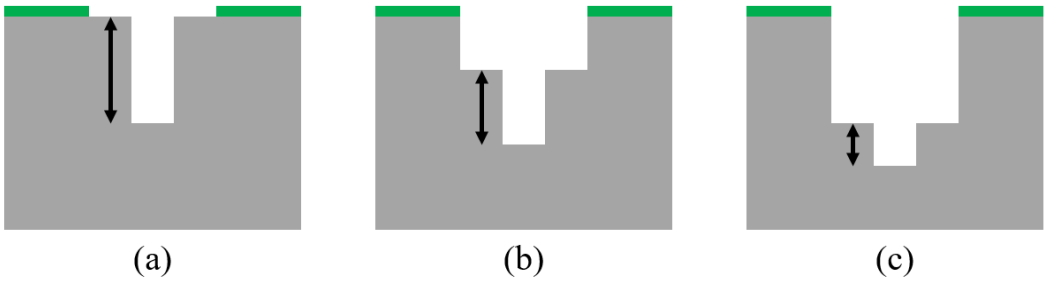

Figure 3.9. The phenomenon of etch lag is depicted. (a) At the beginning of the second etch step, there is a deep trench from the first etch step. (b) As the etch progresses, the etch rate at the top portion of the trench is faster than that at the bottom portion, resulting in a shrinking depth of the middle layer. (c) At the end of the etch, the depth of the middle layer is much smaller than it started.

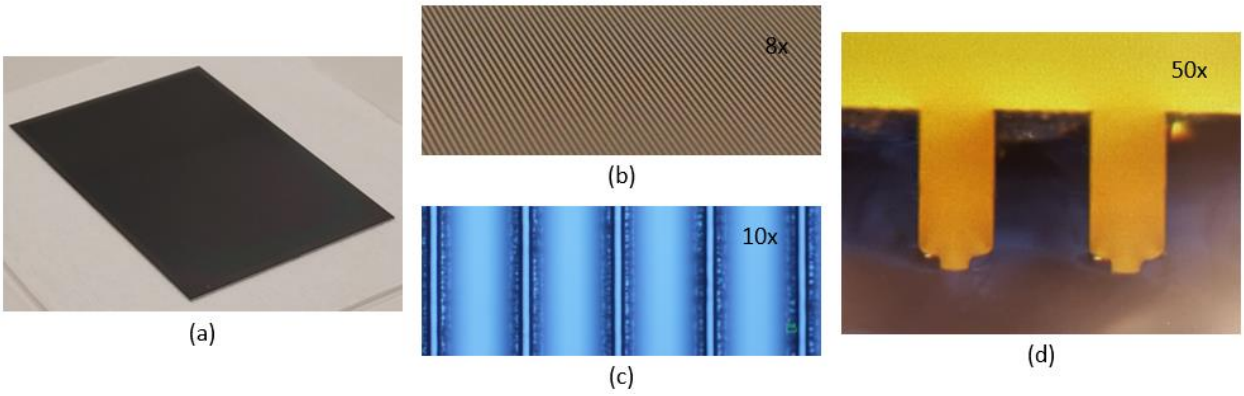

Figure 3.10. Photos of the fabricated J-band spatial power divider prototype. (a) The entire device, diced to a rectangular shape from the round silicon wafer. (b) Zoomed in on the surface to reveal the sub-wavelength periodic corrugations. (c) A microscope image focused on the bottom of the trench. (d) A cross-sectional view of a typical etch profile.

Because of these factors, it was necessary to fabricate several iterations of the power divider, taking measurements and adjusting both design parameters and process parameters for each iteration. However, to minimize the time and cost of this repetitive process, the choice was made to use a single mask set, rather than making new masks for every design iteration. Therefore, control over the widths of the corrugations was relinquished, and only the depths could be experimentally tuned.

The measured dimensions of the final power divider prototype are displayed in Row 3 of Table 3.1. The side wall angles were measured to be 0.23 degrees, and the width of the unit cell is 200 μm, which is less than a fifth of the wavelength. Some photos of the power divider are included in Figure 3.10.

3.3.4 Measurement Results

The reflection and transmission coefficients of the spatial power divider were measured using an Agilent N5245 4-port PNA-X performance network analyzer with two waveguide-based OML frequency extenders, which enable measurements up to 325 GHz. At the output of each frequency extender is a standard pyramidal horn [70] to launch waves for free-space measurements. Note that these standard horns are different from the conical horns fabricated as part of the antenna. They have an aperture measuring approximately 8 mm by 10 mm, and thus a much larger far-field distance than that of the conical horns. A fixture was 3D-printed to support the power divider at the proper 45-degree angle. The transmission measurement is calibrated by comparing the response of the power divider to that of free space. The reflection measurement is calibrated by comparing the reflection from the power divider to that of a wafer covered in a layer of gold acting as a PEC. Due to unavoidable issues of multi-path transmission, it was found that placing the spatial power divider in the near field of both pyramidal horns produced more consistent results than positioning everything in the far field. The power divider is positioned 3 cm from the horn aperture, close enough that the beam is still relatively well collimated, so plane wave incidence is a valid approximation [68]. Additionally, time-gating is used to isolate the primary signal path from any residual multi-path effects. Photos of the measurement setup are shown in Figure 3.11.

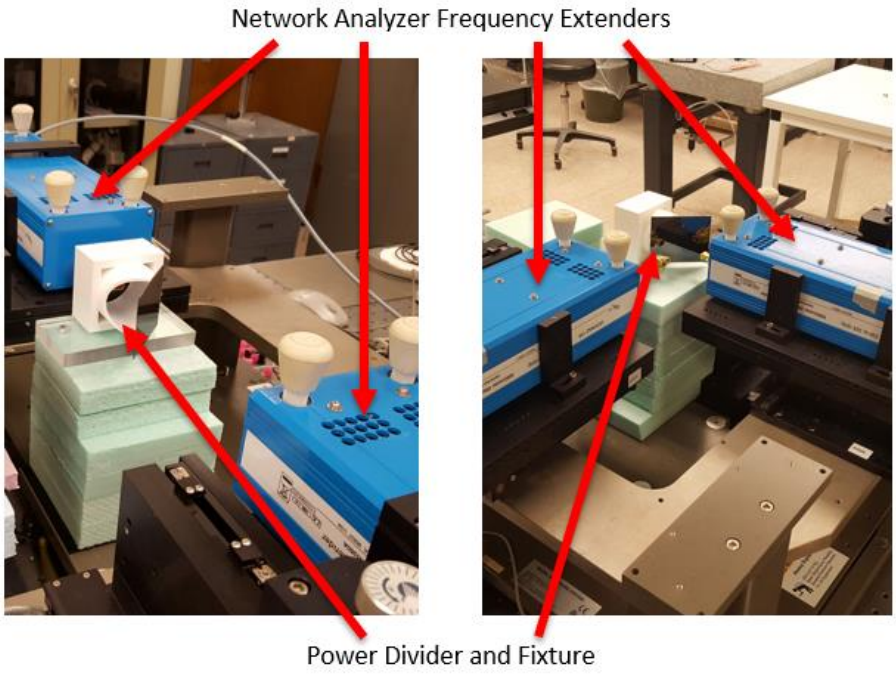

Figure 3.11. The J-band spatial power divider measurement setup for transmission (left) and reflection (right) is shown.

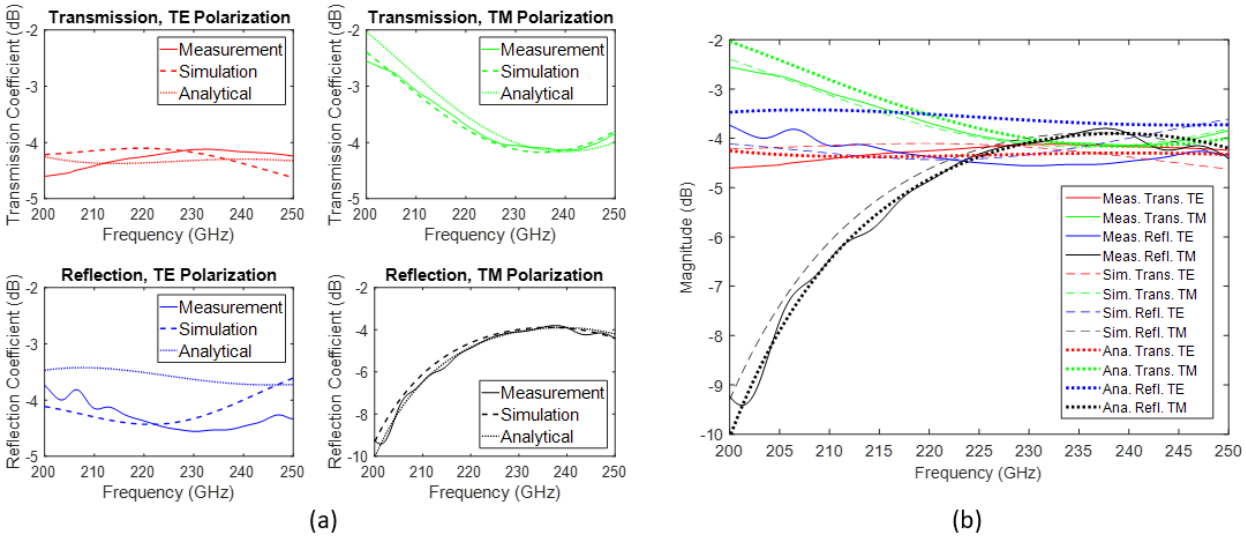

Figure 3.12. Transmission and reflection coefficients of the J-band spatial power divider are shown (a) on individual plots for clarity, and (b) all together for comparison.

The measured transmission and reflection coefficients of the spatial power divider for both TE and TM incident waves at 45-degree incidence are shown in comparison to both the analytical model and the HFSS simulation in Figure 3.12. The parameters used in the analytical model and simulation for these plots are those of the measured prototype, given in Row 3 of Table 3.1. It can be observed that while both models predict the measured behavior well, the HFSS simulation is more accurate due to inclusion of the etch geometry. The maximum difference between reflection and transmission for either polarization in the band of interest is 0.9 dB. There is also loss of approximately 1 dB, since the coefficients are around -4 dB instead of -3 dB.

3.3.5 Discussion

The simulated spatial power divider design showed a maximum difference between reflection and transmission for either polarization of 0.5 dB over the band from 221 GHz to 250 GHz (see Figure 3.7). The fabricated prototype does not perform quite as well, having a difference of at most 0.9 dB over this band. The difference can be attributed to the fact that geometry of the prototype does not exactly match what was intended. This is due to both the lack of control over etch widths and uncertainty in etch rate, which were discussed in the fabrication section. With more time spent perfecting the fabrication process, performance at the level of the simulation could likely be achieved, but this was unnecessary as the measured performance was suitable for the radar antenna application.

A more serious concern is the dielectric loss of the silicon substrate. Not only does this result in the ~1 dB loss of the power divider, but it also seems to force the optimization toward geometries with very thin middle layers (only a few microns). Early simulations assuming lossless substrates had much thicker middle layers. When the middle layer is thin, the power divider design

is not making full use of the power of the three-layer corrugated slab architecture. These are both issues that could be corrected by using special high-resistivity substrates.

If low-loss silicon is used, and all of the design parameters are taken advantage of in optimization, an improved design could be achieved. The parameters are listed in Row 4 of Table 3.1 (note the much thicker middle layer), and the simulated reflection and transmission coefficients are plotted in Figure 3.13. This design has no loss and has a difference between reflection and transmission of at most 0.1 dB for both polarizations over the band from 227 GHz to 239 GHz, which likely represents the best possible performance for a spatial power divider designed by this method.

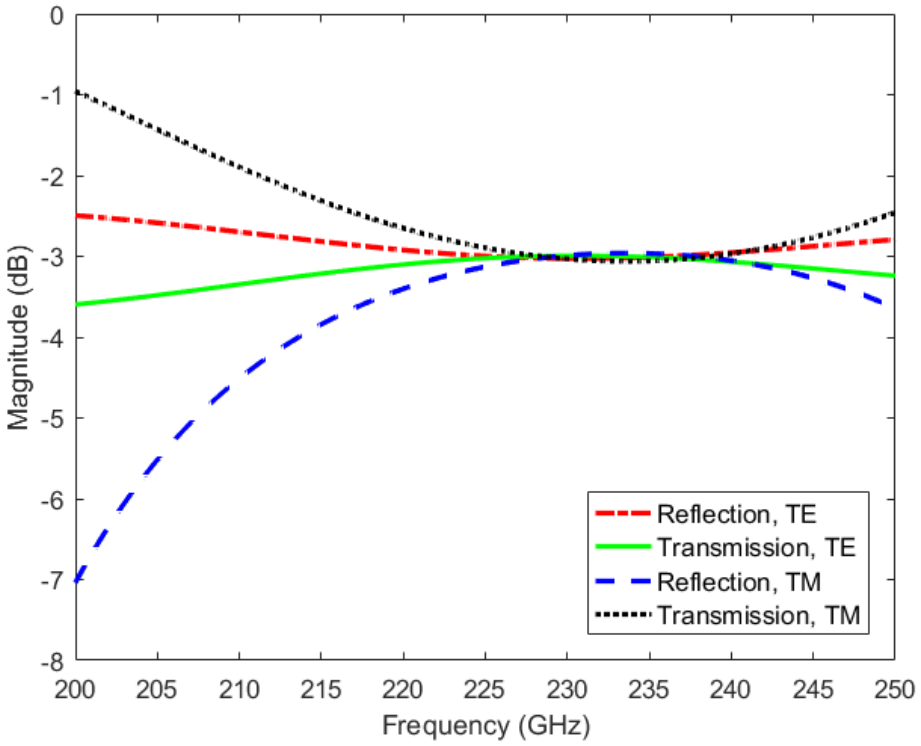

Figure 3.13. The best J-band spatial power divider simulation result achieved, assuming a lossless substrate and control over all geometric model parameters.

3.4 Second J-Band Power Divider Implementation

A second J-band polarization-independent spatial power divider was designed and fabricated for use in the KACST radar operating at 220 – 230 GHz, a band slightly lower than that targeted by the design described above. The interesting aspect of the new design is that it allows a three-layer corrugated slab structure to be achieved using a single etch step. This significantly simplifies the fabrication process and leads to much more repeatable and accurate results.

After completing the GM J-band radar, it was desired to upgrade another existing KACST radar with a similar antenna. This radar operates at a slightly lower band from about 220 to 230 GHz. While the previous power divider design would have provided reasonable performance, it is better suited at frequencies above 230 GHz. At 220 GHz the measured difference between TM reflection and transmission was 1.2 dB. Therefore, it was desired to adjust the parameters to shift the operation frequency down and improve performance at the intended band. This could have been achieved simply by re-optimization in HFSS and repeating the same fabrication steps.

However, the experience from the fabrication process of the first J-band power divider revealed some of the difficulties of a multi-step etch process, most significantly the need to deal with etch lag. A slightly different fabrication approach was devised for the new power divider in an attempt to reduce the impact of etch lag on the predictability and repeatability of the process. Etch lag arises because the reactive ions in the plasma can more easily reach the exposed silicon near the top of the trench. This is in fact a result of a combination of two factors. First, etch rate is dependent on feature size in the plane of the wafer surface, with larger etched areas etching faster than smaller ones. Second, etch rate is dependent on etch depth, with the rate slowing as the feature becomes deeper. In the previous J-band power divider design, two layers of corrugated slabs were achieved by a two-step etch where the second mask had a wider opening than the first one. This

produced a staircase-shaped etch profile, where the middle layer was both narrower and deeper than the top layer, compounding the difference in etch rate in the two portions.

The proposed solution was to instead produce the two layers of corrugated slabs by having two different trenches within the unit cell, each with a single width and depth. This can be fabricated by having the two mask layers directly overlap with each other for one trench, while the second trench is only exposed during the second etch step. Figure 3.14 depicts this masking method in comparison to that used for the previous design. Figure 3.15 shows a comparison of the resulting etch profiles. It was hoped that this change to the fabrication process would reduce the difficulty associated with etch lag because in this case only the etch depth and not feature size plays a role.

From a theoretical standpoint, the two structures should behave identically as long as the parameters t and d/L match for each layer. There may be some minor differences in actuality because the size of the unit cell is not that much smaller than a wavelength ($\sim \lambda/5$) and the deviation from perfect rectangular shapes is somewhat different for the two structures.

The geometry of the new structure was modeled in HFSS, and the set of parameters given in Row 2 of Table 3.1 was used as a starting point. The parameters were then optimized over the band from 220 to 230 GHz. The resulting parameters are shown in Row 1 of Table 3.2. At this point, this design was used to create a set of two masks for fabrication of the power divider. The d/L parameters translate to a mask pattern with openings of 33.3 μm and 43.5 μm.

During the first attempt at fabrication, some difficulties were encountered that prevented the completion of the prototype. However, this turned out to be a fortunate accident, because the circumstances inspired the conception of a process by which the power divider could be fabricated using a single etch step.

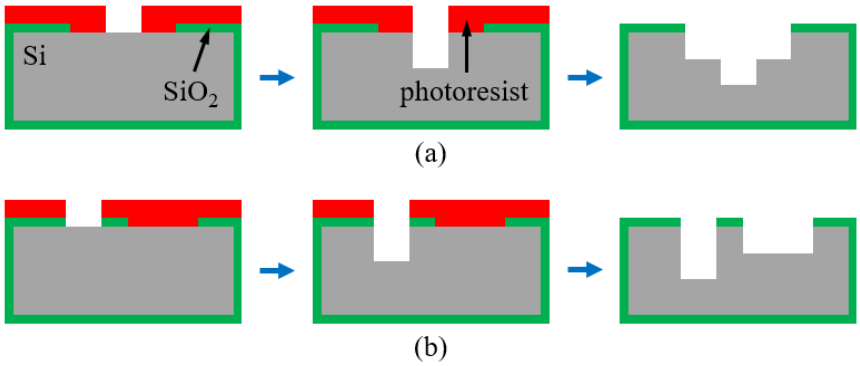

Figure 3.14. A comparison of the fabrication processes (a) used for the first J-band spatial power divider, and (b) proposed for the second J-band spatial power divider.

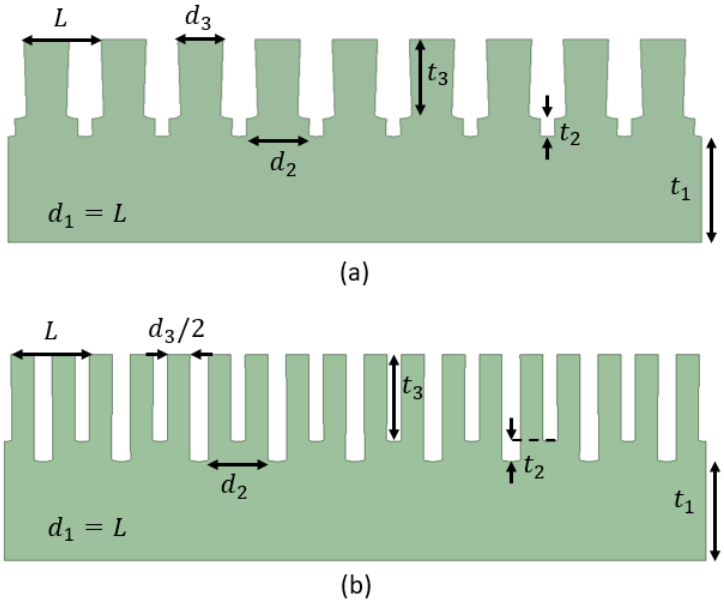

Figure 3.15. A comparison of the resulting geometry from the two processes in Figure 3.14.

Table 3.2
The layer thickness and corrugation ratios of the second J-band three-layer spatial power divider are provided for several different design stages: Row 1: optimized HFSS simulation, Row 2: adjusted parameters to facilitate fabrication with a single etch step, Row 3: measured dimensions of fabricated prototype A, and Row 4: measured dimensions of fabricated prototype B.

		Layer Thickness (μm)			**Layer Corrugation Ratio**			
Row	**Description**	t_1	t_2	t_3	d_1/L	d_2/L	d_3/L	L **(μm)**
1	Simulation	298.7	6.2	220.1	1	0.8333	0.6158	200
2	Sim., Single Etch	298.0	9.5	217.5	1	0.7825	0.6158	200
3	Fab. Prototype A	297.4	10.5	217.1	1	0.7693	0.5883	200
4	Fab. Prototype B	297.3	10.8	216.9	1	0.7691	0.5876	200

Figure 3.16.a shows a properly scaled cross-sectional view of the power divider structure with parameters listed in Row 1 of Table 3.2, where the model parameters t and d/L have been converted into the equivalent physical dimensions w and h of the etched trenches for ease of discussion. It can be seen that there are two periodic sets of trenches, one with a width of $w_1^a = 43.5\ \mu m$ and depth of $h_1^a = 220.1\ \mu m$, and one with a width of $w_2^a = 33.3\ \mu m$ and depth of $h_2^a = 226.3\ \mu m$. The two trenches have very similar depths, which differ only by a few microns. It was mentioned previously that the DRIE etch rate is dependent on feature size, with larger features etching faster than smaller ones. Here the narrower trench has a slightly greater depth than the wider trench. If only these dimensions were reversed, such that the wider trench had a greater depth than the narrower one. Then it may be possible to exploit the difference in etch rate to achieve the desired depths with a single etch step.

The LNF keeps data on the rates associated with several etch processes under typical conditions. This data includes measured etch rates at several different feature size for the particular etch process used in the fabrication of these power dividers [87]. These measurements have been reproduced here in Table 3.3. By assuming the etch rates for trenches of widths 1 µm and 2 µm should be fairly close, these data points have been used to derive a useful heuristic model to estimate etch rate for any feature size, which is given by:

$$R_E = 7 * 1.5^{\log_{10} O_M} \tag{3.19}$$

where R_E is the etch rate in µm/min. and O_M is the mask opening in µm. Using (3.19), the expected etch rates for trenches having widths of 43.5 µm and 33.3 µm are 13.60 µm/min. and 12.98 µm/min., respectively.

The etch rate decreases over time during the etch as the trench grows deeper, so it was not expected that these would be the actual etch rates observed. However, it seemed reasonable to expect that the two trenches would etch at proportional rates (i.e. the wider trench would etch at a rate that is 13.60/12.98 = 1.048 times as fast as narrower trench). Therefore, the power divider design was modified so that the depths of the two trenches were in proportion to the corresponding etch rates, while having an average approximately equal to that of the previous design (trench curvature was also taken into account while making this calculation). This was done with the hope that the change would result in only minor effects on the simulated performance.

The updated design parameters are listed in Row 2 of Table 3.2, and the physical dimensions of the resulting trenches are shown in Figure 3.16.b. The simulated reflection and transmission coefficients for the two versions of the design are displayed in Figure 3.17. Very little difference between the two plots can be discerned. Over the 220 – 230 GHz band, the two-step etch version has a maximum difference between reflection and transmission of 0.5024 dB, while the single-step etch version has a maximum difference of 0.5207 dB, a negligible change.

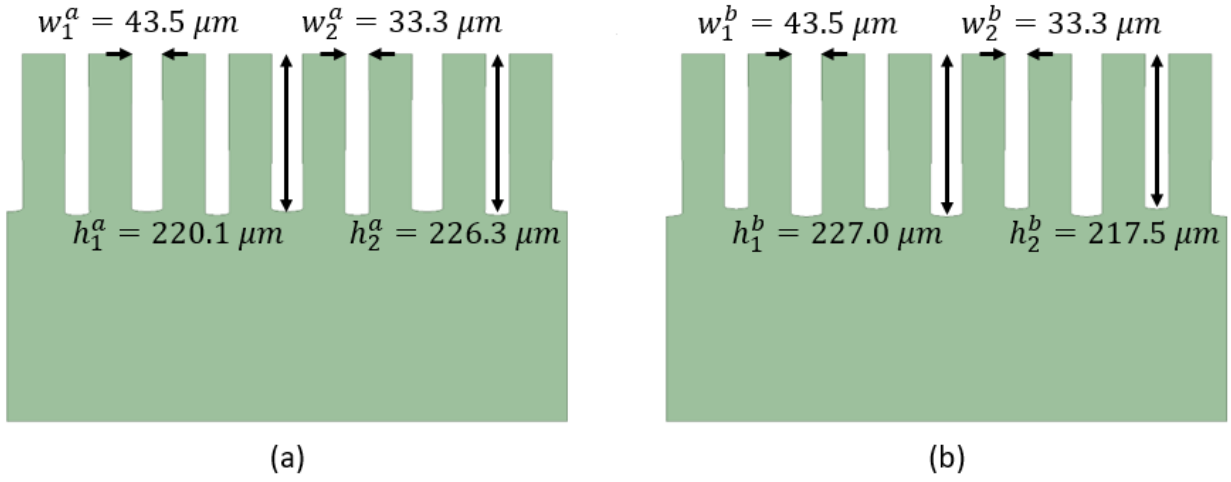

Figure 3.16. Cross-sectional view of the power divider structures with parameters listed in (a) Row 1 and (b) Row 2 of Table 3.2. Model parameters have been converted to physical etch dimensions.

Table 3.3
Measured etch rates of the STS Pegasus LNF 3 DRIE recipe for select features sizes.

Mask Opening O_M (μm)	Etch Rate R_E (μm/min.)
2	7.0
10	10.5
100	15.8

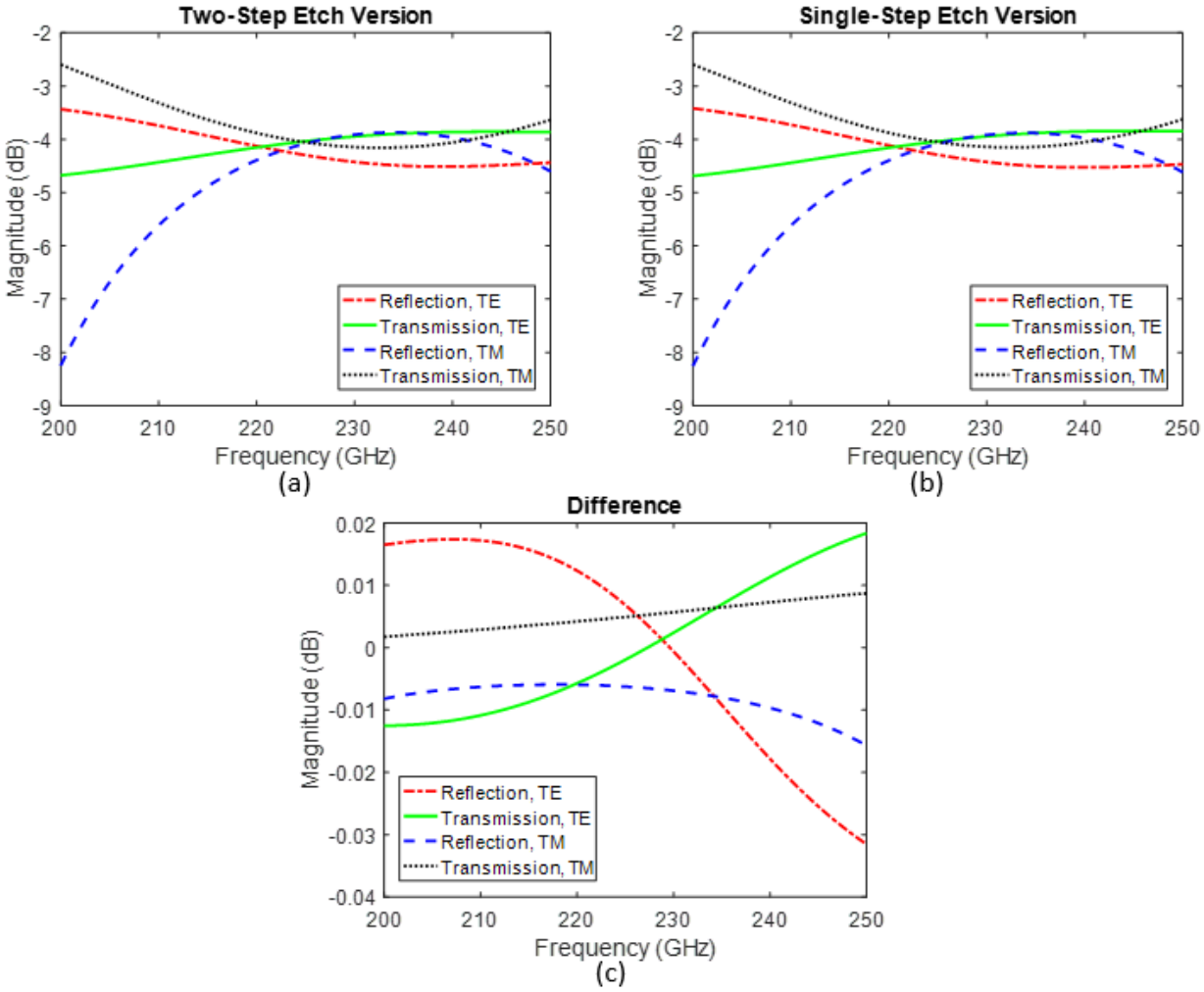

Figure 3.17. Simulated reflection and transmission coefficients are plotted for the spatial power divider designs with parameters given in (a) Row 1 and (b) Row 2 of Table 3.2. (c) A comparison of the magnitudes of the corresponding coefficients of the two designs.

Two spatial power divider prototypes, designated A and B, were fabricated using the simplified single-step etch procedure depicted in Figure 3.18 (compare to Figure 3.14.b). The measured dimensions of the two prototypes are displayed in Rows 3 and 4 of Table 3.2. The etch depths were made to a precision of about 1 μm, while the widths have been over-etched by about 2 – 3 μm due to mask undercut (this is something that can also be taken into consideration and accounted for if desired). These were the first two prototypes attempted with the single-mask fabrication procedure, whereas the two-step etch utilized for the first J-band power divider took multiple iterations to complete successfully. This indicates a much higher level of process repeatability and reliability, in addition to requiring significantly less processing time.

Measurements of two power dividers' TE and TM reflection and transmission coefficients at 45-degree incidence are plotted in comparison to the simulations in Figure 3.19. The parameters used in the simulations for these plots are those of the measured prototypes, given in Row 3 and Row 4 of Table 3.2. Both prototypes agree well with the simulation and with each other. Unfortunately, the etch undercut seems to have worsened the simulated performance, and additionally, the measured TM reflection and transmission coefficients exhibit a greater difference than suggested by the simulation. As a result, there is a difference between reflection and transmission for TM polarization of 1.1 dB at 220 GHz. This is significantly worse than the value of 0.5 dB found for the initial simulation, but it is still an improvement over the 1.2 dB measured for the previous power divider implementation. This fact, in addition to the much easier fabrication, constitute a success. Once again, the performance could likely be improved by adjusting fabrication parameters or using low-loss silicon substrates.

The drawback to this fabrication approach is of course that since the differing etch rates of different size features is being exploited to allow the use of a single etch step, the depth parameters

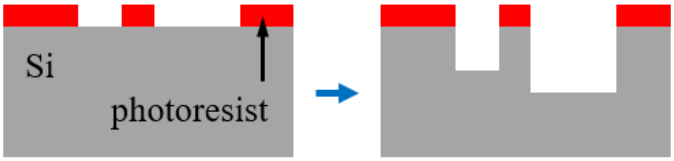

Figure 3.18. The single-step etch process used to fabricate power divider prototypes A and B.

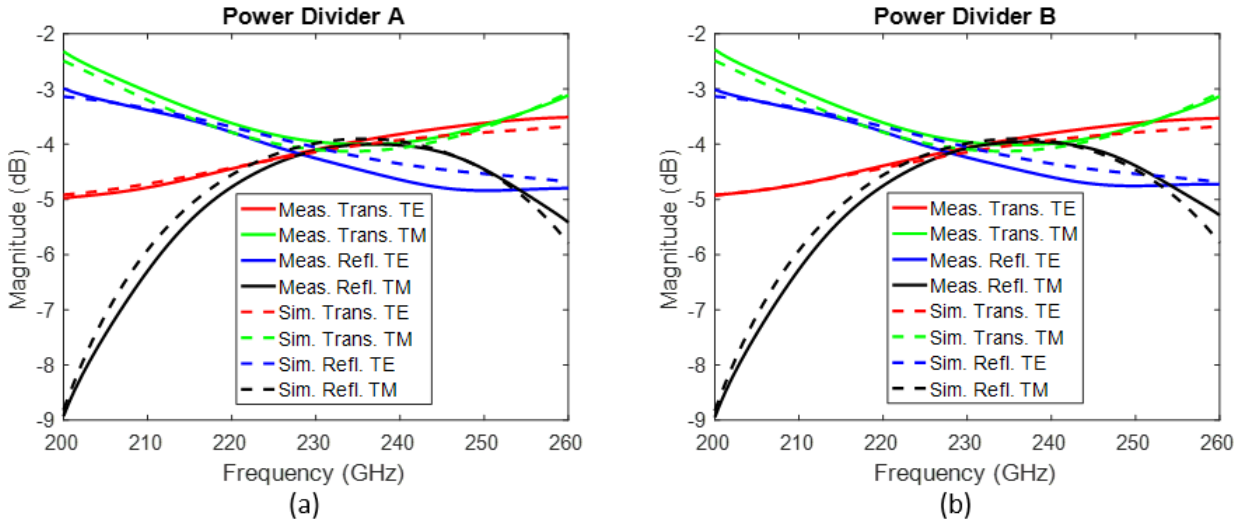

Figure 3.19. Measured transmission and reflection coefficients of spatial power divider prototypes A and B are shown in comparison to simulation results.

are coupled to each other and to the width parameters. Effectively, this reduces the number of free parameters from four to three, which may make this solution less viable for designs at other frequency bands, or with a different set of performance criteria. It is likely suitable in this application mostly because the optimized depths of the two trenches were very close together to begin with.

3.5 E-Band Power Divider Implementation

Another polarization-independent spatial power divider was designed at 76 – 83 GHz for use in the GM E-band radar operating at the modern automotive band. This E-band power divider

was fabricated by combining the corrugated dielectric slab technique discussed in the previous sections with metallic MEFSS elements.

This power divider was designed shortly after the completion of the first J-band power divider. Naturally, the first idea was to simply increase the size of that structure to realize the necessary frequency scaling. Unfortunately, this approach was quickly ruled out, as it was realized that the required dimensions were prohibitive to the fabrication process. Expensive custom silicon wafers with thickness approximately three times the standard would be needed. More importantly, the DRIE etch recipes and masking materials supported by the LNF could not tolerate the very long etch times required to scale the etch depth appropriately. The analytical cascaded corrugated slab model was used to search for other solutions with more practical dimensions, but none were found. It was therefore determined that a different approach would be needed to design the E-band power divider.

3.5.1 Circuit Modeling

It was observed from the analytical model that some two-layer structures consisting of a single anisotropic layer and a single isotropic layer demonstrated the correct behavior for one polarization, while having a total thickness close to that of a standard silicon wafer. This inspired the approach of starting from one of these structures, and adding metallic MEFSS structures to correct the behavior of the other polarization. In order to test whether this would work, the analytical model was converted to a circuit model in Keysight ADS.

In this circuit model (3.5) – (3.18) are implemented as a series of transmission lines. The length of each transmission line corresponds to the thickness of the dielectric layer, while the impedance corresponds to the dielectric constant. Since the effective dielectric constant of a

corrugated dielectric layer is different for TE and TM polarization, two circuits are constructed; one for each polarization. Specifically, the transmission line parameters are given by:

$$Z_n^{TE} = \eta_n^{TE} = \frac{\eta_0}{\sqrt{\varepsilon_n^{TE}}} \frac{1}{cos\,\theta_n^{TE}} \tag{3.20}$$

$$Z_n^{TM} = \eta_n^{TM} = \frac{\eta_0}{\sqrt{\varepsilon_n^{TM}}} cos\,\theta_n^{TM} \tag{3.21}$$

$$L_n^{TE} = k_{y,n}^{TE} \cdot t_n = t_n 2\pi f \sqrt{\mu_0 \varepsilon_0 \varepsilon_n^{TE}}\, cos\,\theta_n^{TE} = t_n \frac{2\pi}{\lambda} \sqrt{\varepsilon_n^{TE}}\, cos\,\theta_n^{TE} \tag{3.22}$$

$$L_n^{TM} = k_{y,n}^{TM} \cdot t_n = t_n 2\pi f \sqrt{\mu_0 \varepsilon_0 \varepsilon_n^{TM}}\, cos\,\theta_n^{TM} = t_n \frac{2\pi}{\lambda} \sqrt{\varepsilon_n^{TM}}\, cos\,\theta_n^{TM}\,. \tag{3.23}$$

Here Z_n^{TE} and Z_n^{TM} are the characteristic impedances of the transmission lines representing corrugated slab layer n, which are set equal to η_n^{TE} and η_n^{TM}, the wave impedances of the TE and TM modes (i.e. the ratio of electric and magnetic field components tangential to the interface). L_n^{TE} and L_n^{TM} are the electrical lengths of the transmission lines. η_0 is the wave impedance of free space, and λ is the free-space wavelength associated with frequency f. As in the analytical model, the index n ranges from 0 to $N+1$ for a structure with N corrugated slab layers, and in this case indices 0 and $N+1$ represent terminations in a reference impedance. In particular, $\varepsilon_0^{TE} = \varepsilon_0^{TM} = \varepsilon_{N+1}^{TE} = \varepsilon_{N+1}^{TM} = 1$ and $\theta_0^{TE} = \theta_0^{TM} = \theta_{N+1}^{TE} = \theta_{N+1}^{TM} = 45°$, so $Z_{N+1}^{TE} = Z_0^{TE} = \eta_0\sqrt{2}$ and $Z_{N+1}^{TM} = Z_0^{TM} = \eta_0/\sqrt{2}$. The impedance and electric length parameters given in (3.20) – (3.23) can be supplied to transmission line component models in ADS and controlled by tuning slab parameters t_n and d_n/L. This circuit model calculates reflection and transmission coefficients identical to those computed by the analytical model.

MEFSS elements are sub-wavelength periodic metallic structures that can be modeled as inductor and capacitor circuit elements. An inductor takes the form of a wire. An incident electric field excites a current along the wire which produces a circulating magnetic field. Only an electric field polarized along the wire excites this effect, so the orthogonal polarization does not see the inductive wire. Similarly, a capacitor has the form of a slot between two metallic sheets. An electric field polarized perpendicular to the slot observes a capacitance. If similar behavior for both polarizations is desired, grids and patches are used. Many different types of unit cells can be created by combining inductive and capacitive elements, such as resonant loop and grid+patch elements. Geometries of some simple MEFSS cells are shown in Figure 3.20. The equivalent inductance and capacitance values can be tuned via the geometric parameters of the unit cell.

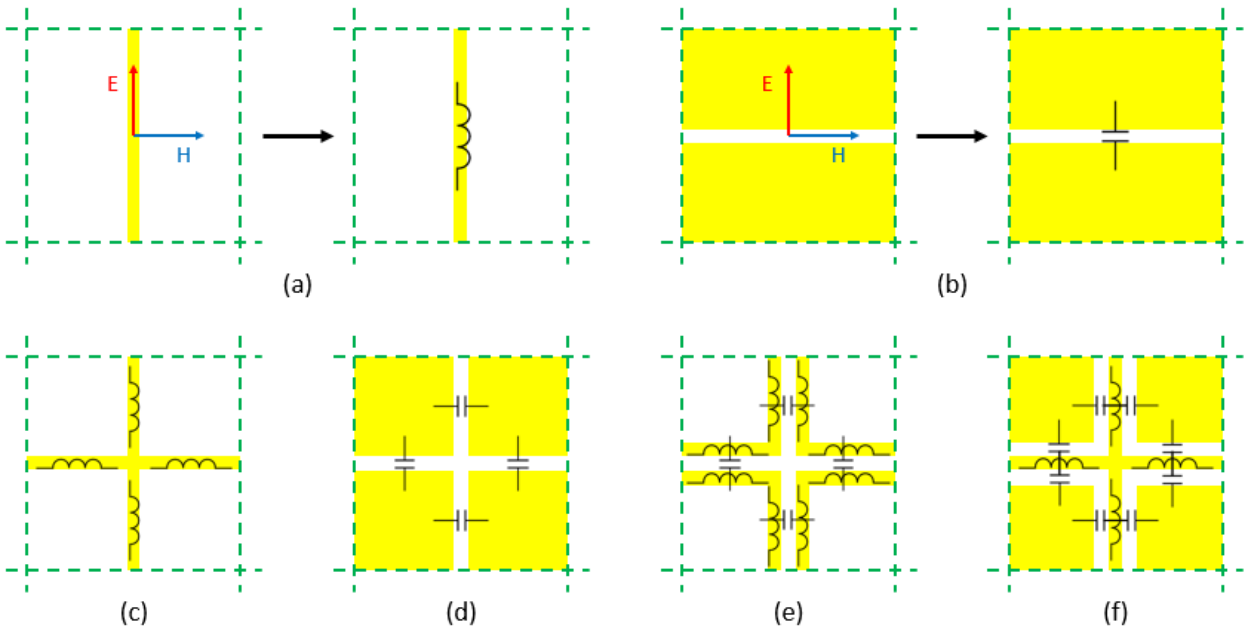

Figure 3.20. Several simple MEFSS structures and their equivalent circuits: (a) a wire, like a (single-polarization) inductor; (b) a slot, like a (single-polarization) capacitor; (c) a grid, like an inductor; (d) a patch, like a capacitor; (e) a square loop, like a series LC; and (f) a grid+patch, like a parallel LC.

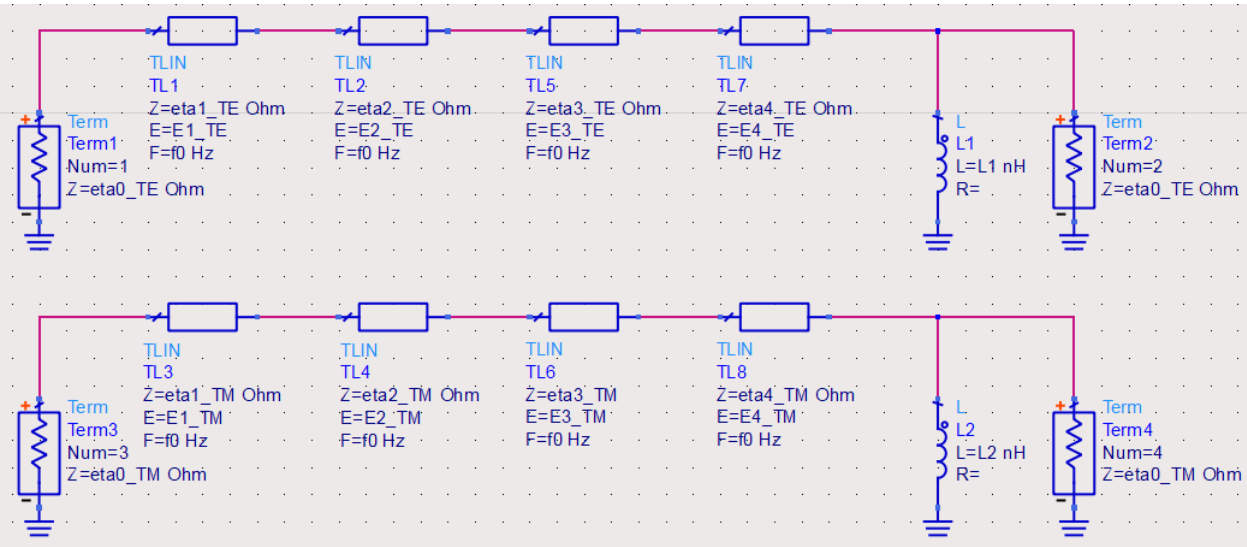

Figure 3.21. A schematic of a circuit model for a four-layer corrugated slab structure with an inductive grid on one side.

Inductive and capacitive MEFSS elements were added to the circuit model by the inclusion of a shunt inductor or capacitor on one or both sides of the transmission line structure. Lumped elements between transmission line segments were not considered because that corresponds to placing a metal layer somewhere in the middle of the silicon wafer. Also, resonant elements were not considered for simplicity. For other applications, it may be useful to include these two possibilities to provide more design freedom if the fabrication process allows.

Models were constructed for up to five corrugated slab layers to search for viable power divider structures. The total thickness was constrained to be equal to a standard silicon wafer thickness. An example of the schematic for one such model consisting of 4 corrugated slab layers and an inductive grid on one side is shown in Figure 3.21.

As mentioned previously, the circuit model was initially conceived because it seemed like adding some MEFSS elements for a single polarization to a two-layer (one isotropic and one anisotropic) corrugated slab structure may yield the desired behavior. In fact, it was found to be

the case that the two-layer dielectric structure could provide equal reflection and transmission for TE polarization over a wide bandwidth, and that adding an inductor for TM polarization could bring TM reflection and transmission close together as well.

The effect of this inductor can be understood easily using intuition from either circuit theory or electromagnetics. From the circuit perspective, an inductor behaves like a short circuit at low frequency and causes total reflection. At high frequency it acts like an open circuit and therefore has no effect on the rest of the circuit. At intermediate frequencies, reflection is increased with decreasing inductance. Similarly, from an electromagnetics perspective, a very thin wire MEFSS element looks like a window, and has no impact on an incident wave. A very thick wire looks like a PEC ground plane and reflects the wave entirely. A wire with intermediate thickness can reflect a portion of the wave, and the thicker the wire, the more reflection.

Though many more complex circuit models were also able achieve similar behavior, their performance did not warrant the added fabrication complexity. Therefore, the structure with two dielectric layers and one inductor was chosen for the E-band power divider design. Figure 3.22 shows the circuit model for this structure, both with and without the inductor. Figure 3.23 shows the reflection and transmission coefficients calculated by ADS over a wide frequency span to show the impact of the inductor as a function of frequency. It is clear that without the inductor, performance is good for TE polarization, but the inductor is needed to correct the response for TM polarization.

The optimized circuit model parameters are given in Row 1 of Table 3.4. The inductor is placed on the outside of the isotropic silicon layer. The reflection and transmission coefficients are plotted again in Figure 3.24, this time with a focus on the band of interest. The difference between reflection and transmission for either polarization is less than 0.5 dB from 71 GHz to 81 GHz.

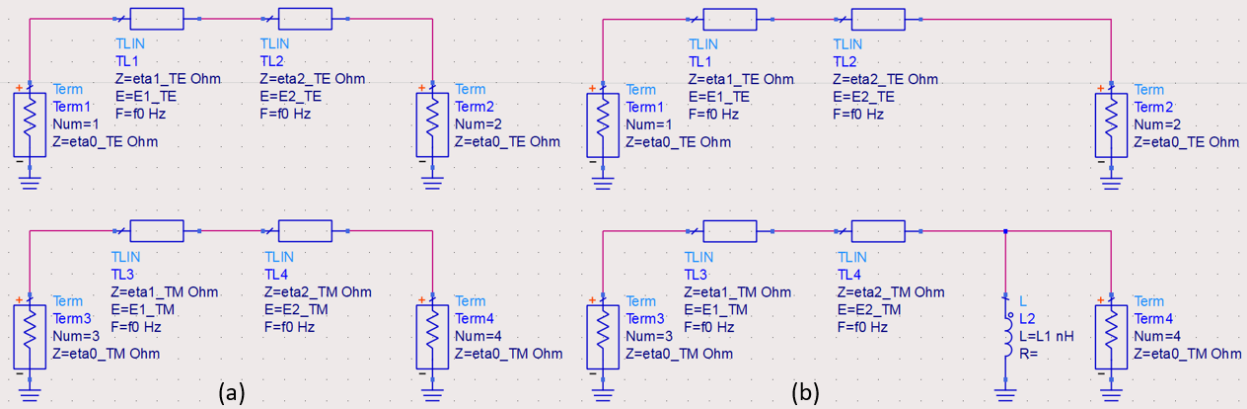

Figure 3.22. Schematic of circuit models for a two-layer corrugated slab structure (a) without and (b) with an added inductor for TM polarization.

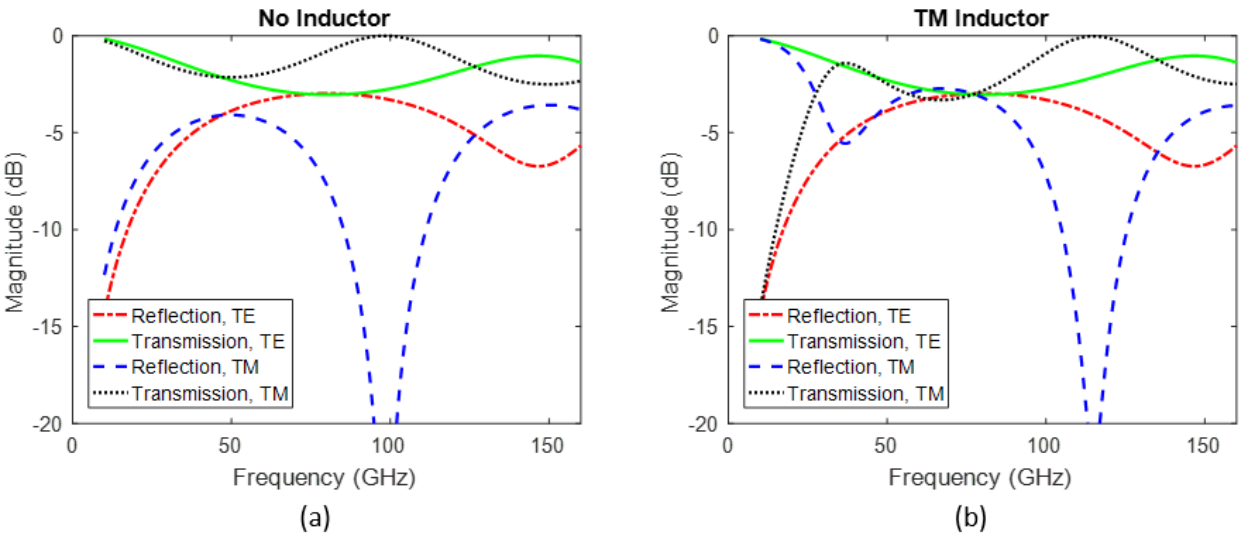

Figure 3.23. The reflection and transmission coefficients of the two circuit models in Figure 3.22, simulated in ADS. The inductor serves to make reflection and transmission closer for TM polarization.

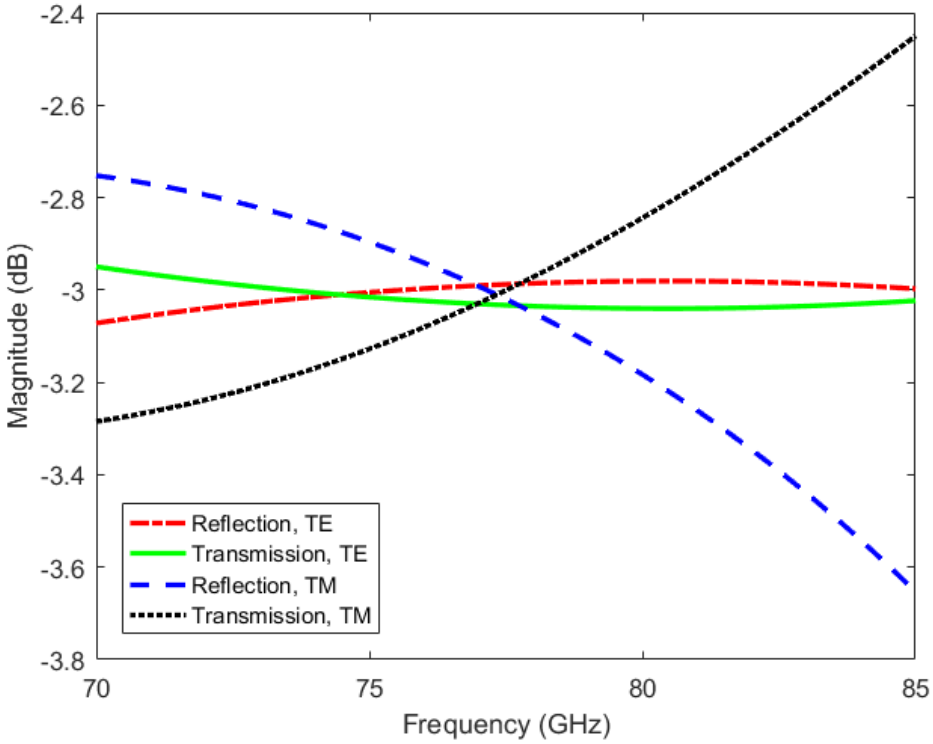

Figure 3.24. The reflection and transmission coefficients for the E-band spatial power divider simulated in ADS are shown for both polarizations.

3.5.2 Simulation Results

As was done for the J-band power divider, the combination of parameters found with the ADS circuit model were used as a starting point for full-wave electromagnetic simulation of the E-band power divider using Floquet analysis in HFSS, taking into consideration both the non-ideal etch profile and the conductivity of the silicon. The geometry of the simulated structure is shown in Figure 3.25. The parameters were then optimized, and are given in Row 2 of Table 3.4. It should be noted that the size of the unit cell, 1200 µm, is approximately one third of the wavelength at the frequency of interest, which is larger than typical for sub-wavelength unit cell designs. This choice will be explained in the following section on fabrication. The inductor has been implemented as a

wire, as in Figure 3.20.a. Its orientation is parallel to the etches so that the TM electric field is along its length. The simulated reflection and transmission coefficients at 45-degree incidence in the *yz*-plane are plotted in Figure 3.26. The difference between reflection and transmission is at most 0.7 dB for both polarizations over the band from 77 GHz to 83 GHz.

Table 3.4
The layer thickness and corrugation ratios, the corresponding physical etch dimensions, and the inductor parameters of the E-band spatial power divider are provided for several different design stages: Row 1: initial starting point found using the ADS circuit model, Row 2: optimized HFSS simulation, Row 3: measured dimensions of fabricated prototype.

		Thick. (μm)		Cor. Ratio		Etch (μm)		Induct. (μm)		L
Row	**Description**	t_1	t_2	d_1/L	d_2/L	w	h	t_m	w_m	**(μm)**
1	Circuit Model	60.0	465.0	1	0.6500	-	-	0.39 nH		-
2	Simulation	112.3	412.7	1	0.6000	480.0	473.0	0.1	64.8	1200
3	Fabrication	109.0	416.0	1	0.5958	485.0	477.0	0.1	64.5	1200

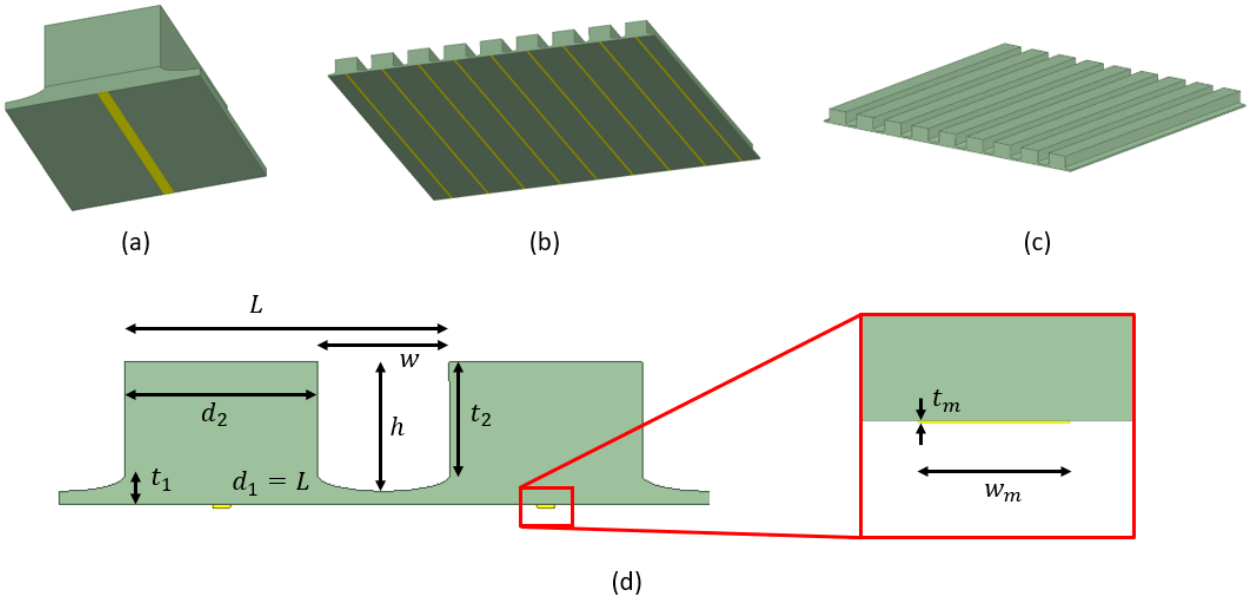

Figure 3.25. The geometry of the E-band power divider structure simulated in HFSS is shown. (a) View of a single unit cell, (b) view of several unit cells looking at bottom, (c) view of several unit cells looking at top, and (d) cross-sectional view showing model parameters and the corresponding physical dimensions.

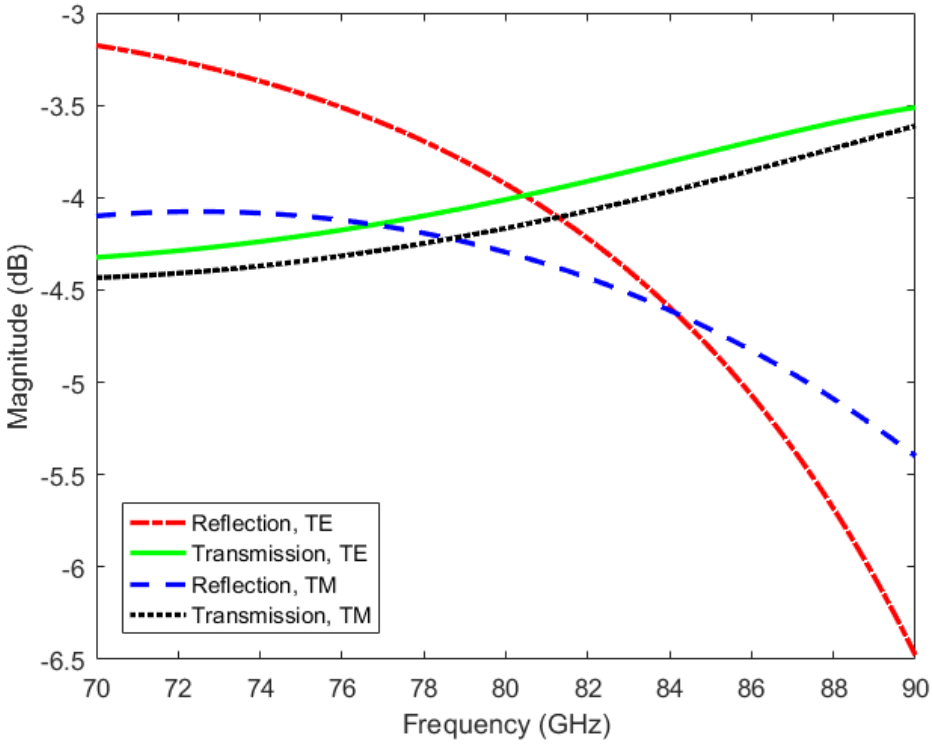

Figure 3.26. The reflection and transmission coefficients for the E-band spatial power divider simulated in HFSS are shown for both polarizations.

3.5.3 Fabrication Process

The E-band spatial power divider was fabricated on a 100 mm silicon wafer with a thickness of 525 µm. The inductors are patterned on the bottom of the wafer using evaporation and liftoff. Then the corrugations are created by performing an etch with DRIE.

First, liftoff resist is coated on the backside of the wafer and patterned with the shapes of the inductive wires using photolithography. Then a 10 nm adhesion layer of chromium followed by 0.1 µm of gold is deposited on the back side of the wafer using electron beam evaporation. The wafer is placed in a solution to liftoff the photoresist and excess metal, leaving the wires behind. Then photolithography is used to pattern the top side of the wafer, and DRIE is used to etch

trenches into the silicon forming the corrugated slab. This process is depicted in Figure 3.27. The features are patterned over the majority of the surface of the wafer, which is then diced into a rectangle with dimensions 58 mm and 80 mm in the x- and z-directions, respectively.

The inductor can in theory be placed on either side of the dielectric structure, although the inductance value would be different for the two sides. Initially it was planned to place the wires on the top side of the wafer between the etched trenches. The reason for this is that the top surface of the wafer is polished, offering a smoother surface for better adhesion of the wires (double-side polished wafers can also be used). Additionally, when performing the etch, the wafer is mounted to a larger carrier wafer with a liquid adhesive, and there was concern of damaging the metal pattern if it were put on the back side of the wafer and subjected to this treatment. However, to place the wires on the top surface, they need to be buried in very thick photoresist so as not to etch them and expose the DRIE chamber to the metals. A number of problems were encountered with this approach, most notably the formation of bubbles in the photoresist during the etch process that ruined the mask and exposed the metal to the chamber. Ultimately, it was decided to put the wires on the bottom side of the wafer instead. On the top side of the wafer, the necessary inductance required the wires to be very thin. In order for them to be made wide enough for the minimum liftoff feature size capability, the unit cell size needed to be quite large. This is why the unit cell was chosen to be 1200 μm instead of smaller. When moving the wires to the back side of the wafer, the wires became larger, but at this point it was easier to leave the design with the large unit cell size instead of creating new masks. The cell size could have been reduced, but the simulation results were good without doing so.

The measured dimensions of the final power divider prototype are provided in Row 3 of Table 3.4. As with the J-band power dividers, the width of the trench is larger than intended by a

few microns due to mask undercut. The etch depth at the center of the wafer was actually measured to be 472 µm, which matches the target from the simulated model to a precision of 1 µm. However, due to non-uniform etch rate across the wafer surface resulting from a thermal gradient, the etch depth gradually increases away from the center of the wafer. The depth value displayed in the table is an average over the footprint on the power divider of the portion of the feed horn's radiation pattern that illuminates the lens. The etch depth variation over this area was found to make an insignificant difference in the simulated electrical performance. The etch actually cuts completely through the wafer around the outside edges of the power divider, which does make the structure less mechanically sturdy. Some photos of the power divider are shown in Figure 3.28. The etch features are large enough to be seen easily with the naked eye.

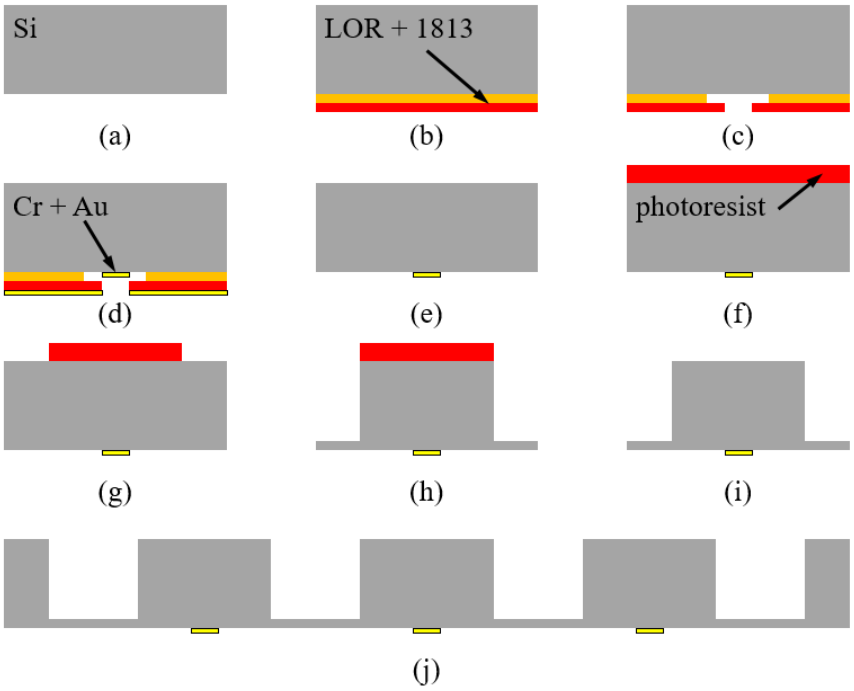

Figure 3.27. Illustration of E-band power divider fabrication process: (a) start with silicon wafer, (b) spin liftoff resist, (c) expose and develop first mask, (d) evaporation, (e) liftoff, (f) spin photoresist, (g) expose and develop second mask, (h) DRIE etch, (i) remove photoresist, (j) zoomed-out view showing several unit cells.

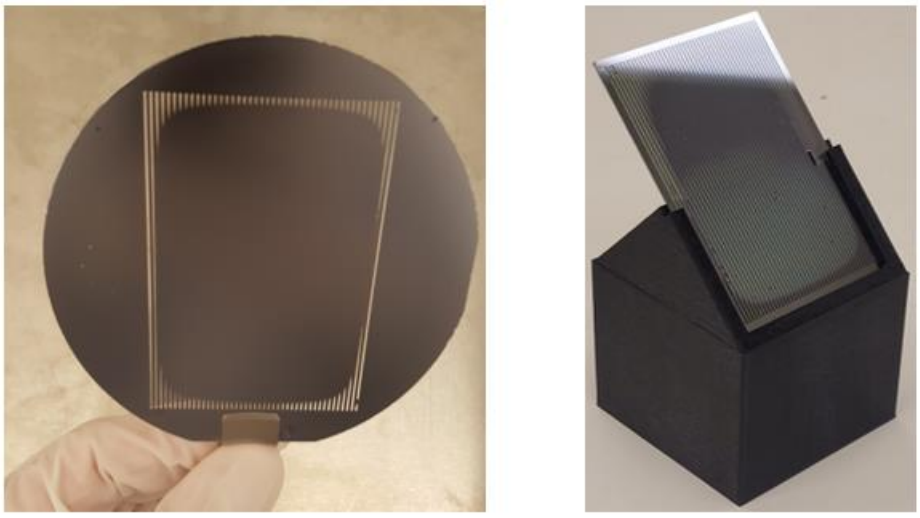

Figure 3.28. Photos of the fabricated E-band spatial power divider prototype. (a) Showing that the wafer has been completely etched through around the edges. (b) In a measurement fixture after being diced to rectangular shape.

3.5.4 Measurement Results

The reflection and transmission coefficients of the spatial power divider were measured using an HP 8510C network analyzer with two waveguide-based W85104A mm-wave Test Set frequency extenders, which enable measurements between 75 GHz and 100 GHz. The measurements were made in a similar manner to those made at J-band, using pyramidal horns to launch free-space waves and a 3D-printed fixture to hold the power divider at a 45-degree angle. Transmission is calibrated by comparing the response of the power divider to that of free space, and reflection is calibrated by comparing to a gold PEC mirror. Again, multi-path was handled by placing the spatial power divider in the near field of both horns, and using time-gating. A photo of the transmission measurement setup is shown in Figure 3.29.

The measured transmission and reflection coefficients of the spatial power divider for both TE and TM incident waves at 45-degree incidence are shown in comparison to the simulation in

Figure 3.30. The maximum difference between reflection and transmission for either polarization in the band from 76 GHz to 83 GHz is 0.9 dB.

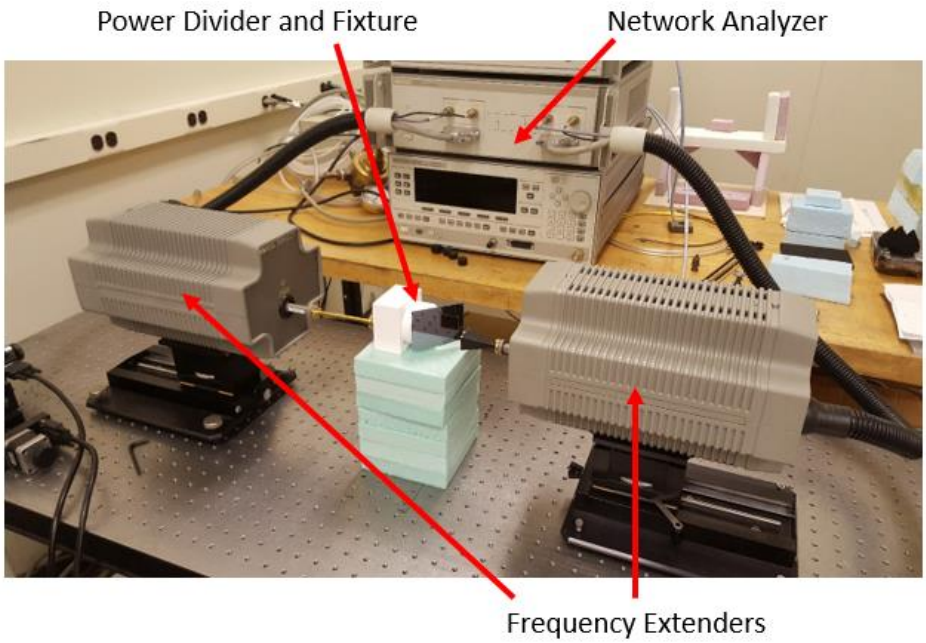

Figure 3.29. The setup for measurement of the E-band spatial power divider transmission coefficient.

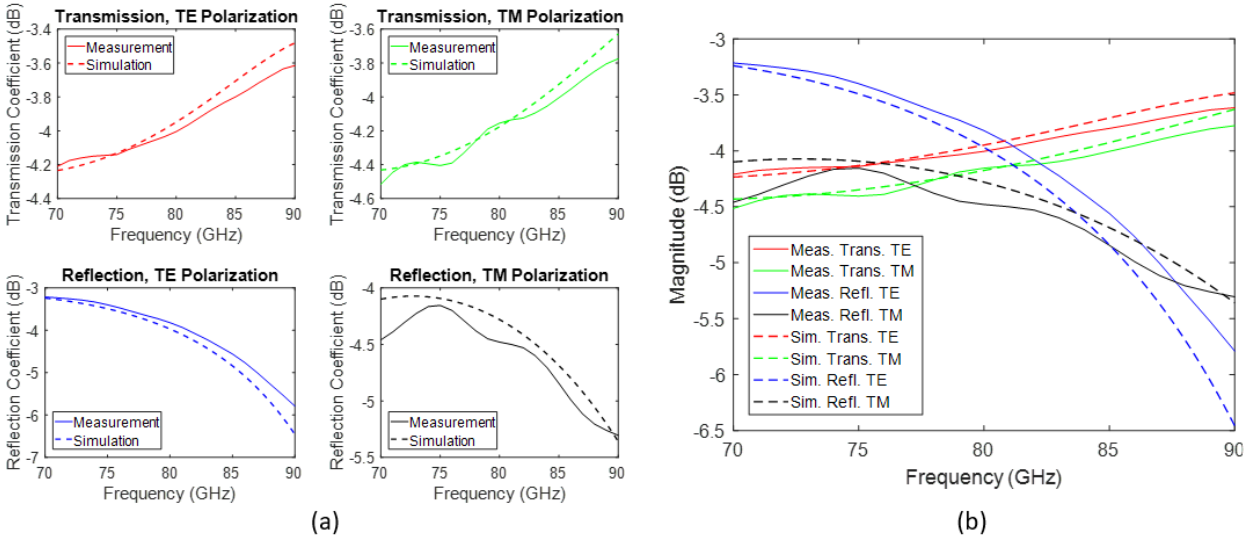

Figure 3.30. Transmission and reflection coefficients of the E-band spatial power divider are shown (a) on individual plots for clarity, and (b) all together for comparison.

3.6 Summary

Several polarization-independent spatial power dividers have been designed at different frequency bands to exhibit equal reflection and transmission for both TE and TM polarizations at 45-degree incidence on their planar surfaces.

Two J-band power dividers were implemented using a dielectric metamaterial technique based on a cascade of corrugated dielectric slabs. They were designed using a combination of an analytical model and full-wave electromagnetic simulation, and fabricated using DRIE of a silicon wafer. An E-band power divider was implemented with corrugated slabs and additional inductive MEFSS elements. It was designed with the aid of a circuit model, and fabricated with DRIE and metal evaporation and liftoff.

The fabricated prototypes have measured reflection and transmission coefficients that agree well with the simulation results, and exhibit no more than about 1 dB of difference between reflection and transmission for either polarization over their operating bands.

These polarization-independent spatial power dividers are key components of the common-aperture dual-polarized transceiver antenna system described in Chapter 2, where they are instrumental in enabling illumination of the same lens by two dual-polarized feed horns. The equal power division ensures that backscattered power received by the polarimetric radar is balanced across its four polarization channels.

CHAPTER 4
Simple-Structure J-Band Orthomode Transducer

Chapter 2 describes an antenna system with two dual-polarized ports. The two polarizations of each port are accessed in practice using an orthomode transducer (OMT), a three-port waveguide device that couples two single-polarization ports to a third common port that supports both polarizations. For the E-band radar, OMTs were purchased from a vendor. However, similar components at J-band are not available in the market, so it was necessary to design and fabricate custom OMTs for use at 220 – 248 GHz for the two J-band radars.

It is challenging to design and fabricate OMTs with the desired level of performance at millimeter-wave frequencies due to the tiny dimensions of the waveguides. Several different designs for OMTs at these frequency ranges have been reported, which have achieved outstanding performance over a wide bandwidth. Some such designs utilize a T-junction structure [88], [89], but involve many different machined steps requiring very high precision. Other designs implement a reverse-coupling structure [90], a double-ridged waveguide and Bϕifot junction [91], or a three-dimensional turnstile junction [92], [93]. Illustrations of these OMT structures are shown in Figure 4.1. These techniques require specialty machining equipment or complex multi-layer silicon micromachining processes to fabricate, and can be costly and have poor yield.

Here a design for an OMT at the 230 – 248 GHz band is presented, which features a simple geometry to facilitate fabrication with modest machining equipment, while still providing excellent performance over a 7% bandwidth. The T-junction structure utilized for this OMT is one

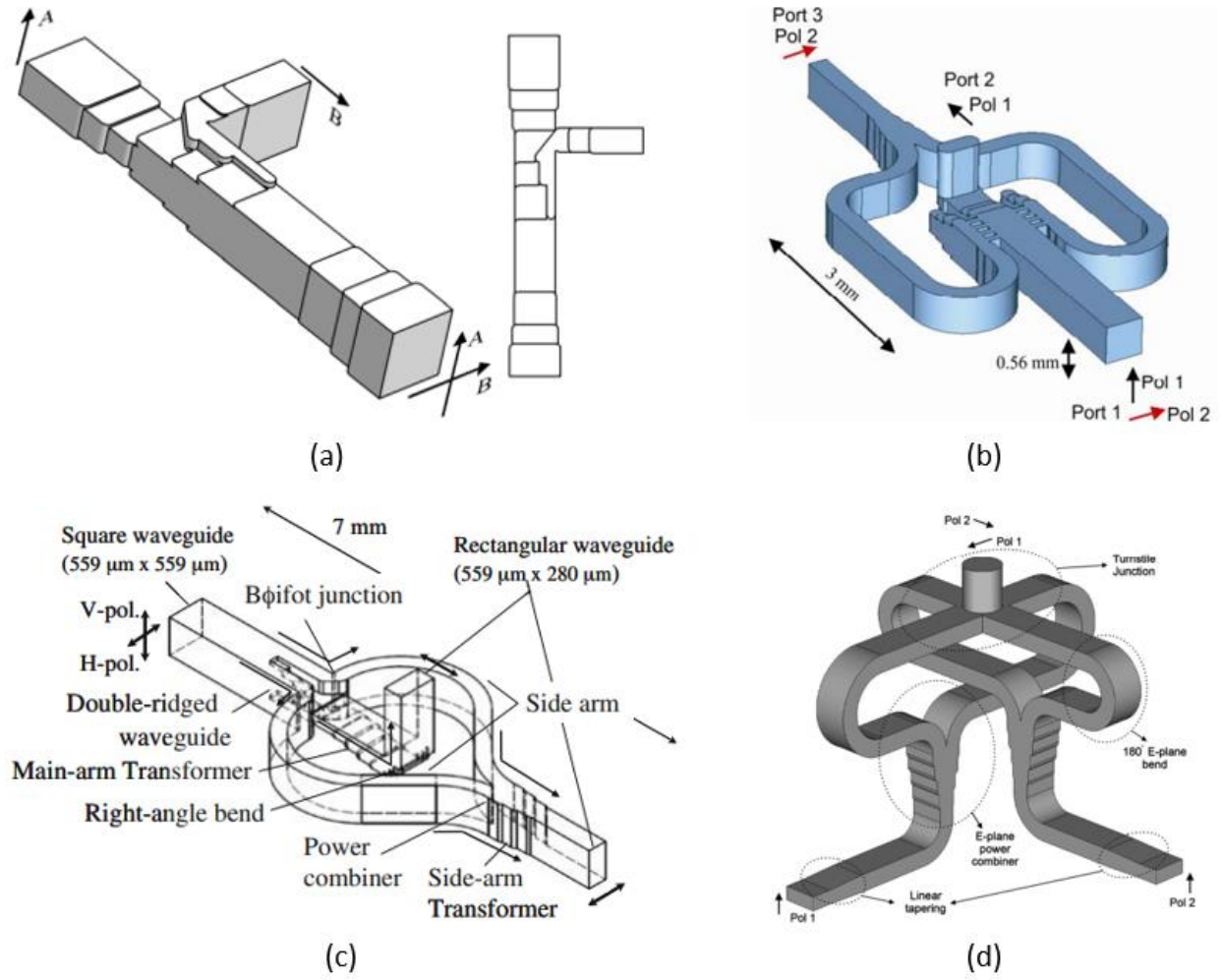

Figure 4.1. Several millimeter-wave OMT design structures: (a) multi-stepped T-junction OMT [88], (b) reverse-coupling structure OMT [90], (c) Bϕifot junction OMT [91], (d) turnstile junction OMT [92] (images have been reprinted from the respective sources).

that has been examined previously [88], [89], and drawbacks of the split-block assembly fabrication technique have been identified [88], [93]. Additionally, this design compromises performance, particularly in terms of bandwidth, compared to the designs described above. However, for engineers and researchers without access to the top-of-the-line machining equipment required to fabricate the small features of these high-performing but complex OMT designs at millimeter-wave frequencies, this design may present an alternative that can be easily fabricated with performance suitable for narrower-band applications. A similar OMT is presented in [94], but

this design provides comparable performance while requiring optimization of fewer geometric parameters and fabrication with fewer machining steps, and demonstrates a much better agreement between simulation and measurement results.

4.1 Orthomode Transducer Design

A diagram depicting the geometry of this OMT design is provided in Figure 4.2. The design is based on a simple T-junction between three sections of square waveguide. Two of these sections are transitioned into rectangular waveguides to form the V- and H- polarized ports of the OMT. The final waveguide section remains square, and forms the common port, which supports both V- and H- polarized modes. For the purpose of describing the performance of the OMT in terms of its scattering parameters, let the V port be defined as port 1, the H port as port 2, the V-polarized mode of the common port as port 3, and the H-polarized mode of the common port as port 4. Thus the OMT may be regarded as a four-port network [95].

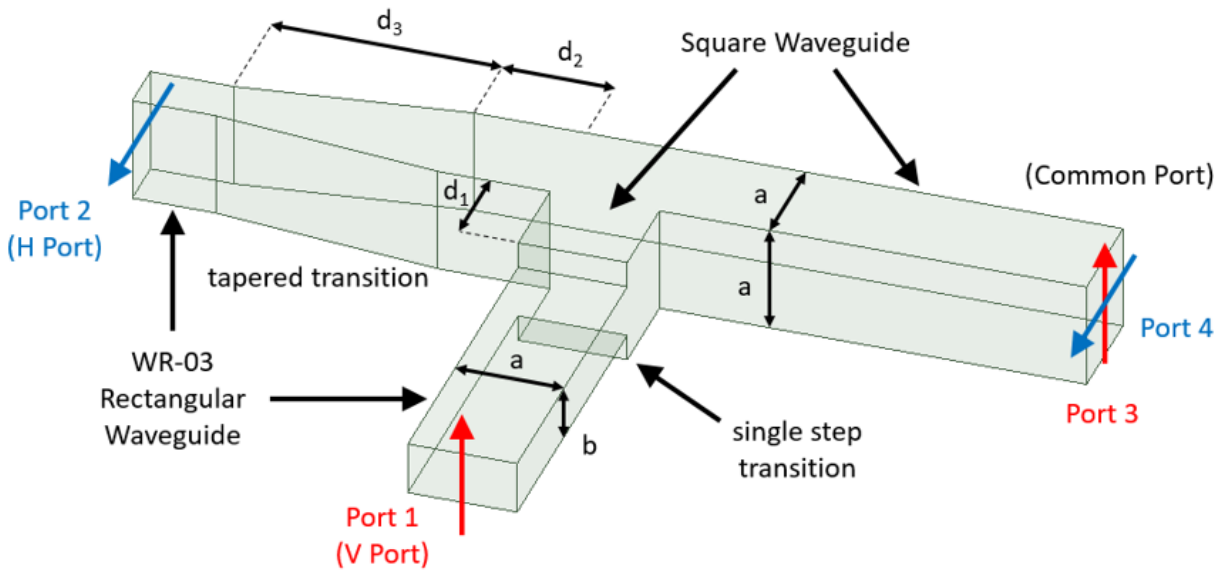

Figure 4.2. The geometry of the OMT is shown, and the ports and relevant dimensions are defined.

The desired operation frequency band for the GM J-band radar is from 230 to 248 GHz. This band is covered by both the WR-04 and WR-03 standard rectangular waveguide sizes. However, since the OMT design includes square waveguides where the side length is the longer dimension of the rectangular waveguides, the TM_{11} and TE_{11} square waveguide modes also need to be considered. Their cutoff frequency is 194 GHz at the WR-04 size, and 245 GHz at the WR-03 size. Therefore, the presence of higher order modes is possible within the entire operation band when using WR-04. Using WR-03 at least prevents this for most of the band of interest. Dimensions consistent with the WR-03 standard have been chosen for this reason.

4.2 Simulation Results

Simulations were performed using the finite element method (FEM) in Ansys HFSS. Initial designs were done assuming PEC boundaries at all the waveguide walls. The first higher order mode at each wave port is included to monitor possible generation of these modes.

Different types of transitions from square to rectangular waveguide were considered for both the V and H ports. Several such transitions are depicted in Figure 4.3. Each transition was first optimized to maximize transmission and minimize reflection. Then various combinations of transitions were integrated into the OMT, and their positions along the waveguides were optimized to maximize transmission between ports 1 and 3, and ports 2 and 4, as well as to minimize reflection at all four ports. The configuration providing the best performance among these combinations is that depicted in Figure 4.2, which features a tapered transition at the H port and a single step transition at the V port.

A tapered transition is expected to provide better performance over a wider band than a transition with discrete steps. In theory, the reflection should be minimized for taper lengths (d_3) of integer multiples of half guide wavelengths [96]. The length chosen here is approximately a full

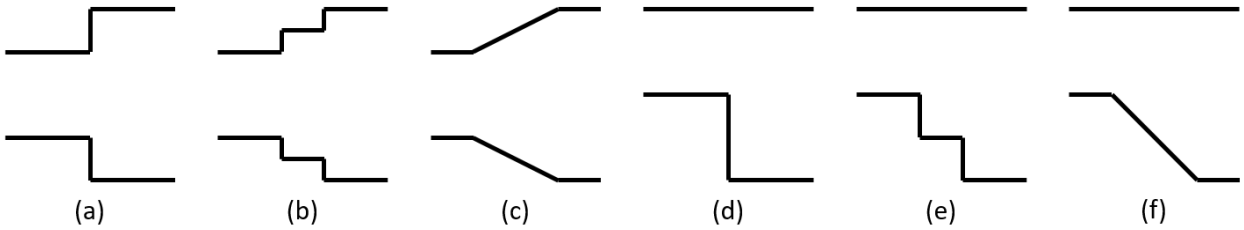

Figure 4.3. Different types of simple transitions from rectangular to square waveguide (shown in E-plane). (a) Single step, (b) double step, (c) tapered, (d) asymmetric single step, (e) asymmetric double step, (f) asymmetric tapered.

guide wavelength at the center frequency of the band. For fabrication with a mill axis along the vertical direction, a tapered transition is not possible for the V port, and thus a stepped transition must be used instead. This limits the bandwidth of the OMT for V-polarized signals. The single step transition was found to provide comparable performance to the double step, and was therefore chosen for its simplicity. The lengths d_1 and d_2 can be thought of as free parameters to assist in impedance matching. The V and H ports see the impedances of two sections of waveguide in parallel. d_1 can be used to help match the H port, while d_2 can be used to help match the V port.

The dimensions of the final optimized OMT design are $a = 0.034\ in.$, $b = 0.017\ in.$, $d_1 = 0.030\ in.$, $d_2 = 0.035\ in.$, and $d_3 = 0.072\ in.$.

For a fair comparison, the simulated results shown in Section 4.4 are obtained using finite conductivity boundaries and the full waveguide lengths of the fabricated OMT. The distances from the center of the T-junction to the V, H, and common ports are 0.375 in., 0.550 in., and 0.550 in., respectively.

4.3 Fabrication Process

Two OMTs were fabricated using CNC milling to carve the waveguides into blocks of brass. For each OMT, two blocks were used. On one block the entire waveguide segment extending

from the common port through the tapered transition to the H port, as well as the short section of square waveguide leading up to the stepped transition of the V port, was milled to the depth of a. Additionally, the remainder of the rectangular waveguide extending to the V port was milled to a depth of $a/2 + b/2$. At the position of the stepped transition, a layer of thickness $a/2 - b/2$ was removed from the top of the block, extending all the way across and toward the V port. The other block is entirely flat, except for a single step of height $a/2 - b/2$ which extends all the way across the block and is positioned to align with the similar step on the first block. Thus the second block simply provides the top walls of all of the waveguides. This approach was taken instead of the usual approach with two symmetric split blocks to avoid the possibility of misalignment. The fabrication process is shown in Figure 4.4. Additional machining was performed to provide screw holes to fasten the two blocks together, as well as to provide flanges by which the OMTs may be mated to other waveguide components.

It was found through measurement that simply fastening the two blocks via screws did not provide sufficient electrical contact between the two pieces. Any small gap between the surfaces allows energy to leak out of the waveguide and results in high insertion loss. To mitigate this problem, two steps were taken. First, the adjoining surfaces of the brass blocks were coated with a thin layer of solder, and the entire structure was heated to melt the solder during the fastening process. Second, the assembled OMTs were plated with an electroless gold plating solution. These steps were found to significantly reduce the insertion loss from upwards of 5 dB to close to 2 dB. Note that a standard WR-03 waveguide of a comparable length typically has an insertion loss of about 1 dB.

Fabrication was carried out by Dr. Adib Nashashibi. Photographs of the OMT are shown in Figure 4.5.

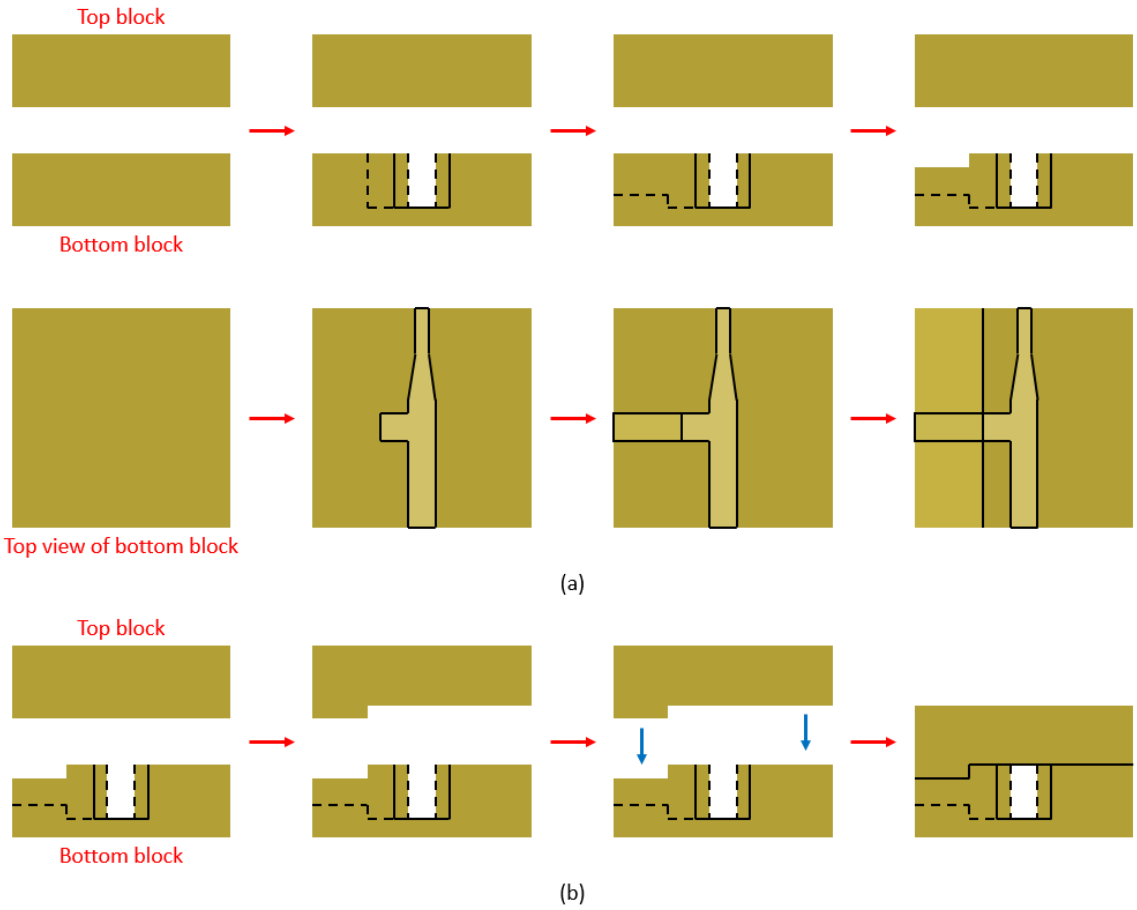

Figure 4.4. OMT fabrication procedure. (a) The bottom block is made in three milling steps. (b) The top block is made in one milling step and the two pieces are assembled together.

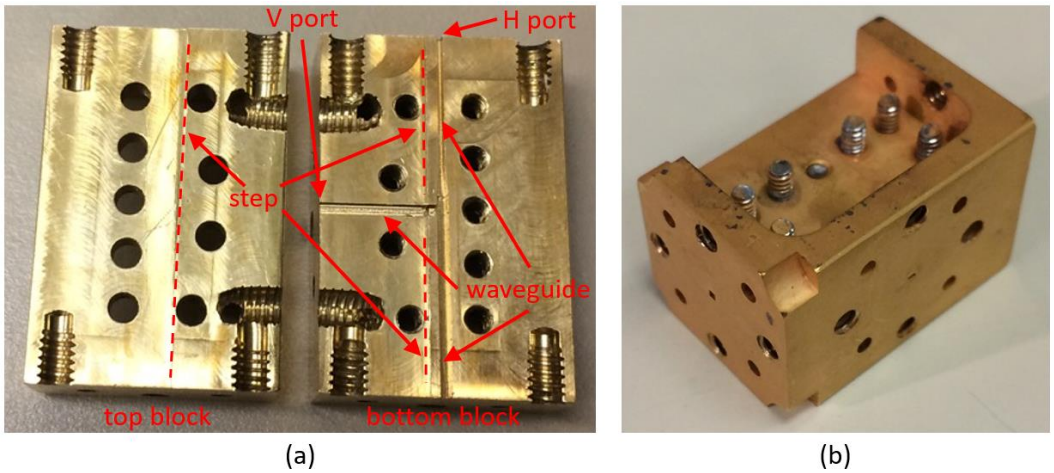

Figure 4.5. (a) The two brass blocks on which the OMT has been milled. The tiny waveguide features are highlighted. (b) The completed gold-plated OMT.

4.4 Measurement Results

The scattering parameters of the two OMTs were measured using the J-band waveguide network analyzer setup discussed previously for measurements of the J-band antennas and power dividers, featuring an Agilent N5245 4-port PNA-X and OML frequency extenders. The extenders were positioned at a ninety-degree angle to each other, and an E-plane waveguide bend was used to facilitate measurements between as many combinations of the four OMT ports as possible. The measurement setup is depicted in Figure 4.6.

The measured scattering parameters of the two OMTs are shown in comparison to the simulation in Figure 4.7. When the V or H port was unused, it was terminated with a matched load. Since no matched load for a square waveguide was available, a horn antenna was placed at the common port when measuring transmission between ports 1 and 2 to approximate a matched condition.

Due to positioning restrictions of the measurement setup, the scattering parameters corresponding to the polarization discrimination of the OMT (i.e. how much V-polarized signal at the V port appears due to an H-polarized excitation at the common port, etc.) were not measured for these prototypes. Instead, a measurement of the S_{21} parameters with the common port shorted is provided. The signal that reaches port 2 due to excitation at port 1 under this condition is a combination of the direct coupling between ports 1 and 2, and reflection from the shorted common port modified by the polarization discrimination.

Note that it is impossible to measure S_{43} and S_{34} as the two ports are coincident in space, but these parameters hold no practical significance.

The return loss is better than 10 dB at all ports for both OMTs over the band from 226.8 GHz to 243.7 GHz, which represents a bandwidth greater than 7%. The measured common port

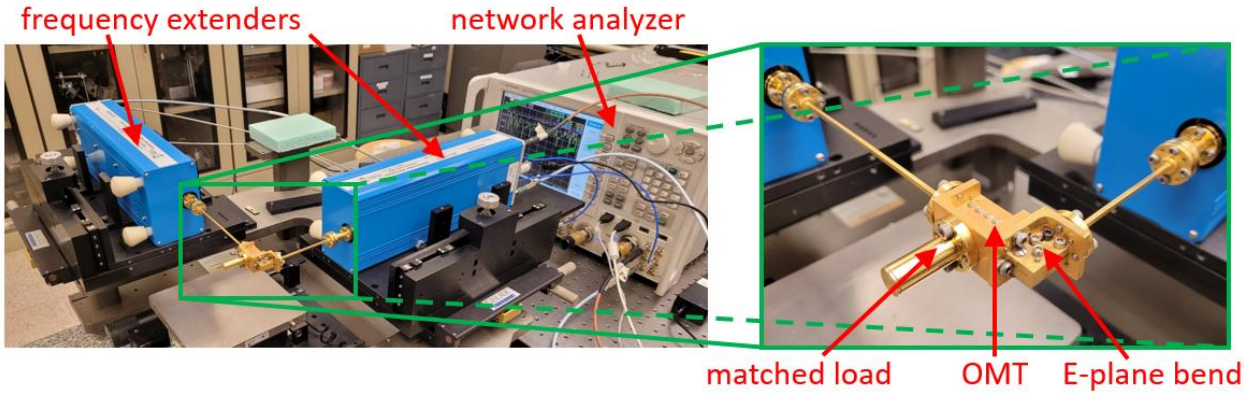

Figure 4.6. Photographs of the OMT S-parameter measurement setup.

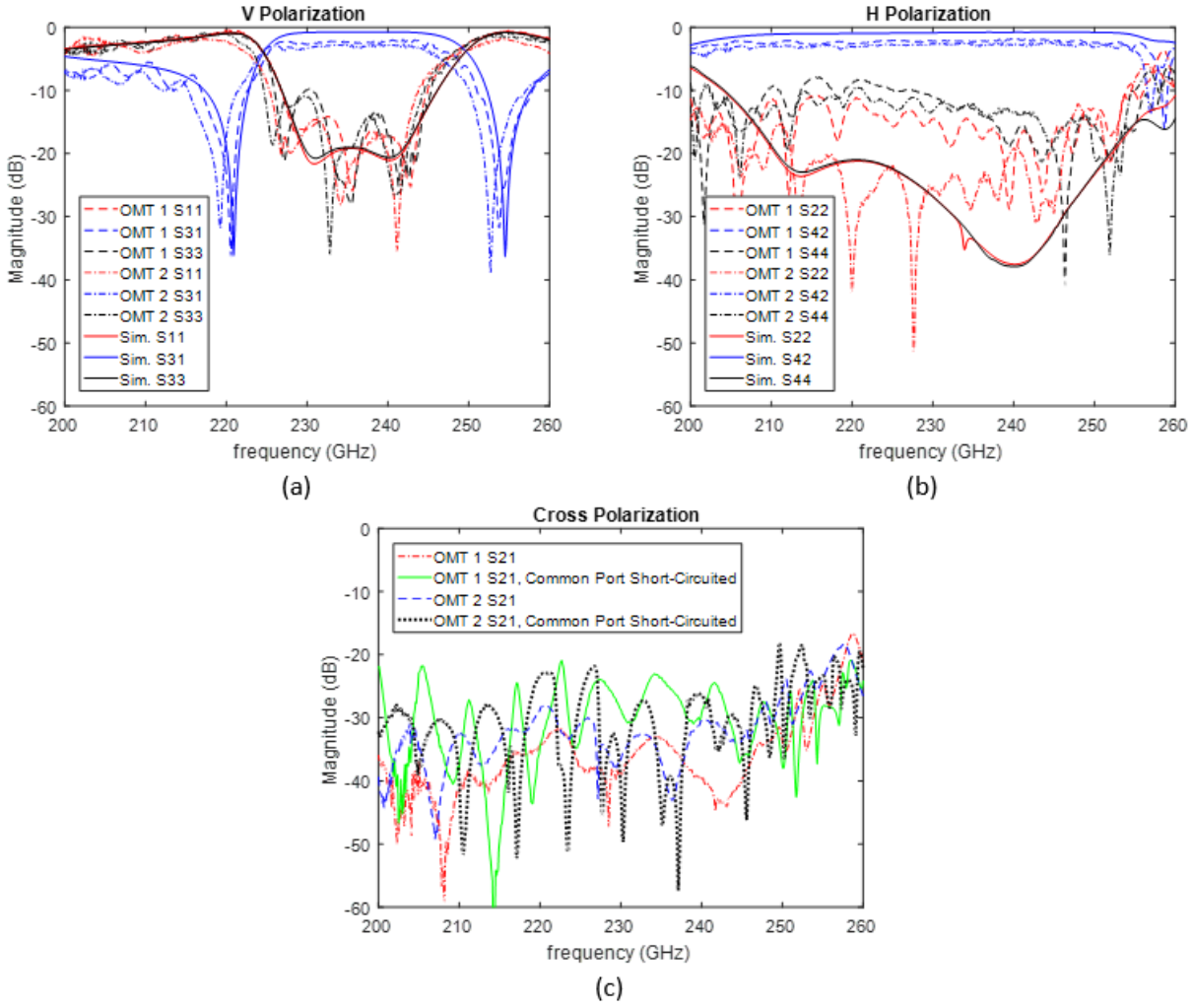

Figure 4.7. Comparison of measured S-parameters for the two OMTs to simulation. For clarity, the S-parameters are split up into those related to (a) V polarization, (b) H polarization, and (c) cross polarization.

return loss is significantly worse than the simulation due to the mismatch between the square and rectangular waveguides. Square-to-rectangular transitions were machined in an attempt to mitigate the mismatch, but this did not improve the measured performance, likely since the transition introduces an additional discontinuity and contributes some loss. There is a slight frequency shift in the operation band compared to simulation due to manufacturing tolerance. Over this band, the average insertion loss from V port to common port for OMT 1 is 2.4 dB, while that from H port to common port is 2.1 dB. The corresponding values for OMT 2 are 3.1 dB and 2.7 dB. Isolation between the V and H ports is better than 30 dB. Although it was not measured directly, the polarization discrimination also seems to be likely on this order of magnitude, based on the short-circuited isolation measurement. The OMTs can operate up to a bandwidth of 10% if performance requirements are relaxed. The similarity in performance between the two measured OMTs indicates a repeatable fabrication process.

4.5 Frequency Scaling

While this design was conceived to make fabrication easier at high frequencies, it may also provide a cost-effective solution at lower bands. Performance is also likely to improve due to reduced loss and sensitivity to machining error. It is therefore useful to briefly discuss the conditions under which frequency scaling can be achieved. A frequency shift can be realized in general by simple geometric scaling, but standard waveguide sizes should also be considered for compatibility with off-the-shelf components.

For a given waveguide size, the lower frequency limit of this design is approximately the minimum frequency of the corresponding band. It can be extended to slightly lower frequency, but this is not recommended in general due to greater dispersion in the waveguides close to the cutoff frequency. The upper frequency limit is determined by the cutoff frequency of the square

waveguide TM_{11} and TE_{11} modes. It can be seen in Figure 4.7.a that the V port's reflection coefficient becomes very large above this frequency (about 245 GHz for the WR-03 waveguide). These limits result in a useable bandwidth of around 15%. Of course, the design instance reported above has a bandwidth of only 7%, so the entire band cannot be covered with a single instance. The parameters d_1, d_2, and d_3 should be optimized to provide the best performance over the specific band of interest.

As an example, the simulated scattering parameters of two different J-band OMTs are shown in Figure 4.8. The first is that described above, which is pushing the high frequency limit of the WR-03 waveguide. The second is a design which has been tuned to the low end of the band for use in the KACST radar. The high J-band OMT sacrifices bandwidth to improve performance around and slightly above 245 GHz.

Figure 4.9 shows the simulated scattering parameters of an OMT that has been scaled to the WR-10 standard waveguide size. Its operation band is 74 – 82 GHz, which covers the modern automotive radar band.

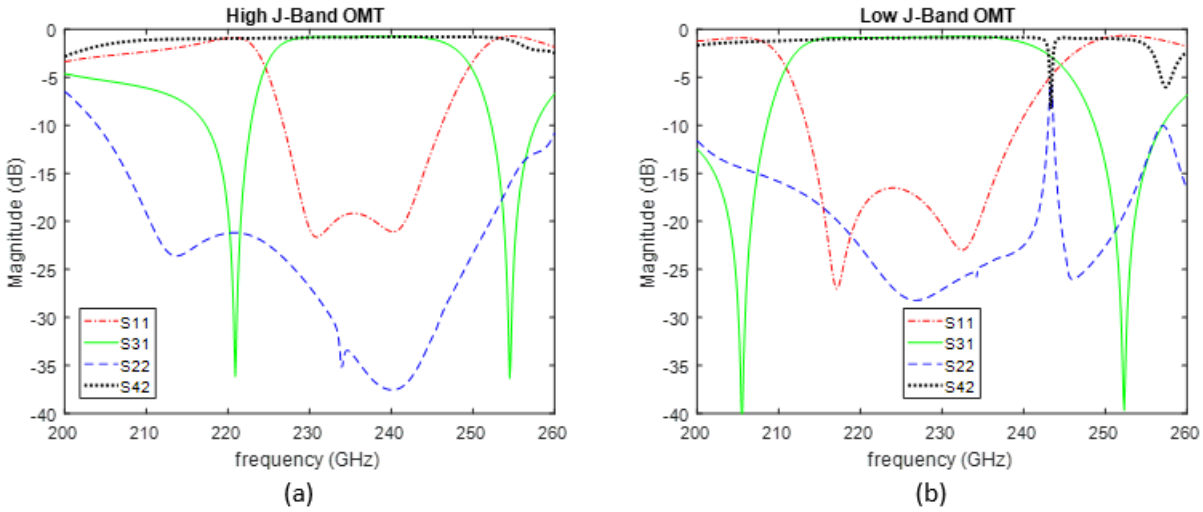

Figure 4.8. Simulated scattering parameters of two instances of the J-band OMT with parameters optimized to tune the performance at (a) the high end of the band for use in the GM radar, and (b) the low end of the band for use in the KACST radar.

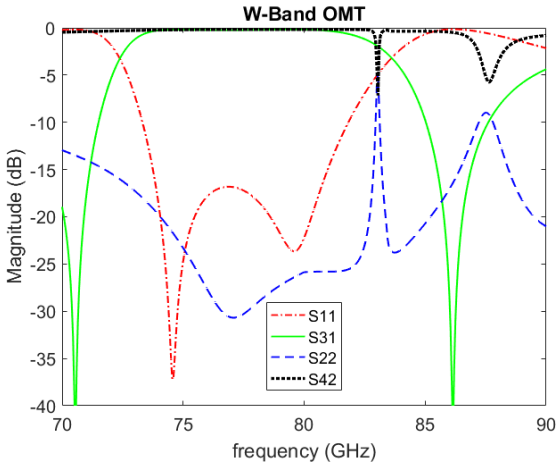

Figure 4.9. Simulated scattering parameters of an OMT scaled to the 77 GHz automotive radar band.

Table 4.1
List of millimeter-wave bands, corresponding rectangular waveguide size, and approximate frequency limits of the OMT design for each band.

Band	**Waveguide Size**	**Minimum Frequency (GHz)**	**Maximum Frequency (GHz)**
V	WR-15	50	56
E	WR-12	60	68
W	WR-10	75	83
F	WR-08	90	104
D	WR-06	110	128
G	WR-05	140	164
–*	WR-04	170	194
J	WR-03	220	245
Y	WR-02	325	417

* No band letter designation found

Table 4.1 shows a list of millimeter-wave bands, their corresponding waveguides, and the frequency range applicable to this OMT design. For applications outside of these ranges, the recommendation is to design the OMT using non-standard rectangular waveguide sizes, and then integrate transitions to mate with other components as needed.

4.6 Second Version

As with the spatial power divider, the initial OMT design needed to be tuned to a lower band for use in the KACST radar at 220 – 230 GHz. The simulation of this adjustment has already been shown in Figure 4.8.b in the previous section. The optimized parameters of the updated version are $d_1 = 0.034\ in.$, $d_2 = 0.005\ in.$, and $d_3 = 0.072\ in.$ (a and b remain the same).

It was mentioned that the fabrication process outlined in Figure 4.4 was used instead of a symmetric split block assembly to avoid possible misalignment between the blocks. However, there was significant leakage through the seams between the blocks, which needed to be mitigated by soldering them together during assembly. In the symmetric split block technique, the seam lies directly on the middle E-plane of the H port waveguide, where a current null is expected. This should serve to improve insertion loss for H polarization. It does not, however, improve the situation for the V port waveguide, where the seam lies along the middle H-plane of the waveguide, so a poor connection between blocks will still disrupt current flow on the side walls. Nevertheless, it was decided to use symmetric blocks for the KACST radar OMTs in an effort to improve the insertion loss. In this case, the fabrication process is similar to the one shown previously, but now two mirror image blocks are milled, and then are aligned with each other to the best precision possible by using guide pins during assembly. Figure 4.10 shows the new process, and two OMTs were fabricated with this method. A photo of the two symmetric blocks of one OMT is shown in Figure 4.11.

Instead of using solder to improve electrical connection between the blocks, the adjoining surface of each block was polished using a manual lapping table prior to milling the waveguides. This provided very smooth and flat surfaces that could make a better connection with each other

without the use of solder. The electroless gold plating technique was also used once again to improve conductivity of the waveguide walls and fill remaining gaps.

Some of the rigid coaxial cables used in the measurement setup were replaced with flexible ones to provide greater range of motion for the frequency extenders. This enabled direct measurement of the polarization discrimination. The measured scattering parameters of the two OMTs are shown in comparison to the simulation in Figure 4.12. Simulated S_{21}, S_{32}, and S_{41} are not shown as they are below -60 dB.

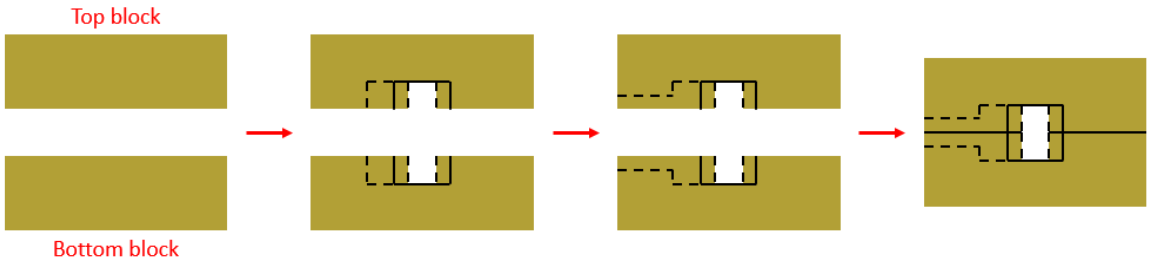

Figure 4.10. Fabrication procedure for second version OMT. The symmetric top and bottom blocks are both made in two milling steps, then the two pieces are aligned and assembled together.

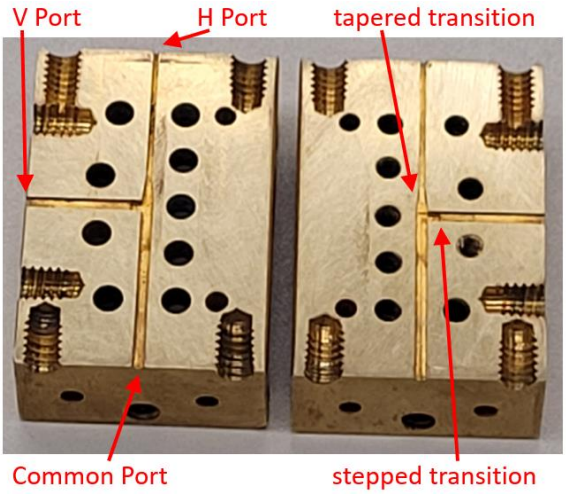

Figure 4.11. Photograph of the two brass blocks on which the second version OMT has been milled. The waveguide features are highlighted.

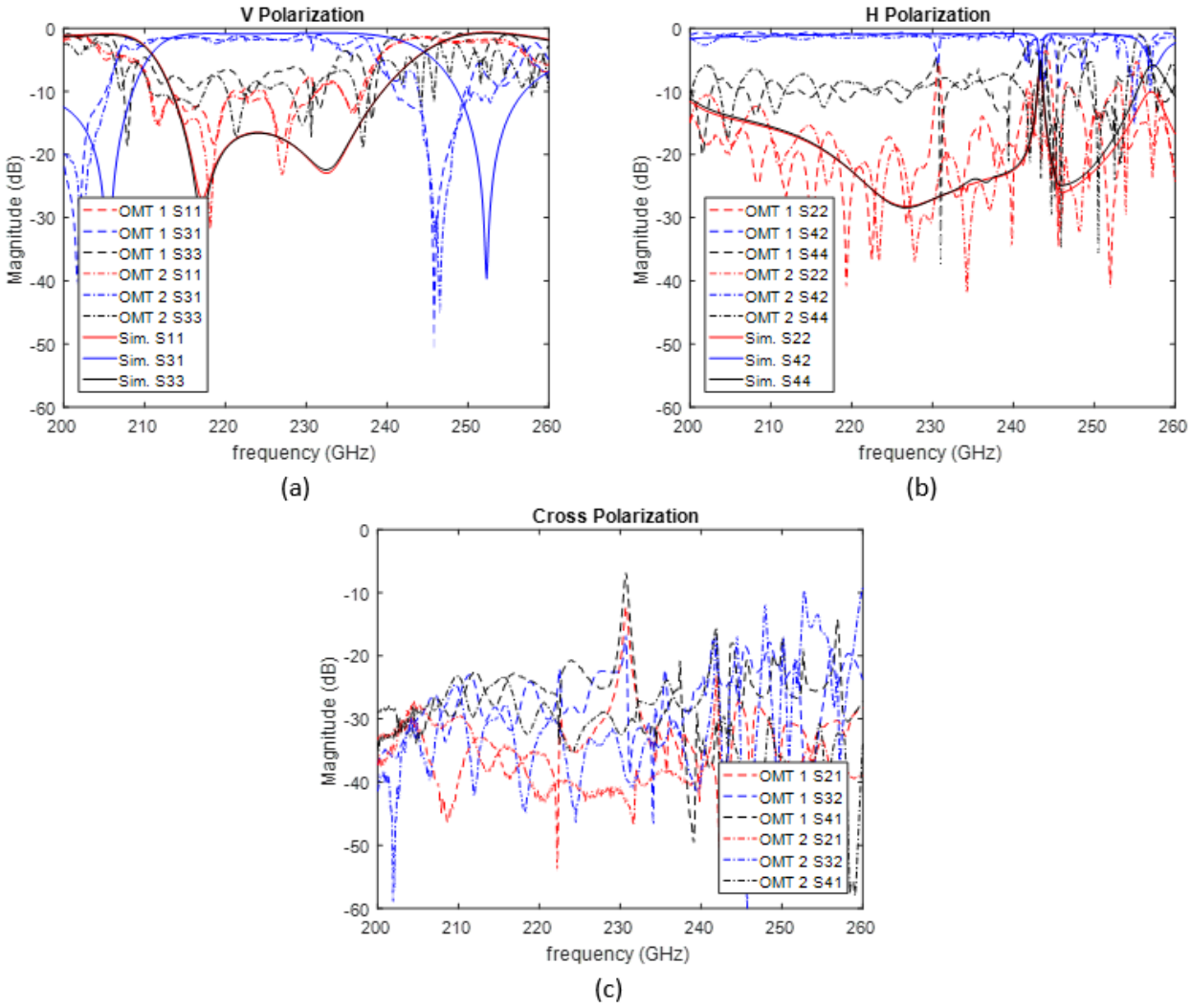

Figure 4.12. Comparison of measured S-parameters for the two second version OMTs to simulation. For clarity, the S-parameters are split up into those related to (a) V polarization, (b) H polarization, and (c) cross polarization.

It is immediately obvious that the reflection coefficients at ports 3 and 4 are quite poor for both OMTs, being greater than -10 dB for much of the desired operation band. Once again, the poor match is due to the fact that the square waveguide of the common port has been connected to a rectangular waveguide at the calibration plane, so considerable mismatch is expected. It is still discouraging to see such a result, when the previous set of OMTs had better return loss. Even disregarding the common ports, the V and H ports still do not maintain 10 dB of return loss over

the desired band, so a 10 dB return loss bandwidth cannot be properly defined. However, the insertion loss is quite low, so it is clear that at least energy is being transmitted through the system as desired. Therefore, for the purpose of discussion, consider an 8 dB return loss bandwidth, excluding the common port. By this definition, the operating band of OMT 1 is 210.4 GHz to 230.1 GHz (about 9%), and that of OMT 2 is 210.3 GHz to 237.7 GHz (about 12%). This compares favorably to the 7% achieved with the first version. There is similarly a slight downward frequency shift compared to the simulation, as observed in the first version. The operating band of OMT 1 will be used in the following discussions of the remaining scattering parameters, since it is a subset of the band of OMT 2 and contains the desired 220 – 230 GHz range.

Over the operating band, the average insertion loss from V port to common port for OMT 1 is 1.7 dB, while that from H port to common port is 1.0 dB. The corresponding values for OMT 2 are 1.7 dB and 1.4 dB. This is an improvement of a full 1 dB compared with the first version, so it appears the updated fabrication process in Figure 4.10 helped to reduce loss in the waveguides.

For OMT 2, isolation between the V and H ports is greater than 30 dB, and polarization discrimination is greater than 23 dB. For OMT 1, isolation is greater than 30 dB up to 228 GHz, but drops to 21 dB at 230 GHz. Similarly, polarization discrimination is greater than 20 dB up to 229.5 GHz, but drops to 16 dB at 230 GHz.

The reason that OMT 1 has a smaller bandwidth than OMT 2, as well as worse isolation and discrimination close to 230 GHz, is the presence of a notch in the H-polarized transmission coefficient at just above 230 GHz. The OMT was disassembled and cleaned several times throughout the process of its construction, and this notch was always present, but sometimes appeared at different frequencies. The notch is also present in the simulation, but shows up at a higher frequency around 243 GHz, where it would not be problematic. While attempting to find a

cause for this behavior, it was found that the notch frequency could be adjusted downward in simulation by increasing d_1, as if there is a resonance between the T-junction and the step transition. Additionally, the observed frequency shift of the overall operation band can be accounted for by increasing the waveguide dimensions. By setting $d_1 = 0.040\ in.$, $a = 0.035\ in.$, and $b = 0.0175\ in.$ in the simulation, quite a good match to the measured scattering parameters of OMT 1 is achieved. This comparison is shown in Figure 4.13. Fabrication tolerance on the order of 0.001 in. for a and b is expected. The difference of 0.006 in. for d_1 is surprising, but can't be ruled out. It is supposed that the observed change in the notch frequency may have been due to a piece of debris inside the OMT near the position of the step transition. It is unfortunate that the simulation suggests the step transition is too far from the junction, otherwise the notch might have been fixed by additional milling. In any case, the performance of OMT 1 was deemed to be satisfactory for the purpose of the KACST radar, so no further action was taken on the matter.

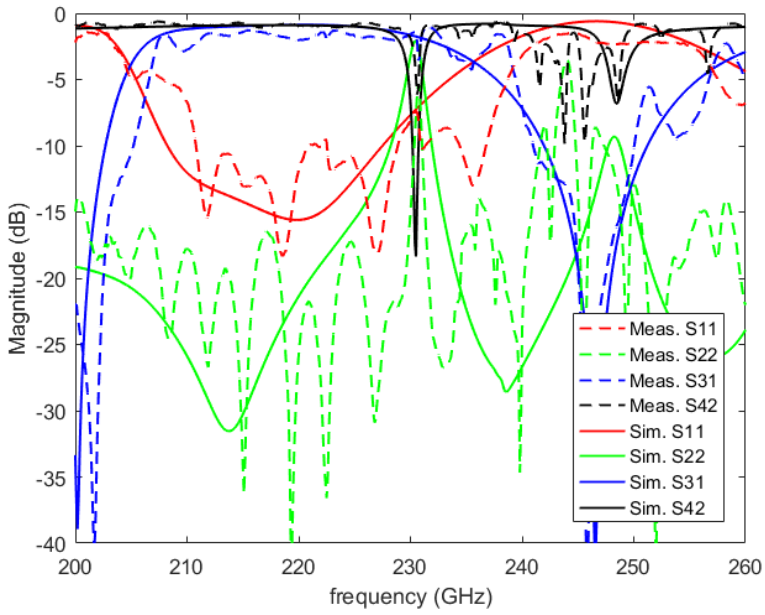

Figure 4.13. Comparison of the measured S-parameters of OMT 1 to a simulated model which has been adjusted to match the measurements. The notch at just above 230 GHz has been reproduced by adjusting the parameter d_1.

4.7 Back-to-Back OMT Measurement

Through use of a time-domain transform, it was found that the poor V and H port return loss performance of second version OMTs 1 and 2 was actually strongly influenced by reflections coming from the mismatched common port. This also indicates that the insertion loss may be quite significantly impacted by this mismatch. In order to obtain more realistic measurements of the OMTs' reflection and transmission coefficients, a series of back-to-back measurements were taken, in which OMTs 1 and 2 were connected to each other at their common ports [97]. This provides a better impedance match at ports 3 and 4 of both OMTs, and results in a more accurate measurement of the V and H port reflection coefficients. It also allows for measurement of the transmission coefficient from either the V or H port of OMT 1 to either the V or H port of OMT 2, from which estimates of the insertion loss can be obtained, also free of the impact of common port mismatch.

There are eight unique transmission configurations possible, corresponding to the two port choices for each OMT, and the relative orientation of the two common ports. Let T_{ij} represent the transmission coefficient from port j of OMT 2 to port i of OMT 1 when the common ports are aligned in alike polarization. Similarly, let C_{ij} represent the transmission coefficient when the common ports are aligned in cross polarization. Here i and j may take values 1 or 2. Under the assumptions that all ports are matched, and that the two common ports are perfectly coupled in aligned polarizations without reflection or leakage to the orthogonal polarization, then the following hold:

$$T_{ij} = S_{i3}^{1} S_{3j}^{2} + S_{i4}^{1} S_{4j}^{2} \tag{4.1}$$

$$C_{ij} = S_{i3}^{1} S_{4j}^{2} + S_{i4}^{1} S_{3j}^{2} \, . \tag{4.2}$$

Here the superscripts denote the OMT number.

For example, when measuring T_{11}, the two OMTs are connected back-to-back at their common ports such that port 3 of OMT 1 is aligned with port 3 of OMT 2 (and port 4 of each are aligned with each other as well). If there is no reflection at any of the OMT ports, and no cross-polarized coupling at the common port interface, then the field that is measured at port 1 of OMT 1 due to excitation at port 1 of OMT 2 is a result of two components. The first component is an entirely V-polarized signal that travels from port 1 to port 3 of OMT 2, and then from port 3 to port 1 of OMT 1. The second component is one that becomes H-polarized during transmission due to the polarization discrimination, and travels from port 1 to port 4 of OMT 2, and then from port 4 to port 1 of OMT 1.

It should be noted that terms S_{14}^1 and S_{41}^2 are very small compared to S_{13}^1 and S_{31}^2 in the example case of T_{11} described above, as evidenced by the previously measured V-polarized insertion loss of around 1.7 dB and polarization discrimination of more than 20 dB. Thus $|S_{13}^1 S_{31}^2| \gg |S_{14}^1 S_{41}^2|$, so the second term may reasonably be ignored. The same argument may be made for back-to-back transmission coefficients T_{22}, C_{12}, and C_{21}. The following approximations are obtained:

$$T_{11} = S_{13}^1 S_{31}^2 + S_{14}^1 S_{41}^2 \approx S_{13}^1 S_{31}^2 \tag{4.3}$$

$$T_{22} = S_{23}^1 S_{32}^2 + S_{24}^1 S_{42}^2 \approx S_{24}^1 S_{42}^2 \tag{4.4}$$

$$C_{12} = S_{13}^1 S_{42}^2 + S_{14}^1 S_{32}^2 \approx S_{13}^1 S_{42}^2 \tag{4.5}$$

$$C_{21} = S_{23}^1 S_{41}^2 + S_{24}^1 S_{31}^2 \approx S_{24}^1 S_{31}^2 \,. \tag{4.6}$$

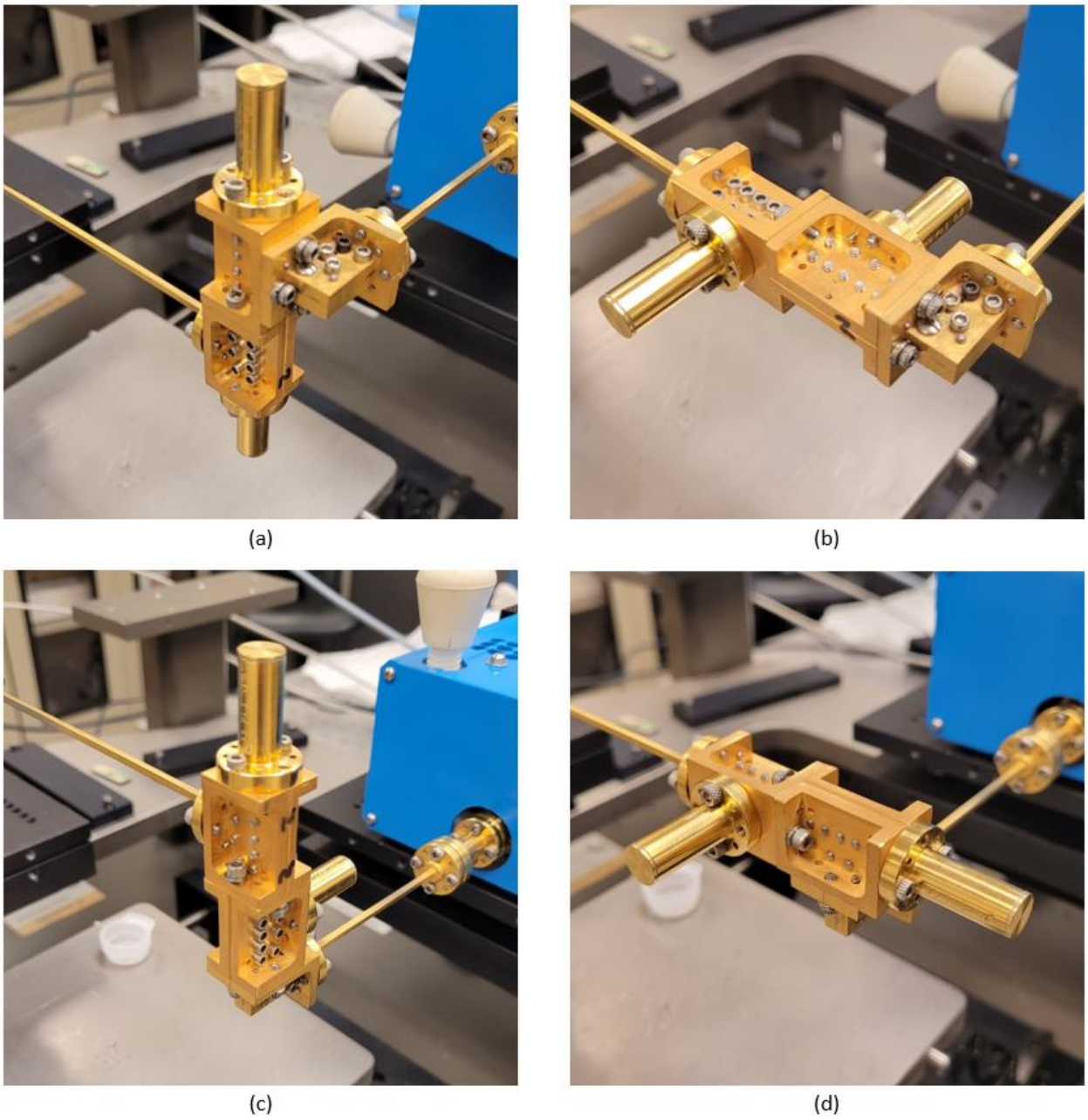

Figure 4.14. Photos of the configurations of two OMTs for back-to-back transmission measurement. (a) T_{11}, (b) T_{22}, (c) C_{12}, and (d) C_{21}.

Figure 4.14 shows photographs of the arrangements of the two OMTs for measurement of T_{11}, T_{22}, C_{12}, and C_{21}. Equations (4.3) – (4.6) represent a system of four equations with four unknowns, which unfortunately does not have a unique solution. Another equation was generated

using the single OMT measurements of the H-polarized transmission coefficients, represented by S_{24}^{1s} and S_{42}^{2s}. It was assumed that these coefficients for OMTs 1 and 2 should maintain approximately the same ratio in both measurements. Thus the following was obtained:

$$S_{42}^{2} = S_{42}^{2s}/S_{24}^{1s} \cdot S_{24}^{1} \,. \tag{4.7}$$

By substituting (4.7) in (4.4), an estimate of S_{24}^{1} was calculated. Then (4.5) and (4.6) were used to calculate S_{13}^{1} and S_{31}^{2}, respectively. A similar approach using the ratio of V-polarized transmission coefficients could be used as well, but the former approach was chosen over the latter because it yielded better results. The V and H port reflection coefficients are measured directly by the back-to-back scattering parameter measurements.

Figure 4.15 shows a comparison of the reflection and transmission coefficients of OMTs 1 and 2, as determined by the single OMT measurements and estimated from the back-to-back measurements. It can be seen that, for the most part, the coefficients measured by the back-to-back method are improved compared to their single OMT counterparts. However, the scattering parameters of the two units have not been completely decoupled from each other, as evidenced by the presence of the notch-like response in the back-to-back measurements of OMT 2.

Using these back-to-back measurements, the two OMTs both now maintain 10 dB return loss over the band from 211.1 GHz to 230.4 GHz. Over this band, the average insertion loss from V port to common port for OMT 1 is 0.9 dB, while that from H port to common port is 0.6 dB. The corresponding values for OMT 2 are 1.2 dB and 1.0 dB. This is an improvement of 0.5 dB on average, compared to the single OMT measurements. This is roughly what should be expected based on a common port reflection coefficient of around -10 dB.

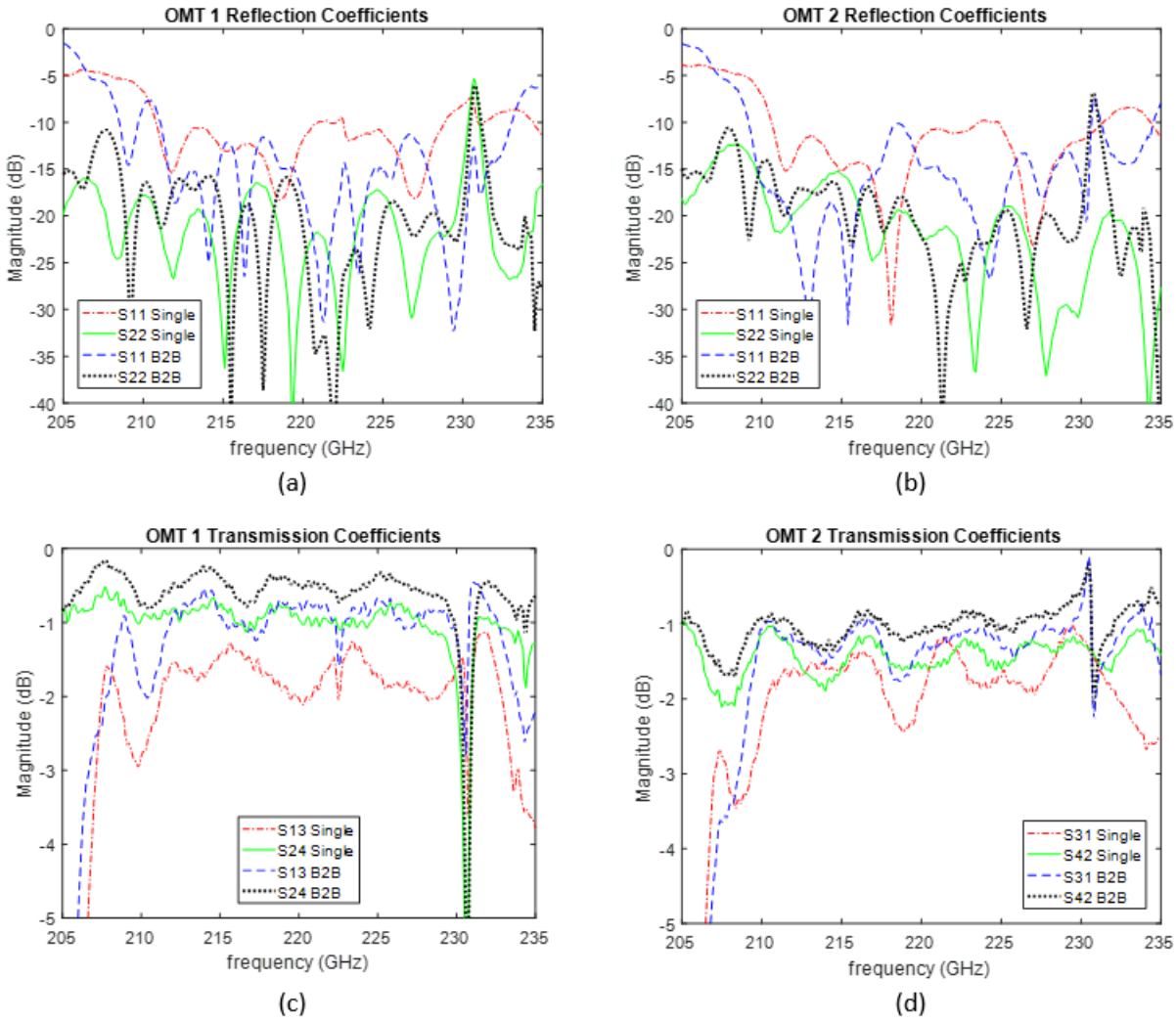

Figure 4.15. Comparison of OMT reflection and transmission coefficients as measured by the single OMT method and the back-to-back method. (a) OMT 1 reflection coefficients, (b) OMT 2 reflection coefficients, (c) OMT 1 transmission coefficients, and (d) OMT 2 transmission coefficients.

4.8 Discussion

The measured performance of both versions (high J-band and low J-band) of this OMT is compared to other similar T-junction OMT designs at millimeter-wave and terahertz frequencies in Table 4.2. With the exception of its bandwidth, this design's performance characteristics are

Table 4.2
Comparison of OMT performance to other millimeter-wave T-junction OMTs.

	This Work			Literature		
Reference	**Version 1**	**Version 2**		**Dunning [88]**	**Reck [89]**	**Qin [94]***
		(Single)	**(B2B)**			
Center Frequency (GHz)	235	220		90	550	215
Bandwidth (%)	7	9		27	18	4.7
Insertion Loss (dB)	< 3.9	< 2.6	< 1.8	< 2	< 8	< 4
Return Loss (dB)	> 10	> 8	> 10	> 24	> 17	> 9
Isolation (dB)	> 30	> 30†		> 37	> 19-28‡	> 30
Machined Steps per Block	2	2		13	8	3

* Values are based on plot of measured scattering parameters presented over the cited 210 – 220 GHz band; the authors claim different values.
† Isolation was greater than 30 dB except for OMT 1, which rises to 21 dB above 228 GHz.
‡ Three prototypes were measured with differing isolation due to block misalignment.

comparable to the others', while requiring only two machining steps per block to form the waveguide structures. Each machining step introduces a source of potential error, so when machining capability is limited, it is best to utilize the simplest geometry with the minimum number of machining steps.

4.9 Summary

An orthomode transducer with simple geometry has been designed to provide good performance over a relatively small bandwidth, while minimizing the fabrication challenges of high millimeter-wave frequency waveguides. The OMT couples the V- and H- polarized modes of a common port to two corresponding single polarization ports, allowing access to the separate polarization channels of dual-polarized radar antennas.

The OMT consists of a square waveguide T-junction with transitions to standard rectangular waveguides for the V and H ports. It was designed using FEM in Ansys HFSS. Two prototypes each of two instances of this OMT were manufactured for operation at slightly different frequencies at J-band. The design can also be scaled easily to other bands of interest.

The fabricated prototypes generally have return loss, polarization discrimination, and isolation better than 10 dB, 20 dB, and 30 dB, respectively, over a fractional bandwidth of at least 7%. Various techniques have been used to reduce the conductive losses, and the final set of OMTs have insertion loss of about 1 dB on average, estimated from back-to-back measurements.

These OMTs have been utilized in the GM and KACST J-band polarimetric radars, where they serve to enable the dual-polarized transmit and receive functionality of the antenna system from Chapter 2.

CHAPTER 5

J-Band Polarimetric Radar Backscattering Measurements of Road Surfaces

As discussed in Chapter 1, a variety of sensor technologies are utilized in the automotive industry for both driver assistance functions and autonomous vehicle operation. Millimeter-wave radar is a very important sensor due to its ability to detect targets at relatively long range and under an assortment of weather conditions, which make it superior to other technologies such as lidar or optical imaging in certain roles [98]. Using Doppler processing, radar is also capable of simultaneously detecting both the distance and speed of multiple targets. Additionally, polarimetric radar is able to exploit the polarization response of the target to obtain even more information. This is particularly useful for both discriminating between different types of road surfaces, and assessing road surface conditions, based on the absolute and relative strengths of co- and cross-polarized backscattering exhibited [99].

The application of radar to road surface identification and condition assessment is of great interest for both ADAS and autonomous vehicles. A human vehicle operator is typically able to tell the difference between a clear road in good condition, and one that may be covered with precipitation or damaged by wear. This is achieved using a combination of visual cues and past experience. For autonomous vehicle operation, this process is emulated by machine learning algorithms, in which sensor data is used to "teach" the vehicle how to discriminate between surfaces in a similar manner. However, in both cases the task can become more challenging at night or during intense weather, when visibility is poor. In that case it is useful to have millimeter-

wave radar sensors to either provide additional feedback to a driver, or to supplement optical sensors.

There is currently a lack of backscattering data to be used for development of the necessary surface assessment capabilities, particularly at J-band. The GM J-band radar was constructed for the purpose (among others) of making many polarimetric measurements of road surfaces to study their backscattering behavior and develop assessment models. The front end of this radar features the common-aperture dual-polarized transceiver antenna system from Chapter 2, as well as the J-band OMT from Chapter 4. This chapter presents a set of measurements made with the J-band radar of the co- and cross-polarized backscattering coefficients from a collection of typical road surfaces under various conditions. The measurements are made at near-grazing incidence to approximate what would be observed by a forward-looking radar mounted near the bumper of a vehicle. This data serves to further highlight the significance of the work described in the previous chapters of this dissertation.

5.1 Radar System Details

The GM J-band radar uses the FMCW modulation scheme. It uses a saw-tooth chirp (i.e. a repeated linearly increasing frequency sweep). The start and stop frequencies of the chirp are programmable within the 230 – 248 GHz band. The chirp is generated by a direct digital synthesizer at frequencies below 1.4 GHz, and is then up-converted to X-band before being multiplied to J-band using a $\times 24$ active frequency multiplier. A heterodyne receiver architecture is used to de-chirp the received signal.

The common-aperture dual-polarized transceiver antenna allows simultaneous reception of both vertically- and horizontally- polarized received waves in response to transmission of either polarization. A single-pole double-throw switch is used to toggle between the two transmit

polarizations, but two dedicated receiver channels enable concurrent measurement of both received polarizations at once. As a result, the complete complex scattering matrix can be measured in the V-H polarization basis using only two signal transmissions.

Owing to the narrow beamwidth, high isolation, and shared aperture of the antenna system, the radar enjoys a two-way beamwidth of 0.55°, effective cross-polarization isolation of 24 dB, and operation free of parallax. It also features 0 dBm effective transmitted power, phase noise of -76 dBc/Hz at 10 kHz offset, and a dynamic range of up to 84 dB. The digital sampler used to collect the baseband signal is capable of sample rates up to 1 GSa/s for a single channel when the radar is operated in block mode or 200 MSa/s in streaming mode. There is not yet any publication on this specific radar, but its very similar counterpart operating at the 77 GHz band is described in [100]. A photograph of the radar is shown in Figure 5.1.

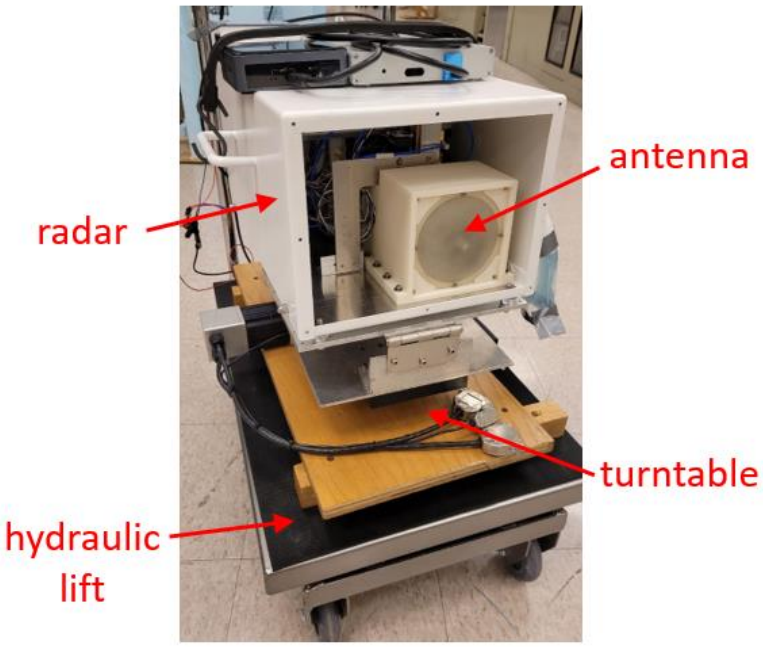

Figure 5.1. Photograph of the GM J-band radar mounted atop a hydraulic lift and turntable for elevation and azimuth scanning.

5.2 Measurement Setup

The radar was mounted to a turntable placed on a hydraulic lift to adjust the position of the antenna aperture to a height of up to 1.05 m above the ground. A discrete set of six heights was selected. At each height, the wooden platform to which the turntable was fixed was shimmed until level to ensure azimuthal rotation parallel to the horizon. Then a trihedral corner reflector was placed on the ground at a horizontal distance of 15 m (at the far field of the antenna), and the radar was pointed at this trihedral by adjusting its azimuth and elevation angles to maximize the return peak. Azimuth angle was controlled with the turntable, while elevation angle was controlled with a small jack at the back of the radar. For each measurement, the approximate incidence angle can be calculated from the target range and aperture height. Additional corrections were made by directly measuring the slope of both the radar housing and the local target spot with an inclinometer. Six incidence angles between 86° and 89° were considered in this manner. A depiction of this setup is shown in Figure 5.2.

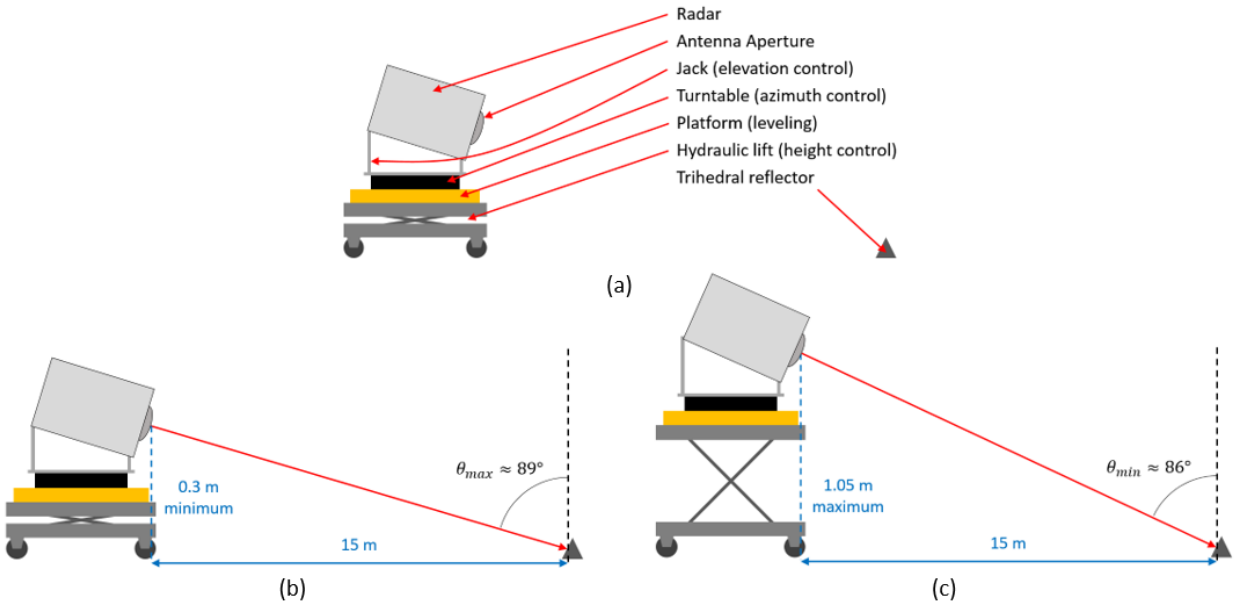

Figure 5.2. Depiction of the procedure for setting the radar at a specific incidence angle. (a) List of components used in the rig for height and angle adjustment. (b) Height of the radar set for a maximum incidence angle. (c) Height of the radar set for a minimum incidence angle.

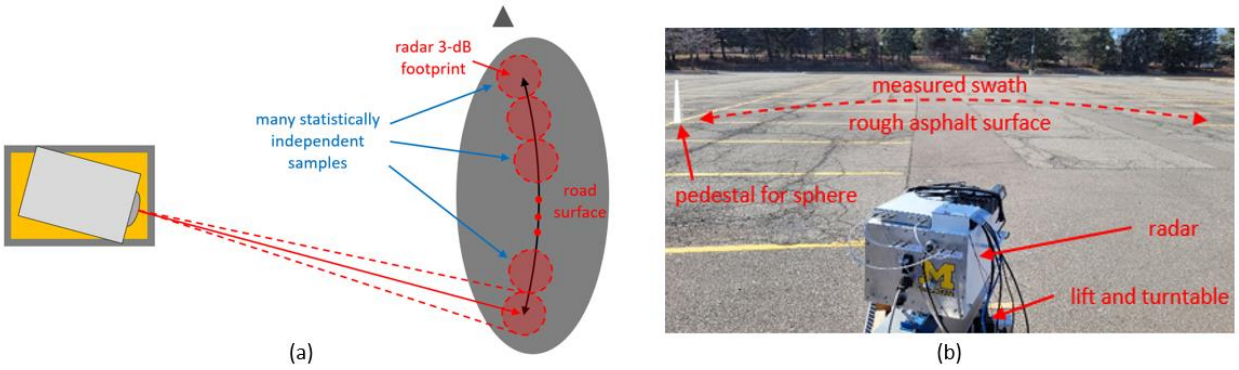

Figure 5.3. (a) Depiction of the azimuthal scan, showing positions of statistically independent samples measured. (b) Photograph of the radar during measurement of a rough asphalt surface.

Once the radar was in the proper position, the trihedral reflector was removed, and backscatter data was collected as the radar was swept in the azimuth direction using the turntable. An angular resolution of 0.5° was used to ensure that each measured spot represents an independent sample of the surface (i.e. the two-way 3-dB footprints of the radar beam do not overlap for adjacent measurements). The angular span of measurements was limited by the size of the available portion of the lot with a sufficiently flat and level surface. A minimum of 71 independent spatial samples were collected per angular sweep (35° total azimuth rotation), but some locations afforded more. A depiction of the azimuthal scan and a photograph of the radar during measurement are shown in Figure 5.3. This process was performed to measure several different surface types: smooth asphalt, smooth asphalt covered in a thin layer of water, smooth asphalt covered in a thin layer of ice, smooth asphalt covered with 5 cm of snow, rough asphalt, concrete, gravel, and gravel covered with 18 cm of snow.

For these measurements, the radar was operated in fully-polarimetric mode, and collected one block of 1000 chirps at each azimuth angle. A chirp duration of 48 μs was used, and the swept bandwidth was 1 GHz, resulting in a range resolution of 0.15 m. The sampling rate was 500 MSa/s. Each angular sweep was measured first at 230 – 231 GHz, and then in the reverse direction at 232

– 233 GHz. For post-processing calibration purposes, a metallic sphere with a radius of 1 in. was measured at both frequency bands several times during the measurement of each surface. The sphere was placed atop a Styrofoam pedestal to minimize interference from the surface or other nearby scatterers.

5.3 Calibration and Backscattering Coefficient Extraction

Figure 5.4 provides a range-domain representation of the measured backscattering from a rough asphalt surface, illustrating the type of response recorded by the radar during these measurements. An average over 1000 chirps is shown, to which a Hanning window has also been applied. This particular measurement was made at the 230 – 231 GHz band and an incidence angle of 86°. Several features of the response are of note. There is a strong peak centered at a range of about 15 m, with a width of about 5 m. This is a result of scattering from different facets of the asphalt surface within the footprint of the beam, which extends over several meters in the range direction due to the high incidence angle. Both the co- and cross-polarized responses are significant, and are about 15 dB above noise level.

The measured responses were calibrated using the isolated antenna calibration technique (IACT) [101]. The 1-inch radius metallic sphere was used as one calibration target. For the depolarizing target, one of the road surface samples with the strongest backscattering at the lowest incidence angle was selected for each surface. Using these two calibration targets, the relative levels of the VV, VH, HV, and HH responses were corrected. Measurements with the radar pointed at the sky were also collected, and used to estimate and remove background noise from the surface measurements.

To obtain absolute values of the backscattering coefficients, the received powers from the surface samples and the calibration sphere were compared through an illumination integral. This

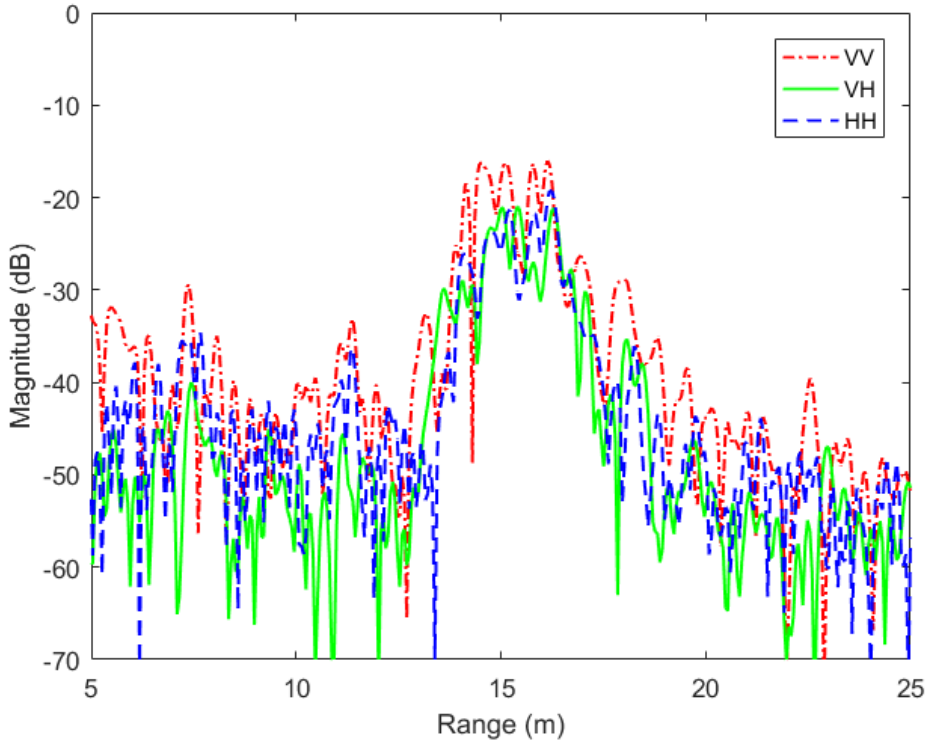

Figure 5.4. Range-domain data representing the backscattering from one sample of rough asphalt at 86° incidence for different transmit-receive polarization configurations.

process accounts for the fact that the road surface is a distributed target, so the backscattered wave from each point within the footprint corresponds to a different part of the antenna beam, and propagates through a different distance.

The bistatic radar equation for a point target such as a small sphere was given in (3.1), and is shown again here for convenience:

$$\frac{P_r^p}{P_t^q} = \frac{G_r^p G_t^q \lambda^2}{(4\pi)^3 {R_r}^2 {R_t}^2} \sigma_{pq} \, . \tag{5.1}$$

In the monostatic case with a target at distance R_0, this can be rewritten while moving the transmit power to the right side as:

$$P_r^p = P_t^q \frac{G_r^p G_t^q \lambda^2}{(4\pi)^3 {R_0}^4} \sigma_{pq} \,. \tag{5.2}$$

For a distributed target, this equation must be extended to account for the antenna radiation patterns and differing propagation distance across the footprint. The result is [72]:

$$P_r^p = \iint_A P_t^q \frac{G_r^p(\theta,\varphi) G_t^q(\theta,\varphi) \lambda^2}{(4\pi)^3 R_A(\theta,\varphi)^4} \sigma_{pq}^0 dA \,, \tag{5.3}$$

where θ and φ are spherical coordinates relative to the boresight of the radar beam, R_A is the distance to a differential element dA within footprint area A, and σ_{pq}^0 is the average pq-polarized backscattering coefficient of the distributed target.

Calibration is intended to correct for channel imbalances within the radar system, including differences in antenna gain. In effect, after calibration it may be assumed that $P_t^V = P_t^H \equiv P_t^0$, $G_r^V(0,0) = G_r^H(0,0) \equiv G_r^0$, and $G_t^V(0,0) = G_t^H(0,0) \equiv G_t^0$. Thus the co-polarized RCS of the sphere placed at the radar boresight at range R_0 may be described by:

$$P_r^{sph} = P_t^0 \frac{G_r^0 G_t^0 \lambda^2}{(4\pi)^3 {R_0}^4} \sigma_{sph} \,, \tag{5.4}$$

where the sphere RCS σ_{sph} can be calculated exactly for a given size and wavelength. The RCS of a 1-inch radius sphere at 230 GHz is -26.9 dBsm. Using $P_t^q = P_t^0$ in (5.3) and dividing by (5.4) results in:

$$\frac{P_r^p}{P_r^{sph}} = \frac{\iint_A P_t^0 \frac{G_r^p(\theta,\varphi) G_t^q(\theta,\varphi) \lambda^2}{(4\pi)^3 R_A(\theta,\varphi)^4} \sigma_{pq}^0 dA}{P_t^0 \frac{G_r^0 G_t^0 \lambda^2}{(4\pi)^3 {R_0}^4} \sigma_{sph}} \,. \tag{5.5}$$

After cancelling terms in the fraction, the backscattering coefficient can be calculated as:

$$\sigma_{pq}^{0} = \sigma_{sph} \frac{P_r^p}{P_r^{sph}} \frac{1}{I}, \tag{5.6}$$

where the illumination integral I is defined as:

$$I = \iint_A \frac{\left(G_r^p(\theta,\varphi)/G_r^0\right)\left(G_t^q(\theta,\varphi)/G_t^0\right)}{\left(R_A(\theta,\varphi)/R_0\right)^4} dA\,, \tag{5.7}$$

which can be seen to involve only the normalized radiation patterns of the transmit and receive antennas and the target range normalized to the sphere distance.

In the case of interest, the radiation patterns are those of the J-band common-aperture dual-polarized antenna system from Section 4 of Chapter 2. The patterns of both ports in both polarizations are very similar to each other, and nearly rotationally symmetric (refer to Figure 2.22). Therefore, for simplicity, a single pattern has been used here which is the average of the measured patterns. Let this pattern be denoted by $F(\theta)$, noting that dependence on φ has been removed. In this case, (5.7) can be simplified to:

$$I = \iint_A \frac{\left(F(\theta)\right)^2}{\left(R_A(\theta,\varphi)/R_0\right)^4} dA\,. \tag{5.8}$$

Using (5.6) and (5.8), the backscattering coefficient of a road surface sample can be calculated from the known sphere RCS, the known antenna radiation pattern, the measured received power from both the sphere and the surface sample, and geometric parameters associated with the radar position.

To calculate the illumination integral, it was assumed that the radar boresight was pointed at a spot on the ground 15 m away along the horizontal, consistent with the measured position of the trihedral reflector used to aim the radar. To avoid excess noise contribution, the radar footprint A was considered to be the 6-dB footprint of the antenna pattern F. This footprint was discretized in a Cartesian coordinate system, and at each point an area contribution ΔA, a range R_A, and an angle θ from boresight were calculated from the height of the antenna aperture. The measured powers were calculated by integrating the range-domain radar response of the sphere and surface samples.

At first, the backscattering coefficients were calculated as an average over the entire 6-dB antenna footprint. However, this resulted in inconsistent estimates of σ_{vh}^0 and σ_{hv}^0, which should be equal to each other due to reciprocity [72]. The footprint was therefore broken into several range bins along its length, with lengths of 0.3 m (which is approximately the width of the footprint). Then the backscattering coefficients were calculated within each of these range bins by computing a separate illumination integral and power integral for each bin. It was found that the ratio $\sigma_{vh}^0/\sigma_{hv}^0$ decreased dramatically as a function of range within the footprint. It is hypothesized that this behavior may be caused by slight misalignment of the antenna beams, or non-identical cross-polarized antenna patterns, which cannot be accounted for by calibration using a point target positioned only at boresight. Therefore, the measured backscattering coefficients presented in the following section have been taken from three range bins that are close enough to the radar boresight that the calibration may be considered valid, and the cross-polarization discrepancy is mitigated.

5.4 Measurement Results

Table 5.1 lists the types of road surfaces measured, and the number of spatial samples collected by the radar. Each point is an average over the three range bins discussed in the previous

section, which represents a total length of 0.9 m. This corresponds to six times the range resolution, so there are effectively six times as many independent samples measured. For some of the surfaces at some incidence angles, a few of the spatial samples have been discarded due to the presence of a strong scatterer such as a curb or post, which interfered with the measurement. Figures 5.5 through 5.12 display plots of the measured backscattering coefficients of each of the surfaces.

There are several additional considerations to note. For the smooth asphalt surface, the sixth incidence angle at 230 – 231 GHz is missing due to corrupted data. Similarly, for snow covered gravel, the measured area was not perfectly flat and had a large-scale undulating topography, so at the highest incidence angle the beam was shadowed at the intended range. For the rough asphalt surface, the points at around 87.5° incidence are likely incorrect because the clamps used to hold the hydraulic lift in place slipped, and radar dropped several inches during the measurement. An attempt was made to account for this by estimating and adjusting the geometric parameters in post-processing, but the exact position of the radar was not known. In some cases, such as the ice- and snow-covered asphalt, the range of the peak of the measured response may have been different than 15 m. In those cases, the actual location of the peak was used in calculating backscattering coefficients, and the incidence angle was adjusted accordingly.

Table 5.1
List of road surfaces measured and the number of spatial samples of each collected.

Surface	**Number of Samples**
Smooth Asphalt	71
Smooth Asphalt + Water	71
Smooth Asphalt + Ice	71
Smooth Asphalt + Snow (5 cm)	71
Rough Asphalt	101
Concrete	81
Gravel	91
Gravel + Snow (18 cm)	121

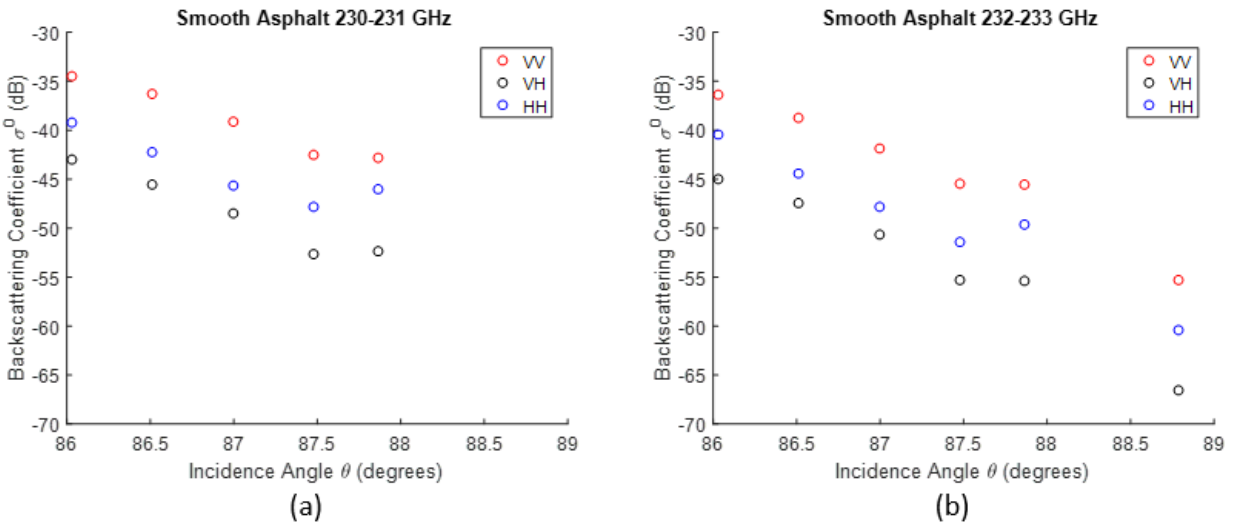

Figure 5.5. Measured backscattering coefficients of smooth asphalt at (a) 230 – 231 GHz, and (b) 232 – 233 GHz.

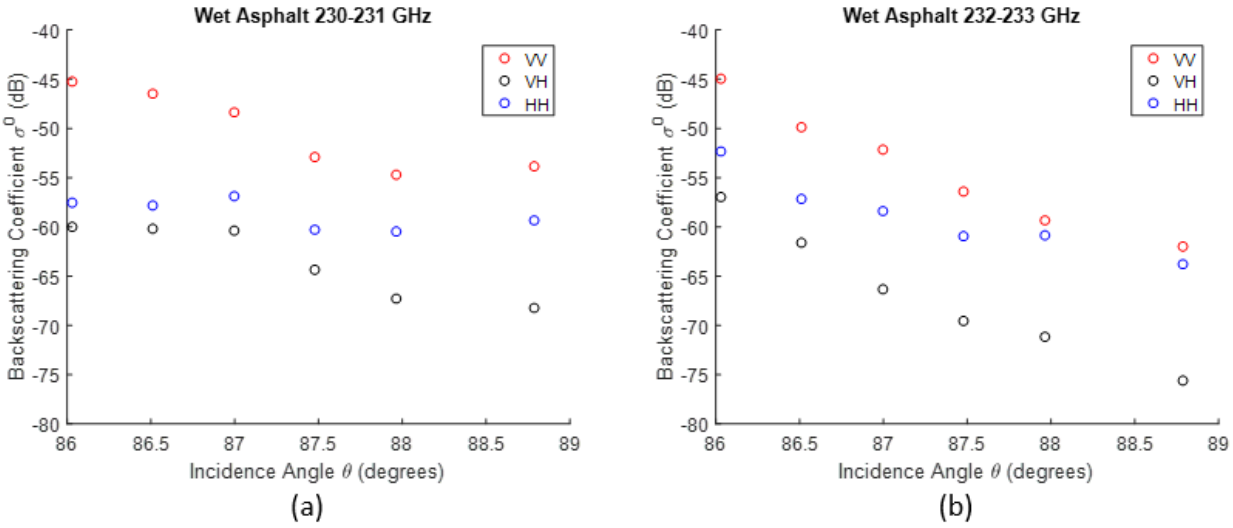

Figure 5.6. Measured backscattering coefficients of smooth asphalt covered in a thin layer of water at (a) 230 – 231 GHz, and (b) 232 – 233 GHz.

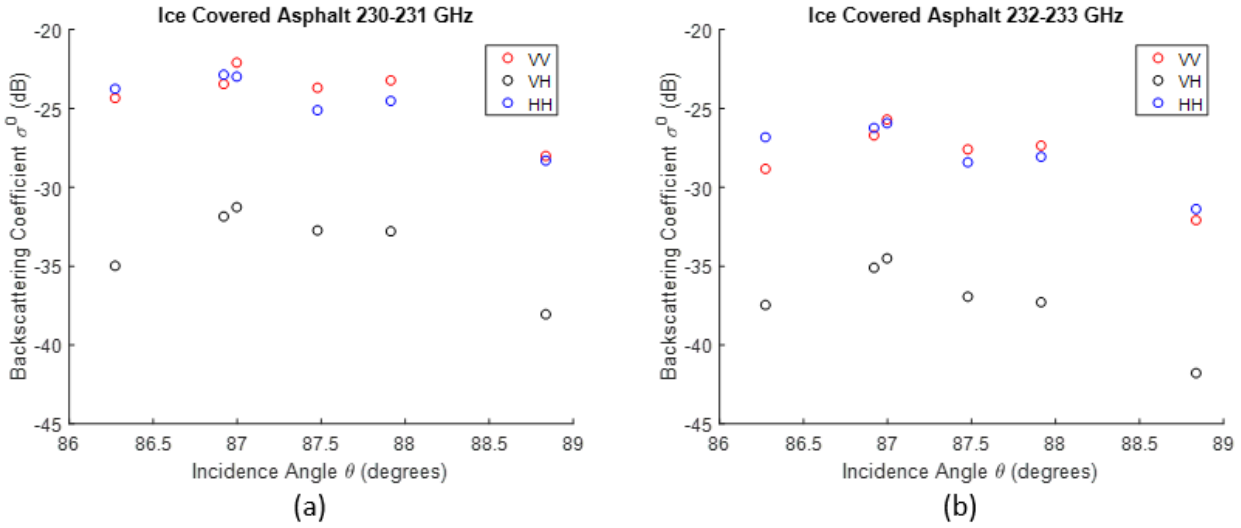

Figure 5.7. Measured backscattering coefficients of smooth asphalt covered in a layer of ice at (a) 230 – 231 GHz, and (b) 232 – 233 GHz.

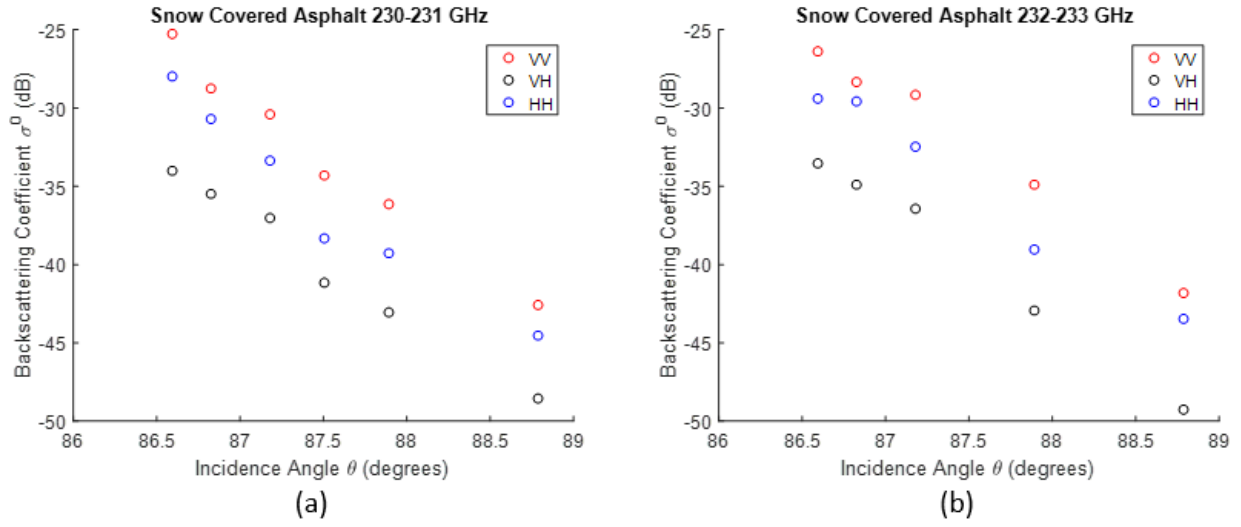

Figure 5.8. Measured backscattering coefficients of smooth asphalt covered in 5 cm of snow at (a) 230 – 231 GHz, and (b) 232 – 233 GHz.

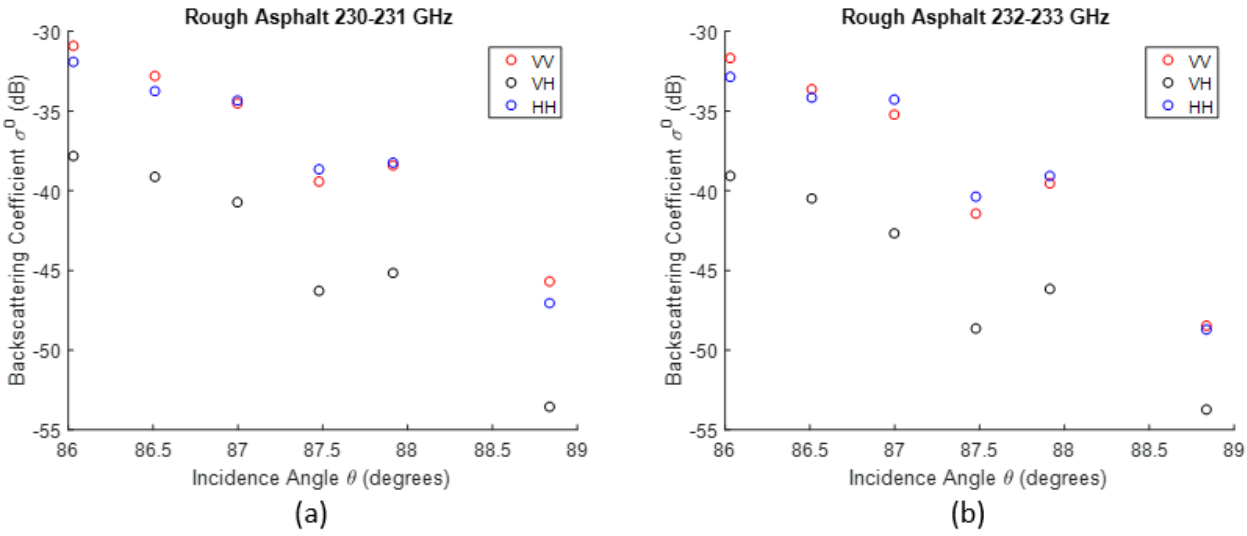

Figure 5.9. Measured backscattering coefficients of rough asphalt at (a) 230 – 231 GHz, and (b) 232 – 233 GHz.

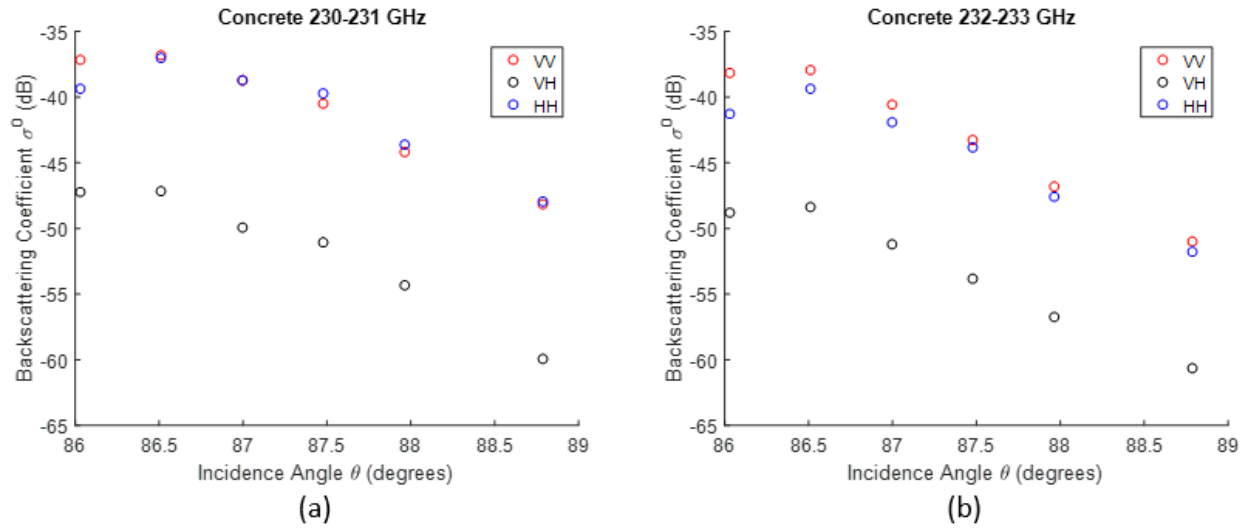

Figure 5.10. Measured backscattering coefficients of concrete at (a) 230 – 231 GHz, and (b) 232 – 233 GHz.

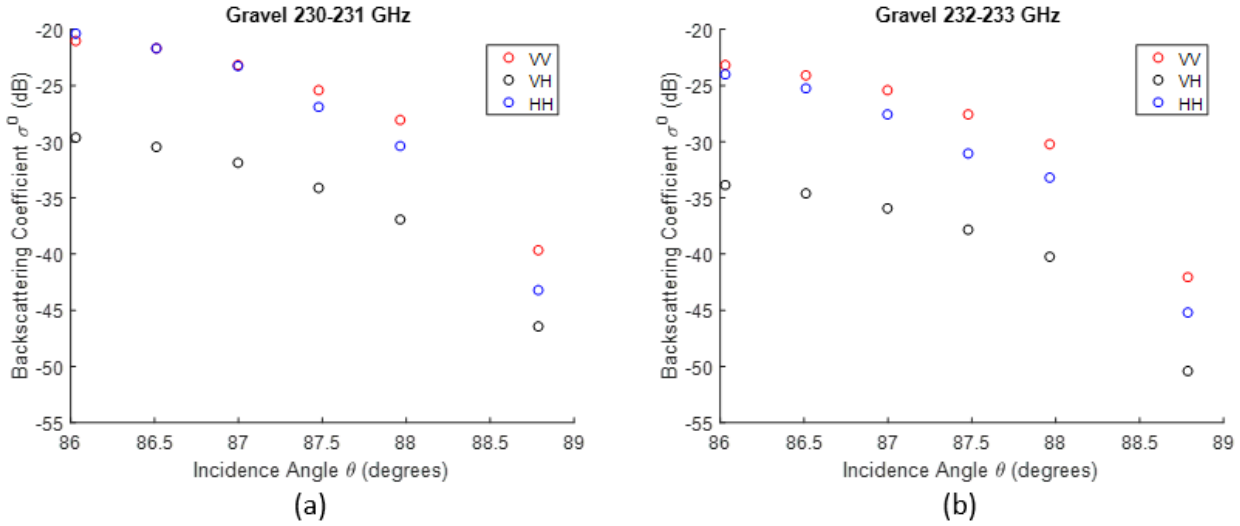

Figure 5.11. Measured backscattering coefficients of gravel at (a) 230 – 231 GHz, and (b) 232 – 233 GHz.

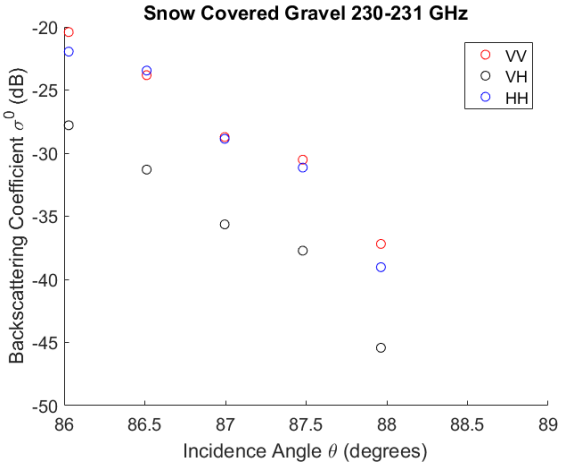

Figure 5.12. Measured backscattering coefficients of gravel covered in 18 cm of snow at 230 – 231 GHz (not measured at 232 – 233 GHz).

Some common trends are observed which are in agreement with the expectation. The backscattering coefficients tend to decrease as a function of incidence angle. The cross-polarized backscattering coefficients are usually smaller than the co-polarized ones by a factor on the order of 5 to 10 dB. VV- and HH-polarized coefficients are typically comparable, but VV is higher on average.

Figure 5.13 shows a comparison of the measured backscattering coefficients of rough asphalt, concrete, and gravel. It can be seen that backscattering strength is correlated to roughness of the surface. The gravel surface is composed of large chunks of loose rock, and is the roughest of the three. The rough asphalt is a hardened mixture of different size particles embedded in a binder, and is somewhat less rough. Concrete has the smallest particles and is quite smooth.

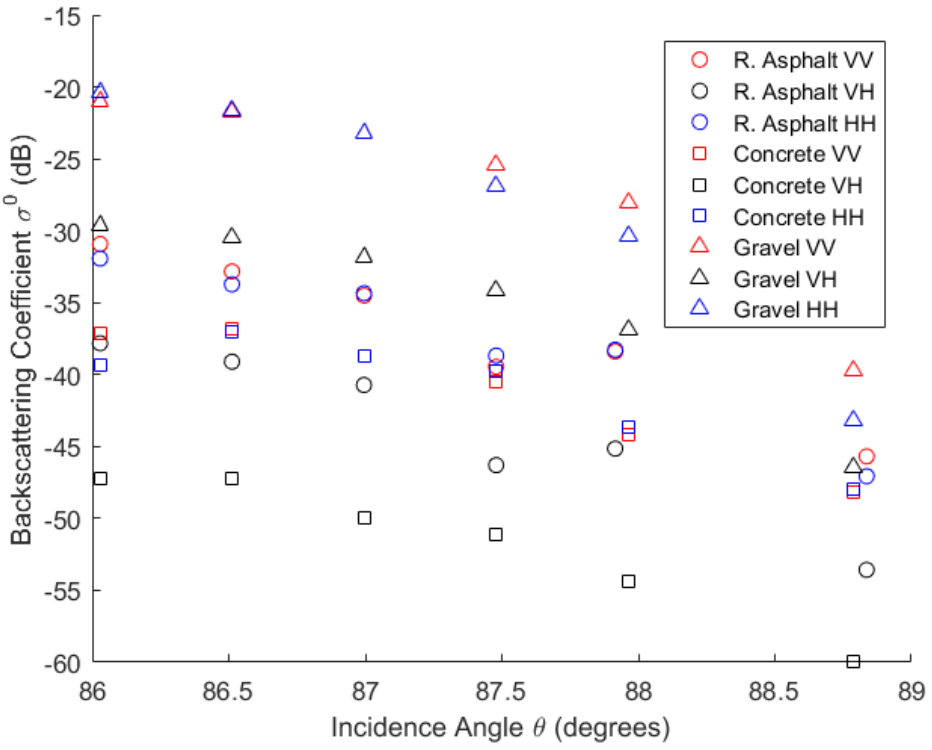

Figure 5.13. Comparison of the measured backscattering coefficients of rough asphalt, concrete, and gravel at 230 – 231 GHz.

The smooth asphalt surface with its different coverings were all measured at the same location. It was impractical to hope for a natural ice covering at the time of the measurements, but an artificial ice cover was generated by pouring ice water over the surface when the temperature was below freezing. However, the ice cubes used to cool the water more quickly produced a somewhat rough ice surface not typical of the ice that normally occurs on roadways (such as black ice). Similarly, rather than making measurements during the rain, water was poured on the asphalt to make a wet surface. Photographs of the wet and ice-covered asphalt surface are shown in Figure 5.14. Samples of the natural snow cover were collected, and the snow was determined to have a volume fraction of 23.7%. In Figure 5.15, the VV-polarized backscattering coefficients of the bare smooth asphalt surface are shown in comparison to those of the same surface with water, ice, and snow cover. It can be seen that the water cover reduces the backscattering coefficient, while the ice and snow increase it. This is likely because the water forms a very flat, smooth, high-dielectric layer over the asphalt as it flows in response to gravity, so most of the scattering occurs in the specular direction. By contrast, there is strong backscattering from the rough ice surface, and due to volume scattering within the snow.

Figure 5.14. Photos of the smooth asphalt surface covered artificially by water and ice.

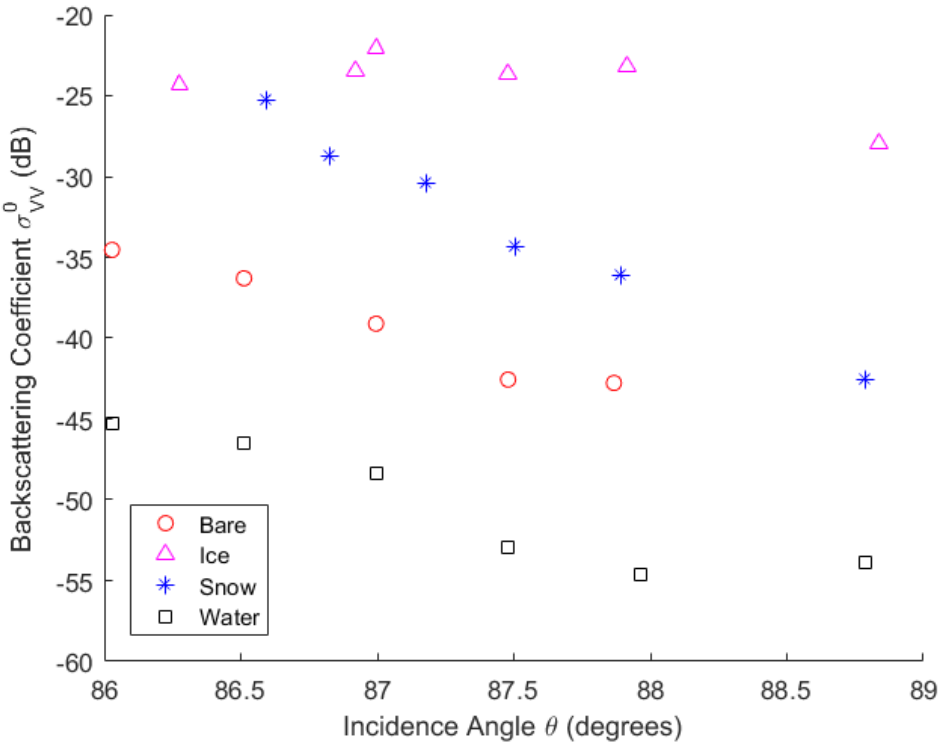

Figure 5.15. Comparison of the measured VV-polarized backscattering coefficients of smooth asphalt when bare and when covered by water, ice, or snow at 230 – 231 GHz.

Figure 5.16 shows a comparison of the backscattering coefficients of the smooth asphalt and gravel surfaces, as well as both surfaces when covered by snow. Snow samples were collected during the gravel measurement, and the snow was determined to have a volume fraction of 18.2%, which is slightly less dense than the snow from the asphalt. The similarity between backscattering coefficients of the two snow-covered surfaces, despite the very significant difference between those of the underlying surfaces themselves, may indicated that backscattering is dominated by volume scattering from the snow. The snow-covered gravel appears to have slightly stronger backscattering than the snow-covered asphalt. This may be due to a contribution from the gravel, or to differences in the snow properties, such as volume fraction or particle size (which was not measured).

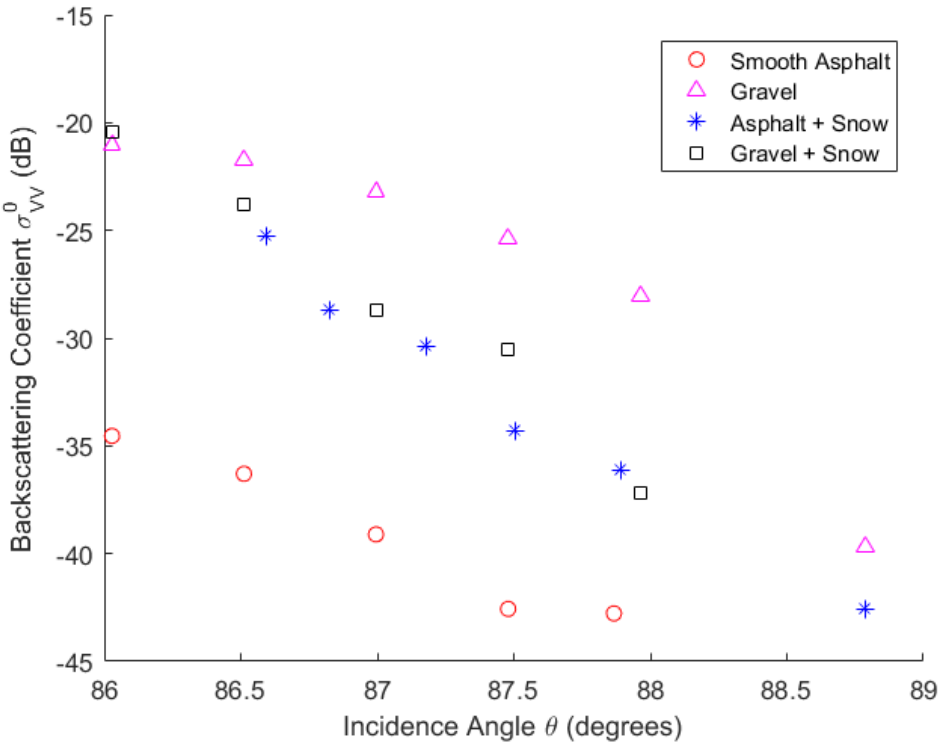

Figure 5.16. Comparison of the measured VV-polarized backscattering coefficients of smooth asphalt, gravel, and both surfaces covered by snow at 230 – 231 GHz.

5.5 Summary

This chapter has presented a set of measurements of the polarimetric backscattering coefficients of several types of road surfaces, including some with cover by water, snow, and ice, at near grazing incidence. These measurements contribute to a currently very limited database, which it is hoped will eventually be expanded and used in algorithms for surface identification and condition assessment by 230 GHz automotive radar in ADAS and autonomous vehicle applications.

The measurements also showcase the capabilities of the GM J-band radar, which utilizes the antenna system and OMTs from previous chapters in the front end. It is challenging to measure

backscattering coefficients of these surfaces at such a high incidence angle. The high gain, high isolation, and beam alignment of the antenna system contribute significantly to the sensitivity of the radar to the small backscattering from these distributed targets.

Backscattering coefficients are measured to be in the range of -20 dB to -60 dB, depending on surface roughness, polarization, and incidence angle. Generally backscattering decreases with increasing incidence angle, and co-polarized backscattering is stronger than cross-polarized backscattering. Additionally, rougher surfaces are found to scatter more strongly than smoother ones, and cover by precipitation is found to significantly impact the backscattering behavior as well.

CHAPTER 6

Low-Profile Passive Reflector for Radar Detection of Road Markings

Automotive radars constitute an important class of sensors in ADAS and autonomous vehicle technology. Recall from Chapter 1 (Table 1.1, in particular) that they are the primary sensor system for several familiar ADAS features such as Blind Spot Detection and Adaptive Cruise Control [18]. While radar sensors offer a number of benefits including precise range and velocity measurement and polarimetric capability, there are applications to which radar is not well suited. For example, cameras are much better at distinguishing target properties such as color and texture [23], making them the sensors of choice for ADAS technologies such as Traffic Sign Recognition, Lane Departure Warning, and Autonomous Parking [18].

Unfortunately, optical imaging instruments such as cameras and lidar suffer performance degradation in poor visibility conditions caused by inclement weather [23]. On the other hand, since attenuation due to atmospheric gas constituents, rain, and fog is relatively small at millimeter-wave frequencies (refer to Figure 1.2), radar is able to operate consistently in any weather condition [24].

ADAS technologies at Level 3 and above (see Figure 1.1) must incorporate multiple sensor modes for both data diversity and robustness. Since cameras and radar have different sets of strengths and weaknesses, they can in many cases supplement each other to provide a more complete picture of the surrounding environment. Additionally, having multiple sensors provides a contingency in the event of the failure of one system, or in adverse conditions that inhibit

reliability. For this reason, it is desired for radar to support the functionality of Traffic Sign Recognition and Lane Departure Warning, tasks typically handled exclusively by camera sensors. Currently road markings and signs are identifiable primarily by color, and there is no mechanism by which radar can accurately detect and discriminate between them.

In this chapter, a design for a low-profile passive radar reflector is presented, which can be embedded in the asphalt or paint of a road surface. This will provide a means for the detection by radar of road markings such as lane dividers, stop lines, pedestrian crossings, etc., enabling all-weather operation of some of the aforementioned ADAS that traditionally rely on cameras, as well as offering robustness in more typical conditions. Discrimination between different types of markings can be achieved through various encodings in the spatial arrangement of reflectors. Thus radar's poor applicability in these tasks can be solved by the presence of infrastructure to allow it to function in this manner.

The concept of dedicating roadway infrastructure to enable ADAS functionality has been around for several decades. For example, as part of the "Automated Highway System" experiments in Japan during the 1990s [26], [102], a Lane Centering system was proposed which involved using magnetic sensors in the car's bumper to detect permanent magnets embedded in the pavement [102], [103]. However, the detection range of the magnets is quite short (less than 1 m), and the placement of such a large quantity of magnets would be expensive and impractical. More recently, some investigations of similar systems based on radar reflectors have been performed. The reflector requirements for such a system have been studied in [104], in which a design based on a flattened trihedral corner reflector was proposed. This reflector is still quite bulky, and requires a minimum height of 4 mm. Therefore, it needs to be embedded into the asphalt itself in order to avoid protruding upward and damaging the tires of passing vehicles.

The reflector presented here is designed specifically with the goal of having an extremely low profile so that it can be positioned on top of the asphalt and covered by a layer of paint. It has been designed to operate at a center frequency of 79 GHz, consistent with the modern automotive radar band. It also has a height above ground of only 0.26 mm or less, significantly thinner than the reflectors considered in [104]. While fabrication of proof-of-concept prototypes has been fairly costly, the fabrication methods utilized are amenable to cheap mass production once the process has been established, which will make distribution across highways feasible.

6.1 Reflector Design

In this section, a very low-profile reflective target is presented, which is inspired by vertically polarized low-profile antennas [105], [106] that when placed over ground, can respond to a vertically polarized incident wave. Usually a low-profile object placed on a ground plane presents a very poor RCS to a horizontally polarized incident wave. This is mainly due to the fact that the target response from the incident wave and that from the ground reflection cancel each other. Also, low-profile objects (height much smaller than the wavelength) do not interact with vertically polarized waves significantly. The reflector presented here consists of an array of several low-profile resonant radiating elements designed to re-radiate when illuminated by a vertically polarized incident wave. This target can produce significant return for a forward-looking automotive radar directed at the road ahead of the vehicle. An illustration of the reflector configuration is shown in Figure 6.1.

For the individual radiating element, a low-profile resonant structure inspired by a folded dipole antenna [107] is achieved by using a transmission line to connect the tops of two short monopoles, which extend a height H upward from a ground plane. This results in a staple-like geometry. The length L of the transmission line is chosen to be about half a wavelength, such that

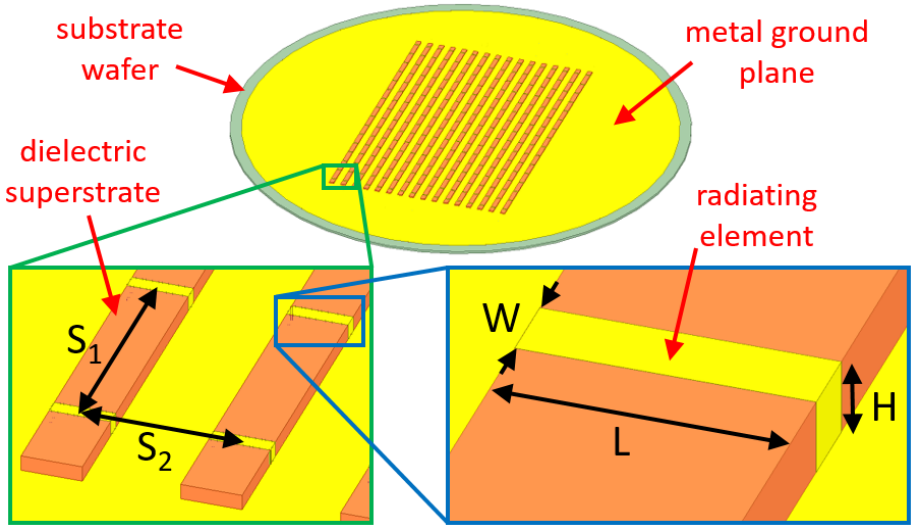

Figure 6.1. Illustration of the reflector design geometry. Zoomed-in views show geometric parameters of the radiating elements and array spacing.

when illuminated by a vertically-polarized plane wave at a high angle of incidence, the currents excited on the vertical segments are in the same direction, and a resonance of the current along the horizontal segment is induced. The resonant condition excites significant currents on the vertical pins. Applying the image theory, the radiation from the vertical currents is enhanced, while that from the horizontal currents nearly cancels. In effect, this produces a radiation pattern similar to that of a two-element broadside dipole array. The structure can produce quite strong backscattering despite having a height only a small fraction of the wavelength. This principle of operation is depicted in Figure 6.2. A similar approach was recently used in [107] to design a novel hexagonal bridge antenna for compact vertically polarized endfire arrays in 5G smartphone applications.

The entire reflector is constructed by placing many instances of this radiating element in a two-dimensional array. For enhanced radiation in the backscatter direction, the element spacing along the incidence direction, S_1, should be a multiple of a half wavelength. There was found through simulation to be a significant shadowing effect on the illumination of elements positioned

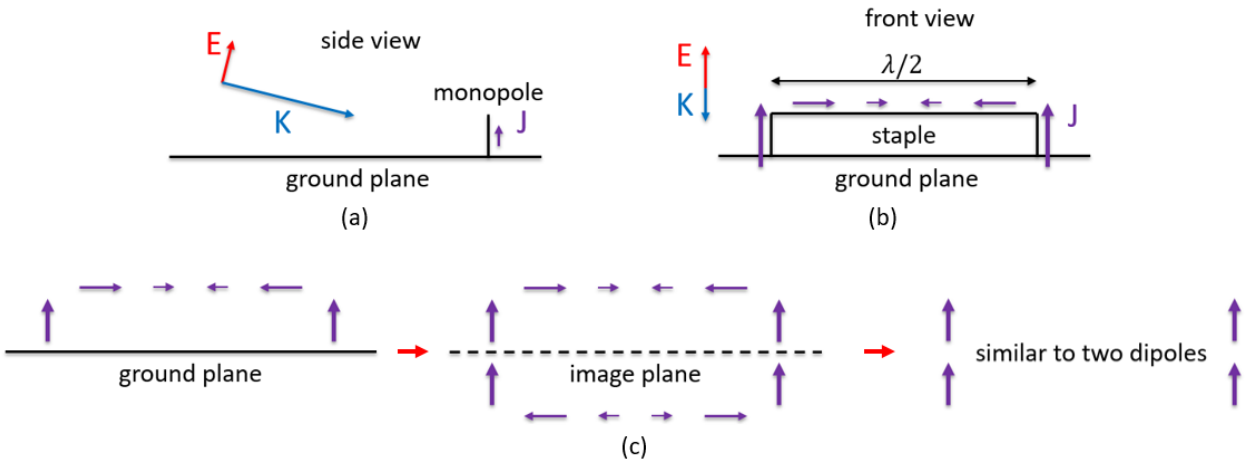

Figure 6.2. The principle of operation of the low-profile staple-like radiating element is shown. (a) A vertically polarized incident plane wave will excite a non-resonant current on a short monopole. (b) If two short monopoles are connected across their tops by a half-wave transmission line, a resonance is excited, producing strong in-phase vertical currents on the monopoles. (c) Using image theory, the resulting re-radiation has a pattern similar to an array of two dipoles.

behind others, and a spacing of a full wavelength was found to improve performance for a given number of array elements. Spacing in the perpendicular direction, S_2, was chosen to be approximately a half wavelength. This parameter was found to have a negligible impact on the simulated peak RCS, but is related to the reflector's RCS beamwidth in the azimuth direction.

6.2 Fabrication Process

Initial simulations were performed using a PEC ground plane and thin PEC wires suspended in free space to form the staple radiating element. These simulations were performed using the integral equations (IE) method, which allowed for quick verification of the operating principle. However, before completing a more in-depth simulation study, a suitable fabrication process needed to be identified to create the tiny suspended metallic features. The proposed process for a proof-of-concept prototype is described here.

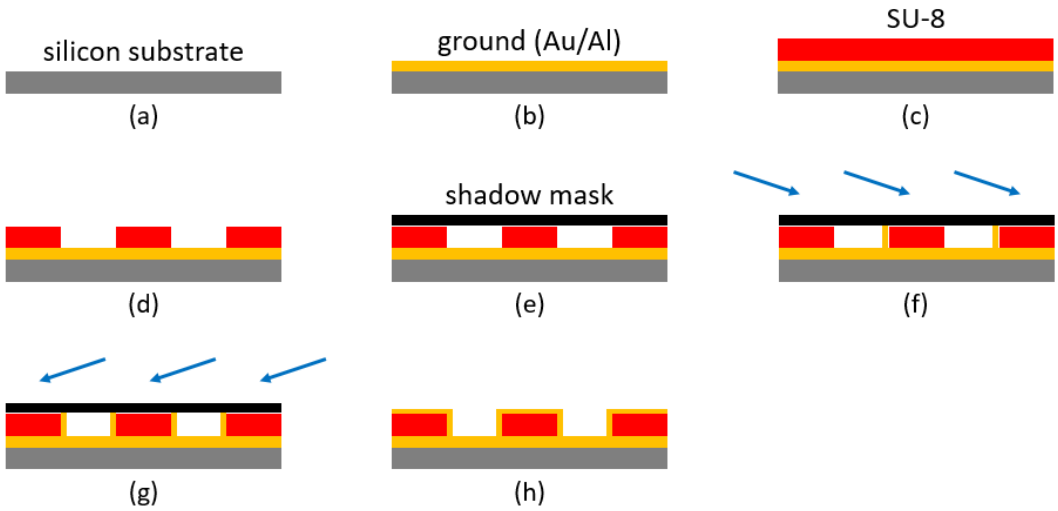

Figure 6.3. Illustration of proposed reflector fabrication process: (a) start with silicon wafer, (b) electron-beam evaporation of metallic ground plane, (c) spin SU-8 photoresist, (d) bake, expose, and develop SU-8 pattern, (e) place shadow mask on top of SU-8, (f) angled evaporation through shadow mask for sidewall coverage, (g) second angle for other sidewall, (h) remove shadow mask, leaving finished reflector.

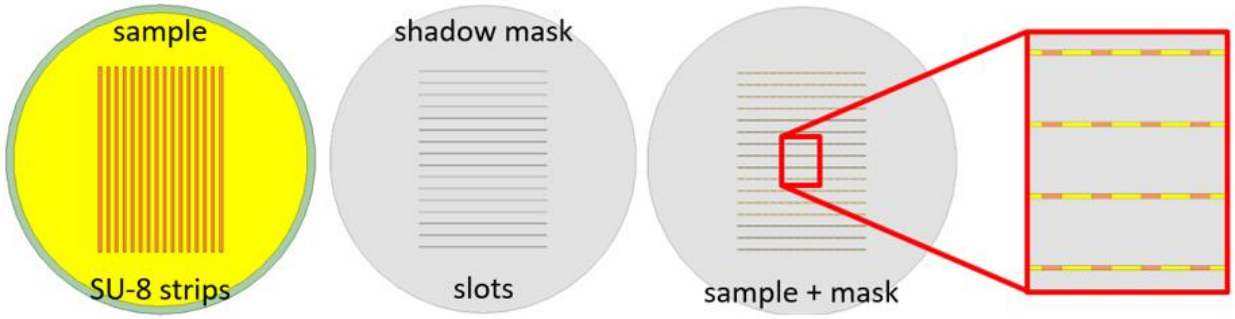

Figure 6.4. Top view of the positioning of the shadow mask with respect to the sample for deposition of the radiating elements.

The general fabrication approach focuses on using SU-8 photoresist, a very viscous resist that can be spun in thicker layers than most others, and is more difficult to remove from most substrates once cured. The design is implemented using a silicon wafer as a substrate so that standard semiconductor processes can be utilized, though it is envisioned that eventually a more durable and flexible substrate will be needed. First, a metallic ground plane is deposited onto the

wafer using electron beam evaporation. Then SU-8 photoresist is spun and patterned above the ground plane to form a dielectric superstrate. The radiating elements are then deposited over the superstrate, again with evaporation. The process is depicted in Figures 6.3 and 6.4.

The first metal experimented with was gold, due to its high conductivity and low reactivity. A thin 10 nm film of chromium is first deposited as an adhesion layer, followed by a thick 1 μm layer of gold. However, it was found that the SU-8 naturally has poor adhesion to gold. Aluminum and titanium were then tested. Both metals adhere well to silicon during evaporation, so an adhesion layer is not required. Additionally, as non-precious metals, the cost is much less than gold. However, both metals oxidize when exposed to air. SU-8 was found to have much stronger adhesion to both. Going forward, aluminum was chosen as the primary ground plane material due to higher conductivity and a more reliable deposition recipe (thick titanium depositions were found to fail on occasion due to film stress, and the deposition chamber often heated up to undesirable temperatures). Unfortunately, the SU-8 still often exhibited poor adhesion, and in particular decreasing adhesion over time after patterning. It was found that using OmniCoat as an adhesion promoter and skipping the optional post-development hard bake step improve the likelihood of successful patterning. Using this method, and after experimental tuning of exposure and baking parameters, SU-8 has been patterned up to approximately 260 μm thick.

The radiating elements need to be deposited onto the wafer in such a way that they adhere to the top and sides of the SU-8 superstrate strips, as well as form an electrical connection with the ground plane. Typically, such sidewall coverage is achieved using sputtering. However, since substrate heating and bombardment are not desired, evaporation is used instead. Evaporation is a line-of-sight deposition process, so to accomplish sidewall coverage, a set of fixtures was machined to support the wafer at an angle in the evaporation chamber. The first fixture was

designed to hold the wafer at approximately a 30° angle. Two successive evaporation steps with the wafer angled at ±30° allow for coverage of both sidewalls.

Since it is not possible to directly pattern the wafer over top of the thick SU-8 with another photoresist, evaporation is performed through a shadow mask, which is a separate piece that rests atop the SU-8 with slots perpendicular to the SU-8 strips corresponding to the locations of the radiating elements (refer to Figure 6.4). The first shadow mask was fabricated using DRIE to etch completely through another silicon wafer. Later, steel solder stencils were purchased as masks, which are cheaper and less likely to crack. The masks are aligned visually with the sample, and held in place using vacuum-compatible tape. Although the design is not very sensitive to alignment, the visual alignment method was found repeatedly to be accurate within 100 μm.

Another significant fabrication challenge has been ensuring electrical connection along the entire length of the radiating element to ground. Many of the first prototypes were found to exhibit a gap in the metal on the SU-8 sidewalls, resulting from shadowing due to a severely concave wall profile. An illustration of the shadowing behavior is shown in Figure 6.5. This issue has been alleviated by two process adjustments. First, the use of an ultraviolet filter during the exposure process has been found to help produce more vertical sidewalls. Second, a new fixture supporting the wafer at a 70° angle was constructed to minimize the possibility of shadowing. These changes have allowed for metal depositions that visually appear to be completely connected from ground, up the sidewalls, and across the top of the SU-8 strip. Even so, it has remained difficult to achieve electrical connectivity because the aluminum and titanium films deposited on top of the SU-8 through the shadow mask have been found to be highly resistive. Though extensive experimentation has been performed, a physical explanation for this observed behavior can still not be determined. However, when a chrome/gold stack is used to deposit the radiating elements,

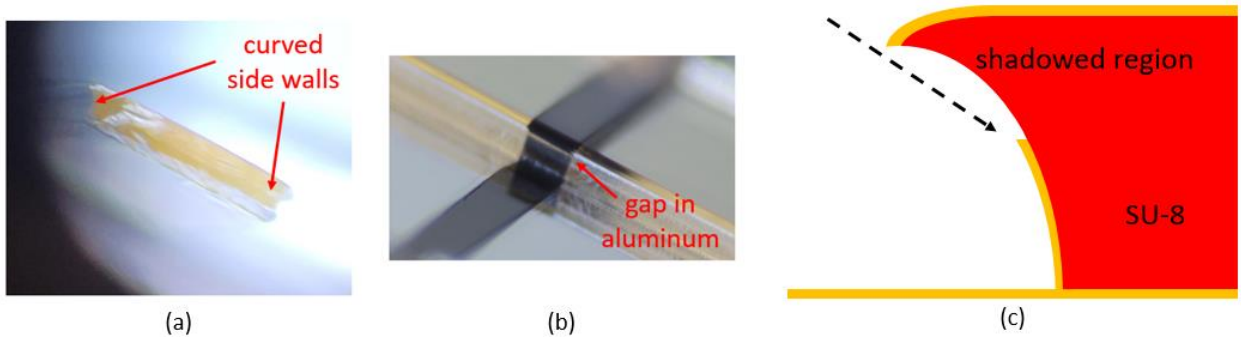

Figure 6.5. A concave sidewall profile of the SU-8 can produce a shadowing effect that prevents an electrical connection in the radiating element. (a) Microscope image of an SU-8 strip cross-section, showing curved sidewalls. (b) Microscope image of a radiating element with a gap due to shadowing. (c) Illustration of the shadowing mechanism.

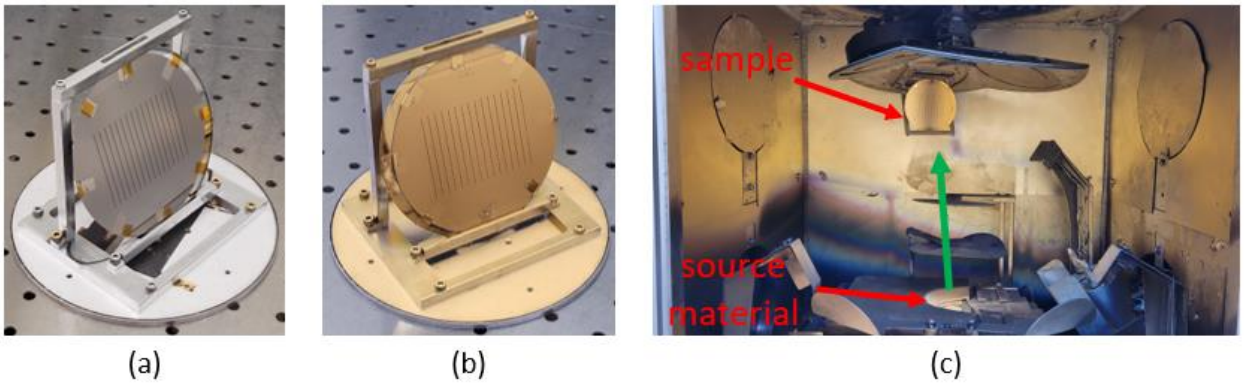

Figure 6.6. Photographs of the sample and shadow mask held in the 70° fixture. (a) Before gold deposition. (b) After gold deposition. (c) Suspended inside the evaporator vacuum chamber.

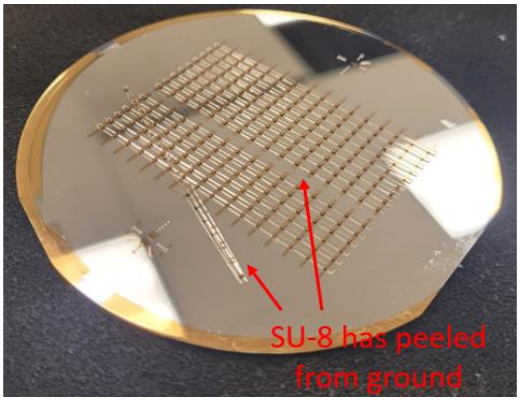

Figure 6.7. One SU-8 strip can be seen to have peeled off from the ground plane of the prototype due to decreasing adhesion over time.

good conductivity is observed, and an electrical connection can be measured using direct current (DC) probe stations. Photographs of a sample with the shadow mask attached, held in the 70° angle fixture, as well as the positioning within the evaporation chamber, are shown in Figure 6.6.

The remaining problem to be solved is the long term adhesion of the SU-8 strips, since after deposition of the radiating elements, the strips still tend to peel off over time and result in electrical disconnection. So far, the best prototype that has been produced has had good connection of roughly half of the radiating elements at the time of fabrication completion. Even for that prototype, over time the SU-8 lost its adhesion, and strips began to peel off as shown in Figure 6.7.

Abdelhamid Nasr and Dr. Adib Nashashibi are recognized and thanked for their assistance with SU-8 processing, and the machining of the angle fixtures, respectively.

6.3 Simulation Results

After some initial tests of the SU-8 fabrication process, simulations were performed to optimize the design parameters of the reflector. Ansys HFSS was used to compute the monostatic RCS of individual radiating elements, as well as arrays of various sizes. While the IE method was utilized for early models consisting of only PEC elements, FEM was used for final design optimization of the new models including the silicon substrate and SU-8 superstrates. The optimized parameters were used to produce the SU-8 photomask and shadow mask, which were then used in the remaining fabrication steps described in the previous section.

The SU-8 is modeled as a dielectric with $\varepsilon_r = 3.0$ and $tan\delta = 0.04$ [108]. The height and width of the radiating elements were found to have only a small impact on the RCS, so long as the height and length are optimized together to ensure a resonant response. The thickness of the SU-8 superstrates was chosen as an estimate of the thickest possible layer to spin with SU-8 2100 at a standard spin speed ($H = 260\ \mu m$). The width was chosen to be $W = 250\ \mu m$ to provide a

suitably large opening in the silicon shadow mask without the wafer breaking during the etch process. The length of the radiating element was then optimized to maximize the RCS at a center frequency of 79 GHz and incidence angle of 85°. A 4 by 4 array was then constructed, and the element spacing in the two directions was optimized for maximum RCS. The optimized parameter values are $L = 1000\ \mu m$, $S_1 = 3800\ \mu m$, and $S_2 = 2600\ \mu m$. A 16 by 16 array was simulated as the complete design, but this was too large for optimization.

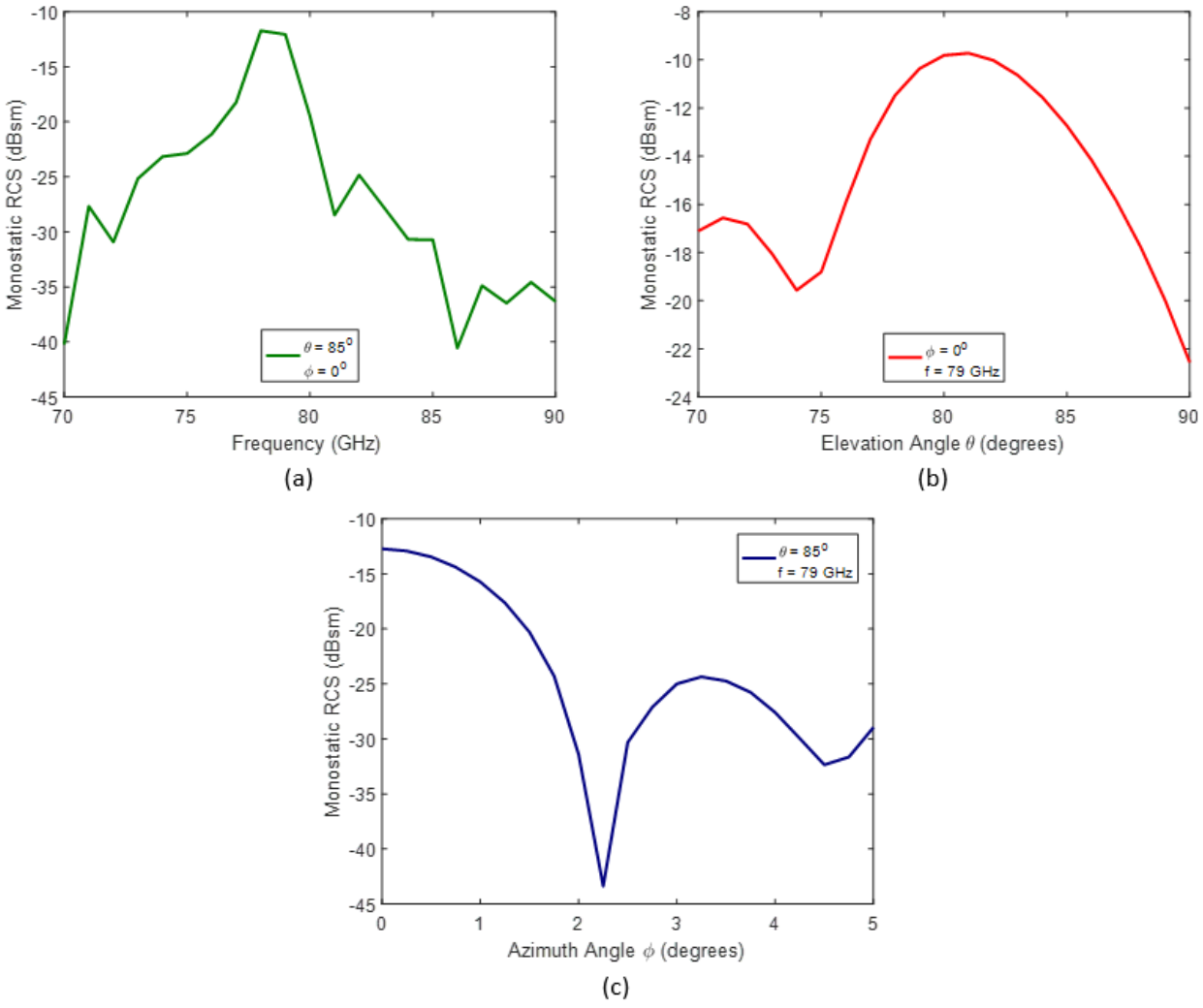

Figure 6.8. Simulated monostatic RCS of the 16 by 16 array reflector: (a) as a function of frequency, (b) as a function of incident elevation angle, and (c) as a function of incident azimuth angle.

Plots of the RCS as a function of frequency and incidence angle are shown in Figure 6.8. The center frequency is 79 GHz. At an incidence angle of 85° in the elevation direction, the reflector exhibits an RCS of -12.7 dBsm with a beamwidth of 2° in the azimuth plane.

The incidence angle of 85° was chosen as a design goal because it corresponds to a range of about 10 m assuming the radar is positioned roughly 1 m from the ground (behind the vehicle's side mirrors, for example). The RCS remains above -15 dBsm from 77° to 86°. It is estimated in [104] that the required RCS for effective detection of such a reflector at this range is approximately -20 dBsm, with larger RCS being needed at longer range. The simulated results are well within this criterion.

6.4 Printed Circuit Board Design

A fabrication solution using printed circuit board (PCB) technology was not initially considered due to the small size of the radiating elements. Most of the feature dimensions are larger than the established minimums, but could be impacted by the relevant tolerances. However, given the fabrication challenges described in Section 6.2, this option was reconsidered as an alternative. Given the irregular shapes of the SU-8 sidewalls and non-uniform thickness of the SU-8 layer across the wafer, the PCB tolerances may be acceptable. Potential benefits of the PCB process include improved durability and flexibility compared to the SU-8 process.

Using the SU-8 design as a starting point, the reflector design was modified to use a PCB fabrication process. Here the ground plane is placed on one side of the substrate, while the transmission lines are placed on the other. The vertical radiating pins are implemented as through vias, connecting the two sides of the board. The new geometry is shown in Figure 6.9. A low-loss microwave substrate, Rogers RO4003C ($\varepsilon_r = 3.55$ at up to 40 GHz and $tan\delta = 0.0027$ at 10 GHz), was selected for its availability at PCB vendors and its dielectric constant similar to SU-8.

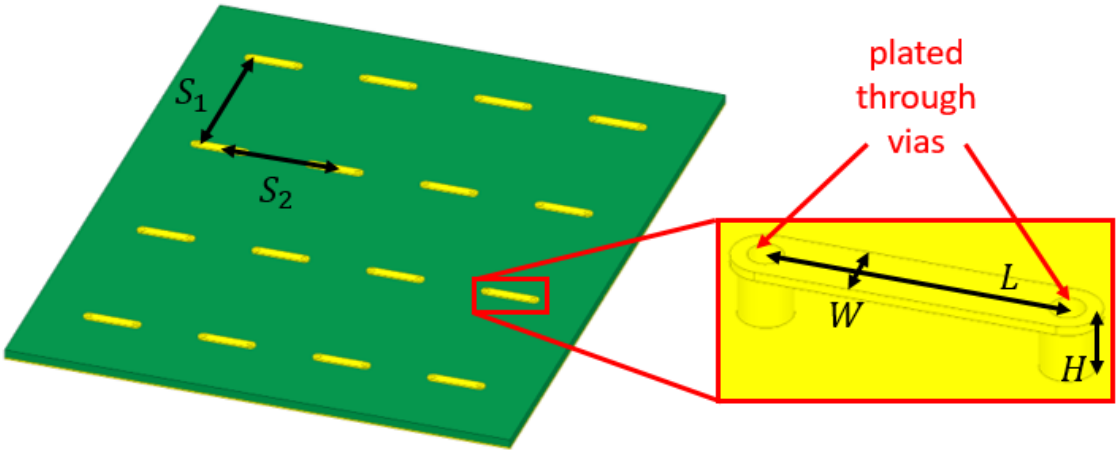

Figure 6.9. Geometry of the PCB implementation of the reflector. The radiating elements are formed by connecting microstrip transmission lines on the top layer to the ground plane on the bottom layer with plated through vias.

Table 6.1
Comparison of geometric parameters of SU-8 and PCB reflector designs.

Design	***L* (μm)**	***W* (μm)**	***H* (μm)**	**S_1 (μm)**	**S_2 (μm)**	**D_{via} (μm)**
SU-8	1000	250	260	3800	2600	–
PCB	1100	250	203	3800	2600	200

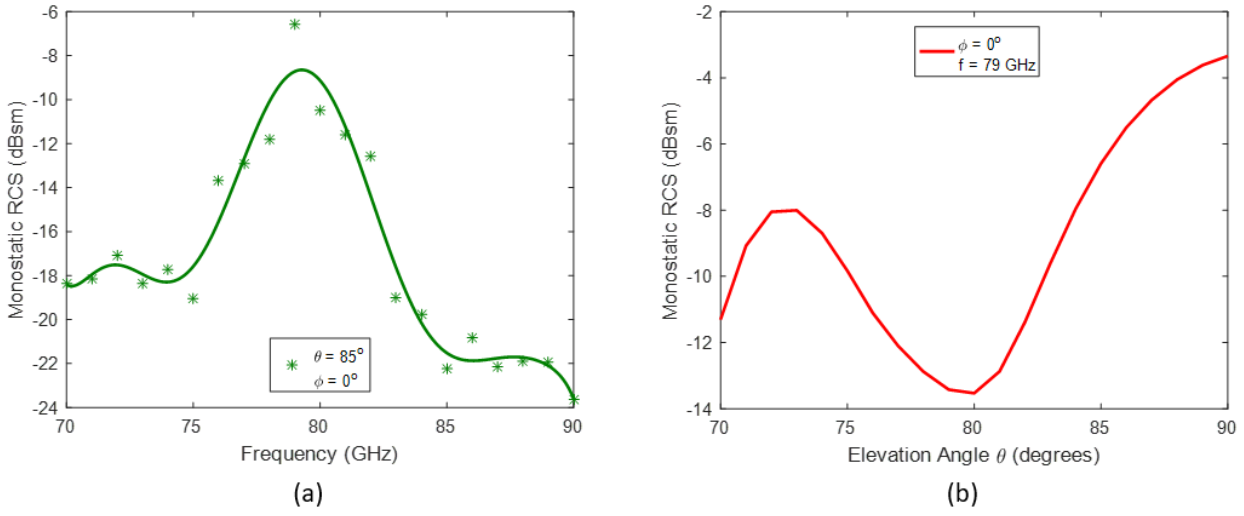

Figure 6.10. Simulated monostatic RCS of the 16 by 16 array PCB reflector: (a) as a function of frequency and (b) as a function of incident elevation angle.

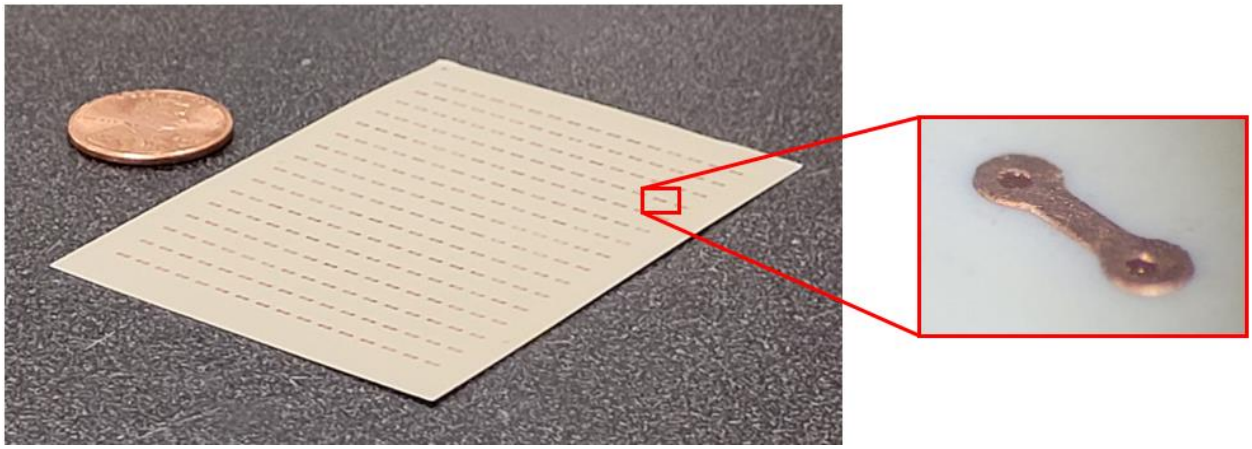

Figure 6.11. Photograph of the PCB reflector prototype next to a penny for size comparison.

The substrate thickness and via diameter were chosen to be 203 µm and 200 µm, respectively, based on the minimum vendor specifications. The width of the radiating element was left unchanged at 250 µm, as it was larger than the minimum line specification.

Once again, simulations were used to optimize the length of the radiating element and the array spacing. The spacing in both directions was found to be the same as in the previous design, while the length needed to be updated to 1100 µm. A comparison of the geometric parameters of the two reflector designs is shown in Table 6.1. The simulated performance of the 16 by 16 array PCB reflector is shown in Figure 6.10, and an RCS of -6.6 dBsm is achieved at 85° incidence.

The PCB reflector was fabricated by PCBWay. To take advantage of reduced per-unit cost, ten reflector variations were made with slightly different parameters. This was intended to help counteract any detuning due to fabrication error or dielectric constant uncertainty. A photograph of one of the reflectors is shown in comparison to a penny in Figure 6.11. The tiny radiating elements and the very thin substrate are of particular note. The vendor changed the transmission line width from 250 µm to 293 µm, and added enlarged circular pads around the vias with a diameter of 550 µm. These changes are reflected in the simulated results shown in the next section.

6.5 Measurement Results

To measure the RCS of the SU-8 reflectors, a simple network-analyzer-based radar system operating at 77 – 81 GHz was used. For initial tests to determine whether or not reflectors were working, they were placed on a Styrofoam pedestal just in the far field of the radar with a block of absorbing material behind. The backscattering was viewed using a time-domain transform to determine the peak response associated with the intended target. The RCS of the reflectors were calculated by comparison to a metallic sphere with a known diameter. The SU-8 reflector prototypes were placed atop the pedestal at a 5° angle with respect to the horizontal, to emulate an 85° incidence angle. The measurement setup is depicted in Figure 6.12.

For appropriate range resolution, a network analyzer bandwidth of 1 GHz was used. Since the simulation results indicate a strongly frequency-dependent reflector RCS, the start and stop frequencies of the sweep were adjusted to tune the band and maximize the received power relative to the sphere. The measured RCS of several targets of interest are shown in Table 6.2, including a few iterations of prototypes of the SU-8 reflector. These measurements were made at a center frequency of 77 GHz, indicating a slight shift from the design frequency. These reflectors did not function as well as was hoped, so at this stage no attempt was made to measure the RCS pattern as a function of elevation or azimuth angle (although the reflectors were adjusted in azimuth to maximize return strength).

At the time of the fabrication completion of the PCB reflectors, the GM E-band radar had conveniently been returned for repairs, and was therefore available for measurement of the PCB reflector RCS. Measurements were made using 1 GHz of bandwidth, and the center frequency was adjusted from 77 GHz to 81.5 GHz in increments of 0.5 GHz. Additionally, a small actuator with elevation and azimuth angle control was used to adjust the orientation of the reflector. Similar to

the SU-8 reflector measurement setup, a Styrofoam pedestal was placed on top of the actuator for the reflectors to rest on, absorbers were placed behind the pedestal, and a metallic sphere was used as a reference RCS. Photos of this setup are shown in Figure 6.13.

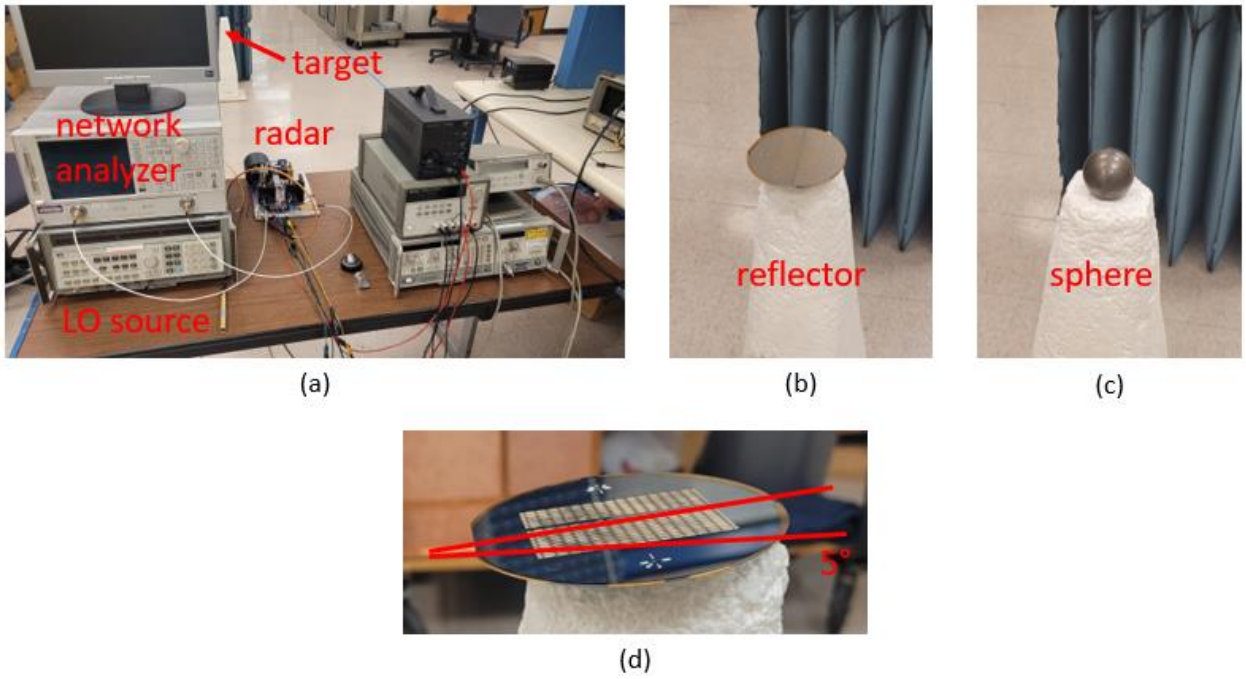

Figure 6.12. SU-8 reflector RCS measurement setup: (a) The network analyzer and local oscillator source used to drive the radar, (b) a reflector mounted on the Styrofoam pedestal, (c) a metallic sphere mounted on the pedestal, and (d) view showing the 5° angle of the reflector.

Table 6.2
Measured RCS of several targets of interest, including some of the SU-8 reflector prototypes.

Target	RCS (dBsm)
Sphere (1.75 in. diameter)	-28.1
Empty Pedestal	-51.3
Metalized Wafer	-46.5
Metalized Wafer with SU-8	-41.5
SU-8 Reflector 1	-37.8
SU-8 Reflector 2	-46.3
SU-8 Reflector 3	-26.7
SU-8 Reflector 4	-20.1

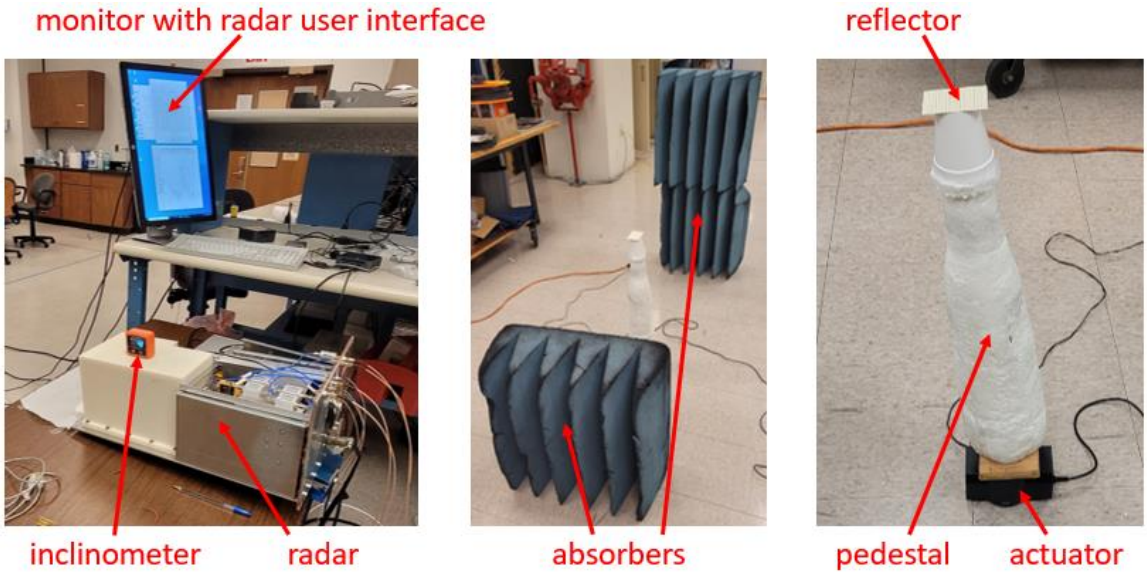

Figure 6.13. PCB reflector RCS measurement setup.

As the incidence angle decreases, the array spacing along the incidence direction is reduced, leading to a resonant response at higher frequency. To capture this behavior, each reflector was oriented to maximize the RCS at each measurement frequency, and the angle at maximum was measured by placing an inclinometer on top of the reflector. The measured RCS and RCS-maximizing elevation angle for the reflector with the default parameter set (PCB 1) is plotted as a function of frequency in comparison to simulated results in Figure 6.14. After updating the simulation model to include the geometry changes made by the PCB vendor, the maximum simulated RCS is -9.9 dBsm at 79 GHz and 82° incidence. PCB 1 achieved a maximum measured RCS of -13.0 dBsm at 77.5 GHz and 84.4° incidence. The trend of lower RCS-maximizing incidence angle at higher frequency compares well between the measurement and simulation.

Table 6.3 shows a summary of the ten PCB reflector variations, along with their maximum measured RCS values and the corresponding frequency and incident elevation angle. PCB 1, which has the default parameter values, seems to have the performance that most closely matches the

expected behavior. It has an RCS of -13.0 dBsm at 77.5 GHz and 84.4° incidence. PCBs 5 and 6 produced larger RCS values, but at incidence angles of 75.0° and 89.7°, respectively, which is far from the intended angle of 85°. Similarly, PCB 9 was able to produce a larger RCS since it had twice as many elements in the array.

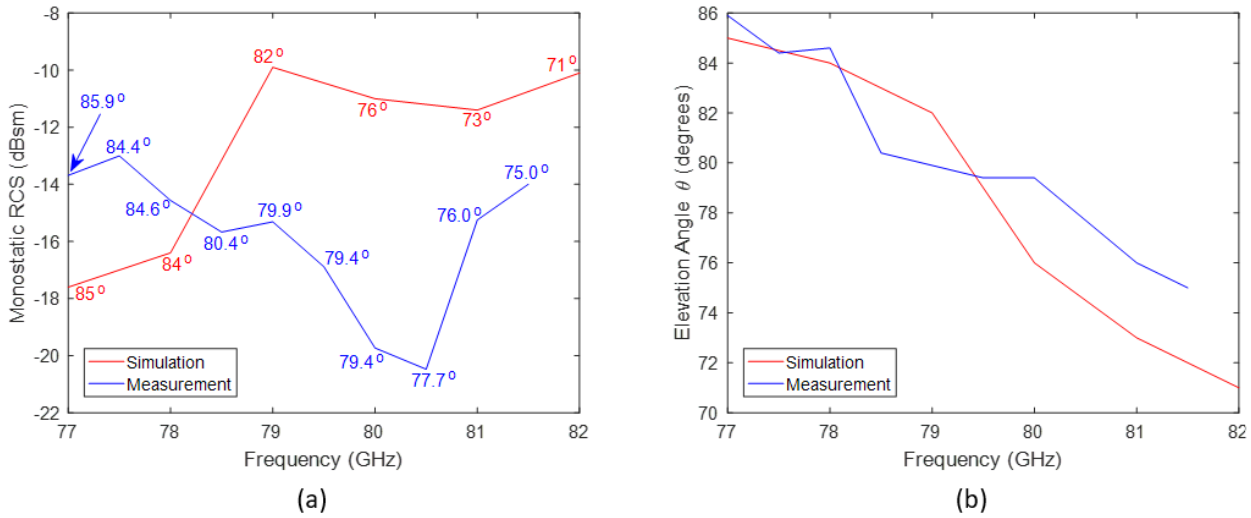

Figure 6.14. (a) Measured maximum RCS of PCB reflector 1 is compared to simulation as a function of frequency. Incidence elevation angles are labeled. (b) The incident elevation angle which maximizes reflector RCS is compared to simulation as a function of frequency.

Table 6.3
Summary of geometric parameters of each of the ten PCB reflector prototypes, and their maximum measured RCS values and corresponding frequency and incident elevation angle. A dash represents an unchanged parameter value with respect to the default.

PCB Reflector Variation	Array Size	L (μm)	S_1 (μm)	S_2 (μm)	Maximum RCS (dBsm)	Frequency (GHz)	Elevation Angle (°)
1 (default)	16 × 16	1100	3800	2600	-13.0	77.5	84.4
2	–	1025	–	–	-14.8	77.5	84.3
3	–	1075	–	–	-13.4	77.5	83.6
4	–	1125	–	–	-13.8	77.5	82.3
5	–	1175	–	–	-12.0	78.5	75.0
6	–	–	3700	–	-12.9	79.0	89.7
7	–	–	3900	–	-14.7	80.0	75.0
8	–	–	–	2200	-14.6	77.5	83.0
9	32 × 16	–	1900	–	-10.9	81.5	75.8
10	32 × 8	–	1900	–	-15.3	81.5	76.2

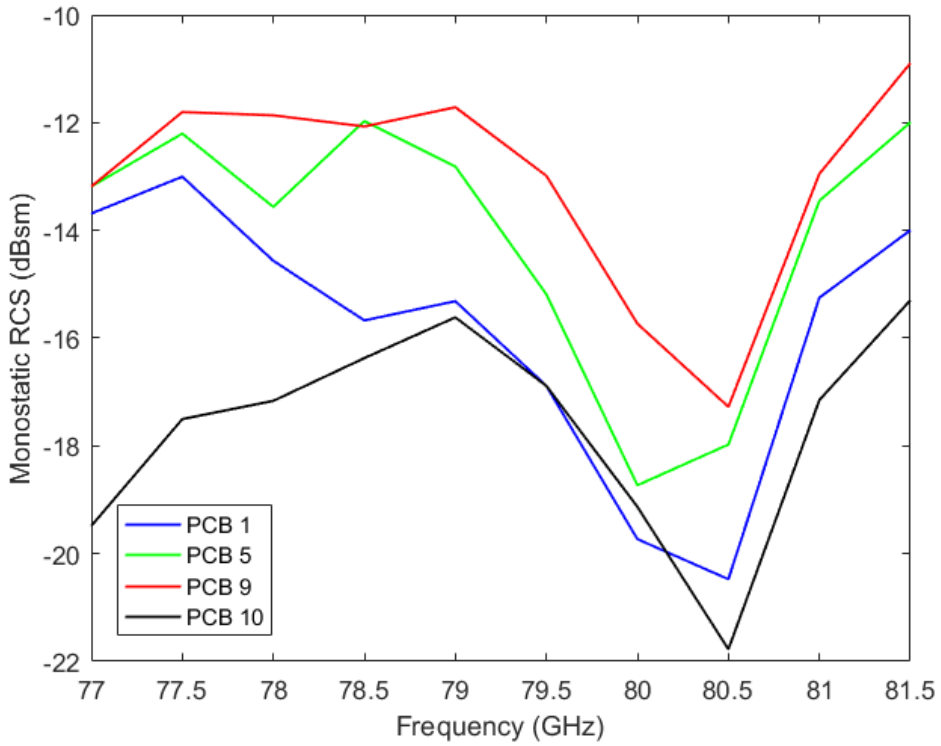

Figure 6.15. Measured maximum RCS of PCB reflectors 1, 5, 9, and 10 as a function of frequency.

Figure 6.15 shows the maximum RCS as a function of frequency for PCBs 1, 5, 9, and 10. PCB 5 has a larger RCS than PCB 1 at all frequencies, but as noted previously, the angles at which its RCS were maximized do not follow the expected trend. The comparison of PCBs 9 and 10, which have 32 by 16 and 32 by 8 arrays, respectively, demonstrates the shadowing effect that was noticed in early simulations. Although PCB 10 has the same number of elements as PCB 1 (just arranged differently), the RCS is significantly lower at most frequencies. Similarly, the RCS of PCB 9 has not scaled proportionally with the doubling of the number of elements.

6.6 Discussion

The simulated RCS of the SU-8 reflector design at a 79 GHz center frequency and 85° incidence angle was -12.7 dBsm. The best performing fabricated prototype (Reflector 4 in Table

6.2) has a measured RCS of -20.1 dBsm. While this is quite far off from the goal, it is clear that the reflector is functioning. For example, its backscattering response is stronger than a fairly large (1.75 in. diameter) sphere, and several orders of magnitude stronger than just a metalized silicon wafer, or a metalized silicon wafer with SU-8 strips and no radiating elements. Additionally, while this prototype was the first to display electrical connection between a significant number of radiating elements and ground as measured by a DC probe station, there were still many that were not connected. Based on the sampled subset of radiating elements, it is estimated that around half of the elements were well connected. Assuming 50% of the radiating elements are non-functional, this would account for 6 dB out the missing 7.4 dB in comparison between measurement and simulation. It remains as future work to solve the fabrication challenges of poor SU-8 adhesion and non-vertical SU-8 sidewalls, which are the most significant contributors to poor connection. The measured results are promising, in that if this can be achieved, the reflectors will likely have the required RCS for the intended application.

The PCB reflectors demonstrated improved performance compared with the SU-8 reflectors. PCB reflector 1 has a measured RCS of -13.0 dBsm at a 77.5 GHz center frequency and 84.4° incidence angle. This is 7.1 dB higher than SU-8 reflector 4, and is only 6.4 dB short of the initial simulation and 3.1 dB short of the simulation with vendor geometry. Possible causes of the discrepancy include dielectric constant uncertainty and conductive loss in the plated vias, as well as measurement uncertainty associated with the high sensitivity of the RCS to the orientation of the reflector with respect to the radar. Furthermore, all of the PCB reflector prototypes had RCS values comparable to each other, while only one SU-8 prototype with reasonable performance was produced.

Additionally, there is much future work to be explored on this project. Since these reflectors are intended to be embedded in the paint used to make road markings, studies of the dielectric constant of such paint, and its effect on the reflector RCS need to be completed. At that point, the reflector design may need to be re-optimized to compensate. Ultimately, it would be ideal to be able to fabricate these reflectors on long strips of a flexible substrate such as a tape. This would make installation on highways easy, as the tape could simply be rolled across the asphalt and then painted over. Finally, the azimuthal beamwidth of these reflectors is currently around 2°, which limits the range of angles from which they can be easily detected. To try to widen the beamwidth, it is desired to explore possible modifications to this design to achieve some degree of retroreflectivity.

6.7 Practical Demonstration

It is proposed that reflectors such as these can be placed within road markings in different spatial arrangements to encode the type of marking. As a demonstration of this concept, three of the PCB reflector prototypes were placed on the ground with a spacing of about 0.4 m. The GM E-band radar was elevated to 0.83 m and tilted at an 85° incidence angle such that its beam was pointed at a spot 9.5 m away in range, coinciding with the position of the reflectors. First the reflectors were placed directly on the floor, which is a very smooth surface with minimal backscattering. Then they were placed on an artificial rough surface consisting of many pebbles attached to a wooden board, covered in a reflective coating [109]. This represents an extremely rough surface with very high backscattering. It is expected that most typical road surfaces will exhibit backscattering somewhere between these two extremes. A photograph of the demonstration setup is shown in Figure 6.16.

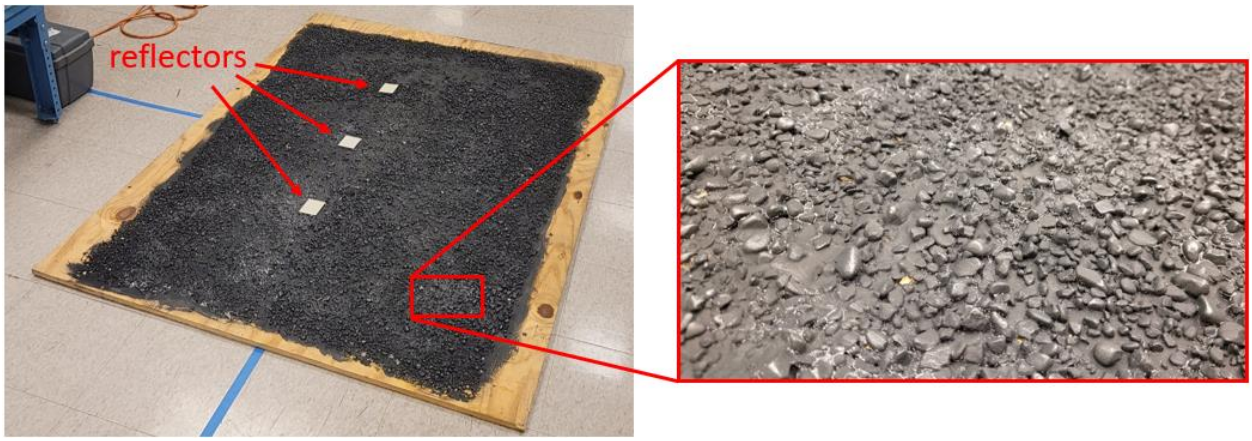

Figure 6.16. A photograph of three reflector prototypes positioned on an artificial rough surface with high backscattering, for the purpose of demonstrating the road marking identification concept.

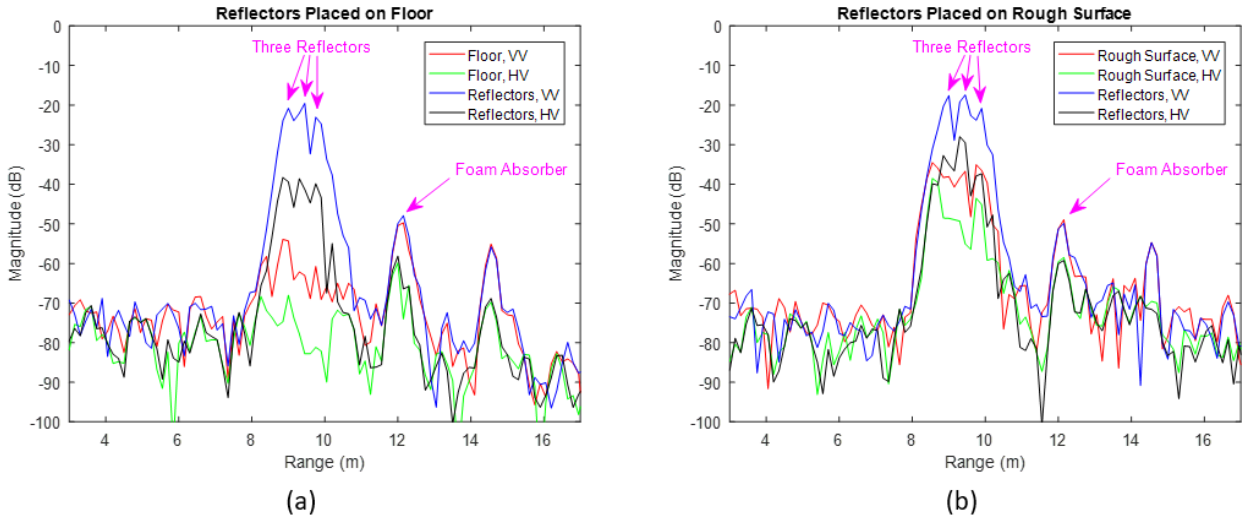

Figure 6.17. Range-domain data representing the backscattering from three PCB reflector prototypes placed (a) on the floor and (b) on the artificial rough surface.

The backscattering response was measured by the radar at a center frequency of 77 GHz with a bandwidth of 1 GHz for a range resolution of 0.15 cm. The measured responses are shown in Figure 6.17, where the response of the reflectors is compared to that of the underlying surface without the reflectors. Several features of these plots are worth discussing. First, the backscattering from the reflectors is quite strong. It is approximately 50 dB above noise, 35 dB above the response

from the floor, and 15 dB above the response from the rough surface. This demonstrates that the reflectors should be distinguishable above the background in a roadway scene by radars with lower sensitivity than that of this one. Second, the peaks from the individual reflectors are clearly resolved, showing that measurement of reflector spacing could be used for identifying different types of markings. Finally, in terms of polarization, the reflectors backscatter mostly in VV polarization. Above the floor, there is a minimum difference of 17 dB between the VV and HV backscattering responses. The rough surface exhibits a difference between VV and HV of as high as 4 dB. These measurements are uncalibrated, and therefore not indicative of absolute cross-polarization values, but clearly the rough surface causes more depolarization than the reflectors. This difference could potentially aid in the classification of targets as reflectors.

6.8 Summary

A low-profile passive reflector has been designed for the 79 GHz automotive radar band. It provides a large RCS that can be detected against the road surface by forward-looking radars, and embedding the reflectors beneath paint can enable detection and identification of various road markings regardless of weather conditions. With a height of less than half a millimeter, this reflector is much thinner than previously designed reflectors for this application, which avoids the requirement of embedding it into the asphalt.

The fabrication process using SU-8 photoresist yielded a reflector with simulated RCS of -12.7 dBsm at 79 GHz and an incidence angle of 85°. Through several challenges in the fabrication process, a prototype has been made with a measured RCS of -20.1 dBsm at a slightly shifted frequency of 77 GHz. Similarly, the PCB fabrication process lead to a simulated RCS of -6.6 dBsm and a measured RCS of -13.0 dBsm. These values are within a range that could be reasonably well detected by forward-looking automotive radars.

Additional studies and redesign may be in order to determine and account for the effects of paint coatings and water films over top of the reflector, as well as to improve the azimuthal beamwidth of the backscattering response. Additionally, the fabrication processes proposed are amenable to mass production of these devices for distribution to new roads, but much work is still required to make the process production-ready.

CHAPTER 7
Conclusion

7.1 Summary of Contributions

The work of this dissertation contributes to the advancement of millimeter-wave polarimetric radar, most relevantly for use in automotive applications. In particular, technologies have been developed for radar front-end components operating at J-band, roughly three times higher in frequency than the modern 79 GHz band used by today's automotive radars. If this band can be leveraged in future systems, it will enable much improved performance as well as size reduction of the antennas and other components. The reliability of ADAS and autonomous vehicle sensor technologies is of utmost importance as the world begins to adopt and integrate driverless transportation. One way to ensure dependable performance is by incorporating a fusion of data from different sensor types that can complement each other and share responsibility when necessary. The research presented here helps progress radar technology in ways that will make it more cost-effective, improve its imaging and mapping resolution, and enable detection of color- and pattern-based symbols. These enhancements will allow radar to assist with sensing tasks traditionally delegated to ultrasonic, lidar, and camera sensors, which will improve robustness of the overall autonomous systems while adding features unique to radar such as polarimetry and weather penetration.

The major contribution of the dissertation is the design of a common-aperture dual-polarized transceiver antenna system, which uses a polarization-independent spatial power divider

to focus two dual-polarized feed horns with a single shared aperture lens. The prominent features of this antenna include high transmit-to-receive isolation, high gain, and narrow beamwidth, enabling radar measurements with high sensitivity and very fine angular and range resolution approaching that of lidar. Additionally, the common aperture shared between dual-polarized transmit and receive elements makes the antenna system compact and eliminates radar parallax, while remaining compatible with full polarimetric measurement capability. Several versions of this antenna system were constructed at different bands, and utilized in three polarimetric radars for automotive phenomenological studies. Depending on the band and lens size, these antennas provide a gain on the order of 33 dB to 39 dB and a beamwidth from 0.8° to 1.7°, as well as isolation greater than 40 dB.

The critical component of this antenna system is a polarization-independent spatial power divider, which is a device that splits an incident wave into two perpendicularly directed components with equal amplitude, regardless of polarization. The power divider was designed using cascaded corrugated dielectric slabs and metallic MEFSS elements, and was made using standard microfabrication techniques including DRIE and electron-beam evaporation. Three versions were produced at different bands for inclusion in the three radar antennas, each of which exhibits a difference between reflection and transmission coefficients no more than 1 dB, and average dielectric loss of 1.1 dB.

To support the dual-polarized operation of the J-band antenna systems, an orthomode transducer was designed with simple geometry to minimize fabrication challenges associated with the small machined waveguides. The OMT allows access to the V- and H-polarized modes of the transmit and receive horn feeds. The fabricated OMT prototypes have return loss greater than 10 dB, polarization discrimination greater than 20 dB, and isolation greater than 30 dB, over a

fractional bandwidth of at least 7% (as much as 12% for one prototype). Through lapping of adjoining block surfaces and electroless gold plating of the internal waveguides, an exceptional insertion loss of approximately 1 dB has been achieved.

The GM J-band radar, which includes the aforementioned antenna and OMT in the front-end, was used to make a set of measurements of the polarimetric backscattering coefficients of several types of road surfaces at near-grazing incidence. Surfaces measured include asphalt (additionally with water, ice, and snow cover), gravel (also with snow cover), and concrete. The measurements indicate trends of smaller backscattering coefficients both at higher incidence angles and for smoother surfaces. Significant volume scattering has also been observed from surfaces with snow cover. These measurements, along with future ones, will help in the development of models for road surface identification and condition assessment using forward-looking automotive radar at J-band.

Finally, a low-profile passive reflector has been designed for use in the detection of road markings using radar. Currently only cameras are capable of this task, and investment into this infrastructure will lead to more robust and reliable lane centering and traffic marking interpretation in ADAS and autonomous vehicles, including expanding the situational applicability to low visibility conditions such as inclement weather. The reflector has a total height less than 1 mm, and potentially as thin as 0.25 mm, and may be integrated into roadways by being covered with a thin layer of paint. Two fabrication methods have been proposed. The microfabrication process using SU-8 photoresist leads to a simulated RCS of -12.7 dBsm at 79 GHz and 85° incidence, and a measured RCS of -20.1 dBsm. The PCB process results in a simulated RCS of -6.6 dBsm and a measured RCS of -13.0 dBsm. This is strong enough for a forward-looking automotive radar to

detect against the backscattering from the road itself. Arrangement of reflectors in different sequences will enable discrimination between different types of markings.

7.2 Future Work

Some of the work presented in this dissertation is ongoing, or has led to new research directions that will be carried on by the research group. Here a brief description of some of these future endeavors is provided to build anticipation for great findings yet to come.

7.2.1 J-Band Polarimetric Radar Antennas

The most recent version of the dual-polarized common-aperture transceiver antenna system discussed in Section 2.5 is currently being integrated into the KACST J-band polarimetric radar operating at 220 – 230 GHz. The interchangeable lens mechanism allows for varying beamwidth to assist with radar measurements that may benefit from either finer resolution or wider field of view. This radar will be used in the near future to conduct many studies of polarimetric backscattering in automotive applications.

One of the noted limitations of this antenna is the transmit-to-receive isolation, which, although it is already quite good, suffers from reflections from the lens surfaces and could be dramatically improved by an order of magnitude or more if those reflections could be eliminated. Improving the isolation would consequently lower the noise floor of the radar. Efforts are underway to design a reflection-less lens using patterned MEFSS elements instead of dielectric refraction to produce the desired spatial phase modulation with a low reflection coefficient.

Since the antenna consists of a lens system with fixed feeds, there is currently no means by which to electronically scan the beam. Due to the bulk of the radar, mechanical scanning in real time is also not feasible. An alternative approach that has been explored for scanning of such radar

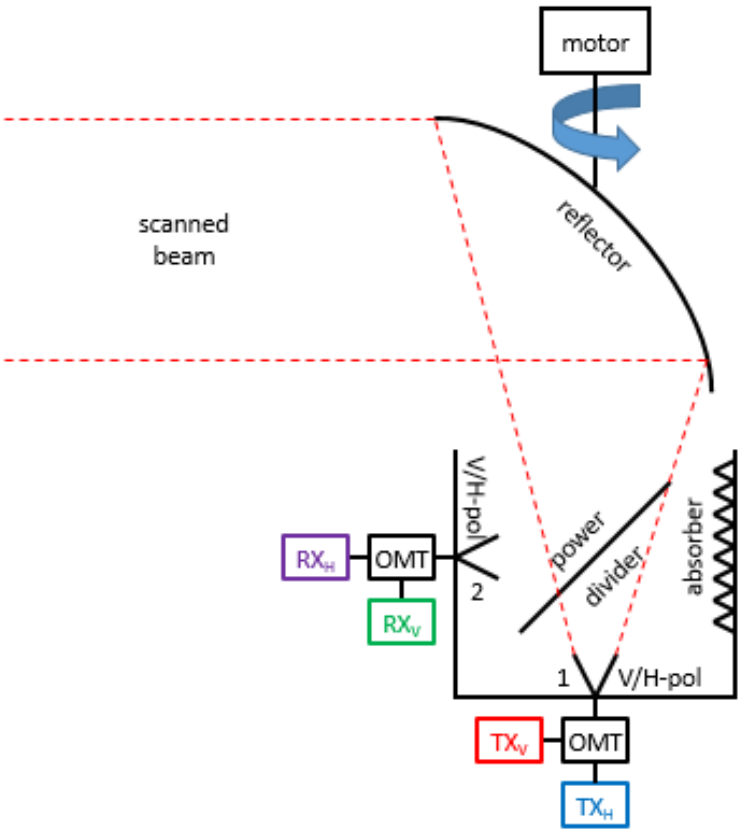

Figure 7.1. Proposed mechanism for mechanical scanning of the radar beam in the azimuthal direction by means of a curved reflector mounted to a motor. Scanning in elevation can also be achieved with a patterned reflective surface to generate a frequency-dependent phase modulation.

systems involves aiming the antenna (or antennas) vertically at a large flat reflector at a 45-degree angle. A motor can then be used to rotate the reflector along a vertical axis, resulting in a horizontally-scanned beam with 360-degree coverage. This technique has been demonstrated in [110], where it was implemented using a two-aperture antenna system. It is planned to use the new J-band radar in a similar fashion to leverage the benefits of the single-aperture antenna system and introduce beam scanning. Additionally, it is hoped to replace both the lens and the flat reflecting surface with a single curved reflector, which will combine the functionality of redirection and collimation of the beam. In that case, reflections from the lens surface are no longer present, and the system isolation can be improved. Investigations are currently underway to determine a

fabrication process suitable for the highly precise curvature required for the reflector, as well as to ensure the structure is momentum-balanced during rapid rotation. Upon successful execution of that idea, the next proposed step is to pattern the reflector with elements such as gratings or MEFSS to achieve a varying phase front as a function of frequency. This would allow for beam scanning in the elevation direction via a frequency sweep. In this manner, the radar can be scanned in both the azimuth and elevation planes, giving virtually complete 3D coverage of the surrounding environment with fine resolution and high sensitivity. Figure 7.1 shows a conceptual illustration of this approach.

7.2.2 J-Band Orthomode Transducers

The OMTs presented in this dissertation were manufactured using CNC machining techniques. The main challenges of this approach are ensuring strong electrical contact between the two split blocks to minimize insertion loss, and dealing with machining tolerances that can cause a shifted frequency response or generate unwanted cross-polarization. The design itself is also amenable to fabrication using micromachining with silicon DRIE. This process would allow for tighter control over waveguide dimensions, lower loss due to smoother waveguide surfaces and sputtered gold coating, and a mechanism for seamless wafer assembly through gold-to-gold thermo-compression bonding [51]. This approach could also potentially dramatically reduce the bulk of radar front-end waveguide components, by integrating waveguide filters and a simple feed horn along with the OMT in the wafer package. Additionally, some past work has developed a method for directly integrating active MMIC chip components with such on-wafer micromachined structures [111]. With these goals in mind, some investigation into the waveguide bends, waveguide-to-transmission-line transitions, and chokes required to implement such an integrated front-end system has begun.

7.2.3 J-Band Radar Phenomenology

The polarimetric backscattering measurements presented in Chapter 5 barely scratch the surface of what can be accomplished using radar at J-band. With the nearly complete KACST radar upgrade, it is hoped that this radar will serve to continue phenomenological studies related to automotive environments with enhanced performance. In addition to measurements of scattering from road surfaces, studies of statistical scattering behavior and Doppler signatures of vehicles, bicycles, pedestrians, and animals are proposed to supplement similar experiments performed at E-band and expand the relatively limited J-band scattering database. Similar work has been undertaken by General Motors with the assistance of their E-band and J-band radars.

It was briefly mentioned in Chapter 1 that NASA has a project involving the study of ice clouds using 239 GHz radar. Related to the field of atmospheric remote sensing, an interesting study of the J-band response of falling snow has been suggested by committee member Professor Xianglei Huang.

7.2.4 Radar Reflectors for Road Markings

As has been discussed at the end of Chapter 6, there is still much work remaining on the low-profile passive radar reflector project, including improving the fabrication process, studying the effects of paint coatings, and improving the RCS beamwidth. Additionally, it is hoped that the J-band radar technologies studied in this dissertation will generate further interest in utilizing this frequency band for future high-performance automotive radar systems. If that is the case, it may become necessary to scale the reflector design to J-band. The 79 GHz design is already at the limit of PCB fabrication processes, so improved microfabrication methods will certainly be needed to implement a J-band reflector.

7.3 List of Publications

Some of the contributions of this dissertation have been published in peer-reviewed journal articles and conference proceedings. A list of these works is included here. In addition, it is planned to submit the contents of Chapters 4, 5, and 6 for publication in journals in the near future.

Journal Articles

T. J. Douglas, A. Y. Nashashibi, H. N. Shaman, and K. Sarabandi, "Sub-Millimeter-Wave Polarization-Independent Spatial Power Divider for a Two-Port Dual-Polarized Antenna," *IEEE Trans. Terahertz Sci. Tech.*, vol. 11, no. 5, pp. 508-518, Sep. 2021, DOI: 10.1109/TTHZ.2021.3088310.

T. J. Douglas and K. Sarabandi, "A High-Isolation Two-Port Planar Antenna System for Communication and Radar Applications," *IEEE Access*, vol. 6, pp. 9951-9959, Feb. 2018, DOI: 10.1109/ACCESS.2018.2807415.

Conference Proceedings

T. J. Douglas and K. Sarabandi, "Low-Profile Passive Reflector for Radar Detection of Road Markings," in *Proc. IEEE Int. Symp. Antennas Propag.*, Denver, CO, Jul. 2022.

T. J. Douglas, A. Y. Nashashibi, M. Kashanianfard, and K. Sarabandi, "Polarimetric Backscatter Measurements of Road Surfaces at J-Band Frequencies for Standoff Road Condition Assessment," in *Proc. USNC-URSI Radio Science Meeting*, Singapore, SG, Dec. 2021, pp. 35-36, DOI: 10.23919/USNC-URSI51813.2021.9703481.

A. Y. Nashashibi, M. Kashanianfard, T. J. Douglas, K. Sarabandi, and S. W. Decker, "High-Resolution Range-Doppler Maps of Moving Targets in Traffic Scene," in *Proc. IEEE Int. Symp. Antennas Propag.*, Singapore, SG, Dec. 2021, pp. 1119-1120, DOI: 10.1109/APS/URSI47566.2021.9704087.

T. J. Douglas, A. Y. Nashashibi, and K. Sarabandi, "A 230 GHz Orthomode Transducer with Simple Fabrication Steps," in *Proc. IEEE Int. Symp. Antennas Propag.*, Singapore, SG, Dec. 2021, pp. 463-464, DOI: 10.1109/APS/URSI47566.2021.9704767.

T. J. Douglas and K. Sarabandi, "High-Isolation Common-Aperture Antenna System Based on Spatial Power Divider for Use in E-Band Fully Polarimetric Radar," in *Proc. IEEE Int. Symp. Antennas Propag.*, Montreal, QC, Jul. 2020, pp. 1537-1538, DOI: 10.1109/IEEECONF35879.2020.9330227.

A. Y. Nashashibi, T. J. Douglas, K. Sarabandi, and H. N Shaman, “Design and Fabrication of Orthomode Transducer for Compact Polarimetric J-Band Radars,” in *Proc. USNC-CNC-URSI North American Radio Science Meeting,* Montreal, QC, Jul. 2020, pp. 105-106, DOI: 10.23919/USNC/URSI49741.2020.9321674.

A. Y. Nashashibi, M. Kashanianfard, T. J. Douglas, K. Sarabandi, and S. W. Decker, “Fully Polarimetric E-Band Instrumentation Radar in Support of Autonomous Vehicle Research,” in *Proc. USNC-CNC-URSI North American Radio Science Meeting*, Montreal, QC, Jul. 2020, pp. 97-98, DOI: 10.23919/USNC/URSI49741.2020.9321601.

T. J. Douglas and K. Sarabandi, “Two-Port, Common Aperture, High-Isolation, Dual-Polarized Sub-Millimeterwave Antenna System Based on Spatial Power Divider,” in *Proc. IEEE Int. Symp. Antennas Propag.*, Atlanta, GA, Jul. 2019, pp. 501-502, DOI: 10.1109/APUSNCURSINRSM.2019.8888741.

T. J. Douglas and K. Sarabandi, “Compact Planar Antenna System for Full-Duplex Wireless Applications,” in *Proc. IEEE Int. Symp. Antennas Propag.*, Boston, MA, Jul. 2018, pp. 1303-1304, DOI: 10.1109/APUSNCURSINRSM.2018.8609281.

T. J. Douglas and K. Sarabandi, “Planar Antenna System for Full-Duplex Applications,” in *Proc. Int. Union of Radio Science General Assembly and Scientific Symp.,* Montreal, QC, Aug. 2017, DOI: 10.23919/URSIGASS.2017.8105210.

APPENDIX

APPENDIX A

High-Isolation Two-Port Planar Antenna System for Full-Duplex Wireless Communication and Radar Applications

This appendix presents an approach to achieve a very high level of isolation between the two ports of a compact antenna system for communication and radar applications. Orthogonal polarization and a special symmetric arrangement of two-element transmit and receive arrays are used to achieve high isolation levels. Identical rectangular patch antennas are designed for operation at 6 GHz, and are arranged in a square grid configuration with ninety-degree rotational symmetry in this design. A pair of transmitters and a pair of receivers are fed perfectly out of phase with one-hundred-eighty-degree couplers. The entire system is simulated and fabricated. The prototype antenna's isolation is measured with a network analyzer, and the absolute gain measurement technique and standard far field antenna pattern measurement techniques are used to characterize its gain and radiation pattern. It is found that exploiting symmetry in this manner leads to isolation of 63.7 dB. This indicates that carefully designed and constructed systems could reasonably exhibit isolation on the order of 70 dB or more using this method.

A.1 Background

As mobile communication technologies continue to develop, and the demand for more, cheaper, and faster data increases, it is necessary to implement spectrum-efficient communication techniques to minimize further cluttering of the already congested radio spectrum. One way to accomplish this is by enabling communication with simultaneous transmit and receive at a single

frequency [112], [113]. Since frequency division duplexing uses separate frequencies for transmitting and receiving, condensing both directions into a single frequency will effectively double the amount of data that can be communicated in a given bandwidth. Additionally, short range radars such as automotive radars make use of a continuous-wave spectrum to keep the peak transmit power low [63], [114], [115]. For such systems, very high isolation between transmit and receive is needed for high receiver dynamic range and small target detection. As a result, the transmit and receive antennas are usually separated to achieve better isolation.

The main challenge to overcome in order to achieve these goals is the coupling between the transmitter and receiver. If the two ports are not sufficiently isolated, the desired communication signal or radar return can easily become indistinguishable due to the radiation coupled from the transmitter to the receiver. An obvious approach is to make use of orthogonal polarization. If the transmitter and receiver are linearly polarized and oriented orthogonal to each other, then ideally they would not interfere with each other. In reality all antennas generate cross-polarized fields, so orthogonal polarization is usually not enough to ensure the required isolation for compact designs.

The concept of full-duplex was first introduced in connection with a common aperture polarimetric active radar calibrator to produce relatively small calibration targets with large radar cross-section in [116]. In this design a square horn was connected to a high isolation orthomode transducer to separate the receive signal from the transmit signal. The same idea was later perfected to achieve more than 80 dB isolation between the two ports [117].

In this work, the use of a special symmetry is investigated to achieve high isolation between orthogonally polarized patch antennas. This will allow for implementation of a compact, two-port, planar antenna system with very high isolation. Rectangular patch antennas are well suited to this

technique for several reasons. In addition to being linearly polarized, their bandwidth can be enhanced by including U-shaped slots in the patch [118], [119], [120]. Two transmitting patch elements and two receiving patch elements are arranged in a square grid with ninety-degree rotational symmetry about the center. In this configuration, the coupling between transmitter-receiver pairs are shown to be equal. Thus by exciting the transmitters perfectly out of phase and subtracting the two receiver signals, very high levels of cancellation can be achieved despite close proximity between the radiating elements. A feed network featuring a pair of one-hundred-eighty-degree hybrid couplers is designed to perform the out-of-phase excitation and signal subtraction. Full-wave electromagnetic analysis in HFSS is then used to simulate the entire system. Finally, a prototype of the device is constructed, and its measured performance is compared to that of the simulation.

This antenna system has potential applications across several disciplines. One major application is in full-duplex communication systems. Assuming a maximum power output of 40 dBm, an additional isolation of about 30 dB that can be achieved at the intermediate frequency (IF) band, and the fact that signal processing algorithms are capable of attenuating known transmit signals at baseband by 30 dB, 80 dB of RF isolation can reduce the transmitter leakage to about -90 dBm or less. This will be sufficient for most practical cases to detect the desired received signals with a relatively high signal to interference ratio. Additionally, the antenna system could be utilized in high-cross-section active radar calibration targets.

The design presented here has a relatively narrow band of operation centered at 6 GHz for demonstration of the concept. The surrounding frequency band from roughly 5 GHz to 7 GHz is licensed by the FCC for applications in mobile communications, fixed-satellite service, radiolocation, and radionavigation, and also includes the 5.8 GHz industrial, scientific, and

medical (ISM) band [34]. With some minor scaling, the antenna system could be adjusted to shift the operation frequency to meet the needs of applications in any of these areas. Furthermore, the bandwidth can be enhanced by using U-slot patch radiating elements and a modified feed network, allowing for operation over a much larger portion of the C-Band (4 – 8 GHz).

A.2 Theory

Figure A.1 shows the configuration of a compact two-port antenna system intended to provide very high isolation (> 60 dB). This antenna system functions by exploiting the ninety-degree rotational symmetry of a square grid. The operating principle behind this design is the near equality of the transmission coefficients between any pair of transmitter patch and receiver patch. In order to illustrate this mathematically, it is most useful to consider the scattering parameters of a four-port network, with each port corresponding to one of the four patch elements.

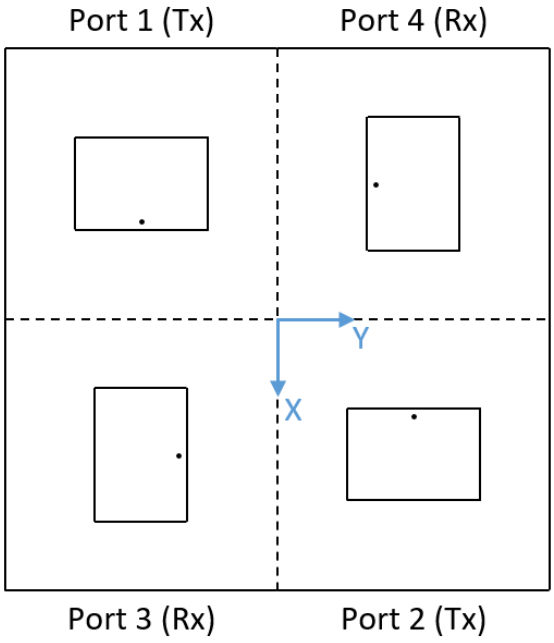

Figure A.1. Geometry of the square grid configuration of the two transmitter patch elements and two receiver patch elements. A coordinate system is also defined.

The scattering parameters for an N-port network are defined as follows:

$$\begin{bmatrix} V_1^- \\ V_2^- \\ \vdots \\ V_N^- \end{bmatrix} = \begin{bmatrix} S_{11} & S_{12} & \cdots & S_{1N} \\ S_{21} & S_{22} & \cdots & S_{2N} \\ \vdots & \vdots & \ddots & \vdots \\ S_{N1} & S_{N2} & \cdots & S_{NN} \end{bmatrix} \begin{bmatrix} V_1^+ \\ V_2^+ \\ \vdots \\ V_N^+ \end{bmatrix}, \tag{A.1}$$

where V_m^- are the reflected voltage waves, V_n^+ are the incident voltage waves, and S_{mn} are the scattering parameters [121].

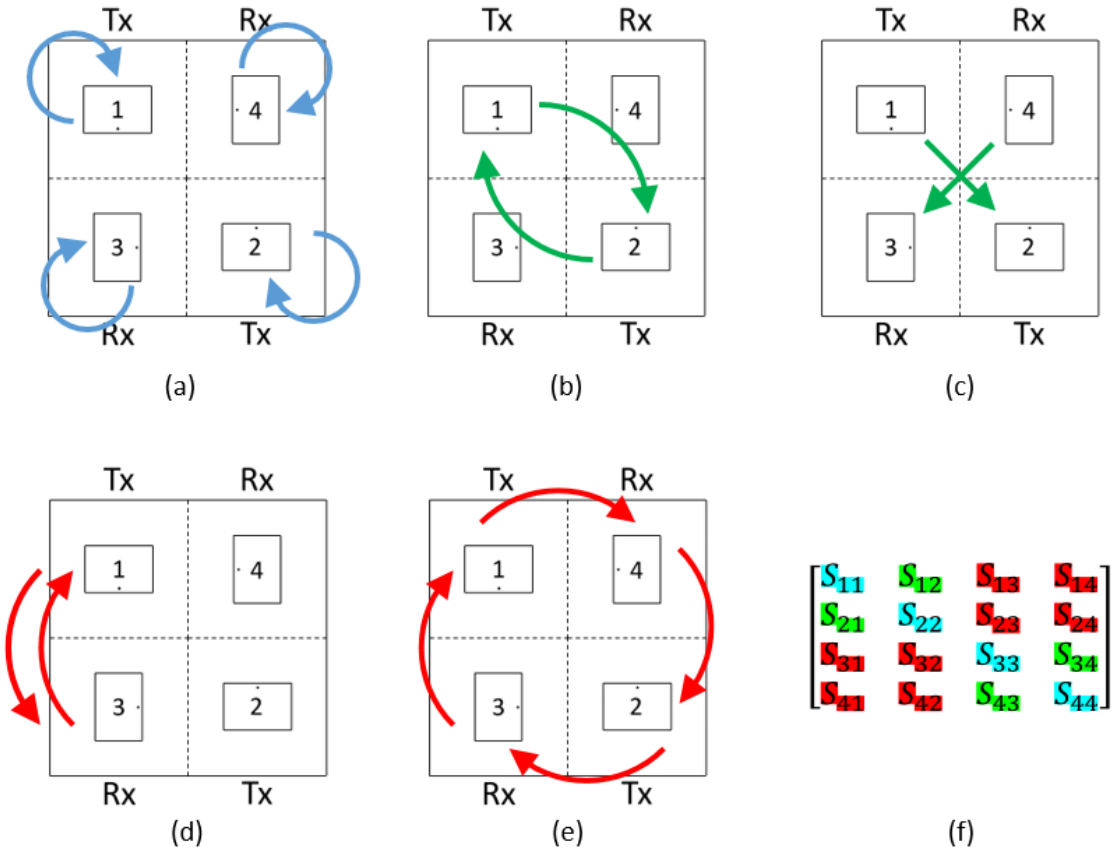

Figure A.2. Visual representation of the reduction of the scattering matrix of the ninety-degree rotationally symmetric array to three unique parameters. (a) The reflection coefficients are equal due to symmetry. (b) Transmission between opposite elements are equal due to reciprocity. (c) Transmission between transmit pairs and receive pairs are equal due to symmetry. (d) Transmission between adjacent elements are equal due to reciprocity. (e) Transmission between any adjacent pair is equal due to symmetry. (f) Equal scattering parameters are color-coded in the matrix.

Suppose the transmitters are assigned port labels 1 and 2, and the receivers are assigned port labels 3 and 4. Due to the ninety-degree rotational symmetry of the geometry, all elements of the diagonal of the scattering matrix are equal. Furthermore, the rotational symmetry in combination with the reciprocity theorem dictate that the coupling between either transmitter element and either receiver element will be equal, and the coupling between the two transmitters is equal to the coupling between the two receivers. Therefore, the scattering matrix can be simplified as follows:

$$\begin{bmatrix} S_{11} & S_{12} & S_{13} & S_{14} \\ S_{21} & S_{22} & S_{23} & S_{24} \\ S_{31} & S_{32} & S_{33} & S_{34} \\ S_{41} & S_{42} & S_{43} & S_{44} \end{bmatrix} = \begin{bmatrix} S_1 & S_2 & S_3 & S_3 \\ S_2 & S_1 & S_3 & S_3 \\ S_3 & S_3 & S_1 & S_2 \\ S_3 & S_3 & S_2 & S_1 \end{bmatrix}. \tag{A.2}$$

Thus the entire scattering matrix consists of only three unique parameters, denoted here by S_1, S_2, and S_3. Figure A.2 shows a visual representation of this derivation.

Suppose that the transmitters are excited with equal magnitude and opposite phase, and that there exist impedance mismatches at the receiver ports. Then the following relations can be made:

$$\begin{aligned} {V_2}^+ &= -{V_1}^+ \\ {V_3}^+ &= \Gamma_3 {V_3}^- \\ {V_4}^+ &= \Gamma_4 {V_4}^- \end{aligned}, \tag{A.3}$$

where Γ_3 and Γ_4 are reflection coefficients due to the receiver port mismatch. These reflection coefficients are defined looking out of ports 3 and 4 and looking into the respective loads, and arise if the loads are not matched to the system impedance. Substitution of (A.2) and (A.3) into the third and fourth rows of (A.1) results in:

$$\begin{aligned} V_3^- &= S_3 V_1^+ - S_3 V_1^+ + S_1 \Gamma_3 V_3^- + S_2 \Gamma_4 V_4^- \\ V_4^- &= S_3 V_1^+ - S_3 V_1^+ + S_2 \Gamma_3 V_3^- + S_1 \Gamma_4 V_4^- \end{aligned}. \tag{A.4}$$

The first two terms of the right hand side of each equation above cancel, and it can easily be shown that the solution of (A.4) is $V_3^- = V_4^- = 0$, unless $(1 - S_1\Gamma_3)(1 - S_1\Gamma_4) = S_2{}^2\Gamma_3\Gamma_4$. However, this condition cannot be the case in general, since there is no deterministic relationship between the scattering parameters and reflection coefficients. Furthermore, it is expected that the scattering parameters and reflection coefficients are close to zero, in which case this condition is clearly false, as the left hand side is approximately one and the right hand side is approximately zero. Thus under these conditions, the coupling from the transmitters to the receivers is entirely canceled. Note that while the transmitters are excited out of phase, they are also oriented in opposing directions. Therefore, the main lobe of the beam still points in the desired boresight direction (out of the page).

To ensure that the receiver beam also points in this direction, the signals at the two receiver ports must be subtracted. For the purpose of simulating the isolation of this configuration, it is assumed that the receivers are presented with matched loads ($\Gamma_3 = \Gamma_4 = 0$). With this assumption, and the relations in (A.3), the fourth row can be subtracted from the third row of (A.1) to obtain:

$$V_3^- - V_4^- = (S_{31} - S_{32} - S_{41} + S_{42})\, V_1^+ . \tag{A.5}$$

Therefore, the isolation can be measured as $S_{31} - S_{32} - S_{41} + S_{42}$. From (A.2), all of these parameters are expected to be equal to each other. Thus nearly perfect isolation is expected.

A.3 Antenna Design

A rectangular patch antenna is designed to operate at 6 GHz. The patch is excited by a coaxial probe fed from behind the ground plane through the substrate [122]. The substrate has a

dielectric constant of $\varepsilon_r = 2.2$ and a height of $h = 0.125\ in$. The geometry of the patch is shown in Figure A.3, while the design parameters are tabulated in Table A.1. Note that at this stage the geometric center of the patch coincides with the geometric center of the substrate. The antenna is well matched, presenting a simulated input reflection coefficient below -70 dB at the design frequency, as shown in Figure A.4. It is linearly polarized and provides a realized gain of more than 8.4 dB.

Table A.1
Design parameters of the patch antenna.

Symbol	Dimension	Length (mm)	Length (in.)
L_s	substrate length	50.80	2.000
W_s	substrate width	50.80	2.000
L_p	patch length	15.14	0.596
W_p	patch width	20.35	0.801
X_f	feed-to-edge distance	0.711	0.028

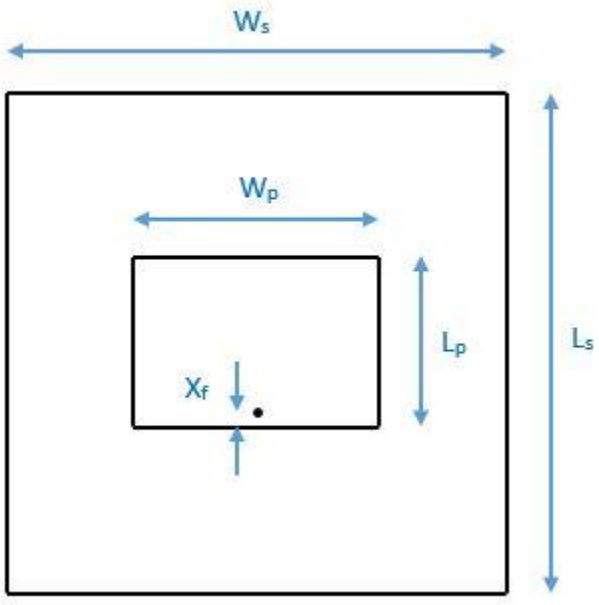

Figure A.3. Geometry of the patch antenna, showing the dimensions of the substrate and patch.

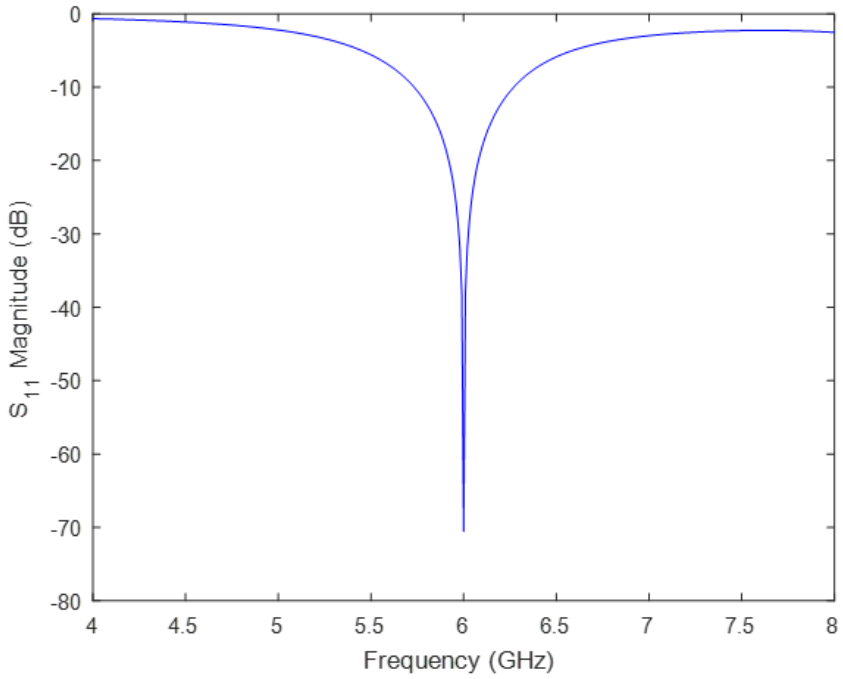

Figure A.4. The simulated input reflection coefficient of the patch antenna is shown.

Next, four of these patch antennas are arranged according to the square grid configuration shown in Figure A.1. Initially the patches are positioned such that their geometric centers align with the geometric centers of their respective quadrants of the substrate. However, since the radiation pattern is now influenced by the array geometry, the distance from the patch center to the array center is allowed to vary, as depicted in Figure A.5. Thus initially the value of the dimension D_c is 1.000 in. This parameter was then optimized to maximize the total boresight gain when both transmitter patches are simultaneously excited out of phase, as shown in Figure A.6. the value $D_c = 0.650\ in.$ is chosen. Therefore, the centers of the patch elements are only 1.300 in. apart, which is less than a free-space wavelength at 6 GHz.

At this stage of the design, the array is treated as a four-port network, and the isolation between the transmitter pair and receiver pair is simulated according to (A.5). The result is shown in Figure A.7. At the design frequency of 6 GHz, an isolation of more than 90 dB is achieved.

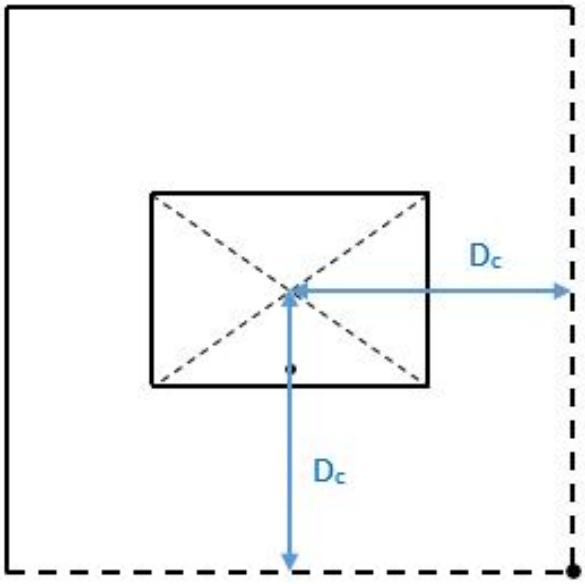

Figure A.5. The distance between the center of the patch and the edge of its quadrant (D_c) is allowed to vary.

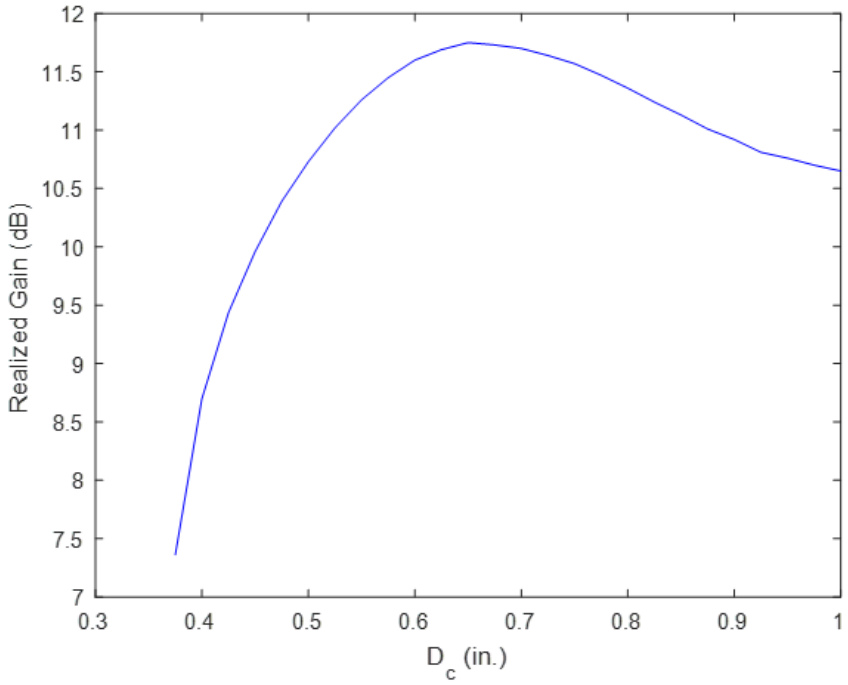

Figure A.6. The total realized gain at boresight is plotted for varying D_c, when ports 1 and 2 are simultaneously excited out of phase. A maximum is observed at 0.650 in.

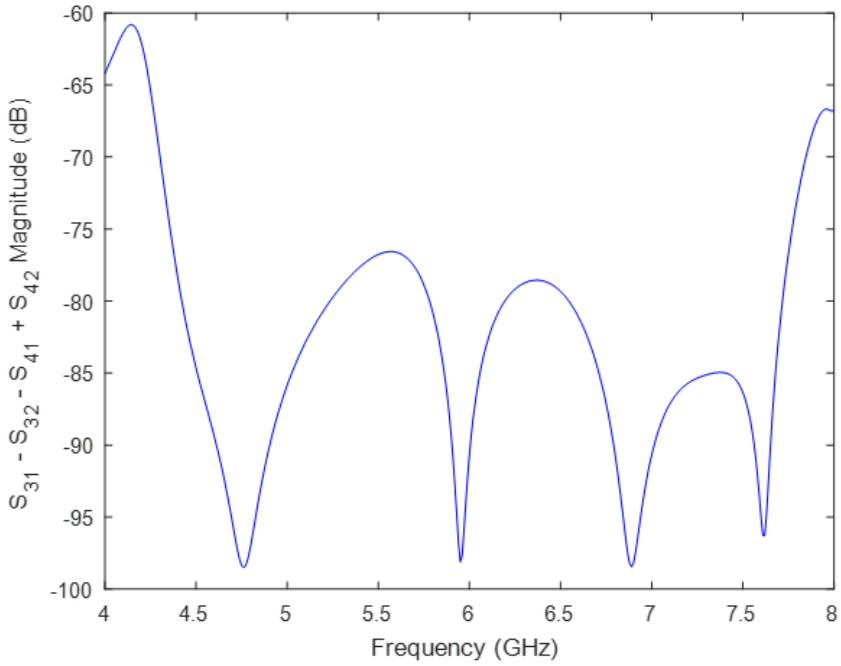

Figure A.7. The quantity plotted on the vertical axis is a measure of the total coupling from the transmitters (ports 1 and 2) to the receivers (ports 3 and 4) when the transmitters are excited perfectly out of phase and the received signals are subtracted, as derived in (A.5). The isolation at 6 GHz is shown to be greater than 90 dB.

Over the band from 4.5 GHz to 7.5 GHz, the isolation is greater than 75 dB. Perfect isolation is not achieved due to numerical round-off error and non-identical meshes for the four antennas. Basically, the automatic meshing does not preserve the geometrical symmetry exactly.

The final step in the design process was to design a feed network for the array of patches. The feed network consists of two one-hundred-eighty-degree hybrid couplers, microstrip transmission lines to connect to the patch probes, and resistor pads to terminate the isolated ports of the couplers. This network shares a ground plane with the patches, and has a substrate with $\varepsilon_r = 2.2$ and a height of $h = 0.005\ in$. The very thin substrate helps to minimize unwanted coupling between the transmission lines, which can reduce the isolation.

Table A.2
Final design parameters of the patch antenna.

Symbol	Dimension	Length (mm)	Length (in.)
L_s	substrate length	50.80	2.000
W_s	substrate width	50.80	2.000
L_p	patch length	14.94	0.588
W_p	patch width	19.91	0.784
X_f	feed-to-edge distance	0.635	0.025
D_c	center-to-edge distance	16.51	0.650

With the transmitters and receivers now connected via the couplers, the antenna is now treated as a two-port network with the transmit port assigned label 1 and the receive port assigned label 2 (note that the choice of transmit versus receive is arbitrary). Isolation can therefore be measured directly by observing the S_{21} scattering parameter. Some minor adjustments were made to the patch dimensions at this stage to attempt to increase the isolation and return loss, and the final design parameters are reported in Table A.2. The simulated isolation at 6 GHz is 66.2 dB.

A.4 Fabrication and Measurement

A prototype antenna was fabricated by Mid-Atlantic Circuits, Inc. using the design described above. The substrate material is Rogers RT/duroid 5880 ($\varepsilon_r = 2.2, tan\delta = 0.0009$ at 10 GHz). Figure A.8 shows photographs of the antenna.

The transmitter and receiver return loss and isolation were measured using a vector network analyzer. The antenna was placed in an anechoic chamber during the measurement to minimize coupling due to reflections from nearby objects.

The gain of both the transmitter and receiver were measured using the absolute gain measurement technique [123], while the radiation patterns were measured using the standard far field antenna pattern measurement technique. The measurement setup is depicted in Figure A.9.

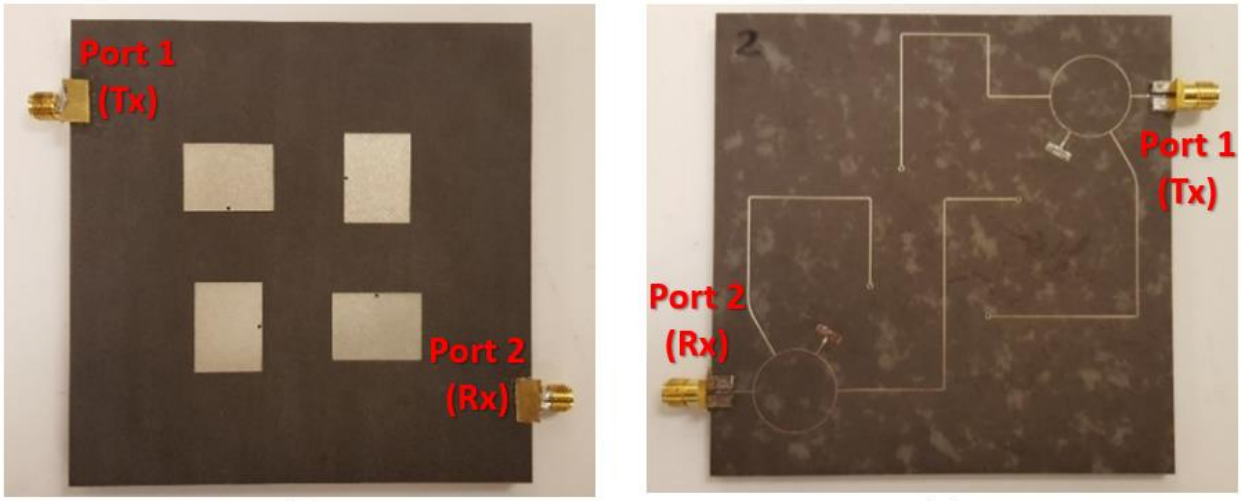

Figure A.8. Photographs of the prototype antenna: (a) top view showing the square grid array of patches, and (b) bottom view showing the feed network.

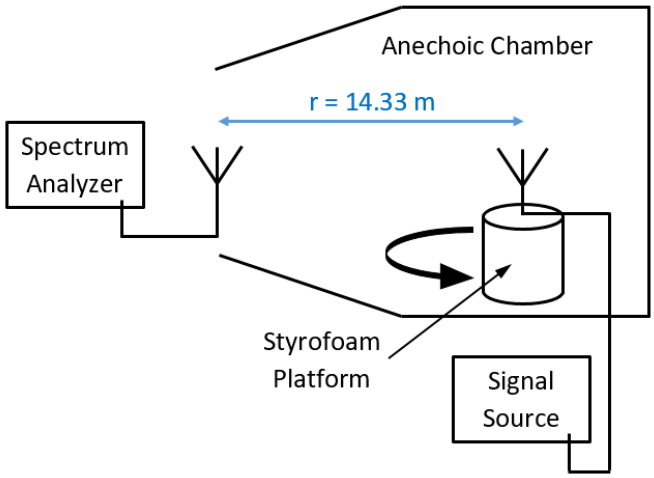

Figure A.9. Setup for absolute gain measurement technique and standard far field antenna pattern measurement technique. For the gain measurement, three antennas are permuted in the two positions. For the pattern measurement the prototype antenna is rotated atop the Styrofoam platform.

Due to the shape of the array, the radiation pattern is the broadest and narrowest at forty-five-degree angles from the E- and H- planes of the individual patches. Therefore, in addition to measuring the patterns in the E- and H- planes ($\phi = 0°$ and $\phi = 90°$), the patterns were also

measured in the $\phi = 45°$ and $\phi = 135°$ planes. Additionally, the cross-polarized gain is measured by orienting the prototype antenna such that its polarization is orthogonal to that of the ancillary antenna, and comparing the received power to the case with the polarizations aligned.

A.5 Results

The measured scattering parameters of the antenna are shown in comparison to the simulation results in Figure A.10. Table A.3 summarizes the measured and simulated return loss and isolation at the design frequency of 6 GHz.

Table A.3
Antenna return loss and isolation performance at 6 GHz.

	Simulation	**Measurement**
Port 1 Return Loss (dB)	49.9	22.1
Port 2 Return Loss (dB)	30.8	31.7
Isolation (dB)	66.2	63.7

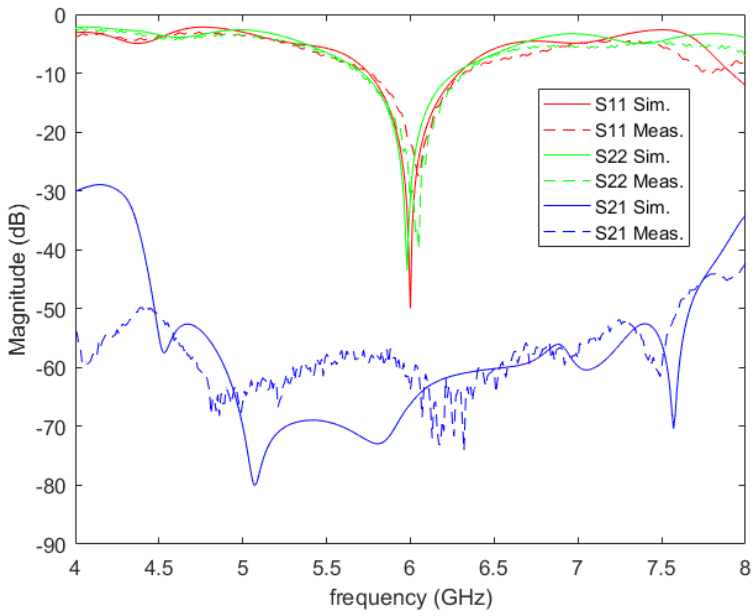

Figure A.10. Simulated and measured scattering parameters of the antenna, showing the return loss and isolation.

Figure A.11 and Figure A.12 show the measured and simulated realized gain patterns for the transmitter and receiver, respectively, both in the E- and H- planes, and for angles $\phi = 45°$ and $\phi = 135°$. These angles correspond to the broadest and narrowest cross-sections of the radiation patterns. Figure A.13 shows the cross-polarized patterns in the E- and H- planes. The features of the radiation pattern are presented in Table A.4.

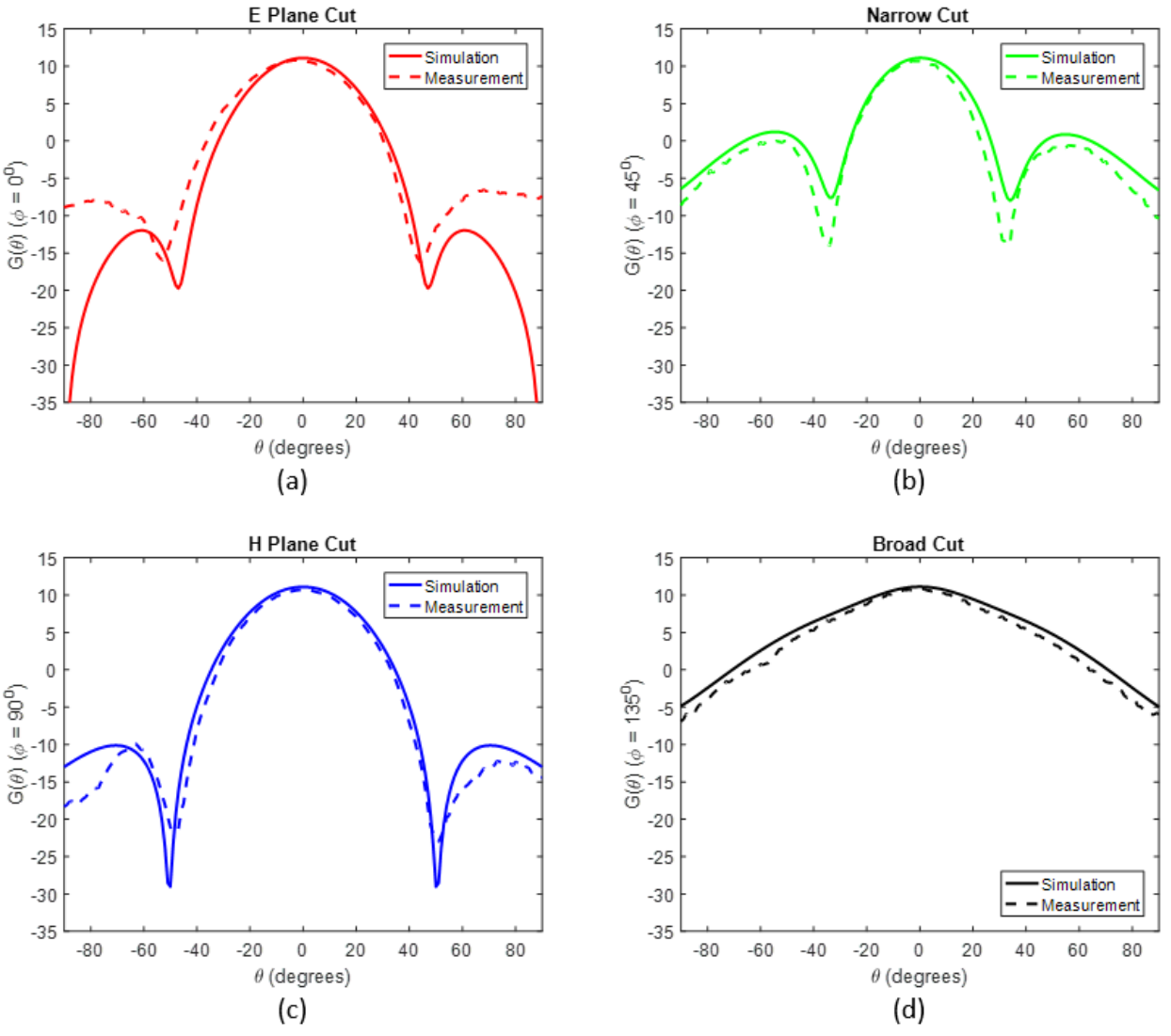

Figure A.11. Port 1 (transmitter) simulated and measured antenna radiation pattern at 6 GHz: (a) measured along the E-plane ($\phi = 0°$), (b) measured along the narrow cross-section of the pattern ($\phi = 45°$), (c) measured along the H-plane ($\phi = 90°$), and (d) measured along the broad cross-section of the pattern ($\phi = 135°$).

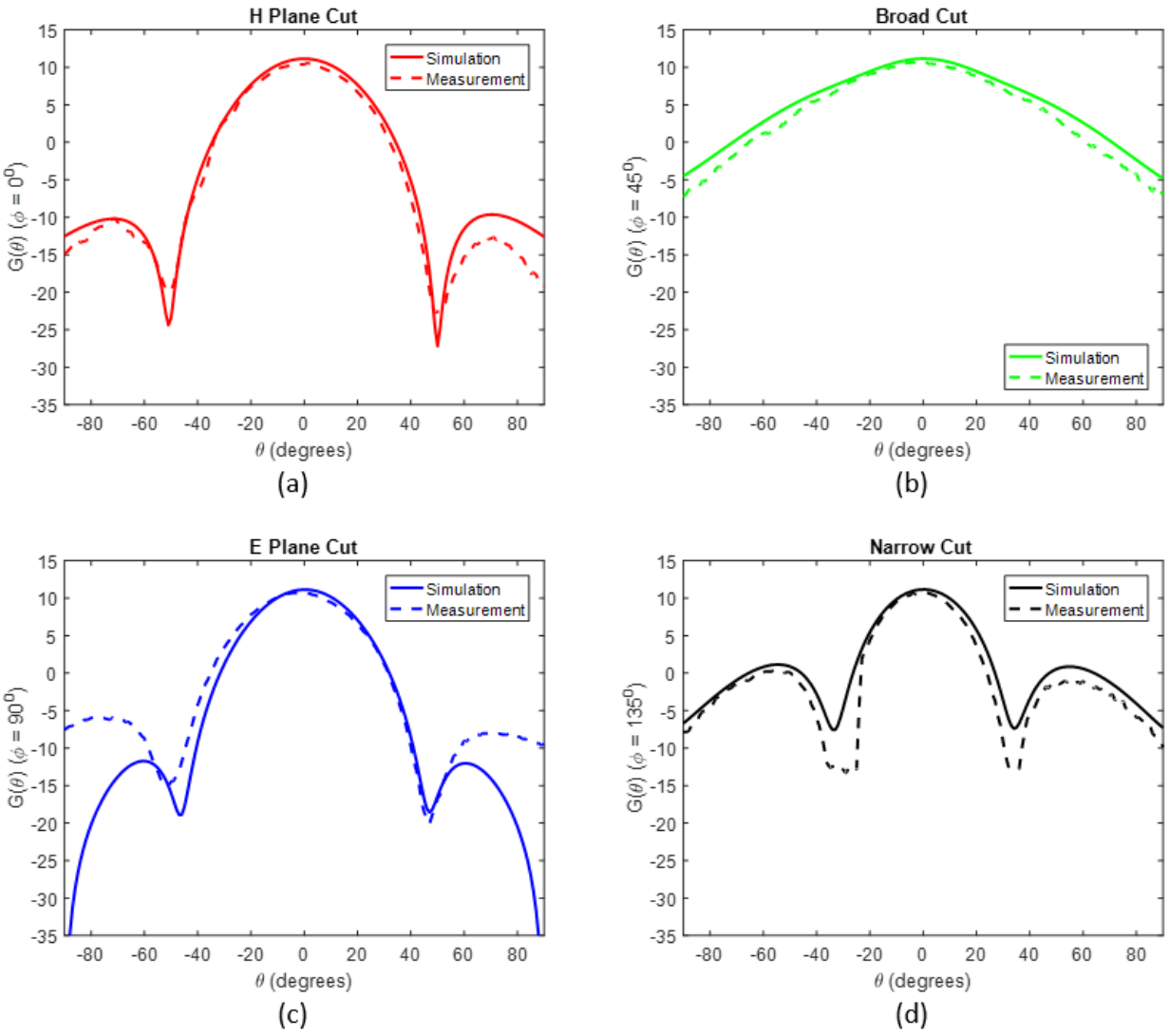

Figure A.12. Port 2 (receiver) simulated and measured antenna radiation pattern at 6 GHz: (a) measured along the H-plane ($\phi = 0°$), (b) measured along the broad cross-section of the pattern ($\phi = 45°$), (c) measured along the E-plane ($\phi = 90°$), and (d) measured along the narrow cross-section of the pattern ($\phi = 135°$).

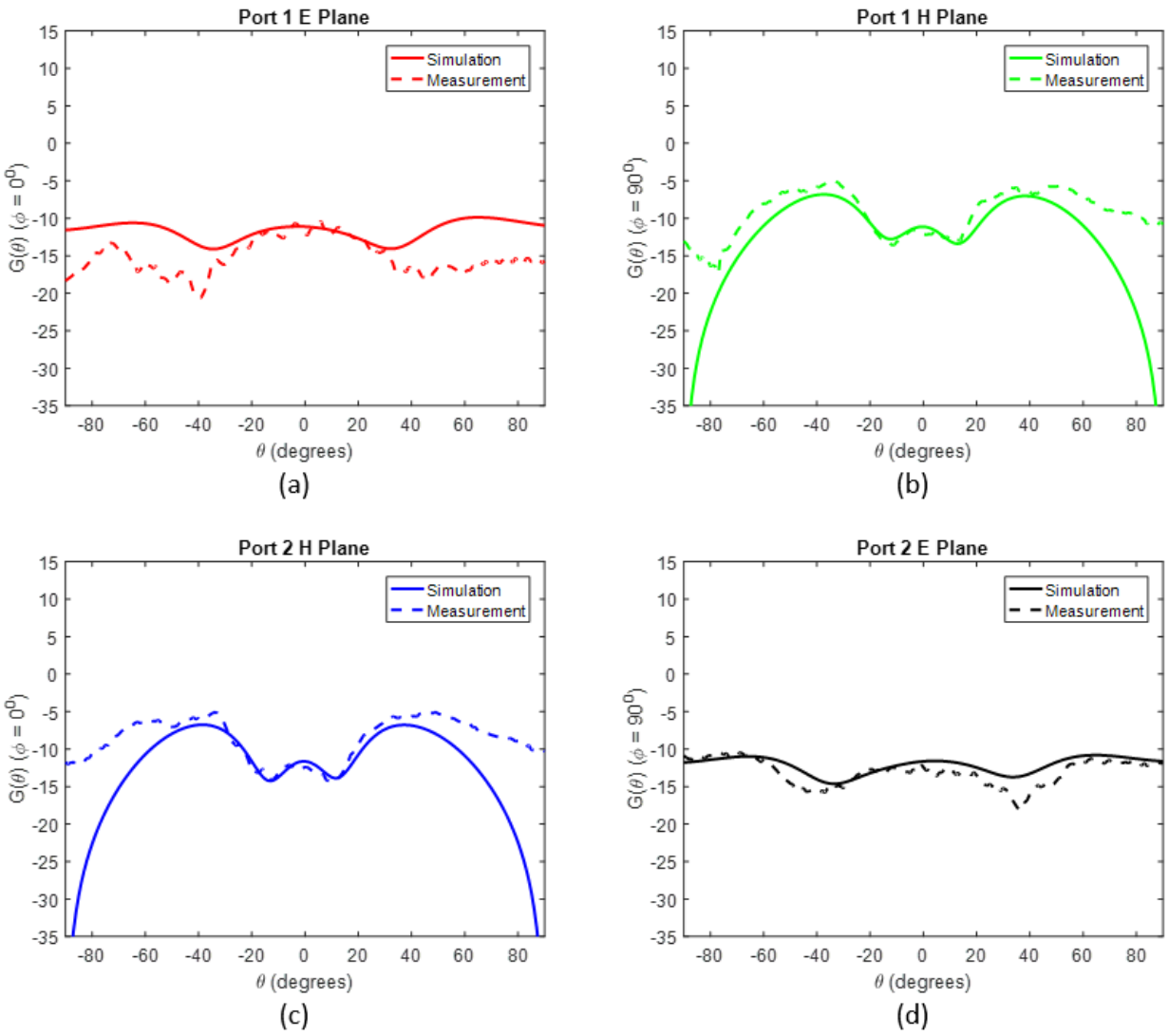

Figure A.13. Simulated and measured cross-polarized radiation pattern at 6 GHz: (a) measured along the E-plane of port 1, (b) measured along the H-plane of port 1, (c) measured along the H-plane of port 2, and (d) measured along the E-plane of port 2.

Table A.4
Antenna radiation pattern features at 6 GHz.

	Simulation	**Measurement**
Port 1:		
Peak Realized Gain	11.1 dB	10.7 dB
Cross-Pol. Gain ($\theta = 0°$)	-11.1 dB	-12.1 dB
3-dB Angles, Narrow Direction	-15°, +15°	-15°, +13°
3-dB Beamwidth, Narrow Direction	30°	28°
Null Angles, Narrow Direction	-34°, +34°	-34°, +33°
Sidelobe Angles, Narrow Direction	-55°, +55°	-57°, +56°
Sidelobe Level, Narrow Direction	-9.9 dB, -10.2 dB	-10.7 dB, -11.3 dB
3-dB Angles, Broad Direction	-29°, +29°	-27°, +26°
3-dB Beamwidth, Broad Direction	58°	53°
Port 2:		
Peak Realized Gain	11.2 dB	10.6 dB
Cross-Pol. Gain ($\theta = 0°$)	-11.6 dB	-12.4 dB
3-dB Angles, Narrow Direction	-15°, +15°	-15°, 14°
3-dB Beamwidth, Narrow Direction	30°	29°
Null Angles, Narrow Direction	-34°, +34°	-29°, +33°
Sidelobe Angles, Narrow Direction	-55°, +55°	-55°, +55°
Sidelobe Level, Narrow Direction	-10.1 dB, -10.3 dB	-10.2 dB, -11.4 dB
3-dB Angles, Broad Direction	-29°, +29°	-29°, +26°
3-dB Beamwidth, Broad Direction	58°	55°

A.6 Discussion

Although theoretically the symmetric array configuration used in this design should exhibit complete cancellation of coupled fields between the patch elements, and although simulations of the array without including the feed network indicated isolation potentially as high as 90 dB, the addition of the feed network reduces the simulated isolation to only 66.2 dB. A major contributing factor to this significant drop-off is the coupling between the microstrip lines within the feed network. For this reason, it is important to minimize the thickness of the feed network substrate in order to confine the fields closely around the copper traces. It is possible that using other transmission line architectures, such as stripline or grounded coplanar waveguide could provide

better performance. However, such transmission lines are more complicated to implement and here microstrip transmission lines were used to demonstrate the concept. Additionally, there is a correlation between the simulated isolation and the fineness of the mesh used in the substrates and copper traces, perhaps because a finer mesh more accurately preserves the structure's symmetry.

The performance of the prototype matches the simulated performance reasonably closely, both in terms of the scattering parameters and in terms of the radiation pattern. The measured isolation of 63.7 dB falls just short of the simulated value. The measured radiation pattern aligns very closely with the simulation, the major differences including a slight angular shift, a difference of around 1 to 2 dB on average over the angular sweep between the measured pattern and simulated pattern, and sharper nulls in the measured pattern along the narrow cross-section compared to the simulated pattern. The angular shift could be attributed to misalignment of the antenna boresights by around a degree during the setup for the measurement. The lower realized gain is likely due to losses in the system that were not accounted for in simulation, such as connector insertion loss and protective tin plating on the copper conductors. Additionally, the absolute gain measurement assumes that the antennas are separated by free space, which is not truly the case in an anechoic chamber, and this could lead to additional uncertainty in the measured gain. The sharp measured nulls may be a reflection of the fact that the total gain in the vicinity of the nulls receives a boost due to the presence of cross polarized fields, which are not received as strongly by the linearly polarized ancillary antenna.

While 63.7 dB is a relatively high isolation between transmit and receive ports in such close proximity, this does fall short of the isolation targeted to implement a communication system with simultaneous transmit and receive. However, several observed phenomena indicate that higher isolation levels should be possible. Although the antenna's isolation was measured in the

anechoic chamber in order to reduce the impact of reflections from the environment, very rapid fluctuations were still observed in the isolation response, which indicates that reflections are not entirely eliminated. Positioning an additional foam absorber in front of the antenna boresight has been found to improve the isolation slightly. Additionally, experimenting with the RF cables attached to the antenna system during the measurement has indicated that the isolation is sensitive to the position of these cables, since they perturb the ninety-degree rotational symmetry. Depending on the particular arrangement of the RF cables and the position of the foam absorber, measured isolation ranges from anywhere in the 60s of dB to more than 70 dB. The reported value of 63.7 dB corresponds to a typical result that is repeatable by simply making the measurement in the anechoic chamber with a direct cable connection and no additional absorber. In practice the transmitter and receiver circuitry would be embedded in the backplane of the antenna system and would thus be invisible to the radiating and receiving antennas. It is believed that the ninety-degree rotational symmetry used in this design is capable of achieving isolation levels of more than 70 dB and possibly more than 80 dB in the absence of the connectors and the RF cables used for the S_{21} measurement, especially with further optimization of the feed network.

A.7 Wideband Design

Additionally, it was intended to implement this concept not only for single frequency designs, but for wideband applications as well. One of the challenges associated with this is the need for a one-hundred-eighty-degree hybrid coupler that functions over a large bandwidth to feed the transmitters perfectly out of phase and subtract the received signals. Since this will be difficult to achieve over a wide bandwidth, it is useful to consider the effect of allowing a small deviation from perfect out-of-phase excitation and subtraction. Consider the following modifications to perfect out-of-phase conditions:

$$V_2^+ = -V_1^+ e^{j\Delta\phi_T}$$
$$V_R = V_3^- - V_4^- e^{j\Delta\phi_R}\,, \tag{A.6}$$

where $\Delta\phi_T$ and $\Delta\phi_R$ are the variations from 180° of the phase differences between the transmitter signals and receiver signals, respectively, and V_R is the total wave coupled to the receivers from the transmitters. Substituting (A.6) and (A.2) into (A.1), and allowing for impedance mismatch as in the second and third equations of (A.3), V_R can be solved for as follows:

$$V_R = V_1^+ \frac{S_3(1 - e^{j\Delta\phi_T})((1 - S_1\Gamma_4 + S_2\Gamma_4) - (1 - S_1\Gamma_3 + S_2\Gamma_3)e^{j\Delta\phi_R})}{(1 - S_1\Gamma_3)(1 - S_1\Gamma_4) - S_2^2\Gamma_3\Gamma_4}. \tag{A.7}$$

Based on estimates from simulations of the scattering parameters S_1, S_2, and S_3, and the reflection coefficients Γ_3 and Γ_4, (A.7) indicates that the received coupling from the transmitters can be kept below -80 dB if $\Delta\phi_T$ and $\Delta\phi_R$ are within about ±3° from zero. This result indicates that a wideband hybrid coupler with low phase imbalance will be required to implement a system using this symmetric configuration over a wide bandwidth.

To design a coupler capable of providing a 3 dB power split with a 180° phase difference over a bandwidth of about 25%, a microstrip rat race coupler (a standard coupler for out-of-phase power division, and the one used in the previous antenna design), is considered as a starting point [124]. However, due to the presence of the transmission line of length $3\lambda/4$ in the rat race, the perfect phase difference between the outputs is not held when the frequency drifts from the center frequency. To address this issue, the $3\lambda/4$ line has been replaced with a coupled line section of length $\lambda/4$ with one end of each line shorted, as in [125] and [126]. This configuration behaves like a quarter-wave transmission line in series with an ideal phase inverter, as shown in Figure A.14. Using this substitution provides a constant phase difference between the two coupler

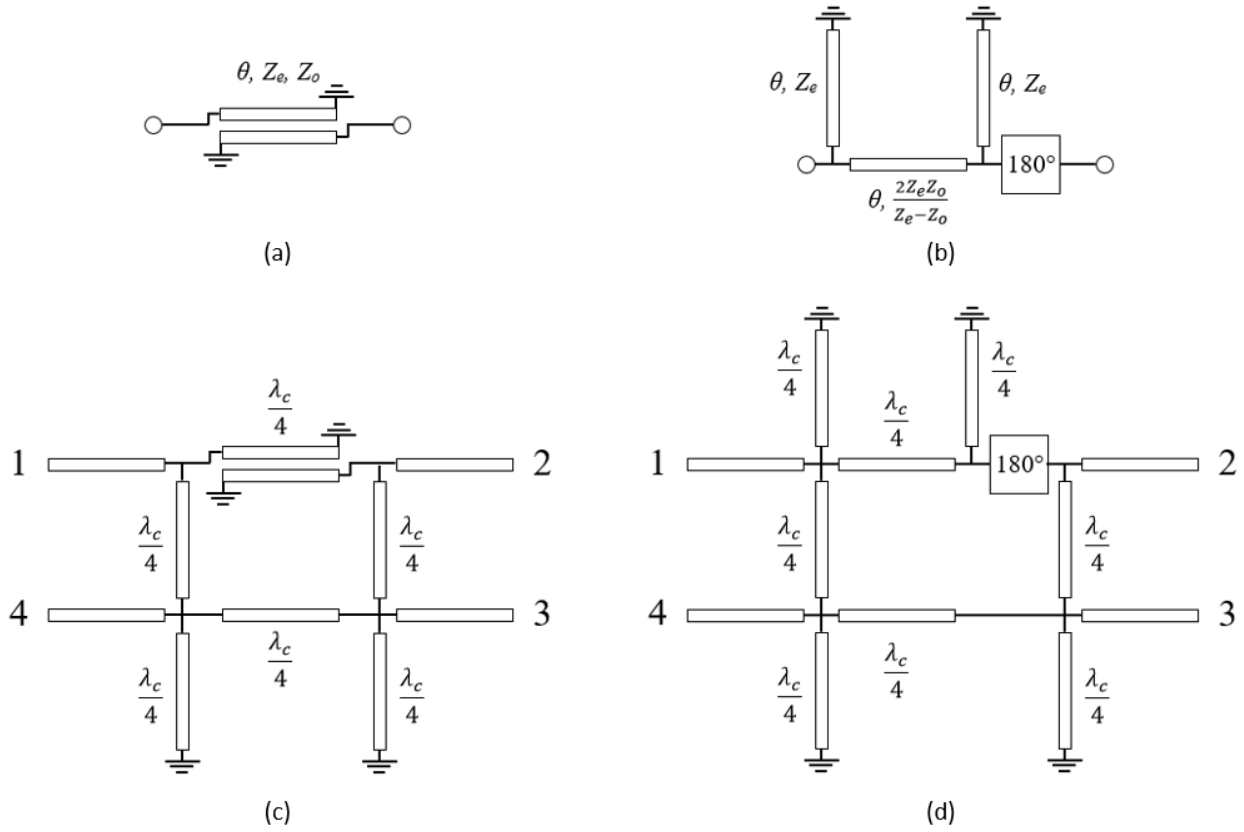

Figure A.14. The coupled line section with opposite ends of each line shorted in (a) can be modeled by the equivalent circuit in (b). Inserting (a) in place of the $3\lambda/4$ line of the rat-race coupler, as shown in (c), produces the equivalent circuit shown in (d). The extra shorted quarter wave lines are required to maintain the symmetry of the design. λ_c is the wavelength at the center frequency of the design band, and the 180° block represents an ideal phase inverter.

outputs (ports 2 and 4 when port 1 is used as the input) as frequency changes, since the two paths between ports 1 and 2 have the same physical length as the two paths between ports 1 and 4. This allows for the design of a wideband one-hundred-eighty-degree coupler. Because of the two shorted quarter-wave lines in the equivalent circuit for the coupled line section, additional shorted quarter-wave lines must be placed near ports 3 and 4 to maintain the symmetry of the coupler.

This method has been used to design a modified rat race coupler, which achieves an equal power split with less than 0.06 dB of amplitude imbalance and less than ±0.5° of phase imbalance over the 5.24 GHz – 6.94 GHz band (about 28% bandwidth). The simulated scattering parameters

of the coupler are shown in Figure A.15, while Figure A.16 shows the amplitude imbalance and phase imbalance.

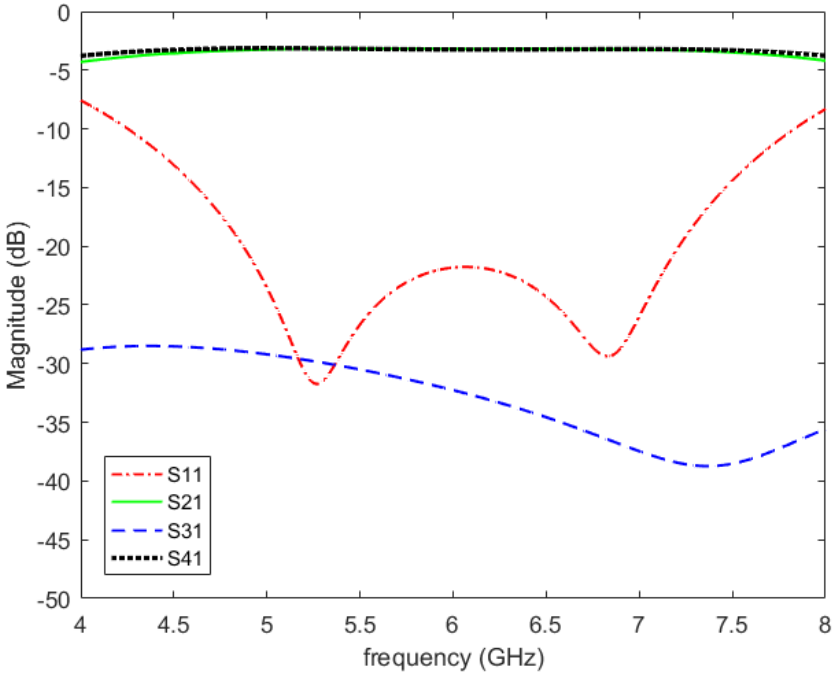

Figure A.15. The simulated scattering parameters of the wideband coupler are shown.

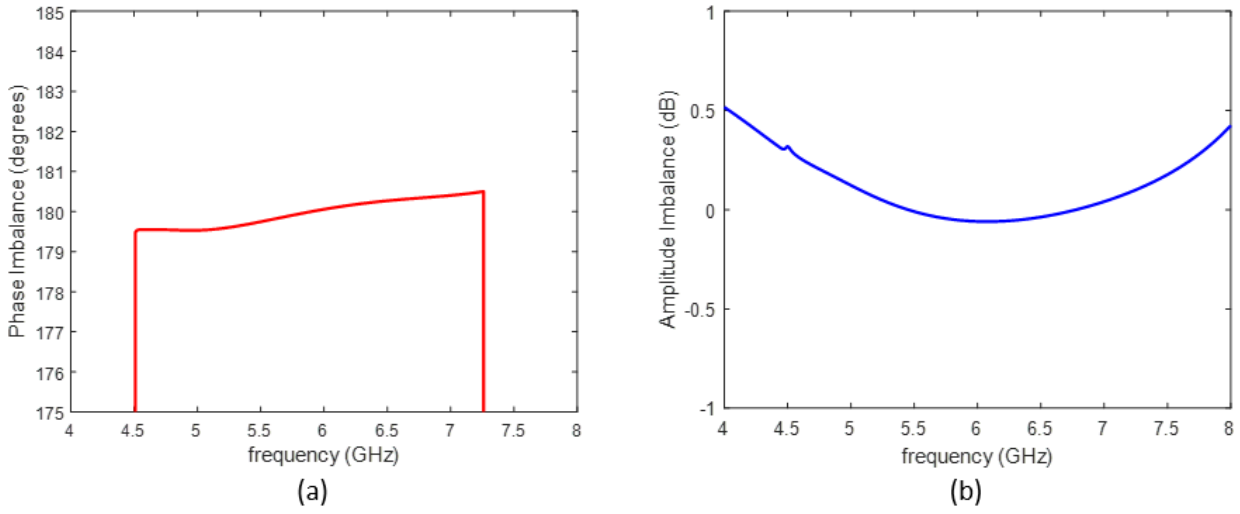

Figure A.16. The phase imbalance (a) and amplitude imbalance (b) between S_{41} and S_{21} of the wideband coupler are shown.

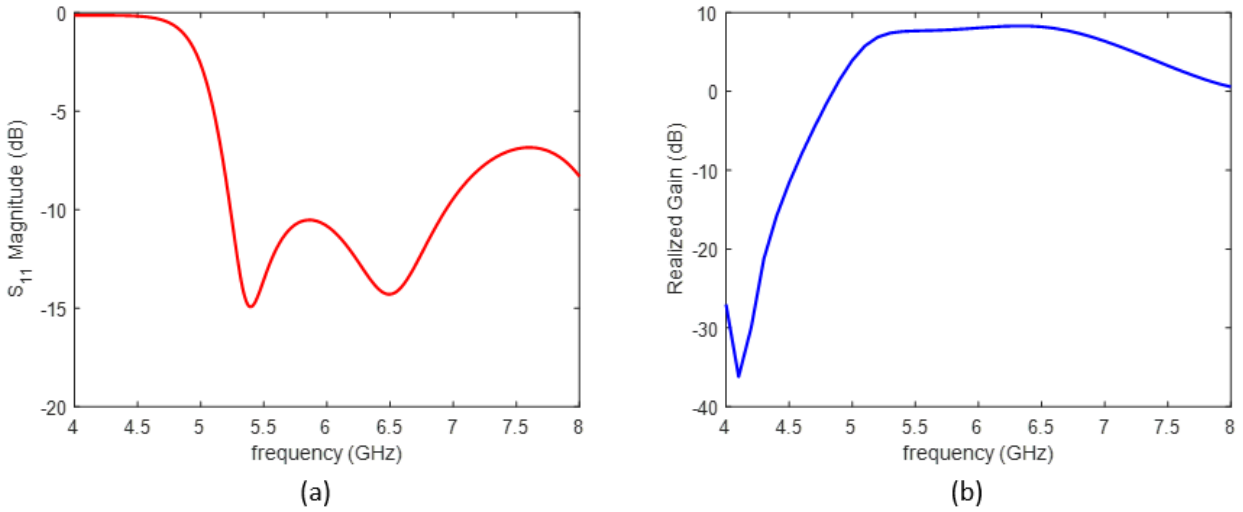

Figure A.17. Simulated (a) input reflection coefficient and (b) realized gain of the wideband U-slot patch antenna.

The patch elements used in the current design are matched only in a narrow frequency band centered at 6 GHz. In order to present the wideband coupler with a well-matched load over its operating band, new radiating elements must be designed. The U-slot patch is capable of bandwidth on the order of 25% – 30%, and should be suitable for this purpose. Figure A.17 shows the simulated reflection coefficient and gain of a U-slot patch designed for this purpose. This patch maintains a reflection coefficient below -10 dB and a gain above 6.6 dB across the 5.24 GHz – 6.94 GHz band.

The U-slot patch element was then arranged in the symmetric array configuration and combined with the wideband coupler to complete a wideband version of the full-duplex antenna. The simulated scattering parameters and gain of this design are shown in Figure A.18, and images of the simulation model are shown in Figure A.19, displaying the U-slot patch and wideband coupler geometry. This antenna achieves simulated return loss greater than 8.1 dB, isolation greater than 52.3 dB, and gain greater than 8.6 dB over the 5.24 GHz – 6.94 GHz band.

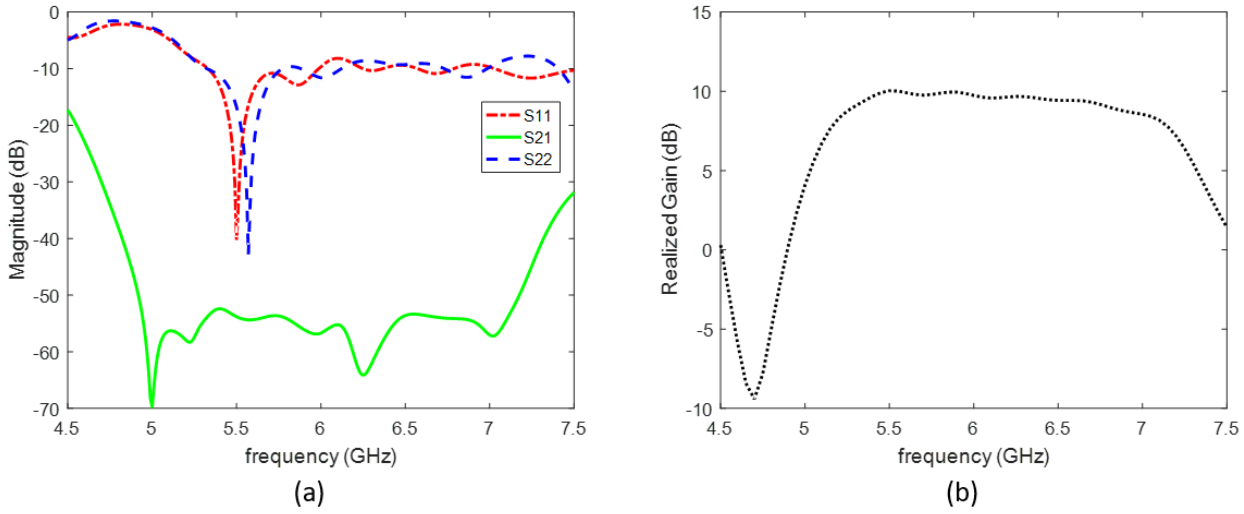

Figure A.18. Simulated (a) scattering parameters and (b) realized gain of the wideband two-port full-duplex antenna.

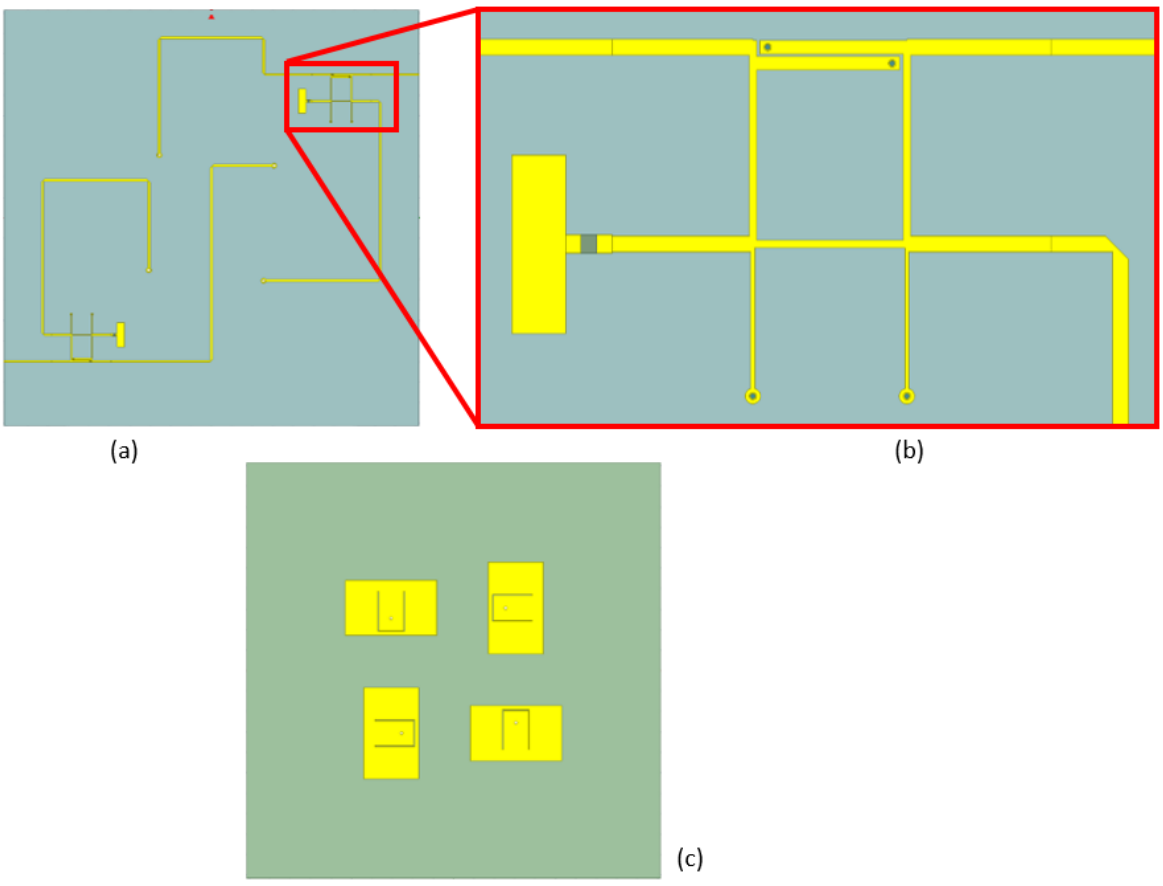

Figure A.19. Images of the wideband antenna model: (a) bottom view showing the feed network, including (b) the wideband coupler, and (c) top view showing the square array of U-slot patches.

A.8 Summary

In this appendix it is shown that using polarization orthogonality and rotational symmetry cancellation, it is possible to design a compact transmitter and receiver antenna system that has very high isolation between the two ports. By using a square grid array with ninety-degree rotational symmetry and one-hundred-eighty-degree hybrid couplers, a prototype antenna was constructed that matched simulation results well and exhibited isolation of 63.7 dB at the design frequency of 6 GHz. This is quite an impressive level of isolation for an antenna system without the aid of any analog or digital cancellation, especially considering that the patches are spaced less than a wavelength apart. These results are promising, since it is believed isolation levels of more than 70 dB and perhaps more than 80 dB are possible with additional design efforts. Isolation at this level would be usable in a full-duplex system with a very high receiver dynamic range.

Additionally, a one-hundred-eighty-degree hybrid coupler with low amplitude and phase imbalance over a bandwidth of 28% has been designed. It has been combined with U-slot patch elements with a similar bandwidth to create a wideband version of the full-duplex antenna system. Though this antenna was not fabricated, it exhibits more than 52.3 dB of isolation in simulation across the entire 5.24 GHz – 6.94 GHz band.

BIBLIOGRAPHY

[1] "Radar," *Merriam-Webster Dictionary*. [Online]. Available: https://www.merriam-webster.com/dictionary/radar.

[2] J. Goodrich, "How the Telemobiloskop Paved the Way for Modern Radar Systems," *IEEE Spectrum*, Nov. 2019. [Online]. Available: https://spectrum.ieee.org/how-the-telemobiloskop-paved-the-way-for-modern-radar-systems.

[3] D. Parry, "NRL History - RADAR," *NRL Press Releases*, U.S. Naval Research Laboratory, Washington, DC, Nov. 2010. [Online]. Available: https://www.nrl.navy.mil/Media/News/Article/2577147/nrl-history-november-1930/.

[4] G. Breit and M. A. Tuve, "A Test of the Existence of the Conducting Layer," *Physical Review*, vol. 28, no. 3, pp. 554-575, Sep. 1926, DOI: 10.1103/PhysRev.28.554.

[5] S. Matsuo, "A Direct-Reading Radio-Wave-Reflection Type Absolute Altimeter for Aeronautics," in *Proc. Inst. Radio Eng.*, vol. 26, no. 7, pp. 848-858, Jul. 1938, DOI: 10.1109/JRPROC.1938.228387.

[6] F. T. Ulaby and D. G. Long, "Introduction," in *Microwave Radar and Radiometric Remote Sensing*, 1st ed., Norwood, MA: Artech House, 2015, ch. 1, pp. 1-33, ISBN: 9780472119356.

[7] C. A. Doppler, "Über das farbige Licht der Doppelsterne und einiger anderer Gestirne des Himmels," May 1842.

[8] W. R. Fried, "History of Doppler Radar Navigation," *J. Inst. Navigation*, vol. 40, no. 2, pp. 121-136, 1993, DOI: 10.1002/j.2161-4296.1993.tb02299.x.

[9] "Everything You Ever Wanted to Know about the NWS WSR-88D," *National Weather Service*, U.S. Dept. of Commerce. [Online]. Available: https://www.weather.gov/iwx/wsr_88d.

[10] A. K. Fung and K. S. Chen, "Introduction to Microwave Scattering and Emission Models for Users," in *Microwave Scattering and Emission Models for Users*, 1st ed., Norwood, MA: Artech House, 2009, ch. 1, pp. 1-8, ISBN: 9781608070374.

[11] A. Viksne, T. C. Liston, C. D. Sapp, "SLR Reconnaissance of Panama," *Geophysics*, vol. 34, no. 1, pp. 54-64, Feb. 1969, DOI: 10.1190/1.1439997.

[12] Y. Oh, K. Sarabandi, and F. T. Ulaby, "An Empirical Model and an Inversion Technique for Radar Scattering from Bare Soil Surfaces," *IEEE Trans. Geosci. Remote Sens.*, vol. 30, no. 2, pp. 370-381, Mar. 1992, DOI: 10.1109/36.134086.

[13] Y. Oh, "Quantitative Retrieval of Soil Moisture Content and Surface Roughness from Multipolarized Radar Observations of Bare Soil Surfaces," *IEEE Trans. Geosci. Remote Sens.*, vol. 42, no. 3, pp. 596-601, Mar. 2004, DOI: 10.1109/TGRS.2003.821065.

[14] E. M. Kennaugh, *Effects of Type of Polarization On Echo Characteristics*, PN, 1952, DOI: 10.21236/ad0002493.

[15] J. R. Huynen, "Phenomenological Theory of Radar Targets," Ph.D. dissertation, Dept. Elect. Eng., Tech. Univ. Delft, Delft, NL, 1970.

[16] W.-M. Boerner, M. B. El-Arini, C.-Y. Chan, and P. M. Mastoris, "Polarization Dependence in Electromagnetic Inverse Problems," *IEEE Trans. Antennas Propag.*, vol. 29, no. 2, pp. 262-271, Mar. 1981, DOI: 10.1109/TAP.1981.1142585.

[17] S.-W. Chen, X.-S. Wang, S.-P. Xiao, and M. Sato, "Fundamentals of Polarimetric Radar Imaging and Interpretation," in *Target Scattering Mechanism in Polarimetric Synthetic Aperture Radar*, 1st ed., Singapore: Springer, 2018, ch. 1, pp. 1-42, DOI: 10.1007/978-981-10-7269-7.

[18] M. Galvani, "History and Future of Driver Assistance," *IEEE Instrumentation Meas. Mag.*, vol. 22, no. 1, pp. 11-16, Feb. 2019, DOI: 10.1109/MIM.2019.8633345.

[19] X. Xue and K. W. Cheng, "Electric Antilock Braking Systems for Electric Vehicles," in *Proc. 8th Int. Conf. Power Electronics Syst. Applications*, Hong Kong, CN, Dec. 2020, DOI: 10.1109/PESA50370.2020.9344016.

[20] "Automated Vehicles for Safety," *National Highway Traffic Safety Administration*, U.S. Dept. of Transportation. [Online]. Available: https://www.nhtsa.gov/technology-innovation/automated-vehicles-safety.

[21] "Laser," *Merriam-Webster Dictionary*. [Online]. Available: https://www.merriam-webster.com/dictionary/laser.

[22] "What is lidar?," *National Ocean Service*, U.S. Dept. of Commerce. [Online]. Available: https://oceanservice.noaa.gov/facts/lidar.html.

[23] M. Gardill, "Automotive Radar – An Overview on State-of-the-Art Technology," in *IEEE MTT-S Webinars*, Jun. 2018. [Online]. Available: https://mtt.org/webinar-library/automotive-radar-an-overview-on-state-of-the-art-technology/.

[24] F. T. Ulaby and D. G. Long, “Microwave Interaction with Atmospheric Constituents,” in *Microwave Radar and Radiometric Remote Sensing*, 1st ed., Norwood, MA: Artech House, 2015, ch. 8, pp. 325-365, ISBN: 9780472119356.

[25] H. P. Groll and J. Detlefsen, “History of Automotive Anticollision Radars and Final Experimental Results of a MM-Wave Car Radar Developed by the Technical University of Munich,” *IEEE Aerospace and Electronic Syst. Mag.*, vol. 12, no. 8, pp. 15-19, Aug. 1997, DOI: 10.1109/62.609525.

[26] H. H. Meinel, “Evolving Automotive Radar - From the Very Beginnings into the Future,” in *Proc. 8th European Conf. Antennas Propag.*, The Hague, NL, Apr. 2014, pp. 3107-3114, DOI: 10.1109/EuCAP.2014.6902486.

[27] W. P. Harokopus, “Application of Radar to Automobile Control and Sensing,” in *Proc. IEEE GMTT Int. Microwave Symp.*, Washington, DC, May 1971, pp. 168-169, DOI: 10.1109/GMTT.1971.1122950.

[28] M. Walden, “Automotive Radar – From Early Developments to Self-Driving Cars,” in *Proc. Automated RF Microwave Meas. Soc. Conf.*, Oxfordshire, UK, Apr. 2015. [Online]. Available: https://www.armms.org/media/uploads/p05---mark-walden---automotive-radar---from-early-.pdf.

[29] J. C. Reed, “Side Zone Automotive Radar Criteria for Target Classification,” in *Proc. Intell. Vehicles Symp.*, Detroit, MI, Sep. 1995, pp. 361-363, DOI: 10.1109/IVS.1995.528308.

[30] H. V. Le, H. T. Duong, A. T. Huynh, R. J. Evans, and E. Skafidas, “A CMOS 77 GHz Radar Receiver Front-End,” in *Proc. European Microwave Integrated Circuit Conf.*, Nuremberg, DE, Oct. 2013, pp. 13-16, ISBN: 978-2-87487-032-3.

[31] J. D. Woll, “Monopulse Doppler Radar for Vehicle Applications,” in *Proc. Intell. Vehicles Symp.*, Detroit, MI, Sep. 1995, pp. 42-47, DOI: 10.1109/IVS.1995.528255.

[32] “Mercedes-Benz Offers DISTRONIC PLUS Radar-Based Adaptive Cruise Control,” *Mercedes-Benz.* [Online]. Available: https://media.mbusa.com/releases/release-f7723158b8e95dfb10f856004e17673f-mercedes-benz-offers-distronic-plus-radar-based-adaptive-cruise-control.

[33] “Amendment of Parts 1, 2, 15, 90 and 95 of the Commission’s Rules to Permit Radar Services in the 76-81 GHz Band,” U.S. Federal Communications Commission, Washington, DC, FCC 17-94, Jul. 2017. [Online]. Available: https://docs.fcc.gov/public/attachments/FCC-17-94A1.pdf.

[34] “FCC Online Table of Frequency Allocations,” U.S. Federal Communications Commission, Washington, DC, 47 C.F.R. § 2.106, Feb. 2021. [Online]. Available: https://transition.fcc.gov/oet/spectrum/table/fcctable.pdf.

[35] D. W. Bliss and K. W. Forsythe, "Multiple-Input Multiple-Output (MIMO) Radar and Imaging: Degrees of Freedom and Resolution," in *Proc. Thirty-Seventh Asilomar Conf. on Signals Syst. Computers*, Pacific Grove, CA, Nov. 2003, pp. 54-59, DOI: 10.1109/ACSSC.2003.1291865.

[36] E. Fishler, A. Haimovich, R. Blum, D. Chizhik, L. Cimini, and R. Valenzuela, "MIMO Radar: An Idea Whose Time Has Come," in *Proc. IEEE Radar Conf.*, Philadelphia, PA, Apr. 2004, pp. 71-78, DOI: 10.1109/NRC.2004.1316398.

[37] S. Rao, "MIMO Radar," Texas Instruments, Dallas, TX, App. Rep. SWRA554A, Jul. 2018. [Online]. Available: https://www.ti.com/lit/an/swra554a/swra554a.pdf?ts=1635618711450.

[38] "ICON^{TM} Digital Radar," Magna International, Aurora, ON, 2021. [Online]. Available: https://www.magna.com/products/product/icon-digital-radar.

[39] "4D IMAGING RADAR: The World's First 2K Ultra-High Resolution Radar Platform," Arbe Robotics, Tel-Aviv-Yafo, IL, May 2021. [Online]. Available: https://arberobotics.com/wp-content/uploads/2021/05/4D-Imaging-radar-product-overview.pdf.

[40] "EAGLE Virtual Aperture Imaging Radar," Oculii, Beavercreek, OH, 2021. [Online]. Available: https://www.oculii.com/eagle.

[41] E. Levine, G. Malamud, S. Shtrikman, and D. Treves, "A Study of Microstrip Array Antennas with the Feed Network," *IEEE Trans. Antennas Propag.*, vol. 37, no. 4, pp. 426-434, Apr. 1989, DOI: 10.1109/8.24162.

[42] Y. Rahmat-Samii and A. Densmore, "A History of Reflector Antenna Development: Past, Present and Future," in *Proc. SBMO/IEEE MTT-S Int. Microwave and Optoelectronics Conf.*, Belem, BR, Nov. 2009, pp. 17-23, DOI: 10.1109/IMOC.2009.5427640.

[43] D. G. Bodnar, "Lens Antennas," in *Antenna Engineering Handbook*, 4th ed., J. L. Volakis, Ed., New York, NY: McGraw-Hill, 2007, ch. 18, DOI: 10.1036/0071475745.

[44] K. B. Cooper and G. Chattopadhyay, "Submillimeter-Wave Radar: Solid-State System Design and Applications," *IEEE Microwave Mag.*, vol. 15, no. 7, pp. 51-67, Nov. 2014, DOI: 10.1109/MMM.2014.2356092.

[45] M. Rodwell, E. Lobisser, M. Wistey, V. Jain, A. Baraskar, E. Lind, J. Koo, B. Thibeault, A. C. Gossard, Z. Griffith, J. Hacker, M. Urteaga, D. Mensa, R. Pierson, and B. Brar, "Development of THz Transistors and (300-3000 GHz) Sub-MM-Wave Integrated Circuits," in *Proc. Int. Symp. Wireless Personal Multimedia Communications*, Lapland, FI, Sep. 2008, pp. 1-5.

[46] A. Y. Nashashibi, A. A. Ibrahim, S. Cook, and K. Sarabandi, "Experimental Characterization of Polarimetric Radar Backscatter Response of Distributed Targets at High Millimeter-Wave Frequencies," *IEEE Trans. Geosci. Remote Sens*., vol. 54, no. 2, pp. 1013-1024, Feb. 2016, DOI: 10.1109/TGRS.2015.2472340.

[47] K. Statnikov, N. Sarmah, J. Grzyb, S. Malz, B. Heinemann, and U. R. Pfeiffer, "A 240 GHz Circular Polarized FMCW Radar Based on a SiGe Transceiver with a Lens-Integrated On-Chip Antenna," in *Proc. European Radar Conf.*, Rome, IT, Oct. 2014, pp. 447-450, DOI: 10.1109/EuRAD.2014.6991303.

[48] F. Teberio, I. Calero, V. Torres, A. Marzo, J. Teniente, and I. Maestrojuán, "Dual Polarized Lens Horn Antenna for Fixed-Beam D-Band Backhaul Systems," in *Proc. Int. Conf. Infrared Millimeter Terahertz Waves*, Chengdu, CN, Sep. 2021, pp. 1-2, DOI: 10.1109/IRMMW-THz50926.2021.9567401.

[49] A. A. Alaqeel, A. A. Ibrahim, A. Y. Nashashibi, H. N. Shaman, and K. Sarabandi, "Experimental Characterization of Multi-Polarization Radar Backscatter Response of Vehicles at J-Band," *IEEE Trans. Intell. Transp. Syst.*, vol. 20, no. 9, pp. 3337-3350, Nov. 2018, DOI: 10.1109/TITS.2018.2876155.

[50] A. Y. Nashashibi, B. Alazem, and K. Sarabandi, "Fully Polarimetric FMCW Instrumentation Radar at 228 GHz," in *Proc. USNC-URSI Radio Science Meeting*, San Diego, CA, Jul. 2017, pp. 35-36, DOI: 10.1109/USNC-URSI.2017.8074884.

[51] K. Sarabandi, A. Jam, M. Vahidpour, and J. East, "A Novel Frequency Beam-Steering Antenna Array for Submillimeter-Wave Applications," *IEEE Trans. Terahertz Sci. Tech*., vol. 8, no. 6, pp. 654-665, Nov. 2018, DOI: 10.1109/TTHZ.2018.2866019.

[52] G. Taylor, "Advanced Satellite System Could Measure Ice Crystals to Improve Weather and Climate Modeling," *NASA's Earth Science Technology Office*, U.S. National Aeronautics and Space Administration, Washington, DC, Jun. 2021. [Online]. Available: https://esto.nasa.gov/advanced-satellite-system-could-measure-ice-crystals-to-improve-weather-and-climate-modeling/.

[53] A. A. Alaqeel, A. A. Ibrahim, A. Y. Nashashibi, H. N. Shaman, and K. Sarabandi, "A Phenomenological Study of Radar Backscatter Response of Vehicles for the Next Generation Automotive Radars," in *Proc. IEEE Int. Geosci. Remote Sens. Symp.*, Valencia, ES, Jul. 2018, pp. 4063-4065, DOI: 10.1109/IGARSS.2018.8517358.

[54] A. A. Alaqeel, A. A. Ibrahim, A. Y. Nashashibi, H. N. Shaman, and K. Sarabandi, "Near-Grazing Radar Backscattering Measurements of Road Surfaces at 222 GHz," in *Proc. IEEE Int. Geosci. Remote Sens. Symp.*, Fort Worth, TX, Jul. 2017, pp. 2322-2324, DOI: 10.1109/IGARSS.2017.8127455.

[55] A. Kuriyama, H. Nagaishi, H. Kuroda, and K. Takano, "A High Efficiency Antenna with Horn and Lens for 77 GHz Automotive Long Range Radar," in *Proc. European Microwave Conf.*, London, UK, Oct. 2016, pp. 1525-1428, DOI: 10.1109/EuMC.2016.7824646.

[56] V. Winkler, R. Feger, and L. Maurer, “79GHz Automotive Short Range Radar Sensor based on Single-Chip SiGe-Transceivers,” in *Proc. European Radar Conf.*, Amsterdam, NL, Oct. 2008, pp. 459-462, DOI: 10.1109/EUMC.2008.4751781.

[57] S. M. Sekelsky and E. E. Clothiaux, “Parallax Errors and Corrections for Dual-Antenna Millimeter-Wave Cloud Radars,” *J. Atmospheric Oceanic Tech.*, vol. 19, no. 4, pp. 478-485, Apr. 2002, DOI: 10.1175/1520-0426(2002)019<0478:PEACFD>2.0.CO;2.

[58] J. D. Fernie, “The Historical Search for Stellar Parallax,” *J. Royal Astronomical Soc. Canada*, vol. 69, pp. 222-238.

[59] A. Y. Nashashibi, J. Lee, and K. Sarabandi, “Compact FMCW Design for Short Range Millimeter-Wave Radar Imaging Applications,” in *Proc. IEEE Radar Conf.*, Kansas City, MO, May 2011, pp. 885-888, DOI: 10.1109/RADAR.2011.5960664.

[60] M. Z. Rangwala, F. Wang, and K. Sarabandi, “Study of Millimeter-Wave Radar for Helicopter Assisted Landing System,” *IEEE Antennas Propag. Mag.*, vol. 50, no. 2, pp. 13-25, Apr. 2008, DOI: 10.1109/MAP.2008.4562254.

[61] K. Sarabandi and E. S. Li, “Characterization of Optimum Polarization for Multiple Target Discrimination Using Genetic Algorithms,” *IEEE Trans. Antennas Propag.*, vol. 45, no. 12, pp. 1810-1817, Dec. 1997, DOI: 10.1109/8.650199.

[62] M. Pehlivan and K. Yegin, “Self-jamming and Interference Cancellation Techniques for Continuous Wave Bi-Static Radar Systems,” in *Proc. Int. Microwave Radar Conf.*, Poznan, PL, May 2018, pp. 255-257, DOI: 10.23919/MIKON.2018.8405192.

[63] A. Melzer, F. Starzer, H. Jäger, and M. Huemer, "Real-Time Mitigation of Short-Range Leakage in Automotive FMCW Radar Transceivers," *IEEE Trans. Circuits Systems II: Express Briefs*, vol. 64, no. 7, pp. 847-851, Jul. 2017, DOI: 10.1109/TCSII.2016.2609467.

[64] C. Granet and G. L. James, “Design of Corrugated Horns: A Primer,” *IEEE Antennas Propag. Mag.*, vol. 47, no. 2, pp. 76-84, Apr. 2005, DOI: 10.1109/MAP.2005.1487785.

[65] P. Wade, “Parabolic Dish Antennas,” in *The W1GHZ Online Microwave Antenna Book*, Mar. 1998, ch. 4. [Online]. Available: https://www.qsl.net/n1bwt/chap4.pdf.

[66] A. V. Boriskin, R. Sauleau, and A. I. Nosich, “Performance of Hemielliptic Dielectric Lens Antennas With Optimal Edge Illumination,” *IEEE Trans. Antennas Propag.*, vol. 57, no. 7, pp. 2193-2198, Jul. 2009, DOI: 10.1109/TAP.2009.2021979.

[67] T. S. Bird and A. W. Love, “Horn Antennas,” in *Antenna Engineering Handbook*, 4th ed., J. L. Volakis, Ed., New York, NY: McGraw-Hill, 2007, ch. 14, DOI: 10.1036/0071475745.

[68] R. C. Hansen, “Aperture Theory,” in *Microwave Scanning Antennas, Volume I: Apertures*, New York, NY, Academic Press, 1964, ch. 1, pp. 1-105, DOI: 10.1016/B978-0-12-323901-3.50008-5.

[69] *IEEE Standard Test Procedures for Antennas*, ANSI/IEEE Standard 149-1979 (R2008), 2008, p. 1-129, DOI: 10.1109/IEEESTD.1979.120310.

[70] A. Jam and K. Sarabandi, "A Submillimeter-Wave Near-Field Measurement Setup for On-Wafer Pattern and Gain Characterization of Antennas and Arrays," *IEEE Trans. Instrumentation Meas.*, vol. 66, no. 4, pp. 802-811, Apr. 2017, DOI: 10.1109/TIM.2017.2654128.

[71] F. T. Ulaby and D. G. Long, "Remote-Sensing Antennas," in *Microwave Radar and Radiometric Remote Sensing*, 1st ed., Norwood, MA: Artech House, 2015, ch. 3, pp. 75-121, ISBN: 9780472119356

[72] F. T. Ulaby and D. G. Long, "Radar Scattering," in *Microwave Radar and Radiometric Remote Sensing*, 1st ed., Norwood, MA: Artech House, 2015, ch. 5, pp. 163-225, ISBN: 9780472119356.

[73] H. Tao, W. J. Padilla, X. Zhang, and R. D. Averitt, "Recent Progress in Electromagnetic Metamaterial Devices for Terahertz Applications," *IEEE J. Selected Topics Quantum Electronics*, vol. 17, no. 1, pp. 92-101, Jun. 2011, DOI: 10.1109/JSTQE.2010.2047847.

[74] A. Alù and N. Engheta, "Enabling a New Degree of Wave Control with Metamaterials: A Personal Perspective," *J. Opt.*, vol. 19, no. 8, Jul. 2017, DOI: 10.1088/2040-8986/aa7790.

[75] X. Fu and T. J. Cui, "Recent Progress on Metamaterials: From Effective Medium Model to Real-time Information Processing System," *Progress Quantum Electronics*, vol. 67, Sep. 2019, DOI:10.1016/J.PQUANTELEC.2019.05.001.

[76] A. Arbabi, Y. Horie, M. Bagheri, and A. Faraon, "Dielectric Metasurfaces for Complete Control of Phase and Polarization with Subwavelength Spatial Resolution and High Transmission," *Nature Nanotech.*, vol. 10, no. 11, pp. 937-943, Nov. 2015, DOI: 10.1038/nnano.2015.186.

[77] A. Ranjbar and A. Grbic, "All-Dielectric Bianisotropic Metasurfaces," in *Proc. IEEE Int. Symp. Antennas Propag.*, San Diego, CA, Jul. 2017, pp. 1719-1720, DOI: 10.1109/APUSNCURSINRSM.2017.8072902.

[78] K. Sarabandi and F. Bayatpur, "Miniaturized-Element Frequency Selective Surfaces," in *Proc. Int. Union Radio Sci. Gen. Assem.*, Chicago, IL, Aug. 2008.

[79] F. Bayatpur and K. Sarabandi, "Design and Analysis of a Tunable Miniaturized-Element Frequency-Selective Surface without Bias Network," *IEEE Trans. Antennas Propag.*, vol. 58, no. 4, pp. 1214-1219, Apr. 2010, DOI: 10.1109/TAP.2010.2041173.

[80] F. Bayatpur and K. Sarabandi, "A Tunable Metamaterial Frequency-Selective Surface with Variable Modes of Operation," *IEEE Trans. Microwave Theory Techniques*, vol. 57, no. 6, pp. 1433-1438, Jun. 2009, DOI: 10.1109/TMTT.2009.2020841.

[81] R. Watanabe, "A Novel Polarization-Independent Beam Splitter," *IEEE Trans. Microwave Theory Techniques*, vol. 28, no. 7, pp. 685-689, Jul. 1980, DOI: 10.1109/TMTT.1980.1130148.

[82] F. T. Ulaby and D. G. Long, "Electromagnetic Wave Propagation and Reflection," in *Microwave Radar and Radiometric Remote Sensing*, 1st ed., Norwood, MA: Artech House, 2015, ch. 2, pp. 35-73, ISBN: 9780472119356.

[83] K. Sarabandi, "Simulation of a Periodic Dielectric Corrugation with an Equivalent Anisotropic Layer," *Int. J. Infrared Millimeter Waves*, vol. 11, no. 11, pp. 1303-1321, Nov. 1990, DOI: 10.1007/BF01015940.

[84] M. Born and E. Wolf, *Principles of Optics: Electromagnetic Theory of Propagation, Interference and Diffraction of Light*, 7th ed. Cambridge, UK, Univ. Press, 1999, DOI: 10.1017/CBO9781139644181.

[85] P. Markoš and C. M. Soukoulis, "Transfer Matrix," in *Wave Propagation: From Electrons to Photonic Crystals and Left-Handed Materials*, Princeton, NJ, Univ. Press, 2008, ch. 1, pp. 1-27.

[86] F. Laermer, S. Franssila, L. Sainiemi, and K. Kolari, "Deep Reactive Ion Etching," in *Handbook of Silicon Based MEMS Materials and Technologies (Micro and Nano Technologies)*, 2nd ed., Norwich, NY, William Andrew, 2015, ch. 21, pp. 444-469, DOI: 10.1016/B978-0-323-29965-7.00021-X.

[87] K. J. Owen, "STS Pegasus 4/Processes/LNF Recipe 3," *LNF Wiki*, Lurie Nanofabrication Facility, Ann Arbor, MI, Mar. 2021. [Online]. Available: https://lnf-wiki.eecs.umich.edu/wiki/STS_Pegasus_4/Processes/LNF_Recipe_3.

[88] A. Dunning, S. Srikanth, and A. R. Kerr, "A Simple Orthomode Transducer for Centimeter to Submillimeter Wavelengths," in *Proc. 20th Int. Symp. Space Terahertz Tech.*, Charlottesville, VA, Apr. 2009, pp. 191-194, DOI: 102.100.100/115122.

[89] T. J. Reck and G. Chattopadhyay, "A 600 GHz Asymmetrical Orthogonal Mode Transducer," *IEEE Microwave Wireless Component Let.*, vol. 23, no. 11, pp. 569-571, Nov. 2013, DOI: 10.1109/LMWC.2013.2280642.

[90] C. Groppi, A. Navarrini, and G. Chattopadhyay, "A Waveguide Orthomode Transducer for 385-500 GHz", in *Proc. SPIE 7741, Millimeter, Submillimeter, Far-Infrared Detectors Instrumentation Astronomy V, 77412D*, San Diego, CA, Jul. 2010, pp. 1-11, DOI: 10.1117/12.857417.

[91] M. Kamikura, M. Naruse, S. Asayama, N. Satou, W. Shan, and Y. Sekimoto, "Development of a Submillimeter Double-Ridged Waveguide Ortho-Mode Transducer (OMT) for the 385–500 GHz Band," *J. Infrared Millimeter Terahertz Waves*, vol. 31, pp. 697-707, Jun. 2010, DOI: 10.1007/s10762-010-9632-1.

[92] A. Navarrini and R. L. Plambeck, "A Turnstile Junction Waveguide Orthomode Transducer," *IEEE Trans. Microwave Theory Techniques*, vol. 54, no. 1, pp. 272-277, Jan. 2006, DOI: 10.1109/TMTT.2005.860505.

[93] A. Gomez-Torrent, U. Shah, and J. Oberhammer, "Compact Silicon-Micromachined Wideband 220–330-GHz Turnstile Orthomode Transducer," *IEEE Trans. Terahertz Sci. Tech.*, vol. 9, no. 1, pp. 38-46, Jan. 2019, DOI: 10.1109/TTHZ.2018.2882745.

[94] T. Qin, X. Q. Lin, and Y. X. Kang, "A Simple Terahertz Orthomode Transducer Based on Equivalent Circuits Analysis," in *Proc. IEEE MTT-S Int. Microwave Workshop Series Advanced Materials Processes RF THz Applications*, Suzhou, CN, Jul. 2020, DOI: 10.1109/IMWS-AMP49156.2020.9199667.

[95] K. Sarabandi and F. T. Ulaby, "A Convenient Technique for Polarimetric Calibration of Single-Antenna Radar Systems," *IEEE Trans. Geosci. Remote Sens.*, vol. 28, no. 6, pp. 1022-1033, Nov. 1990, DOI: 10.1109/36.62627.

[96] G. L. Ragan, "Transition Units," in *Microwave Transmission Circuits*, 1st ed., New York, NY: McGraw-Hill, 1948, ch. 6, pp. 305-405.

[97] A. Navarrini and R. Nesti, "Characterization Techniques of Millimeter-Wave Orthomode Transducers (OMTs)," *Electronics*, vol. 10, no. 15, 1844, pp. 1-33, Jul. 2021, DOI: 10.3390/electronics10151844.

[98] M. Taraba, J. Adamec, M. Danko, and P. Drgona, "Utilization of Modern Sensors in Autonomous Vehicles," in *Proc. 2018 ELEKTRO*, Mikulov, CZ, May 2018, DOI: 10.1109/ELEKTRO.2018.8398279.

[99] K. Sarabandi, E. S. Li, and A. Y. Nashashibi, "Modeling and Measurements of Scattering from Road Surfaces at Millimeter-Wave Frequencies," *IEEE Trans. Antennas Propag.*, vol. 45, no. 11, pp. 1679-1688, Nov. 1997, DOI: 10.1109/8.650080.

[100] A. Y. Nashashibi, M. Kashanianfard, T. J. Douglas, K. Sarabandi, and S. W. Decker, "Fully Polarimetric E-Band Instrumentation Radar in Support of Autonomous Vehicle Research," in *Proc. IEEE USNC-CNC-URSI North American Radio Sci. Meeting*, Montreal, QC, Jul. 2020, pp. 97-98, DOI: 10.23919/USNC/URSI49741.2020.9321601.

[101] K. Sarabandi, F. T. Ulaby, and M. A. Tassoudji, "Calibration of Polarimetric Radar Systems with Good Polarization Isolation," *IEEE Trans. Geosci. Remote Sens.*, vol. 28, no. 1, pp. 70-75, Jan. 1990, DOI: 10.1109/36.45747.

[102] S. Tsugawa, "A History of Automated Highway Systems in Japan and Future Issues," in *Proc. IEEE Int. Conf. Vehicular Electronics Safety*, Columbus, OH, Sep. 2008, pp. 2-3, DOI: 10.1109/ICVES.2008.4640914.

[103] A. Asaoka and S. Ueda, "An Experimental Study of a Magnetic Sensor in an Automated Highway System," in *Proc. Conf. Intell. Vehicles*, Tokyo, JP, Sep. 1996, DOI: 10.1109/IVS.1996.566409.

[104] Z. Feng, M. Li, M. Stolz, M. Kunert, and W. Wiesbeck, "Lane Detection with a High-Resolution Automotive Radar by Introducing a New Type of Road Marking," *IEEE Trans. Intell. Transp. Syst.*, vol. 20, no. 7, pp. 2430-2447, Jul. 2019, DOI: 10.1109/TITS.2018.2866079.

[105] W. Hong and K. Sarabandi, "Low-Profile, Multi-Element, Miniaturized Monopole Antenna," *IEEE Trans. Antennas Propag.*, vol. 57, no. 1, pp. 72-80, Jan. 2009, DOI: 10.1109/TAP.2008.2009731.

[106] J. Oh, J. Choi, F. T. Dagefu, and K. Sarabandi, "Extremely Small Two-Element Monopole Antenna for HF Band Applications," *IEEE Trans. Antennas Propag.*, vol. 61, no. 6, pp. 2991-2999, Jun. 2013, DOI: 10.1109/TAP.2013.2249034.

[107] M. Rao and K. Sarabandi, "A Low-Profile Dual-Band Dual-Polarized Quazi-Endfire Phased Array for mmWave 5G Smartphones," *IEEE Access*, vol. 10, pp. 38523-38533, Apr. 2022, DOI: 10.1109/ACCESS.2022.3165562.

[108] R. G. Pierce, R. Islam, R. M. Henderson, and A. Blanchard, "SU-8 2000 Millimeter Wave Material Characterization," *IEEE Microwave Wireless Components Lett.*, vol. 24, no. 6, pp. 427-429, Jun. 2014, DOI: 10.1109/LMWC.2014.2313475.

[109] A. Elsherbini, "Radar Remote Sensing of Arid Regions," Ph.D. dissertation, Dept. Elect. Eng. Comput. Sci., Univ. Michigan, Ann Arbor, 2011.

[110] A. Y. Nashashibi, A. A. Alaqeel, H. N. Shaman, and K. Sarabandi, "High-Resolution J-Band Radar with Continuous 360° Imaging Capability for Autonomous Vehicle Applications," in Proc. USNC-URSI Radio Science Meeting, Atlanta, GA, Jul. 2019. [Online]. Available: https://usnc-ursi-archive.org/aps-ursi/2019/abstracts/2018.pdf.

[111] A. Jam, J. East, and K. Sarabandi, "A Micromachined Packaging with Incorporated RF-Choke for Integration of Active Chips at Submillimeter-Wave Frequencies," in *Proc. IEEE MTT-S Int. Microwave Symp.*, Honolulu, HI, Jun. 2017, pp. 507-509, DOI: 10.1109/MWSYM.2017.8058610.

[112] J. I. Choi, M. Jain, K. Srinivasan, P. Levis, and S. Katti, "Achieving Single Channel, Full Duplex Wireless Communication," in *Proc. ACM MobiCom*, Chicago, IL, Sep. 2010, pp. 1-12, DOI: 10.1145/1859995.1859997.

[113] M. Duarte and A. Sabharwal, "Full-Duplex Wireless Communications Using Off-the-Shelf Radios: Feasibility and First Results," in *Proc. Asilomar Conf. Signals, Syst., Comput.*, Pacific Grove, CA, Nov. 2010, pp. 1558-1562, DOI: 10.1109/ACSSC.2010.5757799.

[114] M. W. Whitt, F. T. Ulaby, and K. Sarabandi, "Polarimetric Scatterometer Systems and Measurements," in *Radar Polarimetry for Geoscience Applications*, 1st ed., F. T. Ulaby and C. Elachi, Ed., Norwood, MA: Artech House, 1990, ch. 5, pp. 191-272, ISBN: 978-0890064061.

[115] D. Richardson, “An FMCW Radar Sensor for Collision Avoidance,” in *Proc. Conf. Intell. Transp. Syst.*, Boston, MA, Aug. 2002, pp. 427-432, DOI: 10.1109/ITSC.1997.660513.

[116] K. Sarabandi, Y. Oh, and F. T. Ulaby, “Performance Characterization of Polarimetric Active Radar Calibrators and a New Single Antenna Design,” *IEEE Trans. Antennas Propag.*, vol. 40, no. 10, pp. 1147-1154, Oct. 1992, DOI: 10.1109/8.182446.

[117] K. Sarabandi, M. Kashanianfard, A. Y. Nashashibi, L. E. Pierce, and R. Hampton, “A Polarimetric Active Transponder with Extremely Large RCS for Absolute Radiometric Calibration of SMAP Radar,” *IEEE Trans. Geosci. Remote Sens.*, vol. 56, no. 3, pp. 1269-1277, Mar. 2018, DOI: 10.1109/TGRS.2017.2745206.

[118] J. Q. Howell, “Microstrip Antennas,” *IEEE Trans. Antennas Propag.*, vol. 23, no. 1, pp. 90-93, Jan. 1975, DOI: 10.1109/TAP.1975.1141009.

[119] K. F. Lee, S. L. S. Yang, A. A. Kishk, and K. M. Luk, “The Versatile U-Slot Patch Antenna,” *IEEE Antennas Propag. Mag.*, vol. 52, no. 1, pp. 71-88, Feb. 2010, DOI: 10.1109/MAP.2010.5466402.

[120] K. Sarabandi, A. M. Buerkle, and H. Mosallaei, “Compact Wideband UHF Patch Antenna on a Reactive Impedance Substrate,” *IEEE Antennas Wireless Propag. Lett.*, vol. 5, pp. 503-506, Dec. 2006, DOI: 10.1109/LAWP.2006.886302.

[121] D. M. Pozar, “Microwave Network Analysis,” in *Microwave Engineering*, 4th ed., Hoboken, NJ: Wiley, 2012, ch. 4, pp. 165-227, ISBN: 978-0-470-63155-3.

[122] K. F. Tong, K. M. Luk, and K. F. Lee, “Design of a Broadband U-Slot Patch Antenna on a Microwave Substrate,” in *Proc. Asia-Pacific Microwave Conf.*, Hong Kong, CN, Dec. 1997, pp. 221-224, DOI: 10.1109/APMC.1997.659344.

[123] G. H. Bryant, “Antenna Measurements,” in *Principles of Microwave Measurements*, Revised ed., Stevenage, UK: Peregrinus, 1993, ch. 12, pp. 264-344, ISBN: 9780863412967.

[124] D. M. Pozar, “Power Dividers and Directional Couplers,” in *Microwave Engineering*, 4th ed., Hoboken, NJ: Wiley, 2012, ch. 7, pp. 317-379, ISBN: 978-0-470-63155-3.

[125] K. S. Ang, Y. C. Leong, and C. H. Lee, “Impedance-Transforming, Coupled-Line 180° Hybrid Rings with Frequency Independent Characteristics,” in *IEEE MTT-S Int. Microwave Symp. Dig.*, Philadelphia, PA, Jun. 2003, pp. 1239-1242, DOI: 10.1109/MWSYM.2003.1212593.

[126] S. Gruszczynski and K. Wincza, “Broadband Rat-Race Couplers with Coupled-Line Section and Impedance Transformers,” *IEEE Microwave Wireless Components Lett.*, vol. 22, no. 1, pp. 22-24, Jan. 2012, DOI: 10.1109/LMWC.2011.2177649.